Highly Homogeneously Structured Lithium-ion Storage Electrodes via Electrophoretic Deposition

Marianna Rosario Uceda

Doctor of Philosophy

Department of Mining and Materials Engineering

McGill University

Montréal, Québec, Canada

A thesis submitted to the Faculty of Graduate and Postdoctoral Studies of McGill University in partial fulfillment of the degree of Doctor of Philosophy

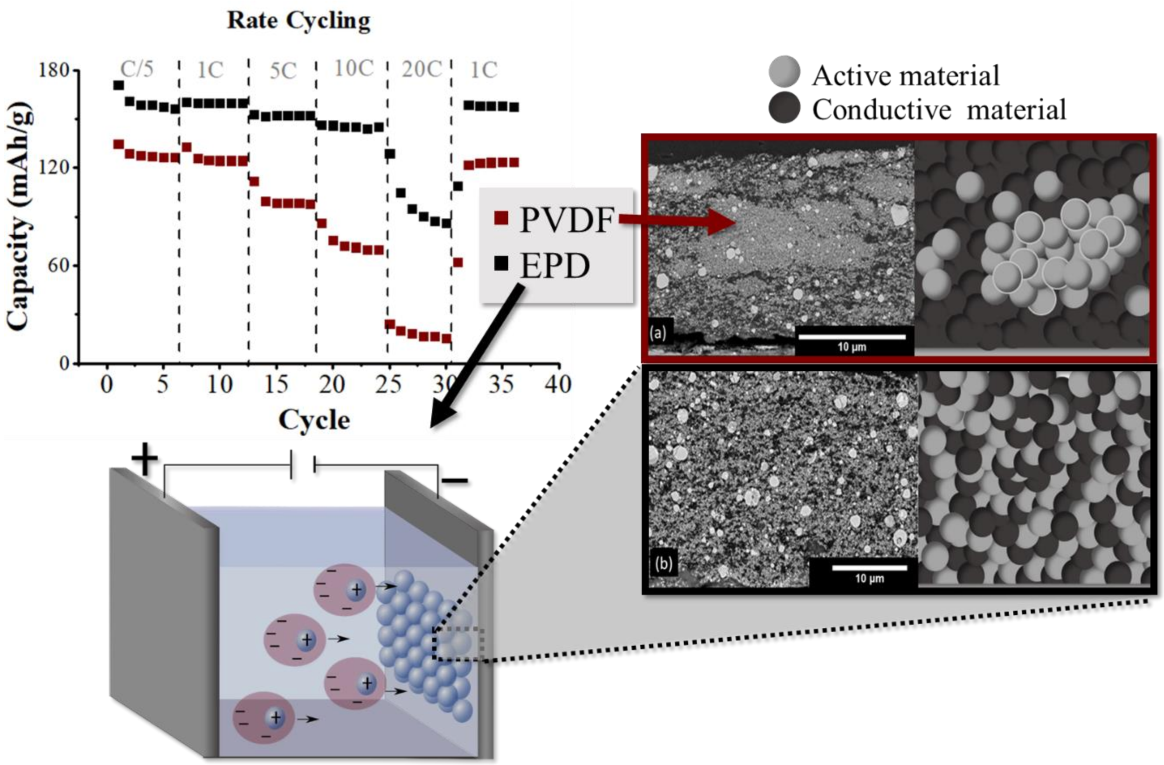
Rate Cycling
C/5
1C
5C
10C
20C
1C
Capacity (mAh/g)
180
120
60
0
0
5
10
15
20
25
30
35
40
Cycle
PVDF
EPD
Active material
Conductive material
(a)
10 µm
(b)
10 µm
+
−

Abstract

Improving lithium-ion battery performance is key in facilitating a green sustainable future. This has led to nanosizing of active materials as means to improve their conductivity by reducing the lithium-ion diffusion length. However, nanomaterials introduce a new challenge during the casting stage of lithium-ion battery electrode fabrication. This technique is unsuited for handling both nanosized and 2D-shaped materials as they introduce rheological challenges. Additionally, the current commercially available casting technique requires the use of a toxic and expensive organic solvent. Thus, the focus of this work was to investigate and design an alternative coating process using electrophoretic deposition (EPD). The work comprises three studies.

In the first study, carbon-coated lithium titanate (LTO) nanoparticles and acetylene black were successfully made into highly-conductive composite anodes via EPD employing styrene butadiene rubber (SBR) as binder in an appropriately selected 90/10 vol.% acetonitrile/water medium. The investigation characterized and optimized the effect of current density on particle movement and deposit growth producing $>20\mu m$ thick mesoporous films on aluminum substrate. The EPD electrode performance was compared to electrodes prepared via the conventional tape-casting. For EPD electrodes, SEM imaging and EDS mapping showed excellent intermixing of carbon components and the active material. Via photoemission electron microscopy (PEEM) coupled with X-ray absorption near edge structure (XANES) it was revealed the SBR binder to be well dispersed within the coating, which translated to the electrode achieving superior rate cycling performance thanks to enhanced conductivity enabled by the hetero-assembling power of electrophoretic deposition.

In the second study, EPD was innovatively applied to fabricate binder-less nanolayered lithium titanate and reduced graphene oxide composite coatings as high-performance Li-ion anodes. This was accomplished by electrophoretically depositing 2D shaped lithium titanate hydrate (LTH) and graphene oxide (GO) precursors and subsequent high temperature reducing annealing to induce the topotactic transformation of LTH into LTO and GO into the so-called reduced graphene oxide (rGO). As graphene (and rGO) is difficult to successfully suspend, using the functionalized precursor circumvented this problem. Likewise, the EPD electrodes are compared to conventionally prepared electrodes with rGO and carbon black. Cross-sectional imaging and EDS mapping showed the EPD electrodes contained a homogeneous coating with the rGO acting as a conductive medium and anchor binder which helped organize the LTO nanosheets into a well built and adherent film. As a result, the EPD nanolayered electrode was found to exhibit superior electrochemical performance in terms of power capability, cyclability and impedance when compared to conventionally prepared electrode.

The final study featured titanium niobate (TNO, $TiNb_2O_7$), this material is a promising replacement anode material for LTO with the potential to deliver higher capacities (378 mAh/g vs. 175 mAh/g of TNO and LTO respectively). Binder-less TNO/rGO electrodes were made through adapting the EPD method developed for the second study – electrophoretically co-depositing TNO and GO followed by high temperature annealing to induce GO to rGO transformation. The final composition of EPD coatings contained 18 wt% rGO which was compared to conventionally prepared electrodes containing 18 wt% rGO and 10 wt% rGO. The rGO was determined in addition to acting as binder and conductive component to have pseudocapacitive contributions to lithium-ion storage. The improved homogeneity in the EPD electrodes allowed better performance in terms of capacity level and retention, i.e. reduced capacity fade in comparison to PVDF-built electrodes of similar composition. This further emphasized the importance of having a uniform composition between active and conductive material to minimize electrode performance degradation.

Overall, through these integrated electrode construction and electrochemical performance analysis studies, EPD is shown to be a superior coating technology with great application potential in manufacturing advanced LIB electrodes.

Résumé

L’amélioration des performances electrochimiques des batteries lithium-ion (Li-ion) est déterminante pour l’atteinte des objectifs de développement durable établis par la communauté scientifique. Parmi les mesures prises en ce sens, la miniaturisation des matières électrochimiquement actives vers les dimensions nanométriques a permis d’améliorer leur conductivité en réduisant la longueur des canaux de diffusion des ions lithium. Cependant, l’utilisation des nanotechnologies amène de nouveaux défis à l’étape de l’enduction lors de la fabrication des électrodes destinées aux batteries Li-ion; l’enduction n’est pas adaptée aux matériaux nanométriques et bidimensionnels puisque qu’elle introduit des problématiques liées à la rhéologie. De plus, les techniques d’enduction utilisées présentement utilisent des solvants toxiques et dispendieux. Ainsi, ce projet a comme objectif d’évaluer et de concevoir une technique d’enduction alternative utilisant les principes de la déposition électrophorétique (DEP). Le travail inclus trois segments.

En premier lieu, des particules nanométriques de titanate de lithium carbonées (LTO) et de noir d’acétylène ont été enduits avec succès comme anode composite hautement conductrice via la DEP en utilisant le styrène-butadiène (SB) dispersé dans un mélange d’acétonitrile et d’eau suivant une proportion volumique 90/10%. Les travaux de recherche ont permis de caractériser et d’optimiser les effets de la densité de courant sur le mouvement des particules et la croissance du dépôt sur le substrat d’aluminium. Ce film pouvait atteindre plus de 20μm d’épaisseur et présenter une structure mésoporeuse. La performance des électrodes ainsi fabriquées a été comparée à celle d’électrodes fabriquée selon la méthode conventionnelle d’enduction. Les analyses en microscopie électronique à balayage (MEB) et la cartographie en spectroscopie dispersive en énergies des rayons-X (EDX) ont montrées que les électrodes provenant de la DEP présentent une excellente mixité des composés carbonés et du LTO. De plus, il a été déterminé via la microscopie électronique par photoémission (MEPE) couplée à la spectroscopie de structure près du front d'absorption de rayons X (XANES) que le liant de SB s’avère être bien dispersé à travers l’enduit. Ceci se traduit par des performances de cyclage supérieure de l’électrode grâce à une meilleure conductivité amenée par la force d’assemblage de la DEP.

Dans un deuxième temps, la DEP a été utilisée pour fabriquer des anodes hautes performances faites d’une nano-couche d’un matériau composite de LTO et d’oxyde de graphène réduit (OGr). Pour ce faire, une matrice composée d’hydrate de titanate de lithium (LTH)

bidimensionnel et d’oxyde de graphène (OG) a été d’abord déposée électrophorétiquement puis recuit à haute température en atmosphère réductrice afin d’induire une transformation topotactique du LTH en LTO et du OG en OGr. Ainsi, l’utilisation du précurseur d’OGr fonctionnalisé a permis de surmonter les problèmes de mise en suspension du GO. Par la suite, les électrodes obtenues par la DEP sont comparées à celles préparées de façon conventionnelle avec le noir de carbone et l’OGr. L’imagerie et la topographie EDX des électrodes en coupe transversale ont démontré qu’elles sont formées d’un enduit uniforme contenant l’OGr agissant comme agent conducteur ainsi que d’agent liant servant à organiser les feuillets nanométriques de LTO en un film adhérent et cohérent. Par conséquent, les électrodes obtenues par DEP ont démontrées des performances électrochimiques supérieures aux électrodes conventionnelles en termes de puissance, d’impédance et de rétention des capacités électrochimiques.

La dernière étude concerne le niobate de titane (TNO, $TiNb_2O_7$) qui s’avère être un matériau anodique prometteur pour remplacer le LTO puisqu’il peut livrer de hautes densités de courant (378 mAh/g vs. 175 mAh/g pour le TNO et le LTO respectivement). Des électrodes de TNO/OGr sans agent liant ont été fabriquées en adaptant le procédé par DEP précédemment développé pour le TNO. Ainsi, les couches électrodéposées sont composées à 18% massique de OGr ce qui correspond à la composition des électrodes conventionnelles soit de 10% ou de 18% massique d’OGr. Par ailleurs, en plus des propriétés liantes et conductrices de l’OGr, il a été déterminé qu’il amenait aussi une contribution pseudo-capacitive à l’emmagasinage des ions lithium dans l’électrode. La plus grande homogénéité des électrodes DEP a permis d’obtenir de meilleures performances électrochimiques en termes de capacité de cyclage et de rétention de cette capacité. Plus précisément, il a réduit les pertes de capacité en comparaison aux électrodes PVDF de composition similaire. Cette amélioration met en évidence l’importance d’avoir une composition uniforme entre la matière active et le composé conducteur afin de minimiser la dégradation des performances des électrodes.

En sommes, suite à l’étude d’une nouvelle méthode intégrée de fabrication des électrodes ainsi que l’analyse de leur performances électrochimiques, la DEP s’avère être une technologie supérieure aux méthodes standards avec de grands potentiels d’application en fabrication avancée des électrodes de batteries Li-ion.

Acknowledgements

I would like to express my appreciation to McGill University, the Natural Sciences and Engineering Research Council (NSERC), Hydro-Québec, and the McGill Engineering Doctoral Award (MEDA) program for the facilities and funding that enabled this project. Furthermore, I thank professors Raynald Gauvin, Nathalie Tufenkji, and Marta Cerruti as well as Aleksandra Djuric, Ranjan Roy, Lihong Shang, David Liu, and Nicholas Broduch for the use of equipment in their laboratories. With respect to my co-authors I would like to thank Dr. Jigang Zhou for his use of the photoemission electron microscope (PEEM) at the Spectromicroscopy (SM) Beamline of the Canadian Light Source (CLS) and internal X-ray near edge spectroscopy (XANES).

I am grateful to Professor Demopoulos for having trusted me with the opportunity to complete this project. His knowledge and guidance helped me persevere through the biggest roadblocks in this project. I would especially like to thank you for your support and kindness, not only throughout the years, but during difficult news related to my loved ones.

I want to thank my fellow students in the HydroMET group who made long hours in the lab bearable with your amazing personalities. I am deeply grateful for the friendships I made through this research opportunity. Rana Yekani, Yan (Helen) Zeng, Hsien-Chieh (Jay) Chiu, Yang Liu, Danae Elizabeth Guerra, Tiffany Turner, Sara Imbriglio, Bo Wang, and Yiwen Chen though this work was physically and mentally taxing, it was made easier and worth it by all of you. As they say, bonds forged through adversity are the strongest. I want to thank my closest friends back home – Jasmine Graham, Tancred Thomas, Kaella-Marie Earle, and Geoff McDonald. I’ve known most of you for longer than a decade and look forward to many more.

I want to thank my loving husband who uprooted his life from Australia to come here with me – an act that served as my greatest inspiration to take chances. You gave me the support I needed to persist and helped me complete this chapter in my life. I would also like to thank my family back home; I will always be grateful for the sacrifice my parents made that served as the stepping stones that ultimately led me here.

This work is a result of all your efforts as well.

Authorship Contributions

Marianna Uceda, Jigang Zhou, Jian Wang, Reynald Gauvin, Karim Zaghib, and George P. Demopoulos (2019). Highly conductive NMP-free carbon-coated nano-lithium titanate/carbon composite electrodes via SBR-assisted electrophoretic deposition. *Electrochimica Acta 299 (2019)* 107-115.

Marianna Uceda, Hsien-Chieh Chiu, Raynald Gauvin, Karim Zaghib, and George P. Demopoulos (2019). Electrophoretically co-deposited $Li_4Ti_5O_{12}$/reduced graphene oxide nanolayered composites for high-performance battery application. Submitted to *Energy Storage Materials*.

Marianna Uceda, Hsien-Chieh Chiu, Raynald Gauvin, Karim Zaghib, and George P. Demopoulos (2019). Percolation Influence on the Fade Mechanism of $TiNb_2O_7$ and reduced graphene oxide composite anodes. To be submitted.

This thesis is presented as a collection of manuscripts as an alternative to the traditional thesis format. Chapters 3, 4, and 5 of this work have been published, or are in revision or submission stages, thus they follow the format of journal papers. The author has conducted the various material preparation, characterization and electrochemical experiments with the exception of the Scanning Electron Microscopy which was done in Professor Gauvin's lab by Nicholas Brodusch and Stephanie Bessette; Transmission Electron Microscopy which was carried out in the Facility for Electron Microscope Research (FEMR) by David Liu; and Photoemission Electron Microscopy and X-ray Adsorption Near Edge Structure (PEEM-XANES) which was done by Jigang Zhou and Jian Wang in Canadian Light Source. While these experiments were carried out by other persons, the author performed all detailed analysis of the experimental results. Professor Demopoulos and fellow lab colleague Hsien-chieh (Jay) Chiu contributed to the electrochemical discussion. The work was performed under the supervision of Professor George P. Demopoulos in collaboration with Dr. Karim Zaghib of Hydro-Québec.

The accuracy of the above statements is attested by the student's supervisor.

G Demopoulos

George P. Demopoulos ____

Table of Contents

1 Introduction 1

1.1 Lithium-ion Batteries and the Global Climate Change Challenge 1

1.2 Thesis Objectives 4

1.3 References 6

2 Literature Review 8

2.1 Battery Mechanism and Key Components 8

2.1.1 Battery Mechanism 8

2.1.2 Capacity-Voltage Curves and Polarization 10

2.1.3 Cathode Materials 13

2.1.4 Battery Separators and Electrolytes 15

2.1.5 Binders 16

2.1.6 Anode Materials 17

2.1.7 Electrode Conductive Additives 21

2.2 Conventional LIB Electrode Fabrication 23

2.3 Electrophoretic Deposition (EPD) 24

2.3.1 Electric Double Layer 25

2.3.2 DLVO model 28

2.3.3 Deposition Mechanisms 29

2.3.4 EPD Modeling 31

2.3.5 Factors Influencing EPD 33

2.3.6 EPD Application in Li-Ion Batteries 35

2.4 References 38

3 Nano-lithium titanate/carbon composite electrodes 50

3.1 Abstract.. 51

3.2 Introduction 51

3.3 Experimental Procedure 54

3.3.1 Materials 54

3.3.2 Carbon Coating on LTO 54

3.3.3 Electrode Preparation... 54

3.3.4 Electrode Characterization and Performance... 55

3.4 Results and Discussion 56

3.4.1 C-coated LTO Nanomaterial.. 56

3.4.2 Deposition Kinetics and Composition 58

3.4.3 Electrochemical Energy Storage Performance 64

3.5 Conclusion.. 67

3.6 Acknowledgements 67

3.7 References 68

4 $Li_4Ti_5O_{12}$/reduced graphene oxide nanolayered composites...................................... 72

4.1 Abstract.. 73

4.2 Introduction 73

4.3 Experimental Procedure 75

4.3.1 LTH Synthesis 75

4.3.2 Electrode Preparation: EPD and PVDF 75

4.3.3 Material/Electrode Characterization 77

4.3.4 Electrochemical Characterization 78

4.4 Results and Discussion 78

4.4.1 Performing EPD 78
4.4.2 Material characterization of EPD LTO/rGO nanolayered composites 79
4.4.3 Electrode Film Homogeneity and Microstructure Engineering via EPD 82
4.4.4 Microstructure-Electrochemistry Relationship 84
4.4.5 Post-mortem analysis of cycled electrodes 87
4.5 Conclusion 93
4.6 Acknowledgements 93
4.7 References 94
5 TiNb2O7 and Reduced Graphene Oxide Composite Anodes 98
5.1. Abstract 99
5.2. Introduction 100
5.3. Experimental Procedure 101
5.3.1. TNO Synthesis 101
5.3.2. Carbon-coating 102
5.3.3. Reduced Graphene Oxide Synthesis 102
5.3.4. Electrode Preparation: PVDF and EPD 102
5.3.5. Material Characterization 103
5.3.6. Electrochemical Characterization 104
5.4. Results and Discussion 104
5.4.1. TNO Synthesis and Suspension Characterization 104
5.4.2. Coating Characterization and EDS Microstructure 106
5.4.3. Electrochemical Performance 111
5.5. Conclusion 118
5.6. Acknowledgements 119
5.7. References 119

6 Synopsis 125

6.1 Global Conclusions 125

6.2 Claims to Originality 127

6.3 Future Work 128

6.4 References 129

7 Appendix 130

A. Supporting information[1] for Chapter 3: Highly conductive NMP-free carbon-coated nano-lithium titanate/carbon composite electrodes via SBR-assisted electrophoretic deposition 130

A.1 Suspension Selection and EPD Parameters 131

A.2 Powder Characterization: SEM and EDS 133

A.3 TGA Curves 134

A.4 Raman Characterization 135

A.5 Hetero-aggregate schematic 136

A.6 PEEM O K-edge 137

A.7 Electrochemical Impedance Spectroscopy 138

A.8 References 139

B. Supporting Information[2] for Chapter 4: Electrophoretically co-deposited Li4Ti5O12/reducedgraphene oxide nanolayered composites for high-performance battery application 140

B.1 GO TEM and Raman 141

B.2 EPD Solvent and Parameter Selection 141

B.3 EPD-Induced Delithiation 144

B.4 Fabrication Schematic 145

B.5 $GO \rightarrow rGO$ transformation XPS 146

B.6 Thermogravimetric Analysis 147

B.7 Cross-sectional EDS for PVDF electrode 148
B.8 EIS Measurements and Modeling 149
B.9 Cyclic Voltammetry 150
B.10 Lithium Diffusivity Calculation 151
B.11 Battery Cycling 152
B.12 References 152

C. Supporting Information[4] for Chapter 5: Percolation Influence on Fade Mechanism of $TiNbO7$ and reduced graphene oxide composite anodes 153

C.1 TNO Synthesis and Carbon-Coating 154
C.2 Ball-milling effect on electrochemical performance 155
C.3 EPD Suspension and Parameter Selection 156
C.4 TGA of EPD Annealed Coating 158
C.5 XPS of C 1s 159
C.6 TNO Structure Schematic and XRD 160
C.7 PVDF Fluoride Maps 161
C.8 Cyclic Voltammetry and Pseudocapacitance 161
C.9 References 164

List of Figures

Figure 1-1: Global primary energy consumption over the years by source (modified from [2]) with magnified section (from years 2000 to 2017) shown inset. 1

Figure 1-2: Ragone plot of different energy storage technologies (modified from [6]). 2

Figure 2-1: LIB schematic of sandwich anode/cathode structure, internally separated by a porous membrane separator, submerged in an electrolyte, and externally connected through a circuit. Li+ ions and electrons are shown moving from anode to cathode during a battery discharge. 9

Figure 2-2: Schematic of an ideal vs actual discharge voltage-capacity curve for LIBs. 12

Figure 2-3: Experimentally observed voltage-capacity discharge curves for various cathode materials [2]. 15

Figure 2-4: Crystal structures of 1D olivine, 2D layered, and 3D spinel and their corresponding lithium ion transport pathways shown by the arrows (modified from [10]). 17

Figure 2-5: Anode lithiation of (a) metallic lithium, (b) ordered graphite[34], (c) LTO [35], and (d) disordered carbon [34]. 21

Figure 2-6: Typical voltage profiles for low rate cycling of (a) LTO at 0.05C [36] and (b) TNO at 0.1C [37]. 22

Figure 2-7: (a) graphite, (b) graphene, (c) graphene oxide, and (d) reduced graphene oxide.. 26

Figure 2-8: (Left) EPD Schematic showing a volume element of the suspension between the electrodes. The particles are positively charged and, under the influence of the electric field, migrating towards the cathode and depositing. (Right) Electric double layer surrounding the particle with potential vs distance from the particle. 29

Figure 2-9: Energy balance diagram (Interaction Energy vs particle distance) for interacting spherical particles. 33

Figure 2-10: EDL distortion 3-step mechanism (adapted from [81,83]). 35

Figure 2-11: EPD schematic with potential gradient (a) before coating forms and (b) after coating forms(adapted from [89–91]). (c) Simplified circuit for EPD cell (adapted from [91]). (d) Mass deposited, w(t), vs. time for a theoretical system................ 37

Figure 3-1: TEM images of (a) pristine LTO and (b, c) C-coated LTO nanoparticles. 56

Figure 3-2: Raman spectra of (a) pristine LTO and (b) carbon-coated LTO (C-LTO)............ 57

Figure 3-3: Deposit growth over stage/time for (a) low and (b) high current densities. 59

Figure 3-4: (a) BSE SEM cross-sectional image of PVDF electrode and corresponding EDS maps of (b) C, (c) Ti, and (d) O. 62

Figure 3-5: (a) BSE SEM cross-sectional image of EPD electrode and corresponding EDS maps of C (b), Ti (c), and O (d).. 62

Figure 3-6: PEEM for EPD electrodes of (a-b) Ti L-edge and (d-e) O K-edge and corresponding XANES image for (c) Ti L-edge and (f) O K-edge. 63

Figure 3-7: EIS Analysis for pressed PVDF and EPD electrodes. The semicircles models are shown inset.. 65

Figure 3-8: (a) Cycling at 1C and (b) Cycling at varying rates of the EPD- and PVDF- based C-LTO/C composite electrodes. 66

Figure 4-1: (a) Cross-sectional SEM image of non-annealed EPD coating consisting of LTH and GO (TEM shown in inset respectively with the corresponding GO SAED). (b) Cross-sectional SEM image of annealed EPD coating consisting of LTO and rGO (LTO TEM shown in inset). (c) Grazing angle XRD patterns for (from top to bottom) PVDF coating ("PVDF LTO"), annealed EPD coating ("EPD LTO"), non-annealed EPD coating ("EPD LTH"), and pristine LTH powder (the peaks are labeled according to ●LTO, ♦LTH, and ▲Cu). (d) XPS Ti 2p spectra for (top to bottom) PVDF coating, annealed EPD coating, and non-annealed EPD coating. (Note: Both SEM cross-sectional images are at the same magnification)........... 81

Figure 4-2: Cross-sectional BSE and EDS mapping of Ti Kα, C Kα, and O Kα for (a) PVDF and (b) EPD coatings showing LTO and rGO distribution. Note that the scale of these two samples is different. Coating schematic for (c) PVDF and (d) EPD electrodes illustrating the contact areas (lithiated LTO shown in blue) between rGO and LTO. 84

Figure 4-3: (a) Cross-sectional SEM BSE image and corresponding Cu Lα EDS mapping of the annealed EPD electrode, and (b) Cu 2p XPS spectra of the annealed EPD electrode. (c) EIS measurements for the EPD, PVDF/rGO, and PVDF/C electrodes normalized for electrode thickness and geometric area, (d) equivalent circuit used to fit the EIS model, and (e) close-up of high frequency zone – R_{Ohm}. 86

Figure 4-4: (a) CV at varying scan rates for (left to right) EPD and PVDF/rGO electrode. (b) EIS comparison of (top to bottom) cycled and pristine EPD and PVDF/rGO electrodes. (c) Ti 2p XPS spectra for (top to bottom) cycled PVDF/rGO, cycled EPD, pristine PVDF/rGO, and pristine EPD electrodes. 89

Figure 4-5: (a) 1C cycling over 150 cycles with coulombic efficiency. (b) 1C voltage-capacity curves for PVDF/C, PVDF/rGO, and EPD electrodes at (top to bottom) cycle 1 and cycle 150 with corresponding differential capacity analysis. (c) Rate cycling for EPD and PVDF/rGO electrodes. (Note: In all the diagrams, EPD is shown in blue, PVDF/rGO in red, and PVDF/C in green). 92

Figure 5-1: (a) XRD pattern (inset is the crystal structure taken from [25]) for pristine and ball-milled/carbon-coated ("BMCC") material. SEM images of (b) pristine and (c) ball-milled/carbon-coated material with corresponding TEM images...................... 105

Figure 5-2: XPS spectra for (a) Nb 3d and (b) Ti 2p of the pristine material, ball-milled TNO ("BM") ball-milled/carbon-coated TNO ("BMCC"), the EPD coating, and the annealed EPD coating. (c) Closeup of XRD pattern showing the main peaks at $2\theta = 24^\circ\ (110), 26^\circ\ (003)$, and $26.4^\circ\ 602$ for pristine, ball-milled, ball-milled/carbon-coated, untreated (non-annealed) EPD coating, and treated (annealed) EPD coating. 108

Figure 5-3: cross-sectional SEM images and EDS maps for (left to right) electrodes made with EPD (after annealing), PVDF with 10 wt.% rGO ("PVDF/10rGO"), and PVDF with 18 wt.% rGO ("PVDF/18rGO") showing SE images and C Kα, Ti Kα, and Nb Kα maps. Please note, the scale varies between the SEM images but remains the same for the corresponding EDS maps. 110

Figure 5-4: (a) CV for 0.1 mV/s showing PVDF electrodes carbon black ("PVDF/CB"), with 10% rGO ("PVDF/10rGO"), 18 wt% rGO ("PVDF/18rGO"), and EPD electrode with 18 wt% rGO ("EPD/rGO"). (b) Corresponding dQ/dV for first cycle at 0.5C of the aforementioned electrodes. CV at sweep rates from 0.1-2 mV/s for (c) EPD/rGO (18 wt% rGO), (d) PVDF/18rGO, and (e) PVDF/10rGO electrodes. Note, all are ball-milled and carbon-coated. 113

Figure 5-5: (a) 0.5C cycling capacity and coulombic efficiency for EPD/rGO and PVDF/rGO electrodes. Charge/Discharge curves for cycles 1, 20, 50, 150 with corresponding dQ/dV plots for (b), (c) PVDF/rGO electrodes and (d) EPD/rGO electrode...... 116

Figure 5-6: EIS for pristine (solid line) and cycled (dotted line) electrodes built with (a) EPD, (b) PVDF/10rGO, and (c) PVDF/18rGO and corresponding equivalent circuits. Please note this EIS model disregards the solid/solution interphase resistance and possible formation of SEI. Additionally, the plots are normalized by dividing by their respective thickness and multiplying by the electrode geometric area 0.785 cm2.. 118

Figure A-1: SEM 2.0kV, 2.6mm, x60k of pristine LTO... 133

Figure A-2: SEM image of carbon-coated LTO (C-LTO) powder with corresponding EDS maps of (b) C, (c) O, and (d) Ti.. 133

Figure A-3: TGA curves for pristine carbon-coated LTO (C-LTO) and electrodes composed of 93/3/4 and 80/10/10 C-LTO/C/SBR respectively. (Inset) TGA for Pure SBR... 134

Figure A-4: C-coated LTO and Carbon (Acetylene Black) nanoparticles are assembled into hetero-aggregates via the bridging action of SBR polymers. 136

Figure A-5: (a, b) PEEM O-K edge of coating of pure SBR and (c) XANES of pure SBR.. 137

Figure A-6: EIS comparison between pressed ("P") and non-pressed ("nonP") electrodes made with (a)PVDF and (b) SBR-EPD... 138

Figure A-7: EIS circuit model. In this model $R1$ is the resistance experienced due to the electrolyte and the current collector and $R2$ is the charge transfer resistance within the deposited layer. The variables $Q1$ and $Q2$ are constant phase elements and the $W1$ is the Warburg element. 138

Figure B-1: (a) TEM for Pristine GO powder and (b) accompanying SAED pattern showing a multi-stacked structure. Raman Spectroscopy of Pure GO and rGO (after annealing) showing (c) D and G peaks and (d) the 2D, D+G, and 2D’ peaks.... 141

Figure B-2: Coatings made of (a) DMF/15s/5stages/35V after drying, (b) ethanol/60s/5stages/35V, and (c) ethanol/15s/20stages/35V. (d) Zeta potential distribution of LTH/GO suspension in ethanol... 143

Figure B-3: (a) Cu 2p XPS spectra of the Cu substrate, (top) native oxide and (bottom) the Cu metal underneath. (b)EPD coatings made from ethanol at 35, 50, 70, and 100V and (c) Ti 2p and Cu 2p spectra for (top) 35V and (bottom) 100V.......................... 144

Figure B-4: EPD fabrication flowchart showing 1. EPD of precursors, 2. Re-lithiation and pressing of the coating, and 3. Annealing to induce precursor transformation to LTO and rGO. 145

Figure B-5: XPS C1s spectra for (a) non-annealed and (b) annealed EPD coating. (c) A schematic of the functional groups on the GO and rGO. (d) XPS C1s spectra for pristine rGO powder. 146

Figure B-6: TGA results and corresponding DTG for (a) for the pristine and annealed EPD coating and (b) pristine LTH slurry and GO powder. 147

Figure B-7: Cross-sectional EDS map of PVDF electrode, (a) BSE image, (b) Ti Kα, (c) C Kα, and (d) F Kα. 148

Figure B-8: Preliminary EIS data – Pristine. 149

Figure B-9: EIS data taken after 10 cycles with closeup of the high frequency range. 149

Figure B-10: Cyclic voltammetry at varying scan rates for the PVDF/C electrode. 150

Figure B-11: Ip vs $v1/2$ relationship from CV curves. 151

Figure B-12: (a) Discharge/Charge curves and (b) corresponding differential capacity analysis dQ/dV for EPD, PVDF/rGO, and PVDF/C electrodes at (left to right) cycle 1, cycle 10, and cycle 150. 152

Figure C-1: Solid-state synthesis flowchart for ball-milled and carbon-coated TNO. 154

Figure C-2: carbon-coating temperature profile and resulting carbon-coating identified through Raman by the “D” and “G” peaks shown in inset. 154

Figure C-3: (a) 0.5C cycling and (b) 0.1 mV/s CV from 0.5 to 3 V vs. Li+/Li of the PVDF coatings using pristine material and milled material mixed with carbon black (“PVDF/CB”). 155

Figure C-4: Current response for varying suspension compositions of GO with achieved coating after ten 15-second deposition stages. 156

Figure C-5: EPD annealed coating cross-sectional (a) SE image, (b) EDS of Cu Lα, and (c) XPS of Cu 2p for non-annealed and annealed EPD coating. 157

Figure C-6: TGA of (a) ball-milled carbon-coated TNO and (b) annealed EPD coating 158

Figure C-7: C 1s spectra for (a) untreated (as is deposit formed through EPD) and (b) treated (i.e. annealed at high temperature) EPD coating 159

Figure C-8: XRD pattern for the EPD coating before and after annealing with ♦ denoting the position of the Cu substrate.. 160
Figure C-9: TNO structure where the inserted lattice planes are: green (110), purple (003) and red (602). The cyan-colored octahedra consist of the transition metals Ti and Nb at the center with the red spheres representing oxygen atoms............................... 160
Figure C-10: cross-sectional SEM images of the PVDF/18rGO and PVDF/10rGO with corresponding F Kα showing PVDF binder dispersion. 161
Figure C-11: Cyclic voltammetry for rGO/PVDF 80/20 wt.% electrode at (a) 0.1 mV/s and (b) at varying scan rates 0.1-2 mV/s. 161
Figure C-12: Cyclic voltammetry at increasing scan rate for (a) EPD/rGO, (b) PVDF/10rGO, and (c) PVDF/18rGO electrodes along with the plotted log of peak cathodic $Nb5+/Nb4+$ current vs. log of sweep rate. 162
Figure C-13: correlation between $i(V)/v0.5$ vs. $v0.5$ for the cathodic sweep of the (a) EPD, (b) PVDF/10rGO, and (c) PVDF/18rGO electrode from 0.6V-3V at sweep rates of 0.1, 0.5, 1, and 2 mV/s showing loss of linearity at varying voltages. 163

List of Tables

Table 1-1: List of LIB-powered electric vehicles organized by driving range compared to the gas-powered 2019 Nissan Maxima. Prices are taken from the respective websites and are given without consideration to governmental incentive subsidies. 3

Table 2-1: Dispersant and their associated mechanism [93] 37

Table 2-2: Electrophoretically deposited graphene coatings or composites for electrochemical energy storage. 40

Table 5-1: Charge/Discharge gap determined from dQ/dV interpeak distances. 115

Table A-1: Raman Peaks of pristine LTO, and carbon-coated LTO (C-LTO) compared to literature values (taken from [2]). 135

Table A-2: Raman D and G carbon peaks of carbon-coated LTO (C-LTO). 136

Table B-1: EPD Parameter selection and water content for ethanol suspension. Solids were 2.5 g/L LTH/GO 93/7 wt% respectively.. 143

Table B-2: XPS C1s de-convoluted peaks and corresponding binding energy (BE) and area intensity normalized relative to the C-C peak.. 146

Table B-3: Decomposition temperatures and cumulative mass loss for pristine LTH/GO and pristine and annealed coating determined through the derivative thermogravimetric curves (DTG). 148

Table B-4: Pristine and Cycled EIS calculated resistance (divided by 103 as per the EIS graphs) and pseudocapacitance values. All values are normalized with respect to the coating thickness and geometric area (divided by thickness and multiplied by area – 0.785cm2). The model used is given in Figure 4-3. 150

Table B-5: Li+ diffusion coefficient values calculated from CV... 151

List of Abbreviations

BET	Brunnaer-Emmett-Teller
CMC	Carboxymethyl Cellulose
CV	Cyclic Voltammetry
DEC	Diethyl carbonate
DLVO	Derjaguin, Landau, Verwey, Overbeek Model
EC	Ethylene carbonate
EDL	Electric Double Layer
EDS	Electron Dispersive Spectroscopy
EIS	Electrochemical Impedance Spectroscopy
EPD	Electrophoretic Deposition
GO	Graphene Oxide
HOMO	Highest Occupied Molecular Orbital
LCO	Lithium cobalt oxide
LFS	Lithium iron silicate
LIB	Lithium-ion battery
LMO	Lithium manganese oxide
LMP	Lithium metal phosphate
LTH	Lithium Titanate Hydrate
LTO	Lithium titanate
LUMO	Lowest Occupied Molecular Orbital
MPV	Mid-point voltage
NMC	Lithium nickel manganese cobalt oxide
NMP	N-2-methyl-Pyrrolidone
OCV	Open current voltage
PAA	Polyacrilyc Acid
PEEM	Photoemission Electron Microscopy
PVDF	Polyvinylidene Fluoride
rGO	Reduced Graphene Oxide
SAED	Selected Area Electron Diffraction

SBR	Styrene Butadiene Rubber
SEI	Solid electrolyte interphase
SEM	Scanning Electron Microscopy
SOC	State-of-Charge
TEM	Transmission Electron Microscopy
TGA	Thermogravimetric Analysis
TNO	Titanium Niobate
XANES	X-ray Near Edge Spectroscopy
XPS	X-ray Photoelectron Spectroscopy
XRD	X-ray Diffraction

List of Symbols

F	Faraday's constant = 96485 C/mol = 26.8 Ah/mol
F_G	Degrees of freedom (Gibbs phase)
C_G	Number of Components (Gibbs phase)
P_G	Number of Phases present (Gibbs phase)
M	Molar mass (g/mol)
n	# of electrons exchanged in reaction
Q_c	Specific capacity (mAh/g)
k_m	Mass transfer coefficient (cm/s)
C_B	Bulk Concentration (mol/cm^3)
D	Diffusion coefficient (cm^2/s)
δ	boundary-layer thickness (cm)
i, i_L	Current density, limiting current density (A/cm^2)
τ	Lithium diffusion time (s)
η	Overpotential (V)
a, b	Tafel constants (V)
ψ_o	Surface potential (mV)
ψ_d	EDL potential after Stern layer at $x = \delta$ (mV)
ψ_ζ	Zeta potential (mV)
k^{-1}	Debye Length
e	Electronic Charge (1.6×10^{-19}C)
ε	Dielectric constant (unitless)
ε_o	Permittivity of a vacuum (C^2/Nm^2)
I	Ionic Strength (mol/m^3)
K_B	Boltzmann constant ($1.38 \times 10^{-23} kgm^2/s^2K$)
a	Particle radius (m)
μ	Electrophoretic mobility (m^2/sV)
v	Particle velocity (m/s)
S	Surface area (m^2)
r	Reaction rate (mol/scm^2)

V_T	Total energy of Interaction (J)
V_A	Van der Waals attractive forces (J)
V_R	Repulsive forces (J)
A	Hamaker constant (J)
$\Delta\phi_1, \Delta\phi_2$	Potential drops (V) at electrode/electrolyte interphase in EPD
$\Delta\phi_d$	Potential drop (V) due to deposit in EPD
$\Delta\phi_s$	Potential drop (V) in suspension during EPD
$R_{p,d}$	Resistance (Ω) due to solid particles in deposit
$R_{i,d}$	Resistance (Ω) due to interparticle liquid in deposit
$R_{p,s}$	Resistance (Ω) due to particles in suspension
$R_{i,s}$	Resistance (Ω) due to ions in suspension
dw/dt	Rate of particle deposition (g/s)
E	Electric field (V)
f	EPD efficiency factor (unitless)
t	Time (s)

1 Introduction

1.1 Lithium-ion Batteries and the Global Climate Change Challenge

Historically, the advent of coal-powered steam engines drove the industrial revolution (that improved quality of life) and enabled the boom in population. This growth in population was accompanied with an equal growth in energy demand. Fossil fuels (such as coal, oil, and gas) are now recognized as having a negative environmental impact due to greenhouse gas emissions (such as carbon dioxide) [1]. In response, renewable energy sources (e.g. solar and wind) are considered the answer to meeting the energy demand whilst reducing further environmental impact. However, despite knowing the effects of fossil fuels, much of the total global energy consumed still comes from these sources. The striking contrast between sources is seen in Figure 1-1.

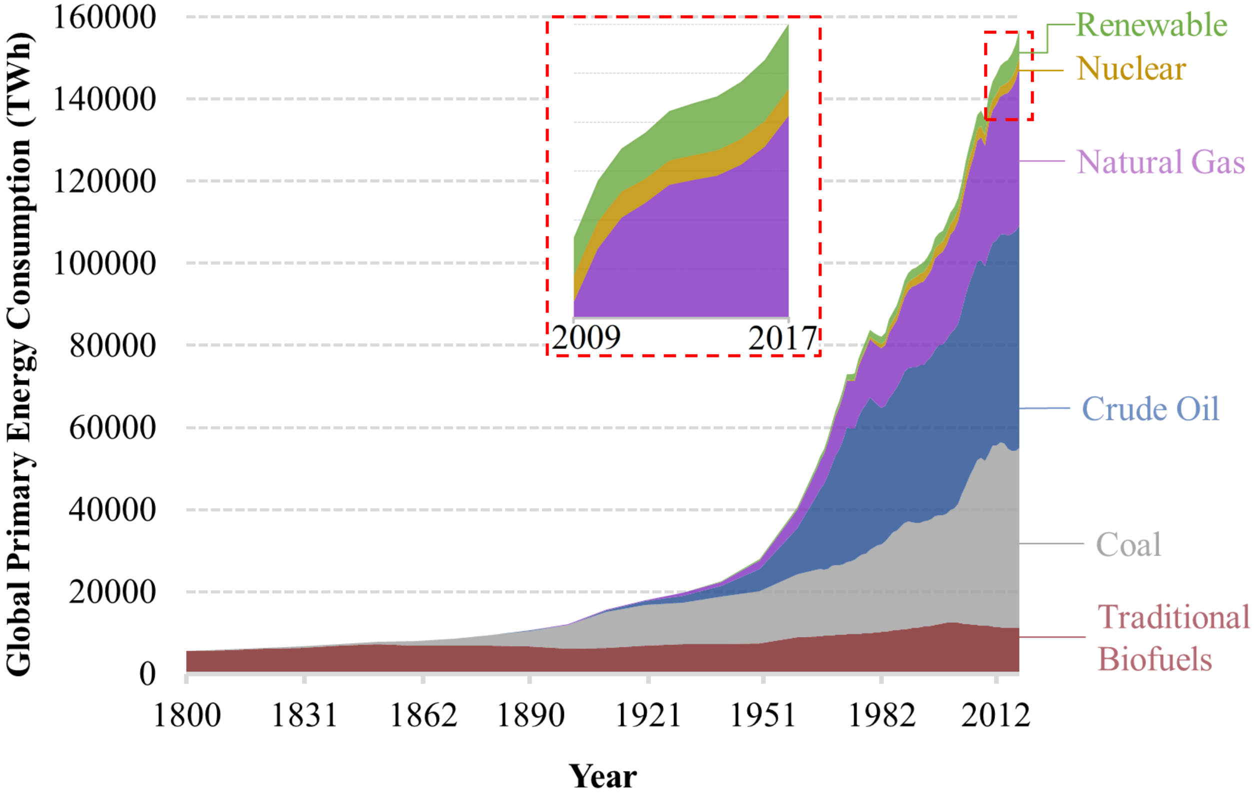

Figure 1-1: Global primary energy consumption over the years by source (modified from [2]) with magnified section (from years 2000 to 2017) shown inset[1].

---

[1] In this graph renewable energy includes solar, wind, hydropower, and other renewable energies (i.e. geothermal, hydrogen, and ocean).

A major issue that has stalled the full implementation of some renewable energy sources (such as wind, and solar) is their intermittent nature which results in downtime [1]. As a result, the energy must be stored for use when energy production is low; hence why energy storage is often referred to as the “missing piece” in the renewable energy solution.

Another major issue with fossil fuel use is the transport sector. Currently, this sector (as measured in 2017) is responsible for 25% of global carbon dioxide emissions. In fact, transport and the above mentioned electricity/heat generation sectors constitute 66% of the total global carbon dioxide emissions and, as reported by the International Energy Agency, are almost solely responsible for the entire global growth in emissions since 2010 [3]. Thus, in an attempt to mitigate further damage from the transport sector the 2015 “Paris Declaration on Electro-Mobility and Climate Change and Call to Action” initiative stated that in order to meet the projected goal of reducing climate change by 2 degrees then electric vehicles must account for 20% of vehicles used by 2030 [4]. This has driven the development of clean electric powered vehicles making use of electrochemical energy conversion or storage technologies [5]. Thus, in the two major sectors which contribute to carbon dioxide gas emission – transportation and electricity/heat production – electrochemical energy storage holds the key to reducing the negative environmental impact.

Figure 1-2 shows a Ragone plot of specific energy vs. specific power for different electrochemical energy storage technologies. In essence, if these systems were used to power a vehicle, the specific energy would dictate how far the car would go and the specific power the speed it could achieve [6].

By virtue of their relatively high specific energy, light weight, good cycle life, and high energy efficiency lithium-ion batteries (LIB) standout from other electrochemical energy storage devices. They have thus become the dominant battery technology in consumer electronics in the last two decades. Currently, they are the preferred battery technology for electric and hybrid vehicles. It is important to note that electric vehicles have consumer-imposed requirements such as long driving range on one charge, short recharge times, and cost parity (whole of life cost per km) [7] among others that must be comparable or better than the internal combustion engine vehicles in order to effectively replace them. Table 1-1 lists LIB-powered electric vehicles and corresponding base retail value, battery size, charge time, and driving range. The gas-powered Nissan Maxima is added as comparison to show the typical driving range of a 68L combustion vehicle. The difference in cost to driving range of the gas-powered vs. the electric vehicles shows the latter technology has yet to meet industry needs.

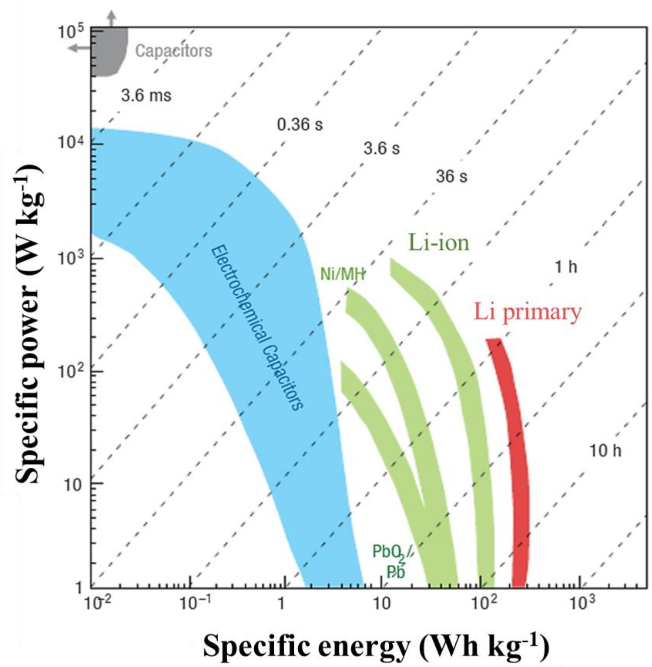

Figure 1-2: Ragone plot of different energy storage technologies (modified from [6]).

Table 1-1: List of LIB-powered electric vehicles organized by driving range compared to the gas-powered 2019 Nissan Maxima. Prices are taken from the respective websites and are given without consideration to governmental incentive subsidies.

Year and Model	**Starting Cost ($CAD)**	**Battery size (kWh)**	**Charge time (min)[2]**	**Range (kmh)**
2019 Nissan Maxima	34,850			680[3]
2019 Tesla Model S	108,990	100	30	595
2018 Kia e-Niro	56,105	64	40	455
2018 Hyundai KONA electric	44,999	64	40	450
2019 Nissan Leaf S+	44,898	62	30	363
2019 Audi e-tron	90,000	95	30	329
2018 BMW i3	57,700	42.2	40	277
2017 Volkswagen e-Golf	35,995	36	40	230

---

[2] charge time to reach 80% charge using 150 kW

[3] Range calculated from 24 mpg (~10 kpL) combined City/Highway gas mileage

This means that in order to use LIBs to achieve the ambitious goal set by the Paris initiative this battery technology – that will enable renewable energy sources and replacement of gas-powered cars by electric vehicles – must be optimized. Furthermore, with LIBs becoming part of the green energy solution it is important that this technology does not actively contributing to the problem it is trying to fix. However, assessing the life cycle of a LIB will show there are stages where this technology cannot be considered environmentally friendly. Among these are the mining and availability of the minerals used (notably cobalt [8]); the toxicity of these materials which furthers the need for recycling battery components [9,10]; fire/explosion risks [11]; and the use of toxic chemicals during production [12]. In essence, optimizing LIB quality must go hand-in-hand with reducing its environmental impact.

Much research has focused on improving LIB quality through developing higher performing electrode materials using metals selected for their high availability and low toxicity. This thesis addresses the fabrication stage and aims at eliminating the use of toxic organic solvents while simultaneously improving electrode physical properties (and therefore LIB quality) through utilizing an alternative fabrication technique: Electrophoretic Deposition (EPD).

EPD is an electrochemical coating (e-coating) technique that involves the suspension of charged particles and subsequent deposition through the application of an electric field (explained in detail in section 2.3) [13,14]. The suspension used is versatile and can be tailored to suit a wide variety (type, size, and shape) of materials. Thus, depending on the type of suspension used, EPD can make the fabrication stage environmentally friendly or even binder-free for apparent cost benefits. Another strength of this technique – and one that is key in the studies included in this thesis – is its self-assembling property and ability to fabricate homogeneous multi-component coatings [15].

1.2 Thesis Objectives

This work investigates electrophoretic deposition (EPD) as an alternative fabrication technique for lithium-ion battery electrodes. The main objectives are to:

1) Engineer systems that allow for the sustainable fabrication of electrodes with improved multiscale (nano-, micro-, and meso-) structural characteristics via the innovative application of EPD.
2) Explore binder-less fabrication of highly conductive nanolayered electrodes using graphene oxide (GO) as de facto binder during EPD that is converted to conductive reduced

graphene oxide (rGO) upon annealing. The graphene is added in order to lower internal electrode polarization and improve electrochemical performance.

3) Control the electrophoretic deposition of different assemblies of active (LTO, LTH, TNO) and conductive (acetylene black or rGO) components and study the resulting coating structure (percolation network) and effect on electrode performance (with emphasis on how it affects capacity fade).

To this end, the physical/chemical/electrochemical properties of the EPD suspension and composite coatings must be studied. A variety of characterization techniques are undertaken including zeta potential analysis of suspension to determine suspension stability; Scanning Electron Microscopy (SEM), Electron Dispersive Spectroscopy (EDS), and Photoemission Electron Microscopy (PEEM) coupled with X-ray Absorption Near Edge Structure spectroscopy (XANES) is performed to determine the microstructure of multicomponent coatings; Thermogravimetric Analysis (TGA) is used to determine amount of active/conductive/binder material present in the multicomponent coatings; pristine materials and coatings are further characterized through X-ray Diffraction (XRD), X-ray photoelectron Spectroscopy (XPS), Raman Spectroscopy, Transmission Electron Microscopy (TEM) coupled with Selected Area Electron Diffraction (SAED); Electrodes are electrochemically tested using Cyclic Voltammetry (CV), Electrochemical Impedance Spectroscopy (EIS), and repeated galvanostatic charge/discharge at a constant rate and rate cycling.

This thesis comprises 5 chapters in addition to this Introductory one. Chapter 2 is a literature review that outlines the theory and mechanisms for LIBs and EPD. Chapters 3, 4, and 5 follow the format of journal papers published (or in revision or submission stages). Chapter 3 focuses on the deposition of multi-component anode composed of nano lithium titanate spinel (LTO, $Li_4Ti_5O_{12}$), carbon black, and styrene butadiene rubber (SBR) through EPD. The EPD cells are compared to conventionally PVDF-made slurry cast electrodes using physical and electrochemical characterization. This chapter serves as an introduction to demonstrate the effectiveness in fabricating composite electrodes using EPD vs. the conventional method. Chapter 4 details the fabrication of binder-less lithium titanate and reduced graphene oxide (rGO) through deposition of 2D precursors via EPD and subsequent annealing to induce transformation from precursors into LTO/rGO. The EPD cells are likewise compared to conventionally prepared cells using reduced graphene oxide or carbon black. This study focuses on the effect of using EPD and a graphene material through post-mortem characterization of the cycled cells. Chapter 5 expands the use of rGO to another anode material: titanium niobate ($TiNb_2O_7$, TNO). Binder-less TNO/rGO electrodes are fabricated to examine the effect of a homogeneous rGO network and pseudocapacitive behaviour of electrophoretically deposited rGO/TNO. Emphasis is placed on the effect of rGO percolation network on the capacity fade. Finally, Chapter 6 summarizes the global conclusions and contributions to originality drawn from this work.

1.3 References

[1] V. Quaschnig, Renewable Energy and Climate Change, 2nd ed., 2019.

[2] H. Ritchie, M. Roser, Energy Production & Changing Energy Sources, Our World Data. (2019). https://ourworldindata.org/energy-production-and-changing-energy-sources.

[3] International Energy Agency, CO2 Emissions from Fuel Combustion 2019: Overview, 2019. https://webstore.iea.org/co2-emissions-from-fuel-combustion-2019-overview.

[4] United Nations Framework Convention on Climate Change, The Paris Declaration on Electro-Mobility and Climate Change and Call to Action | UNFCCC, 2015. https://unfccc.int/news/the-paris-declaration-on-electro-mobility-and-climate-change-and-call-to-action (accessed August 4, 2019).

[5] L.A.-W. Ellingsen, C.R. Hung, G. Majeau-Bettez, B. Singh, Z. Chen, M.S. Whittingham, A.H. Strømman, Nanotechnology for environmentally sustainable electromobility, Nat. Nanotechnol. 11 (2016) 1039–1051. doi:10.1038/nnano.2016.237.

[6] V. Dusastre, Materials for Sustainable Energy: A collection of peer-reviewed research and review articles from Nature Publishing Group, Nature Publishing Group UK, 2010.

[7] F. Sioshansi, J. Webb, Transitioning from conventional to electric vehicles: The effect of cost and environmental drivers on peak oil demand, Econ. Anal. Policy. 61 (2019) 7–15. doi:10.1016/j.eap.2018.12.005.

[8] K. Nansai, K. Nakajima, S. Suh, S. Kagawa, Y. Kondo, W. Takayanagi, Y. Shigetomi, The role of primary processing in the supply risks of critical metals, Econ. Syst. Res. 29 (2017) 335–356. doi:10.1080/09535314.2017.1295923.

[9] C. Liu, J. Lin, H. Cao, Y. Zhang, Z. Sun, Recycling of spent lithium-ion batteries in view of lithium recovery: A critical review, J. Clean. Prod. 228 (2019) 801–813. doi:10.1016/j.jclepro.2019.04.304.

[10] F. Pagnanelli, E. Moscardini, P. Altimari, T. Abo Atia, L. Toro, Cobalt products from real waste fractions of end of life lithium ion batteries, Waste Manag. 51 (2016) 214–221. doi:10.1016/j.wasman.2015.11.003.

[11] B. Liu, Y. Jia, C. Yuan, L. Wang, X. Gao, S. Yin, J. Xu, Safety issues and mechanisms of lithium-ion battery cell upon mechanical abusive loading: A review, Energy Storage Mater. (2019). doi:10.1016/j.ensm.2019.06.036.

[12] D. Claus, Oak Ridge National Labratory (ORNL), Lithium ion batteries and their manufacturing challenges, The Bridge. 45 (2015) 21–24.

[13] L. Besra, M. Liu, A review on fundamentals and applications of electrophoretic deposition (EPD), Prog. Mater. Sci. 52 (2007) 1–61. doi:10.1016/j.pmatsci.2006.07.001.

[14] P. Amrollahi, J.S. Krasinski, R. Vaidyanathan, L. Tayebi, D. Vashaee, Electrophoretic Deposition (EPD): Fundamentals and Applications from Nano- to Microscale Structures, in: M. Aliofkhazraei, A.S.H. Makhlouf (Eds.), Handb. Nanoelectrochemistry Electrochem. Synth. Methods Prop. Charact. Tech., Springer International Publishing, Cham, 2016: pp. 561–591. doi:10.1007/978-3-319-15266-0_7.

[15] L. Ye, K. Wen, Z. Zhang, F. Yang, Y. Liang, W. Lv, Y. Lin, J. Gu, J.H. Dickerson, W. He, Highly Efficient Materials Assembly Via Electrophoretic Deposition for Electrochemical Energy Conversion and Storage Devices, Adv. Energy Mater. 6 (2016). doi:10.1002/aenm.201502018.

2 Literature Review

In this Chapter, information regarding the LIB working principles, commonly used cathode and anode materials, and the conventional fabrication method is provided. Problems arising from the conventional method are discussed to explain the need for alternative fabrication processes. Section 2.3 goes into detail behind the mechanisms that govern EPD as this fabrication technique forms the core of this thesis.

2.1 Battery Mechanism and Key Components

2.1.1 Battery Mechanism

Lithium-ion batteries are a type of rechargeable battery that consist of an anode, cathode, separator, electrolyte, connective wiring, and a casing which encloses the components. A simplified cell schematic is shown in Figure 2-1; in this image the cathode and anode are composed of lithium cobalt oxide ($LiCoO_2$, LCO) and graphite, respectively, coated onto metallic current collectors. The electrodes are held within the casing and submerged in a 1M electrolyte consisting of lithium hexafluorophosphate ($LiPF_6$) salt dissolved in ethylene carbonate (EC) and diethyl carbonate (DEC). The cathode is composed of alternating cobalt oxide arrays and freely-moving lithium-ions and, similarly, the graphite is composed of stacked graphene with *sp2* hybridized layers. They are referred to as intercalating compounds because the lithium ions may move freely between the anode and cathode depending on whether the battery is being charged or discharged. When the battery is in a charged state, the lithium ions are contained within the graphite matrix. Once connected, both lithium ions and electrons migrate towards the cathode (albeit through different paths) where the reduction of $the\ Co^{4+}/Co^{3+}$ couple allows for the lithium to be stored. The corresponding cathodic and anodic reactions that occur during discharge are shown in equations Eq. 2-1 and Eq. 2-2 respectively. Connecting this cell to a power source can reverse these reactions and recharge the battery. During charging (intercalation into the anode), the lithium ion maintains the charge and the carbon is reduced which achieves overall charge balance.

$$xLi^+ + xe^- + Li_{1-x}CoO_2 \rightarrow LiCoO_2 \qquad \text{Eq. 2-1}$$

$$Li_xC_6 \rightarrow xLi^+ + xe^- + xC_6 \qquad \text{Eq. 2-2}$$

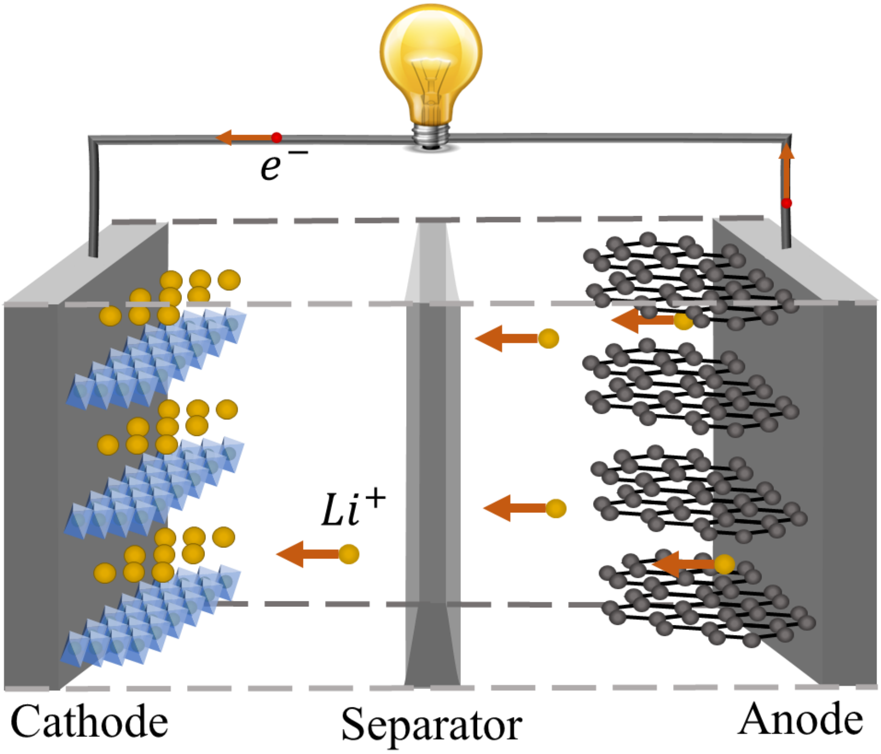

Figure 2-1: LIB schematic of sandwich anode/cathode structure, internally separated by a porous membrane separator, submerged in an electrolyte, and externally connected through a circuit. Li^+ ions and electrons are shown moving from anode to cathode during a battery discharge.

To describe battery performance, some key parameters commonly used are energy density, power density, rate capability, and cycle life [1].

The **energy density** of a battery is defined by the quantity of energy stored per unit volume (Wh/L). It is also commonly expressed as gravimetric or specific energy density which is the battery energy per unit mass (Wh/kg). Energy density is the product of the open circuit voltage (V_{OC}) and the specific capacity (Q_c); the latter represents the amount of charge stored per unit mass (Ah/g). The theoretical specific capacity for a material is a useful property that can be calculated from the amount of charge transferred (n), Faraday's constant (F, C/mol), and the molar mass (M, g/mol) of the material as shown in Eq. 2-3. For LCO the theoretical capacity is calculated to be 274 mAh/g assuming a full lithium ion can be extracted per mol of material, however due to structural instability this is not possible therefore the observed capacities are closer to 140-150 mAh/g [2,3]. This property varies depending on the type of material with some having a much higher capacity.

$$Q_c = \frac{nF}{M} \qquad \text{Eq. 2-3}$$

For a one electron exchange reaction with LCO the theoretical specific capacity would be calculated as:

$$Q_c = \frac{(1)\left(96500\frac{C}{mol}\right)}{97.87\frac{g}{mol}} \times 1000\frac{mA}{A} \times \frac{h}{3600s} = 273.8\frac{mAh}{g}$$

The **power density** is defined as the rate of energy transfer (W/kg, W/L) that the material can handle per unit volume or mass.

Rate capability refers to the rate of charge and discharge, typically the applied current (to charge the battery) is normalized with respect to its theoretical capacity – this is referred to as the C-rate. For example, 1g of LCO may deliver 274 mAh (according to theoretical capacity), to charge for 1 hour 274 mA must be applied – this is referred to as 1C charging rate. Similarly, to charge for 30 mins $\left(274\ mAh \times \frac{1}{0.5\ h}\right)$ 548 mA must be applied – this is referred to as 2C rate.

Cycle life refers to the amount of cycles (at a given C-rate) that the battery can efficiently perform. Battery capacity diminishes with age due to instability of the electrolyte in the operating potential of the battery which leads to unwanted side reactions that trap and deplete the lithium ions – this is referred to as chemical degradation. Mechanical degradation also occurs due to the diffusion of lithium ions within the electrode material that introduces diffusion induced stresses (DIS) due to volume changes. These stresses may cause particle fracture which would expose new surface area to the electrolyte and facilitate further unwanted reactions (further explained in Section 2.1.3) [4].

2.1.2 Capacity-Voltage Curves and Polarization

During battery cycling, the capacity can be measured as a function of potential to produce discharge/charge curves (discharge curve shown in Figure 2-2). During discharge, while the lithium ions migrate from anode to cathode, the cell voltage will drop. The mid-point voltage (MPV) is the nominal voltage and it's the quoted voltage in batteries. A flat discharge curve means less voltage variation which is ideal in many electronic designs. LIBs often do not have this ideal flat discharge curve which means they are unable to maintain a constant voltage over time.

The shape of the discharge curve is important to understand the behaviour of the cell. At the start, the initial voltage is the open circuit voltage (OCV) – this is the initial potential difference between anode/cathode when there is no current. Ideally the cell would discharge at this constant voltage however in practice the potential drops during discharge. The potential drop can be attributed to [1]:

1) Activation polarization
2) IR drop – Ohmic polarization
3) Concentration polarization

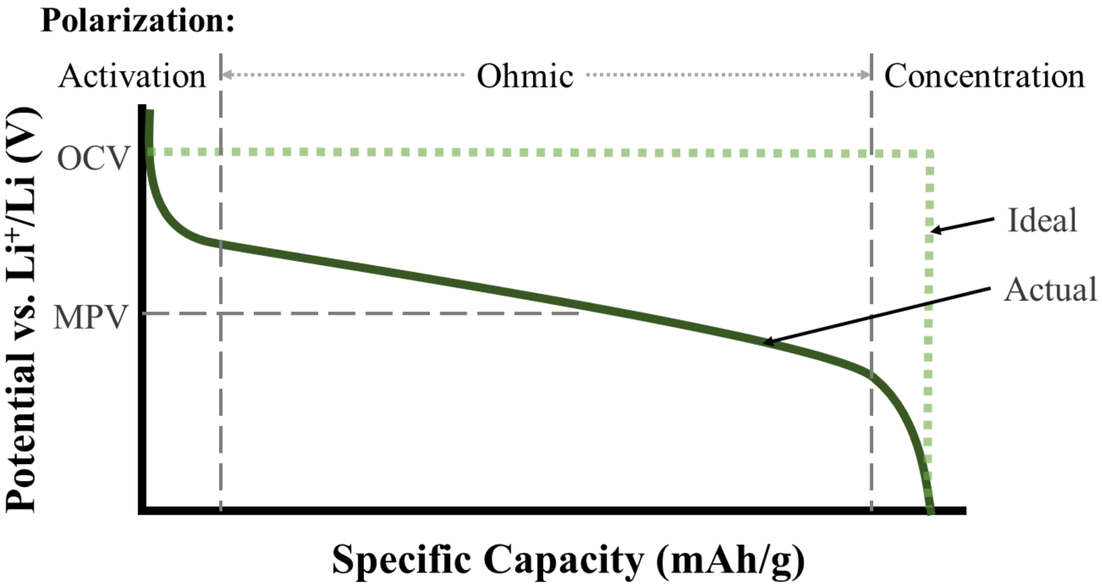

Figure 2-2: Schematic of an ideal vs actual discharge voltage-capacity curve for LIBs.

Activation polarization refers to the electrochemical drive needed for the redox reaction to occur. It is important to note that a reaction occurs in a series of steps at the electrode/electrolyte interface. Reaction rates are determined by the slowest step referred to as the rate limiting step. The term “activation” is used since the slowest step is determined by the largest activation energy required. For LIBs this is the slow charge transfer reaction at the interface.

The current flow resulting from the electrode polarization, or overpotential, can be determined through the Tafel relationship:

$$\eta = a \pm b \log i \qquad \text{Eq. 2-4}$$

Where η = overpotential (V), i = current density ($\mathrm{A/cm^2}$), and a and b = Tafel constants (V). The rate of an electrochemical reaction refers to the charge transfer reaction (only when there is no concentration limitation), thus the rate of (the forward) reaction can be related to the current density:

$$r = \frac{i}{nF} = \frac{\left(\frac{A}{cm^2}\right)}{\frac{C}{mol}} = \frac{\left(\frac{A}{cm^2}\right)}{\frac{A \cdot s}{mol}} = \frac{mol}{s\ cm^2}$$

$$i = nFr \qquad \text{Eq. 2-5}$$

Where r is the reaction rate which is proportional to the reaction rate constant and concentration of redox species. The reaction rate constant can be directly related via the Arrhenius equation to the temperature. The system is said to be in activation polarization when there are sufficient reactants at the interface, namely the reaction is not limited by supply of reactants (mass transport). Thus, the initial drop after discharge of a battery begins is associated to the activation energy required. This drop can be altered by varying the temperature of the cell. A higher temperature will lead to a faster reaction rate and larger currents – however, in practice a higher temperature may also accelerate unwanted side reactions such as electrolyte decomposition [5].

The gradual decrease in voltage during discharge is attributed to Ohmic IR drop due to internal cell resistance/impedance and thus referred to as **ohmic polarization.** The total internal impedance is the sum of 1) the electrolyte ionic resistance, 2) electronic resistance of the active mass, and 3) contact resistance between layer + current collector. In other words, the IR drop represents the resistance against electron and ion flow through electrode and electrolyte. This can be reduced by increasing electrolyte conductivity, pressing the electrode to minimize contact resistance and electronic resistance, and increasing temperature. The presence of a flat discharge curve results when the effect of changing reactant to product is minimal (i.e. the composition does not matter). Typically, this occurs with materials that exhibit two phases due to the Gibbs phase rule:

$$F_G = C_G - P_G + 2 \qquad \text{Eq. 2-6}$$

Where F_G is the degrees of freedom, C_G is the number of components (i.e. Li^+ ions and host matrix, C=2) present, and P_G is the number of phases present. For systems such as lithium titanate spinel ($Li_4Ti_5O_{12}$, LTO), lithiation causes transformation of the spinel phase to the lithiated rock-salt phase. This means that C=2, P=2, and consequently F=2, when the temperature and pressure are fixed there are no degrees of freedom which in turn fixes the potential. Materials may have a remaining degree of freedom, this means the system is not fully defined and in these cases the potential will vary depending on other parameters such as composition [6,7].

At high overpotentials when the reactants are completely consumed the reaction rate is driven by the diffusion of reactants to the electrode surface and referred to as **concentration polarization**.

The maximum current, referred to as the limiting current i_L, is reached. The rate can be related to Fick's diffusion law where the concentration gradient dictates the diffusion rate:

$$r = D\frac{dC}{dx}$$

$$i_L = nFD\frac{dC}{dx}$$

$$i_L = \frac{nFD(C_B - C_s)}{\delta}$$

$$i_L = nk_mFC_B \qquad \text{Eq. 2-7}$$

Where $D =$ diffusion coefficient ($\mathrm{cm^2/s}$) of the reactants, δ =boundary-layer thickness (cm), $\mathrm{C_B}$ =bulk concentration ($\mathrm{mol/cm^3}$), $\mathrm{C_s}$=surface concentration ($\mathrm{mol/cm^3}$), and $\mathrm{k_m = D/\delta}$ is the mass transfer coefficient ($\mathrm{cm/s}$).

Thus, the cell voltage, E (V), can be expressed as [1]:

$$E = E_{OCV} - \left(\eta_{ct,a} + \eta_{c,a}\right) - \left(\eta_{ct,c} + \eta_{c,c}\right) - iR_i \qquad \text{Eq. 2-8}$$

Where E_{OCV} is the open-circuit voltage (V), $\eta_{ct,a}$ and $\eta_{ct,c}$ are the anodic and cathodic overpotential due to charge transfer respectively (V), $\eta_{c,a}$ and $\eta_{c,c}$ are the anodic and cathodic overpotential due to concentration overpotential (V), i is the operating current density of cell ($\mathrm{mA/cm^2}$), and R_i is the internal cell resistance (Ω).

2.1.3 Cathode Materials

The cathode electrode is made of the active intercalation material, a conductive material (typically acetylene black) and a binder. LCO has been the most common type of LIB cathode material used in portable electronic devices. It holds this privilege due to the fact that it was the first material successfully tested and commercially applied [8,9]. However, among the current problems associated with the use of LCO are the accessibility to cobalt and safety concerns. LCO is toxic and has poor thermal stability, this is problematic in cases where the battery is damaged (allowing for a short circuit) or used at high temperatures. At high temperature the material decomposes and releases oxygen gas which further fuels the exothermic reaction and leads to a fire [2]. This safety issue, coupled with the relatively low observed capacity and unavailability of cobalt, has driven research towards new cathode materials.

Aside from safety, cathode materials must satisfy other performance-related requirements including providing a high working voltage, reversibly storing and releasing lithium ions with minimal structural changes, and the material must have a high ionic and electronic conductivity. Thus, new chemistries have emerged such as lithium metal phosphate (LMP, $LiMPO_4, M = Fe, Mn$) lithium nickel manganese cobalt oxide (NMC, $LiNiMnCoO_2$), lithium manganese oxide (LMO, $LiMn_2O_4$), and lithium iron silicate (LFS, Li_2FeSiO_4) among others. A performance comparison for some of these materials is shown in Figure 2-3.

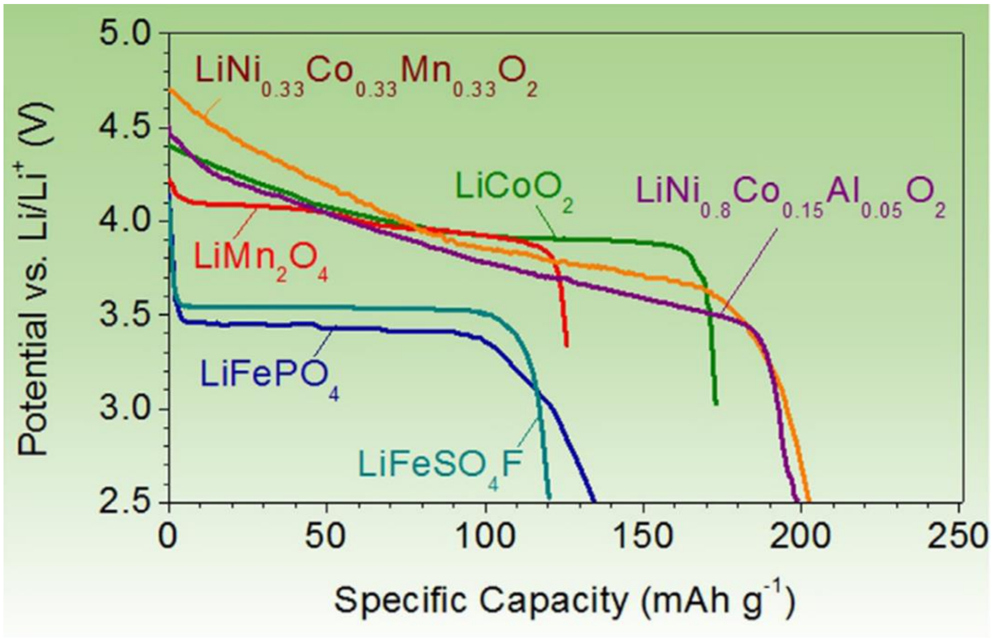

Figure 2-3: Experimentally observed voltage-capacity discharge curves for various cathode materials [2].

For the intercalation mechanism, the cathode crystal structure may be layered, spinel, or olivine (Figure 2-4). These materials are classified based on the lithium ion diffusion pathways as 1D, 2D and 3D [10]. Perpendicularly to the lithium diffusion paths, the host material is subject to expansion and shrinkage during lithium diffusion which can lead to exfoliation of the structure. This leads to the mechanical degradation of the material mentioned in Section 2.1.1.

Improving the overall performance of the material involves adding a conductive substance to the coating mix and/or engineering the material. For the latter, the optimum way to improve battery performance is to minimize particle size [11]. This increases the contact area between the particle and the electrolyte which will improve charge transfer kinetics. Additionally, it minimizes the diffusion length the lithium ions must travel to reach the interior of the particle [12]. This highlights the need for nanosized materials [13].

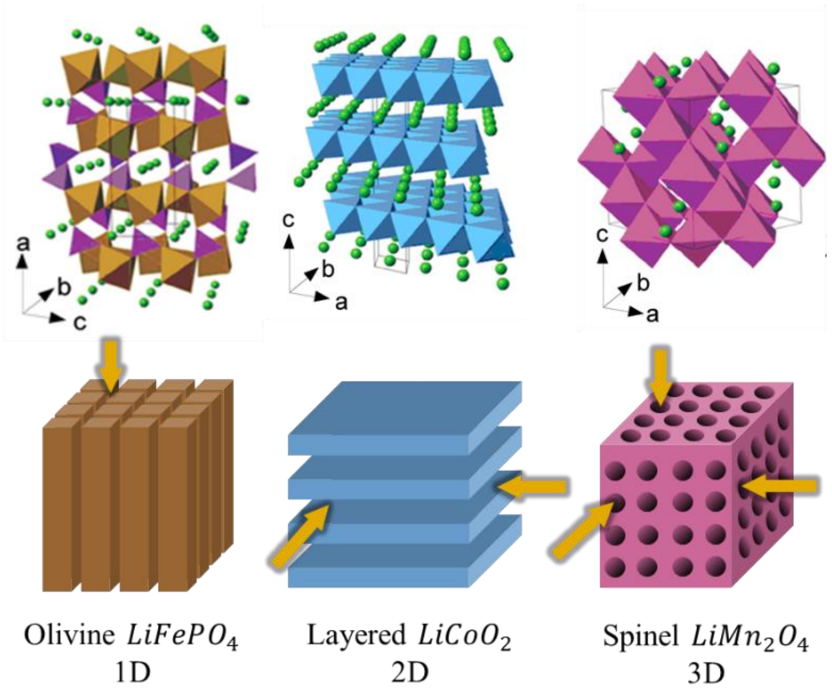

Olivine $LiFePO_4$ 1D

Layered $LiCoO_2$ 2D

Spinel $LiMn_2O_4$ 3D

Figure 2-4: Crystal structures of 1D olivine, 2D layered, and 3D spinel and their corresponding lithium ion transport pathways shown by the arrows (modified from [10]).

2.1.4 Battery Separators and Electrolytes

The separator, typically composed of single or multilayer polymer sheets made of polyolefins, prevents electrical contact between the electrodes whilst allowing for Li-ion transport due to its microporous structure. Due to these necessary functions there are various membrane properties that must be controlled such as permeability, wettability, porosity, chemical stability, mechanical strength, thickness, and thermal shrinkage [1]. Preventing contact between electrodes is paramount to safety as this will cause a short circuit which may lead to thermal runaway reactions. This means there is always a trade-off between the mechanical and transport-related properties. The membranes are designed with a shutdown mechanism, for multilayer membranes this is accomplished by using two layers with lower phase transition temperatures. At higher temperature the component with the lower phase transition temperature will melt and close the pores preventing ion transport and current flow. This permanently damages the battery [14,15].

The electrolyte is typically a dissolved lithium salt in an organic solvent. Among the solvents is ethylene carbonate, dimethyl carbonate, ethyl acetate, propylene carbonate, and mixtures of them. The most common salts are $LiPF_6$, $LiBF_4$, $LiClO_4$, and $LiAsF_6$ [16]. The type of electrolyte used is determined by its stability with respect to the potential window of the anode/cathode selected in order to prevent electrolyte decomposition.

2.1.5 Binders

Binders are key enabling polymers in the fabrication of the cathode or anode electrodes. Binders have stringent requirements that relate to battery performance and mechanical properties. Due to the oxidative/reductive environment in a battery the binder must be inactive over the working potential of the battery and remain stable in the electrolyte. In terms of mechanical properties, it must have a high melting point and allow for flexible coatings while still maintaining good interparticle adhesion/contact. A key requirement for an effective battery is to minimize the amount of non-active material present – this includes the binder, conductive material, separator, and current collectors. At the same time there must be sufficient binder to maintain the coating integrity and the adhesion between coating and current collector. The most common type of binder is polyvinylidene fluoride (PVDF) which is a long nonreactive fluoropolymer. Polymers will swell when in contact with an electrolyte which can lead to cracks in the coating, separation between the coating and current collector, and ultimately battery degradation. Thus, the use of a polymer introduces a new binder requirement: limited swelling. Finally, the binders must also be cost-effective and environmentally safe.

PVDF has two key problems, 1) indirectly, it is environmentally unfriendly due to the nature of the solvent used (discussed in Section 2.2) and 2) it is unsuitable for high capacity electrodes. The latter is because these high energy density materials tend to experience large volume changes which generate more stress and lead to separation of the coating from the current collector (as is the case for Si and Si-alloy anodes) [17]. Binders work due to intermolecular interactions such as the weak Van der Waals and hydrogen bond forces that exist between the binder and active/conductive components. These interactions are heavily influenced by the functional groups that may cause induced dipoles. Fluoride is the most electronegative element meaning PVDF has a permanent dipole between -F and -H in the backbone. However, these dipole interactions are not enough to hold the active/conductive material together if it undergoes large volume expansion. Studies have shown having carboxylate functional groups leads to hydrogen bonding and/or covalent bonding between the carboxylate groups and the hydrogen on the active material[18,19]. To this end carboxylate-containing binders such as polyacrylic acid (PAA) and carboxymethyl cellulose (CMC) have been researched. CMC has the advantage of being water-soluble (as opposed to the organic-soluble PVDF), another such binder researched is styrene butadiene rubber (SBR) [17,19]. Employment of an aqueous-based binder has the advantage, other than its green character, of requiring a less intensive heating stage to remove the solvent (N-2-methyl-pyrrolidone, NMP, boiling point is $\sim 203℃$) from the coating. Furthermore, the binders have been shown to perform better or on par with the conventional PVDF electrodes [20] and are cheaper to buy than PVDF [21] making them economically more attractive. Nevertheless PVDF is still the dominant cathodic binder but CMC and SBR have now become the dominant anodic binders [22,23].

2.1.6 Anode Materials

Similar to the cathode, there are various anode chemistries available. At the early stage of LIB development researchers tried to use lithium metal as anode due to its high theoretical capacity of 3860 mAh/g and low density of 0.59 $\mathrm{g/cm^2}$ [24]. The reaction whereby lithium is stored is Li^+/Li plating, this becomes problematic during cycling as some deposits form unevenly on the anode surface and form dendrites (Figure 2-5 (a)). Growth of these dendrites could eventually lead to a short circuit which poses a safety risk. Alternatively, carbonaceous materials with varying graphitisation have become the standard in LIB anodes. This is because the carbon structure allows for reversible lithium insertion (as shown in Figure 2-1 and Eq. 2-2) whilst avoiding dendrite formation. The level of graphitisation is important as less graphitic carbon tends to have lower capacity. During intercalation graphitic carbon accommodates lithium by arranging the carbon layers in “AAA…” stacking (the pristine carbon stacking will vary) with an accompanying interlayer distance change from 0.325-0.335 to 0.356-0.376nm [25,26] (Figure 2-5 (b)). Carbon with a turbostratic arrangement (i.e. amorphous carbon) displays lower capacities in comparison to graphitic carbon as it is unable to rearrange into the “AAA…” stacking (Figure 2-5 (d)).

Types of carbon can also be categorized based on its propensity to graphitize upon treatment. Soft carbons are moderately disordered crystallites that are graphitizable at high temperatures [27]. At high temperature the turbostratic arrangement is removed which reduces strain in the material. On the other hand, hard carbons are highly disordered crystallites that are not easily graphitizable. Soft carbon was the first carbonaceous anode material adopted by Sony that displayed a large gravimetric energy density of 80 Wh/kg and high reversibility. The second generation saw these replaced by hard carbon anodes which provided a larger gravimetric energy density of 120 Wh/kg and preserved the high reversibility [28]. The lithiation process of hard carbons is explained by the "falling cards model" proposed by Dahn et al. [29]. This theory claims that annealing allows for the graphene layers to shift within the hard carbon and form organized regions whilst causing two pores to coalesce. Additionally, each layer of non-stacking graphene can accommodate lithium ions on either side which – coupled with the increased micropore size – allows for a higher capacity. The hard carbon proved problematic with electronics as the overall cell voltage changes drastically during charge/discharge. Additionally, to achieve a high enough capacity the cut-off voltage must be placed close to 0 V vs. Li/Li^+ which risks for lithium to plate on the carbon material and begin forming dendrites. To address these issues, the third generation Sony batteries switched to graphite which allowed for a higher gravimetric energy density of 160 Wh/kg, a specific capacity of 372 mAh/g, and a lithiation/delithiation potential of 0.1 V vs. Li/Li^+ [28]. Modification of the electrolyte allowed for the formation of a solid-electrolyte interphase (SEI) layer. This is a surface layer that forms on the anode when the electrolyte reacts with the graphite which leads to the irreversible entrapment of lithium ions. Thus, while initially a protective layer, the SEI causes capacity loss and eventually battery failure [30]. Another disadvantage of this material is the volume change that occurs during (de)lithiation of ~13 vol% [31].

The need to eliminate SEI formation led to the use of transition metal anodes such as lithium titanate spinel ($Li_4Ti_5O_{12}$, LTO). LTO has a 3D spinel structure, shown in Figure 2-5 (c), that allows for lithium insertion at a working voltage of 1.55V vs. Li/Li^+ and yields a lower capacity of 175 mAh/g. The voltage profile can be seen in Figure 2-6, the stable voltage plateau observed is the result of the two-phase transformation (as explained in section 2.1.2).

During lithiation spinel $Li_4Ti_5O_{12}$ (8.3595Å) changes to the rock-salt $Li_7Ti_5O_{12}$ (8.3538Å) by accepting 3 Li^+ due to the Ti^{4+}/Ti^{3+} redox couple using a potential window of 1-3V (vs. Li^+/Li). After rock-salt formation this material may be further lithiated to form $Li_9Ti_5O_{12}$ to yield a theoretical 293 mAh/g capacity, however this requires a potential window of 0.01-3V (vs. Li^+/Li) and results in loss of the working potential plateau, increase in polarization, and reduced electrochemical reaction kinetics [32,33]. The lithiation reaction is given by:

$$Li_4Ti_5O_{12} + xLi^+ + xe^- \rightarrow Li_{4+x}Ti_5O_{12}; 0 \leq x \leq 5 \qquad \text{Eq. 2-9}$$

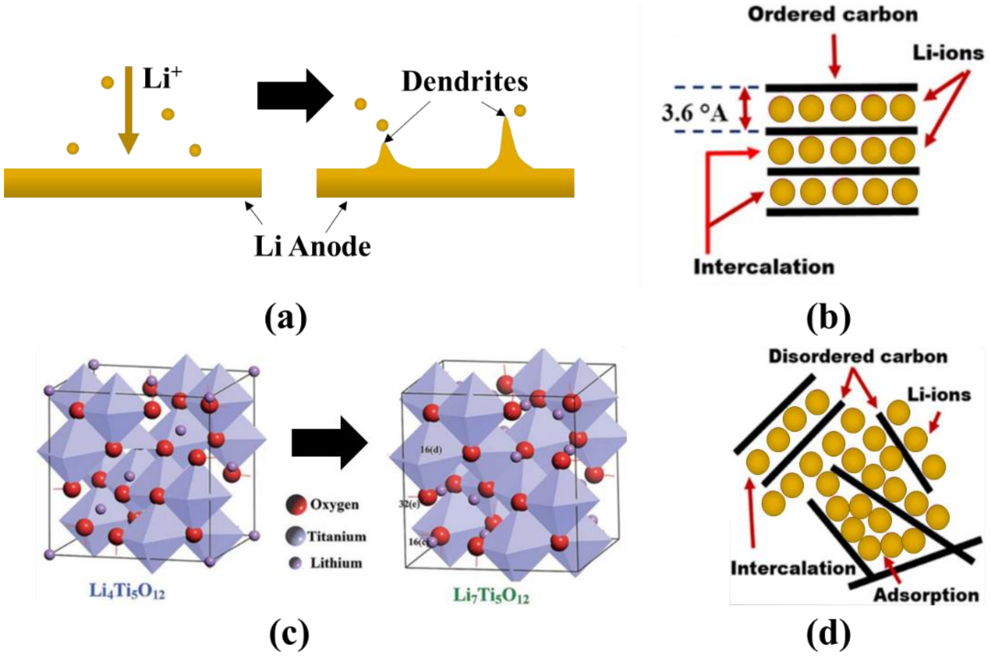

Figure 2-5: Anode lithiation of (a) metallic lithium, (b) ordered graphite[34], (c) LTO [35], and (d) disordered carbon [34].

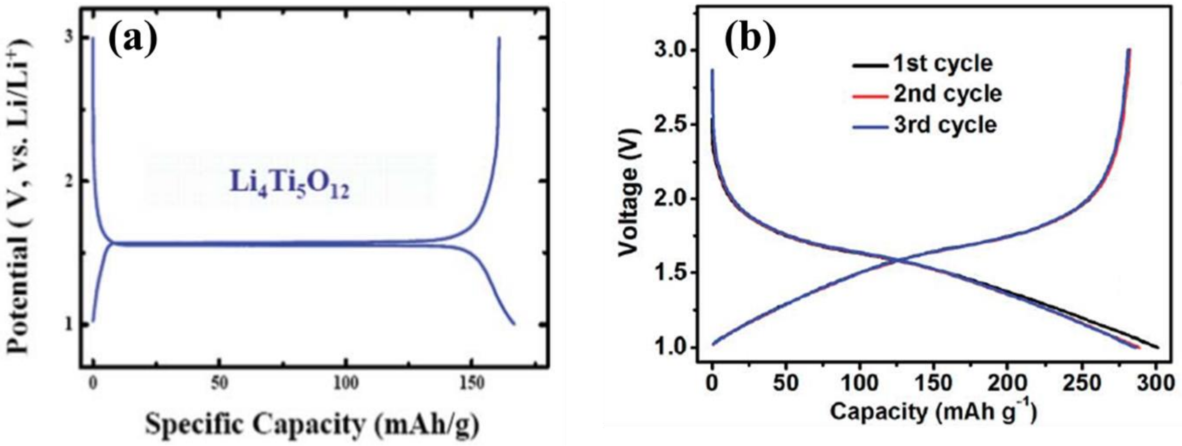

Figure 2-6: Typical voltage profiles for low rate cycling of (a) LTO at 0.05C [36] and (b) TNO at 0.1C [37].

Within the spinel structure most of the lithium ions are stored in the 8α tetrahedral sites which gives a $(Li_3)_{8a}[Li_1Ti_5]_{16d}(O_{12})_{32e}$ composition. Lithiation induces the Li^+ ions to move from the 8α to 16c position along with further Li^+ ions inserted up to a final composition of $Li_7Ti_5O_{12}$ which is denoted by $[Li_{0.16}]_{8a}[Li_1Ti_5]_{16d}[Li_{5.84}]_{16c}[O_{12}]_{32e}$. Lithiation beyond this composition to $Li_9Ti_5O_{12}$ occurs through storage of the 16c sites first and then in the 48f and 8a sites and is denoted by $[Li_{0.62}]_{8a}[Li_1Ti_5]_{16d}[Li_6]_{16c}[Li_{0.38}]_{48f}[O_{12}]_{32e}$ [38,39].

The advantages of using LTO are many: the insertion potential takes place at 1.55V (1-3V vs. Li^+/Li range) which is too high to cause SEI formation [40] and gives LTO excellent cyclability and safety while avoiding the dendrite formation observed for Li metal; The secondary rock-salt phase formed during insertion gives rise to a flat discharge curve which is beneficial for stable battery performance; Finally, LTO undergoes negligible volume change (<0.2%) during (de)lithiation and is referred to as a “zero-strain” material as there is almost no change in lattice dimensions during (de)intercalation [40].

Despite these benefits, the low energy density is still a drawback. Thus, titanium niobium oxides (TNO) such as $TiNb_2O_7$, $Ti_2Nb_{10}O_{29}$, and $TiNb_{24}O_{62}$ have been researched as replacement anode materials for LTO. They have the same advantage of largely avoiding SEI formation, similar operating voltage of ~1.6 V vs Li^+/Li, but can deliver significantly higher capacities (equivalent to graphite) at ~387-390 mAh/g) [41]. The high capacity is possible due to TNO (hereafter referring to $TiNb_2O_7$) having a possible 5 Li^+ exchange reaction due to Nb^{5+}/Nb^{4+}, Ti^{4+}/Ti^{3+}, and Nb^{4+}/Nb^{3+} redox couples. However, to fully realize the 5 Li^+ reaction the voltage range must reach below 1V (0.6V – 3V range) [42].

$$TiNb_2O_7 + xLi^+ + xe^- \rightarrow Li_xTiNb_2O_7; 0 \leq x \leq 5 \qquad \text{Eq. 2-10}$$

TNO has a monoclinic “shear ReO_3” structure with space group *C2/m* consisting $3 \times 3 \times \infty$ blocks of MO_6 (where M= Ti, Nb) octahedra which share edges and corners. The lattice parameters are $a = 20.315$ Å, $b = 3.801$ Å, and $c = 11.882$ Å [43]. This material has been reported to undergo a volume change during (de)lithiation of 8-10 vol%, a larger value in relation with LTO and comparable to graphite intercalation. Volume changes are problematic as this will cause cracking and separation between particles (i.e. loss of electrical contact – mechanical degradation) which directly contributes to capacity fade [44].

A major disadvantage for both TNO and LTO is their low ionic and electronic conductivity [45,46]. The low ionic issue may be addressed through nanosizing the material which shortens Li^+ diffusion paths [12,47], for LTO this may be done by controlling the synthesis stage to prevent formation of large particles as has been previously performed in this group [48–51] or encourage nanoporous particles [46,52,53]. The electronic conductivity can be improved via carbon-coating the material [54], doping [46], and mixing with conductive additives such as graphene. As an example, the latter may been done by dispersing the graphene precursor GO during or after hydrothermal synthesis of LTO followed by post treatment to induce GO transformation [55,56]. The key for this idea to work lies in the ability to make homogeneously dispersed mixtures to improve contact area and therefore the percolation network. These studies usually employ sonication or stirring to improve active/conductive dispersion [55–58] followed by drying to recover the mixture.

Due to their safety and performance, this work centres around improving the performance of LTO or TNO composite electrodes through minimization of internal polarization and battery degradation. Consequently, this would lead to lowering the capacity fade during cycling. Reduced graphene oxide is used as conductive additive to improve coating conductivity. Further explanation is given in sections 2.2 and 2.3. The former section expands on the importance of active/conductive dispersion and the corresponding effect on capacity fade and electrochemical performance.

2.1.7 Electrode Conductive Additives

As mentioned in section 2.1.3, conductive material such as carbon black is often added into the coating mixture to improve the electronic conductivity. It does so by lowering the internal resistance which helps improve power density [59,60]. This added conductive material is not electrochemically active, meaning it does not contribute to the redox reaction required for lithium intercalation. However, it contributes to the overall mass/volume of the electrode which in turn affects the energy density. The amount of conductive material is often less than 10% relative to the total coating mass [59] and involves a trade-off between power and energy density.

For composite materials, the percolation theory (PT) [59,61,62] can be used to model or mathematically describe the system. PT defines the minimum amount of conductive material required for all these particles to make contact and form conductive channels (hence the term percolation network). Experimentally, a sharp drop in resistivity is observed when this “critical volume”, or “percolation threshold”, of conductive material is reached. In practice, the amount of conductive material is not selected solely based on the percolation threshold as the internal resistance will also depend on particle size distribution of both types of materials throughout the coating, porosity/tortuosity, electrode thickness, and the materials ability to adsorb electrolyte. Aside from the electrochemical properties, the type of conductive additive used will influence the mechanical strength of the electrode, compaction behavior, and rheological conditions during the electrode manufacturing stage (see section 2.2).

The most common type of carbon additive is carbon black (semi crystalline, obtained through the pyrolysis of hydrocarbons – may be graphitizable at high temperatures making it part of the soft carbon family) and graphite powder. Other carbonaceous materials with higher conductivities have also been tested, among these are carbon nanotubes [63,64] and graphene [65,66].

Graphene is a combination of mono- and few-layer sheets of *sp2* hybridized carbon atoms arranged in a honeycomb structure. Within the graphene plane each carbon is attached to three other carbons – one with a π bond. The delocalized nature of π bonds leaves an electron free for electronic conduction giving this material its excellent conductivity. This material can be synthesized through various techniques, notably by exfoliation of graphite, chemical vapour deposition of carbon-containing gases on metal surfaces [67], and reduction of graphene oxide (GO) [68]. GO is mono- or few-layer sheets of functionalized graphene. Among these are hydroxyl (OH), carbonyl(C=O), epoxy (C-O-C), and carboxyl (COOH) functional groups which are attached through *sp3* bonds. These groups tend to form at different points in the graphene plane, with epoxy and hydroxyl groups scattered throughout the basal plane and the other groups (e.g. carboxyl and carbonyl) mainly located at the edges or defective areas [69,70]. It is important to note that the final structure and functional group composition of GO depends on the synthesis technique used. The presence of the functional group within the carbon plane influences the charge transfer abilities (as opposed to the edge groups), consequently the removal of epoxy and hydroxyl groups is important to restoring conductive properties [68].

The GO functional groups may be removed through high temperature annealing thereby producing graphene sheets with few remaining functional groups (defects) – due to the remaining defects, this material is differentiated from true graphene and referred to as reduced graphene oxide (rGO). The quantity of functional groups remaining – typically defined by the carbon/oxygen atomic ratio where GO has a ratio of C/O≈2 – may be controlled by the temperature selected. Annealing at $800℃$ and $1000℃$ reduces the GO and shifts the C/O ratio to ~10 and ~ 30 respectively [71]. This process may be carried out in a vacuum or under a reductive environment where the presence of hydrogen catalyzes the GO reduction [68]. In thermal annealing removal of hydroxyl and epoxy groups occurs through desorption which produces $H_2O, CO,$ and CO_2 gas byproducts [72].

A comparison between the graphite, graphene, graphene oxide, and reduced graphene oxide is given in Figure 2-7.

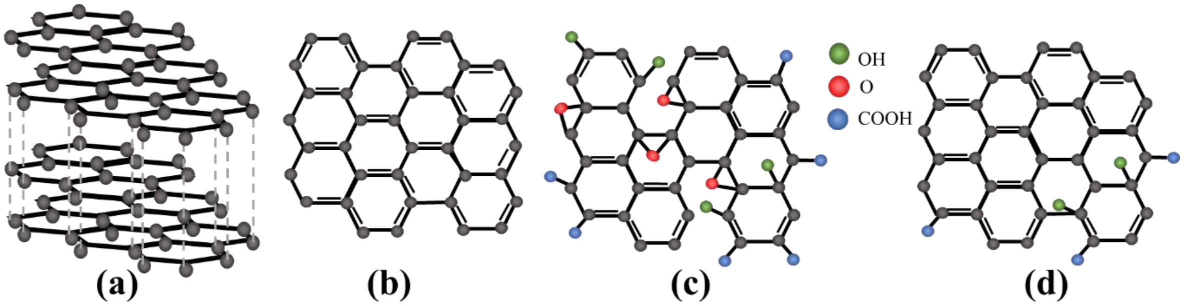

Figure 2-7: (a) graphite, (b) graphene, (c) graphene oxide, and (d) reduced graphene oxide.

2.2 Conventional LIB Electrode Fabrication

The current commercial manufacturing technique used to fabricate lithium-ion electrodes is tape-casting. The fabrication technique is important as it influences not just coating homogeneity but also its porosity, electrode thickness, and mechanical stability – these properties in turn affect the electrochemical performance.

Tape-casting involves mechanical mixing of the active, conductive, and binder material within a liquid medium (N-2-methyl-pyrrolidone – NMP) to make a slurry. Mixing can be accomplished through different machinery such as ball mills, planetary mixers, and universal type mixers [73]. This slurry is then coated onto a current collector followed by drying and calendering. The drying and calendaring steps remove the solvent from the layer, improve particle connectivity, and reduce surface roughness.

To ensure homogeneous material dispersion the slurry rheological properties must be controlled. However, as indicated in section 2.1.3, the active material must be nanosized to minimize lithium-ion diffusion. Nanosized materials tend to form a more viscous slurry than coarser materials which introduces a rheological challenge for tape-casting during the mixing stage. This problem may lead to bad particle dispersion in the electrode coating due to aggregation of the nanosized active material at the mesoscale [74]. As the active materials available tend to have low conductivity, the electrode performance relies on intimate mixture (point contact) between active and conductive components to maintain a uniform current density throughout. Uneven current distribution will affect transport kinetics [75], lead to polarization, overcharge/overdischarge [76], non-uniform phase transformation [77], and lower material utilization [74–76]. All factors that ultimately contribute to capacity fade and battery failure.

Aside from the active and conductive material, the PVDF polymer binder must also have good dispersion which requires the PVDF to completely dissolve in the solvent. This is a two-step process that first involves 1) polymer swelling which weakens polymer-polymer bonds followed by 2) dissolution itself which requires the polymer-solvent interactions to be greater than the polymer-polymer interactions. This ultimately allows the polymer to be evenly dispersed throughout the solvent and, consequently, the electrode [78]. For the PVDF binder, this dissolution process is found to be limited to a few solvents including NMP. This is problematic as NMP is a hazardous teratogen which led to its use being regulated in some countries [79]. As a consequence battery manufacturers have to incorporate an NMP recovery system during the drying stage which incurs large capital costs [80]. Thus, the research has focused on finding alternative binders (which require different solvents – discussed in section 2.1.5) or changing the fabrication method altogether.

2.3 Electrophoretic Deposition (EPD)

EPD is an effective electrocoating technique used in fabricating ceramic coatings from colloidal suspensions. This technique can be used to coat a variety of materials (including multi-component combinations) on uniform and non-uniform substrates (i.e. deposition on flat vs cylindrical surfaces). This wide versatility has led to widespread interest from both academic and industrial sectors.

Overall, EPD is a four-step process that involves 1) developing a stable suspension of the material/s that is/are to be deposited, 2) submerging two electrodes – the substrate on which deposition occurs and the counter, 3) applying an electric field to induce particle migration, and finally 4) deposition of the particles to form a coating. The coating may occur on the positive or negative electrode depending on the charge of the suspended particles. An example of cathodic deposition (i.e. positively charged particles depositing on the negative electrode) is shown in Figure 2-8 (a). It is important to note that for EPD there are no redox reactions occurring to induce particle deposition (a key difference between EPD and electrowinning), meaning the particles should not lose their oxidation state after deposition and reversal of the electric field will strip the coating [81]. The effectiveness of this technique is controlled by several factors that relate to suspension stability or process parameter selection. These are examined in further detail in section 2.3.5.

2.3.1 Electric Double Layer

When referring to suspension stability the role of the electric double layer (EDL) is essential. The *Stern layer* is the hypothetical layer closest to the particle that consists of counterions that are attracted to the particle surface, closely attached (due to the electrostatic force), and immobile. The second layer is the *Diffuse layer* which consists of freely-moving ions. A schematic of the EDL can be seen in Figure 2-8 (b) along with the electric potential with respect to distance from the particle surface. At the surface ($x = 0$) the potential is at its highest value (ψ_o) and drops exponentially as you move away from the surface ($x \to \infty$).

The interaction between particles in suspension is governed by their respective EDL overlap, meaning the potential at the boundary of the Stern and Diffuse layers ($x = \delta$) which is referred to as ψ_δ. The potential difference between the Stern and Diffuse layers, with respect to distance, can be represented by the Poisson-Boltzmann equation [81] where κ is the Debye-Hückle parameter (m^{-1}):

$$\psi(x) = \psi_\delta \exp -\kappa x \qquad \text{Eq. 2-11}$$

At distance $x = \kappa^{-1}$, the potential drops to $\psi = \frac{1}{e}\psi_\delta$, where e is the base of the natural logarithm ($e = 2.71$). This distance is defined as the thickness of the double layer (also called Debye length). This EDL thickness can be calculated through [81]:

$$\kappa^{-1} = \sqrt{\frac{\varepsilon\varepsilon_o K_B T}{2e^2 I}} \qquad \text{Eq. 2-12}$$

Where ε is the dielectric constant (unitless) of the medium, ε_o is the permittivity of space (C/Nm^2), K_B is the Boltzmann constant ($1.38 \times 10^{-23} J/K$), T is temperature (K), e in this case is the elementary charge ($1.6 \times 10^{-19} C$), and I is the ionic strength of the solution (mol/m^3).

Within the diffuse layer there is a slipping or shear plane, while the particle is in motion the layer within this shear plane remains attached to the surface and moves with the particle (i.e. the velocity of the liquid relative to the particle is zero). The potential at this slipping plane is called the zeta potential (ψ_ζ) which is an important and measurable property that gives an indication of suspension stability. Particles with a zeta potential that have a large magnitude will repel each other, conversely particles with a small zeta potential will tend to flocculate and heavy flocs will sediment out of suspension. The zeta potential is commonly used to replace the stern potential as the latter cannot be measured – this, however should be done with caution as, by definition, they are not the same.

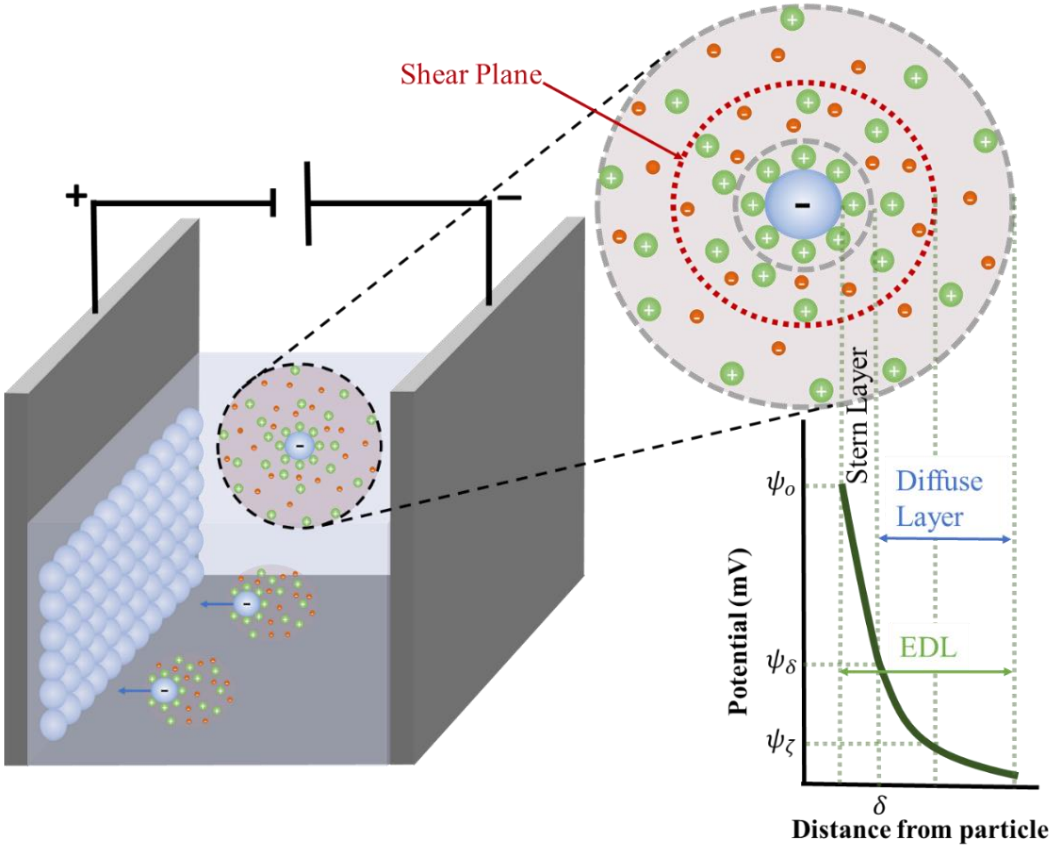

Figure 2-8: (Left) EPD Schematic showing a volume element of the suspension between the electrodes. The particles are positively charged and, under the influence of the electric field, migrating towards the cathode and depositing. (Right) Electric double layer surrounding the particle with potential vs distance from the particle.

The zeta potential of a colloid in suspension can be determined by applying an electric field (E, V/m) and measuring the particle velocity ($v, m/s$). The electrophoretic mobility ($\mu, m^2/sV$) is then calculated as the ratio between particle velocity and electric field ($\mu = v/E$). The electrophoretic mobility can then be related to the zeta potential using either the Smoluchowski or Hückel equation. The equation used will depend on the radius of the particle (a) relative to the

EDL thickness (κ^{-1}). Often this comes down to whether the medium is polar or non-polar. The general equation is given by [81,82]:

$$\mu = \frac{\varepsilon\varepsilon_o\zeta}{\eta} f(\kappa a) \qquad \text{Eq. 2-13}$$

Where ζ is the zeta potential (V), η is the suspension viscosity ($Pa \cdot s$), and $f(\kappa a)$ is Henry's function [81,82]:

$$f(\kappa a) = \frac{2}{3}\left[1 + \frac{1}{2\left(1 + \frac{2.5}{\kappa a\{1 + 2\exp(-\kappa a)\}}\right)^3}\right] \qquad \text{Eq. 2-14}$$

For polar media with high electrolyte concentrations the EDL thickness is often small (as per Eq. 2-12), thus satisfying the condition $a \gg k^{-1}$, meaning $\kappa a \rightarrow \infty$ and $f(\kappa a) \rightarrow 1$. Thus, the Smoluchowski equation is used:

$$\mu = \frac{\varepsilon\varepsilon_o\zeta}{\eta};\ \kappa a \rightarrow \infty \qquad \text{Eq. 2-15}$$

For nonpolar media the EDL size is often large, giving a new condition of $a \ll \kappa^{-1}$, where $\kappa a \rightarrow 0$ and $f(\kappa a) \rightarrow \frac{2}{3}$. Thus, the Hückel relationship must be used:

$$\mu = \frac{2}{3}\frac{\varepsilon\varepsilon_o\zeta}{\eta}; \kappa a \rightarrow 0 \qquad \text{Eq. 2-16}$$

Both models are limited to spherical particles. For cylindrical particles the electrophoretic mobility will depend on the orientation of the particle (perpendicular or parallel relative to the applied electric field) and requires a different $f(\kappa a)$ equation which is more complex.

The development of the surface charge (and subsequent formation of EDL) will depend on whether the medium is aqueous or organic. In organic systems the most common reasons for surface charge formation is surface group dissociation/ionisation and adsorption of ionic compounds [81,83]. The former uses functional groups that can undergo protonation/deprotonation (e.g. hydroxyl groups) – the groups that will dissolve preferentially in this way are classified as potential determining ions. The latter refers to adding charging agents into the suspension that ionise and adsorb onto the particle surface. This includes ionic compounds and polymer surfactants. Once the surface charge forms this will attract counter-ions and repel co-ions. This surrounding cloud of charges is referred to as a lyosphere and forms the EDL.

2.3.2 DLVO model

The DLVO model (established and named after Derjaguin, Landau, Verwey, and Overbeek) relates the suspension stability to particle interactions through their repulsive and attractive forces. The theory assumes that the liquid is stationary, movement occurs due to Brownian motion (i.e. it is not viable during the application of an electric field), and the total energy of interaction (V_T, J) between particles (as they approach each other) is the sum of the electrostatic repulsive (V_R, J) and Van Der Waals attractive (V_A, J) forces. This theory may be extended to include the steric force [84] which may be attractive or repulsive if the suspension has macromolecules adsorbed or bonded on the particle surface (e.g. polymers or lipids). The following equations are for two spherical particles in proximity for large κa values [85]:

$$V_T = V_A + V_R \qquad \text{Eq. 2-17}$$

$$V_A = -\frac{aA_{131}}{12D} f(P) \qquad \text{Eq. 2-18}$$

$$V_R = \frac{\varepsilon\varepsilon_o a\psi_\delta^2}{2} \ln[1 + \exp(-\kappa D)] \qquad \text{Eq. 2-19}$$

Where D is distance between particles of radius a, A_{131} is the Hamaker constant (J), and $f(P)$ is the retardation factor (effects that appear due to the finite speed of light). An electromagnetic signal will take time to travel between two particles. When it returns, it may find the instantaneous dipole orienting itself differently. This weakens the interacting forces and causes “retarded” van der Waals forces. In relation to interparticle distance, the attractive force will drop by a factor of $1/D^6$. When two particles (being composed of the same material denoted by subscript 1) are separated by a liquid media (denoted as subscript 3), the Hamaker constant, A_{131} may be calculated by [86]:

$$A_{131} = A_{11} + A_{33} - 2A_{13} \approx \left(\sqrt{A_{11}} - \sqrt{A_{33}}\right)^2 \qquad \text{Eq. 2-20}$$

Where A_{ij} represents the Hamaker constant for interacting materials i and j in vacuo (i.e. A_{11} represents the interactions between two particles of the same type 1 in vacuo and, similarly, A_{33} is the interaction between two particles of medium 3 in vacuo). For different materials 1 and 2 separated by suspension 3, the Hamaker constant can be calculated as [86]:

$$A_{132} \approx \left(\sqrt{A_{11}} - \sqrt{A_{33}}\right)\left(\sqrt{A_{22}} - \sqrt{A_{33}}\right) \qquad \text{Eq. 2-21}$$

Equation Eq. 2-20 assumes the Hamaker constant between two like particles is positive meaning the interaction is attractive, whereas Eq. 2-21 shows interactions between dissimilar materials can be either attractive or repulsive.

Eq. 2-18 and Eq. 2-19 are shown graphically in Figure 2-9, along with the total energy of interaction (Eq. 2-17). At short distances the repulsion force is greater and the V_T graph presents a maximum or energy barrier. As particles approach, they must collide with enough energy to overcome this energy barrier in order to begin coagulation. Thus, this barrier is necessary to maintain particles in suspension – it must be larger than the thermal energy. In practice, stabilizing the suspension involves manipulating this maximum and the height of the maximum is dictated by the magnitude of ψ_δ (and consequently ψ_ζ). At short distances, once the energy barrier is overcome, the particles are held in a primary minimum where escape is difficult.

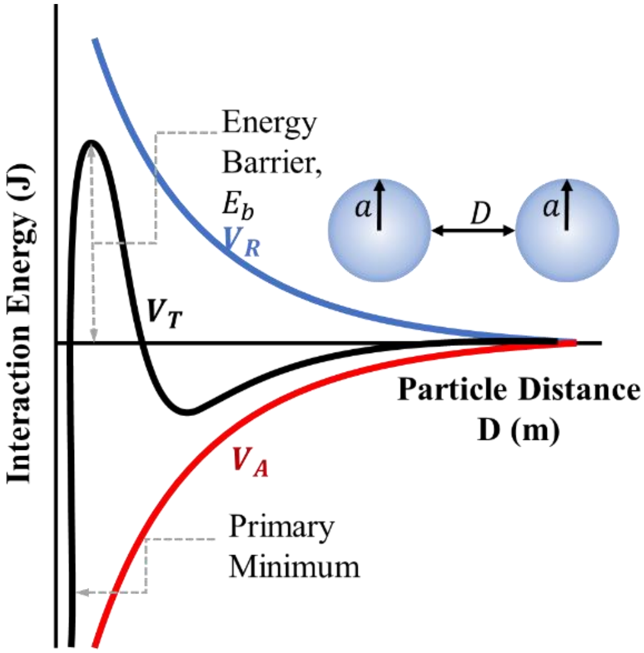

Figure 2-9: Energy balance diagram (Interaction Energy vs particle distance) for interacting spherical particles.

2.3.3 *Deposition Mechanisms*

Depending on the nature of the suspension/system there are numerous suggested mechanisms by which deposition occurs. The five suggested theories are [81,87,88] 1) Electrosedimentation 2) particle charge neutralization, 3) electrochemical particle coagulation, 4) EDL distortion, and 5) polymer-related deposition.

Electrosedimentation states that deposition from a suspension under an electric field is akin to sedimentation under gravity. Without the electric field the suspension will sediment and produce a strongly adhering coat on the floor of the container. Under the influence of an electric field, the particles will instead move horizontally along the direction of the field towards the electrode where they accumulate, and deposition occurs under the pressure (compaction) induced by incoming particles. This mechanism is often referred to as electrosedimentation. This mechanism works for systems where deposition doesn't occur on a charged electrode but, as an example, on a membrane located between the electrodes. This theory is heavily dependant on solid loading of the suspension.

Particle neutralization claims deposition occurs due to the particles becoming neutralized and static upon contact with the electrode. This mechanism would explain single particles depositing (without the influence of surrounding particles being needed as in electrosedimentation), monolayer formation, and deposition from very dilute suspension. However, it can't explain the formation of thick deposits.

Electrochemical coagulation theory expects there will be an increase of ionic strength on the electrode surface. This in turn (as per Eq. 2-12) decreases the EDL thickness thereby allowing particles to flocculate and deposit (a decrease of zeta potential is also observed). As this theory requires the buildup of ion concentration then it is important to note that a finite time must have passed before deposition can occur. Another key factor is this theory is only valid if there are ions forming during EPD at the surface of the electrode such as OH^- in aqueous suspensions.

The most commonly used theory is **EDL distortion**. This mechanism occurs through three steps shown in Figure 2-10. First, the double layer begins distorting under the influence of the applied electric field as the lyosphere lags behind the moving particle. This means the EDL becomes thinner in front of the particle and wider behind it. Second, the lyosphere ions in the back (furthest away from the moving particle) will be attracted by surrounding counter ions, thereby removing them from the EDL. This results in the EDL becoming thinner. Thus, two particles with thinned EDLs can now approach close enough for the Van der Waal forces to dominate and cause coagulation. This theory explains thick deposits and deposits that form when there is no increase in ionic strength near the electrode.

In the case of polymers being present, **bridging flocculation** may also occur. Similar to electrosedimentation, the electric field acts as a carrier to bring the particles towards the electrode. The anchor segments of polymers may then bridge particles together. Another polymer-related mechanism is referred to as **squeezing out**. When polymers act as a stabilizing agent, they may be forced out from between particles due to the electrophoretic force. The space between the particles, relative to the rest, will now be low in solute which will force the solvent between the particles to rush out where the solute is in high concentration. This allows for the particles to get close enough for attractive forces to dominate. This is also referred to as depletion flocculation.

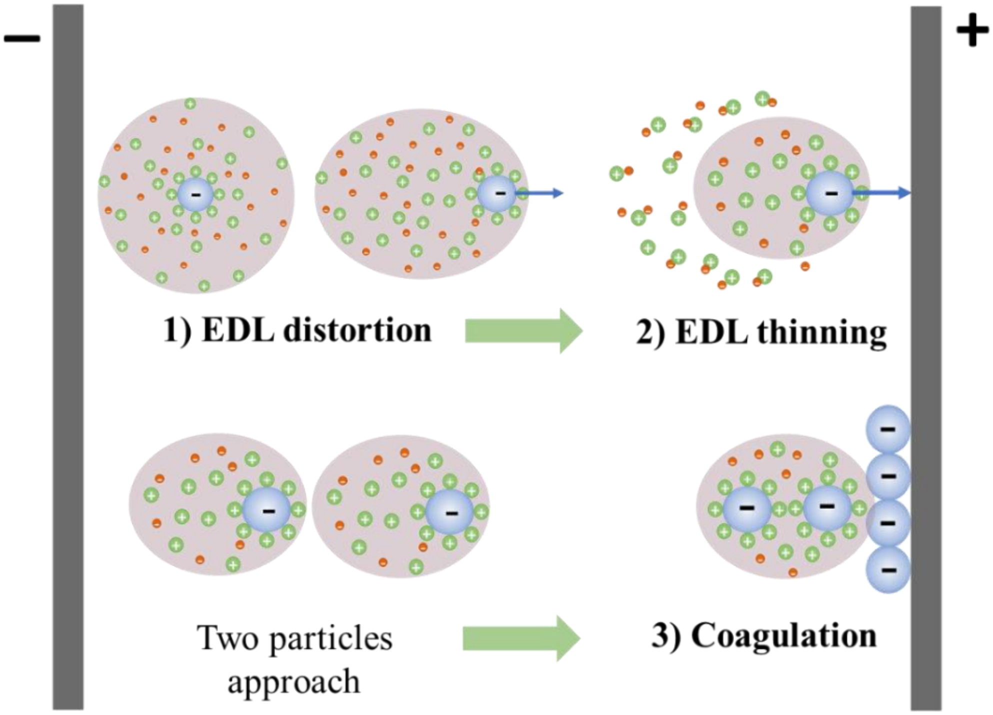

Figure 2-10: EDL distortion 3-step mechanism (adapted from [81,83]).

2.3.4 *EPD Modeling*

Figure 2-11 (a) and (b) shows an EPD schematic with the corresponding theoretical electric field across the cell. This potential drop is described by [89–91]:

$$V_A = \Delta\phi_1 + \Delta\phi_d + \Delta\phi_s + \Delta\phi_2 \qquad \text{Eq. 2-22}$$

Where V_A is the applied voltage, $\Delta\phi_1$ and $\Delta\phi_2$ are potential drops due to the electrode solid/liquid interphase at the depositing surface and counter respectively, $\Delta\phi_d$ is a potential drop due to the film thickness, and $\Delta\phi_s$ is the potential drop in the suspension. The $\Delta\phi_d$ deposit potential drop is a factor of the resistance due to the solid particles, $R_{p,d}$, forming the deposit and the interparticle liquid, $R_{i,d}$, still contained within the deposit. The $\Delta\phi_s$ suspension potential drop is a factor of the resistance due to the particles in suspension, $R_{p,s}$, and ions in suspension, $R_{i,s}$. A simple circuit is shown in Figure 2-11 (c) [89–91].

This model can be used to understand the mass deposited during EPD. The kinetics may be modelled by the widely applied Hamaker and Sarkar and Nicholson equations [92]:

$$\frac{dw}{dt} = f\mu SEC \tag*{Eq. 2-23}$$

$$w(t) = w_o(1 - e^{-\kappa t}) \tag*{Eq. 2-24}$$

Where w is the mass of powder remaining in suspension, S is deposition area (m^2), E is the electric field (V), f is the efficiency factor, and t is time (s). If all particles that gather at the electrode surface deposit, then the system is ideal and $f = 1$.

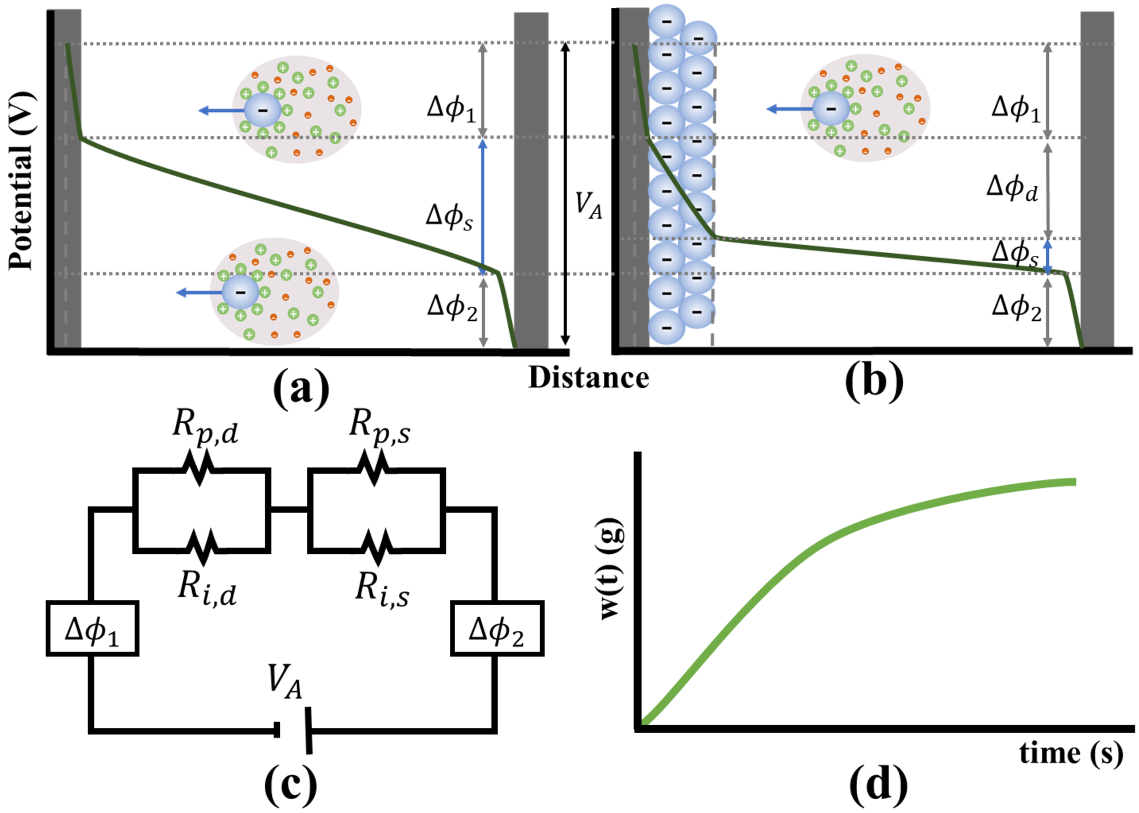

Figure 2-11: EPD schematic with potential gradient (a) before coating forms and (b) after coating forms(adapted from [89–91]). (c) Simplified circuit for EPD cell (adapted from [91]). (d) Mass deposited, w(t), vs. time for a theoretical system.

Graphically, and experimentally, plotting the deposit mass vs time will lead to an initially linear increase that plateaus after a certain time (shown in Figure 2-11 (d)). This is because the deposit, depending on the system, has thickness limitations due to the insulating nature of the coating (relative to the metal substrate on which deposition is occurring) which increases $\Delta\phi_d$. Depending on the type of system the plateau can also be due the decreasing concentration of solids around the electrode. This insulating layer will also lead to a decrease in electrical driving force (or voltage per unit length) across the suspension with time as seen by comparing $\Delta\phi_S$ for Figure 2-11 (a) and (b).

2.3.5 Factors Influencing EPD

The key factors that affect EPD performance relate to either the suspension or process parameters. Suspension-related factors refer to stabilizing the suspension whereas the process parameters refer to EPD conditions that lead to a suitable coating.

2.3.5.1 Suspension and Stability

The suspension stability, quantified by the zeta potential, is influenced by a variety of factors including the mediums dielectric constant, conductivity, viscosity, the solids particle size, and solid loading/concentration.

The **zeta potential** defines the interparticle interactions making it a useful parameter in determining particle stability. Additionally, it also dictates the direction of particle migration.

The solvent **dielectric constant** is a measure of its polarizability, solvents such as water (that have molecules with dipole moments), are easily polarizable and have a high dielectric constant (80.1 at room temperature) when compared to toluene (2.38 at room temperature). Generally, a polar solvent is required for polar solutes and a non-polar solvent for non-polar solutes. It has also been reported that solvents with high dielectric constants will have high conductivities [81].

The **suspension conductivity** can affect the kinetics and deposition of the coating. The current is carried by the charged particles and free ions. The effect of ionic strength and charging agents can be seen through Eq. 2-12 – the ionic strength is inversely proportional to the EDL thickness. This means large ionic strengths will lead to a small EDL and an unstable suspension. However, if the conductivity is too low then the suspension will be resistive and charge during the electric field application. This will also result in loss of stability [81]. This would indicate that there is an optimum range of conductivity which will invariably differ depending on the system. Dispersants may be used to alter ionic content and conductivity. These are ionic compounds added to manipulate the charge of the suspension and are classified depending on their stabilizing mechanism shown in Table 2-1 [93].

Table 2-1: Dispersant and their associated mechanism [93]

Dispersant	**Mechanism**
Potential-determining ions (pH)	Electrostatic repulsion
Electrolytes (inorganic salts)	Electrostatic repulsion
Surfactants (amphiphilic chains)	Adsorption + Electrostatic repulsion
Adsorbed Polymers	Steric Hindrance
Non-adsorbing polymers	Depletion stabilization

The **viscosity** of the suspension can also affect EPD kinetics as shown through Eq. 2-13 and Eq. 2-23, the viscosity decreases the electrophoretic mobility which in turn lowers rate of particle deposition.

Particle size affects suspension stability as larger particles have a higher tendency to sediment. Nanosized particles have a larger surface area and produce more viscous suspensions when compared to microsized systems, this is an important factor when considering the charge per unit area of particles – this means less resistivity (i.e. higher conductivity). Additionally, a large particle will move slower as can be seen in Eq. 2-13 and will lower the electrophoretic mobility which in turn lowers rate of particle deposition. It is also important to note that the particle size of the dry powder may not translate to the particle size in suspension as there will be a degree of agglomeration [93]. Larger particle sizes or agglomerates will lead to uneven coatings due to the sedimenting effect where the deposit is thicker at the bottom relative to the top.

The **solid concentration** in suspension may lead to instability and sedimentation. However, a higher concentration means that the particles will not be depleted fast at the electrode surface. This is important when considering multicomponent systems that will have different zeta potentials. If the particles are depleted at the electrode surface than deposition depends on mobility and consequently zeta potential, this means the fastest particles will form most of the deposit. However, if the particles are not depleted then deposition rate is equal for all components [81].

2.3.5.2 Process Parameters

The most important factors related to process parameters are: electric field magnitude, whether it is a constant-current or constant-voltage, and deposition time.

The **electric field magnitude** is needed to overcome the electrostatic repulsive forces and encourage particle migration. From Eq. 2-23, voltage is found to be directly proportional to rate of deposition meaning a larger electric field will lead to faster migration. However, this may affect the quality of the deposit. This is because the particles are depositing too fast to find the optimal position for a closed-packed structure [88]. Additionally, the high electric field will cause turbulence in the suspension disturbing the deposit. Conversely too low a field will not trigger electrophoresis.

EPD may be performed under **constant-voltage** or **constant-current**. Under constant-voltage the potential between electrodes is maintained, however the increasing deposit thickness introduces a progressively larger resistance meaning a higher voltage is required for deposition. Additionally, the potential drop in suspension is lowered which removes the driving force for electrophoresis. Experimentally this is seen through a drop of current. On the other hand, a constant-current system avoids this limitation as it progressively manipulates the voltage to maintain a set current [83].

As mentioned in section 2.3.4, the coating resistance introduces a plateau in the deposited weight. This is a limitation of the EPD system due to the insulating nature of the deposit, it can be modified by increasing the electric field magnitude but the effectiveness of this will vary depending on the system. At the plateau the small increase in weight may not justify the prolonged **deposition time** meaning, as with many of the EPD parameters, there is an optimum time value.

2.3.6 EPD Application in Li-Ion Batteries

As mentioned in section 2.1.7, homogeneity is key for reduction of electrode internal resistance and ultimately improving battery performance – as is nanosizing to minimize Li^+ diffusion length. The conventional tape-casting method is unsuitable for fabrication of composite coatings particularly when using nanosized materials (see section 2.2). In contrast, it is well accepted that EPD has excellent self-assembling capabilities [94] and herein lies its advantage to being used to fabricate composite lithium-ion electrodes. Moreover, methods such as pulsed laser deposition and vapor deposition methods are expensive making them difficult to scale up. EPD provides a simplified coating technique with short process times [94]. The versatility of the suspension also allows EPD to be potentially environmentally friendly.

This technique has already been applied to fabricate lithium-ion electrodes composed of a variety of different materials. Among these composite coatings are LFP/carbon black/CMC coatings [95], LFP/carbon black/xantham gum binder [96], binderless Cu/Fe_3O_4 [97], binderless copper/multi-walled carbon nanotubes [98], binderless nanotitania and carbon [99], NMC/alumina

[100], NMC/carbon black with Poly(diallyldimethylammonium chloride) as dispersant [101], binderless pure Nb_2O_5 [102], and binderless pure LTO nanoparticles [103]. EPD has also been shown to successfully deposit graphene and graphene composite electrodes for electrochemical energy storage (listed in Table 2-2). However, when graphene is involved many of these studies employ pre-treatment stages to encourage homogeneity (i.e. ball-milling materials together prior to EPD dispersion [104] or mixing during the synthesis stage of one of the materials [105,106]). In other words, these studies prepare homogeneous nanocomposite powders prior to EPD meaning they do not take advantage of the self-assembly capabilities that EPD inherently has. This particularly has not been done with LTO and TNO as active materials. Furthermore, few studies have compared the microstructure achieved by EPD with other kinds of casting techniques [107].

Uniform composition in the LIB multi-component systems is essential as explained in section 2.2. Thus, the assembling abilities for EPD indicates this efficient coating technique can be highly beneficial in improving the electrode percolation network. Thus, this work examines the nature of the coating composition – this being quantitative composition and dispersion (i.e. microstructure) – when electrophoretically deposited graphene, and LTO or TNO are involved and the underlying effect on the electrode performance in battery applications (i.e. how it affects percolation network and ultimately kinetics) when compared to conventionally cast electrodes.

Table 2-2: Electrophoretically deposited graphene coatings or composites for electrochemical energy storage.

Material	**Pre-treatment**	**EPD parameters**	**Post-treatment**	**Application**	**Ref**
Fe_2O_3/TiO_2 + graphene	Fe_2O_3/TiO_2 mixed in ball mill and suspended with graphene in water	15 V/cm, 5 min	Air dry	LIB anode	[104]
Co_3O_4 + graphene	Pre-fabrication of Co3O4/graphene powder prior to EPD through solvothermal method, then mixed in Acetone +I_2	pulsed EPD 25V, 100Hz	300^{o}C drying to remove solvent	LIB anode	[105]
$\boldsymbol{MnO_2}$+carbon nanotube + graphene	Pre-synthesis of MnO_2/rGO/carbon nanotube nanocomposite followed by EPD in isopropanol charged with HCl	50V for 2 mins	Dried in oven 110^{o}C for 12h	Pseudocapacitors	[106]
$LiFePO_4$ + rGO	LiFePO4 and GO sonicated with $Mg(NO_3)_2$ charger in isopropanol	90V	300^{o}C annealing to transform GO to rGO	LIB cathode	[108]
Graphene	GO sonicated with $Mg(NO_3)_2$ charger in isopropanol	100V for 20s	Reduced to graphene using hydrazine	Supercapacitors	[109]
Carbon spheres and graphene	Carbon spheres and graphene synthesized mixed in ethanol/water	10V	Immersion in hydroiodic acid at 100^{o}C to reduce GO	Supercapacitors	[110]
Graphene	Graphite suspended in water with poly(sodium-4-styrenesulfonate)	300 mA for 1h	Dried in vacuum oven 60^{o}C	LIB anode	[111]
Carbon nanotube + graphene	Carbon nanotube + graphene + $Ni(NO_3)_2$ dispersed in isopropanol	100V, 10 min	Drying in vacuum oven 80^{o}C	LIB anode	[112]

2.4 References

[1] D. Linden, T. Reddy, Handbook of Batteries, 4th ed., McGraw Hill, 2010.

[2] N. Nitta, F. Wu, J.T. Lee, G. Yushin, Li-ion battery materials: present and future, Mater. Today. 18 (2015) 252–264. https://doi.org/10.1016/j.mattod.2014.10.040.

[3] Z. Yang, R. Li, Z. Deng, A deep study of the protection of Lithium Cobalt Oxide with polymer surface modification at 4.5 V high voltage, Sci. Rep. 8 (2018) 1–8. https://doi.org/10.1038/s41598-018-19176-6.

[4] J. Xu, R.D. Deshpande, J. Pan, Y.-T. Cheng, V.S. Battaglia, Electrode Side Reactions, Capacity Loss and Mechanical Degradation in Lithium-Ion Batteries, J. Electrochem. Soc. 162 (2015) A2026–A2035. https://doi.org/10.1149/2.0291510jes.

[5] M.-S. Song, R.-H. Kim, S.-W. Baek, K.-S. Lee, K. Park, A. Benayad, Is Li4Ti5O12 a solid-electrolyte-interphase-free electrode material in Li-ion batteries? Reactivity between the Li4Ti5O12 electrode and electrolyte, J. Mater. Chem. A. 2 (2013) 631–636. https://doi.org/10.1039/C3TA12728A.

[6] J. Gao, S.-Q. Shi, H. Li, Brief overview of electrochemical potential in lithium ion batteries, Chin. Phys. B. 25 (2016) 018210. https://doi.org/10.1088/1674-1056/25/1/018210.

[7] R. Huggins, Principles Determining the Voltages and Capacities of Electrochemical Cells, in: Energy Storage, 2nd ed., Springer, 2016: pp. 145–160.

[8] K. Mizushima, P.C. Jones, P.J. Wiseman, J.B. Goodenough, LixCoO2 (0<x<-1): A new cathode material for batteries of high energy density, Mater. Res. Bull. 15 (1980) 783–789. https://doi.org/10.1016/0025-5408(80)90012-4.

[9] G.E. Blomgren, The Development and Future of Lithium Ion Batteries, J. Electrochem. Soc. 164 (2017) A5019–A5025. https://doi.org/10.1149/2.0251701jes.

[10] C. Julien, A. Mauger, K. Zaghib, H. Groult, Comparative Issues of Cathode Materials for Li-Ion Batteries, Inorganics. 2 (2014) 132–154. https://doi.org/10.3390/inorganics2020132.

[11] R. Malik, D. Burch, M. Bazant, G. Ceder, Particle Size Dependence of the Ionic Diffusivity, Nano Lett. 10 (2010) 4123–4127. https://doi.org/10.1021/nl1023595.

[12] Y. Wang, H. Li, P. He, E. Hosono, H. Zhou, Nano active materials for lithium-ion batteries, Nanoscale. 2 (2010) 1294–1305. https://doi.org/10.1039/C0NR00068J.

[13] L.S. Roselin, R.-S. Juang, C.-T. Hsieh, S. Sagadevan, A. Umar, R. Selvin, H.H. Hegazy, Recent Advances and Perspectives of Carbon-Based Nanostructures as Anode Materials for Li-ion Batteries, Materials. 12 (2019) 1229. https://doi.org/10.3390/ma12081229.

[14] Y. Kim, W.-Y. Lee, K.J. Kim, J.-S. Yu, Y.-J. Kim, Shutdown-functionalized nonwoven separator with improved thermal and electrochemical properties for lithium-ion batteries, J. Power Sources. 305 (2016) 225–232. https://doi.org/10.1016/j.jpowsour.2015.11.106.

[15] B. Xiong, R. Chen, F. Zeng, J. Kang, Y. Men, Thermal shrinkage and microscopic shutdown mechanism of polypropylene separator for lithium-ion battery: In-situ ultra-small angle X-ray scattering study, J. Membr. Sci. 545 (2018) 213–220. https://doi.org/10.1016/j.memsci.2017.10.001.

[16] B. Liu, Y. Jia, C. Yuan, L. Wang, X. Gao, S. Yin, J. Xu, Safety issues and mechanisms of lithium-ion battery cell upon mechanical abusive loading: A review, Energy Storage Mater. (2019). https://doi.org/10.1016/j.ensm.2019.06.036.

[17] Y. Shi, X. Zhou, G. Yu, Material and Structural Design of Novel Binder Systems for High-Energy, High-Power Lithium-Ion Batteries, Acc. Chem. Res. 50 (2017) 2642–2652. https://doi.org/10.1021/acs.accounts.7b00402.

[18] L. Wei, C. Chen, Z. Hou, H. Wei, Poly (acrylic acid sodium) grafted carboxymethyl cellulose as a high performance polymer binder for silicon anode in lithium ion batteries, Sci. Rep. 6 (2016) 19583. https://doi.org/10.1038/srep19583.

[19] Y. Ma, J. Ma, G. Cui, Small things make big deal: Powerful binders of lithium batteries and post-lithium batteries, Energy Storage Mater. (2018). https://doi.org/10.1016/j.ensm.2018.11.013.

[20] R. Wang, L. Geng, W. Yang, Y. Zhang, Y. Zhang, W. Bai, B. Liu, W. Zhang, Effect of Different Binders on the Electrochemical Performance of Metal Oxide Anode for Lithium-Ion Batteries, Nanoscale Res. Lett. 12 (2017). https://doi.org/10.1186/s11671-017-2348-6.

[21] F. Jeschull, D. Brandell, M. Wohlfahr-Mehrens, M. Memm, Water-Soluble Binders for Lithium-Ion Battery Graphite Electrodes: Slurry Rheology, Coating Adhesion, and Electrochemical Performance, Energy Technol. 5 (2017) 2108–2118. https://doi.org/10.1002/ente.201700200.

[22] N. Yabuuchi, Y. Kinoshita, K. Misaki, T. Matsuyama, S. Komaba, Electrochemical Properties of LiCoO2 Electrodes with Latex Binders on High-Voltage Exposure, J. Electrochem. Soc. 162 (2015) A538–A544. https://doi.org/10.1149/2.0151504jes.

[23] A. Guerfi, M. Kaneko, M. Petitclerc, M. Mori, K. Zaghib, LiFePO4 water-soluble binder electrode for Li-ion batteries, J. Power Sources. 163 (2007) 1047–1052. https://doi.org/10.1016/j.jpowsour.2006.09.067.

[24] M.S. Whittingham, Electrical Energy Storage and Intercalation Chemistry, Science. 192 (1976) 1126–1127. https://doi.org/10.1126/science.192.4244.1126.

[25] X. Yuan, H. Liu, J. Zhang, Lithium-Ion Batteries: Advanced Materials and Technologies, 1st ed., CRC Press, Boca Raton, 2011.

[26] S.J. An, J. Li, C. Daniel, D. Mohanty, S. Nagpure, D.L. Wood, The state of understanding of the lithium-ion-battery graphite solid electrolyte interphase (SEI) and its relationship to formation cycling, Carbon. 105 (2016) 52–76. https://doi.org/10.1016/j.carbon.2016.04.008.

[27] G. Crabtree, E. Kocs, L. Trahey, The energy-storage frontier: Lithium-ion batteries and beyond, MRS Bull. 40 (2015) 1067–1078.

[28] N. Loeffler, D. Bresser, S. Passerini, M. Copley, Secondary Lithium-Ion Battery Anodes: From First Commercial Batteries to Recent Research Activities, Johnson Matthey Technol. Rev. 59 (2015) 34–44.

[29] J.R. Dahn, W. Xing, Y. Gao, The “falling cards model” for the structure of microporous carbons, Carbon. 35 (1997) 825–830. https://doi.org/10.1016/S0008-6223(97)00037-7.

[30] T. Nordh, R. Younesi, D. Brandell, K. Edström, Depth profiling the solid electrolyte interphase on lithium titanate (Li4Ti5O12) using synchrotron-based photoelectron spectroscopy, J. Power Sources. 294 (2015) 173–179. https://doi.org/10.1016/j.jpowsour.2015.06.038.

[31] S. Schweidler, L. de Biasi, A. Schiele, P. Hartmann, T. Brezesinski, J. Janek, Volume Changes of Graphite Anodes Revisited: A Combined Operando X-ray Diffraction and In Situ Pressure Analysis Study, J. Phys. Chem. C. 122 (2018) 8829–8835. https://doi.org/10.1021/acs.jpcc.8b01873.

[32] T.-F. Yi, S.-Y. Yang, Y. Xie, Recent advances of Li4Ti5O12 as a promising next generation anode material for high power lithium-ion batteries, J. Mater. Chem. A. 3 (2015) 5750–5777. https://doi.org/10.1039/C4TA06882C.

[33] C. Han, Y.-B. He, S. Wang, C. Wang, H. Du, X. Qin, Z. Lin, B. Li, F. Kang, Large Polarization of Li4Ti5O12 Lithiated to 0 V at Large Charge/Discharge Rates, ACS Appl. Mater. Interfaces. 8 (2016) 18788–18796. https://doi.org/10.1021/acsami.6b04239.

[34] A. Shellikeri, V. Watson, D. Adams, E.E. Kalu, J.A. Read, T.R. Jow, J.S. Zheng, J.P. Zheng, Investigation of Pre-lithiation in Graphite and Hard-Carbon Anodes Using Different Lithium Source Structures, J. Electrochem. Soc. 164 (2017) A3914–A3924. https://doi.org/10.1149/2.1511714jes.

[35] W. Lv, J. Gu, Y. Niu, K. Wen, W. He, Review—Gassing Mechanism and Suppressing Solutions in Li4Ti5O12-Based Lithium-Ion Batteries, J. Electrochem. Soc. 164 (2017) A2213–A2224. https://doi.org/10.1149/2.0031712jes.

[36] Z. Guo, X. Dong, D. Zhou, Y. Du, Y. Wang, Y. Xia, TiO2(B) nanofiber bundles as a high performance anode for a Li-ion battery, RSC Adv. 3 (2013) 3352–3358. https://doi.org/10.1039/C2RA23336C.

[37] B. Guo, X. Yu, X.-G. Sun, M. Chi, Z.-A. Qiao, J. Liu, Y.-S. Hu, X.-Q. Yang, J. B. Goodenough, S. Dai, A long-life lithium-ion battery with a highly porous TiNb 2 O 7 anode for large-scale electrical energy storage, Energy Environ. Sci. 7 (2014) 2220–2226. https://doi.org/10.1039/C4EE00508B.

[38] M. Wagemaker, F.M. Mulder, Properties and Promises of Nanosized Insertion Materials for Li-Ion Batteries, Acc. Chem. Res. 46 (2013) 1206–1215. https://doi.org/10.1021/ar2001793.

[39] H. Liu, Z. Zhu, J. Huang, X. He, Y. Chen, R. Zhang, R. Lin, Y. Li, S. Yu, X. Xing, Q. Yan, X. Li, M.J. Frost, K. An, J. Feng, R. Kostecki, H. Xin, S.P. Ong, P. Liu, Elucidating the Limit of Li Insertion into the Spinel Li4Ti5O12, ACS Mater. Lett. 1 (2019) 96–102. https://doi.org/10.1021/acsmaterialslett.9b00099.

[40] B. Zhao, R. Ran, M. Liu, Z. Shao, A comprehensive review of Li4Ti5O12-based electrodes for lithium-ion batteries: The latest advancements and future perspectives, Mater. Sci. Eng. R Rep. 98 (2015) 1–71. https://doi.org/10.1016/j.mser.2015.10.001.

[41] Y.-S. Lee, K.-S. Ryu, Study of the lithium diffusion properties and high rate performance of TiNb 6 O 17 as an anode in lithium secondary battery, Sci. Rep. 7 (2017) 16617. https://doi.org/10.1038/s41598-017-16711-9.

[42] K. Ise, S. Morimoto, Y. Harada, N. Takami, Large lithium storage in highly crystalline TiNb2O7 nanoparticles synthesized by a hydrothermal method as anodes for lithium-ion batteries, Solid State Ion. 320 (2018) 7–15. https://doi.org/10.1016/j.ssi.2018.02.027.

[43] S. Lou, Y. Ma, X. Cheng, J. Gao, Y. Gao, P. Zuo, C. Du, G. Yin, Facile synthesis of nanostructured TiNb2O7 anode materials with superior performance for high-rate lithium ion batteries, Chem. Commun. 51 (2015) 17293–17296. https://doi.org/10.1039/C5CC07052J.

[44] S. Müller, P. Pietsch, B.-E. Brandt, P. Baade, V.D. Andrade, F.D. Carlo, V. Wood, Quantification and modeling of mechanical degradation in lithium-ion batteries based on nanoscale imaging, Nat. Commun. 9 (2018) 1–8. https://doi.org/10.1038/s41467-018-04477-1.

[45] H. Song, Y.-T. Kim, A Mo-doped TiNb2O7 anode for lithium-ion batteries with high rate capability due to charge redistribution, Chem. Commun. 51 (2015) 9849–9852. https://doi.org/10.1039/C5CC02221E.

[46] X. Sun, P.V. Radovanovic, B. Cui, Advances in spinel Li4Ti5O12 anode materials for lithium-ion batteries, New J. Chem. 39 (2014) 38–63. https://doi.org/10.1039/C4NJ01390E.

[47] A.G. Kashkooli, G. Lui, S. Farhad, D.U. Lee, K. Feng, A. Yu, Z. Chen, Nano-particle size effect on the performance of Li4Ti5O12 spinel, Electrochimica Acta. 196 (2016) 33–40. https://doi.org/10.1016/j.electacta.2016.02.153.

[48] H.-C. Chiu, X. Lu, J. Zhou, L. Gu, J. Reid, R. Gauvin, K. Zaghib, G.P. Demopoulos, Capacity Fade Mechanism of Li4Ti5O12 Nanosheet Anode, Adv. Energy Mater. 7 (2017). https://doi.org/10.1002/aenm.201601825.

[49] H. Chiu, N. Brodusch, R. Gauvin, A. Guerfi, K. Zaghib, G.P. Demopoulos, Aqueous Synthesized Nanostructured Li4Ti5O12 for High-Performance Lithium Ion Battery Anodes, J. Electrochem. Soc. 160 (2013) A3041–A3047. https://doi.org/10.1149/2.008305jes.

[50] H.-C. Chiu, X. Lu, J. Zhou, L. Gu, J. Reid, R. Gauvin, K. Zaghib, G.P. Demopoulos, Annealing-regulated elimination of residual strain-induced structural relaxation for stable high-power Li4Ti5O12 nanosheet anodes, Nano Energy. 32 (2017) 533–541. https://doi.org/10.1016/j.nanoen.2016.12.063.

[51] H.-C. Chiu, X. Lu, S. Elouatik, K. Zaghib, G.P. Demopoulos, Formation of Lithium Titanate Hydrate Nanosheets: Insight into a Two-Dimension Growth Mechanism by in Situ Raman, Cryst. Growth Des. 16 (2016) 3898–3904. https://doi.org/10.1021/acs.cgd.6b00470.

[52] S. Lou, X. Cheng, Y. Zhao, A. Lushington, J. Gao, Q. Li, P. Zuo, B. Wang, Y. Gao, Y. Ma, C. Du, G. Yin, X. Sun, Superior performance of ordered macroporous TiNb2O7 anodes for lithium ion batteries: Understanding from the structural and pseudocapacitive insights on achieving high rate capability, Nano Energy. 34 (2017) 15–25. https://doi.org/10.1016/j.nanoen.2017.01.058.

[53] L. Buannic, J.-F. Colin, M. Chapuis, M. Chakir, S. Patoux, Electrochemical performances and gassing behavior of high surface area titanium niobium oxides, J. Mater. Chem. A. 4 (2016) 11531–11541. https://doi.org/10.1039/C6TA03813A.

[54] X. Li, J. Xu, P. Huang, W. Yang, Z. Wang, M. Wang, Y. Huang, Y. Zhou, M. Qu, Z. Yu, Y. Lin, In-situ carbon coating to enhance the rate capability of the Li4Ti5O12 anode material and suppress the electrolyte reduction decomposition on the electrode, Electrochimica Acta. 190 (2016) 69–75. https://doi.org/10.1016/j.electacta.2015.12.176.

[55] Y. Shi, J. Gao, H.D. Abruña, H. Liu, H. Li, J. Wang, Y. Wu, Rapid synthesis of Li4Ti5O12/graphene composite with superior rate capability by a microwave-assisted hydrothermal method, Nano Energy. 8 (2014) 297–304. https://doi.org/10.1016/j.nanoen.2014.06.009.

[56] H. Ge, T. Hao, H. Osgood, B. Zhang, L. Chen, L. Cui, X.-M. Song, O. Ogoke, G. Wu, Advanced Mesoporous Spinel Li4Ti5O12/rGO Composites with Increased Surface Lithium Storage Capability for High-Power Lithium-Ion Batteries, ACS Appl. Mater. Interfaces. 8 (2016) 9162–9169. https://doi.org/10.1021/acsami.6b01644.

[57] S. Li, X. Cao, C.N. Schmidt, Q. Xu, E. Uchaker, Y. Pei, G. Cao, TiNb2O7/graphene composites as high-rate anode materials for lithium/sodium ion batteries, J. Mater. Chem. A. 4 (2016) 4242–4251. https://doi.org/10.1039/C5TA10510B.

[58] H. Noh, W. Choi, Preparation of a TiNb2O7 Microsphere Using Formic Acid and Wrapping with Reduced Graphene Oxide for Anodes in Lithium Ion Batteries, J. Electrochem. Soc. 163 (2016) A1042–A1049. https://doi.org/10.1149/2.1181606jes.

[59] M. Yoshio, R.J. Brodd, A. Kozawa, Lithium ion Battery Science and Technologies, Springer, New York, NY, 2009.

[60] M.E. Spahr, D. Goers, A. Leone, S. Stallone, E. Grivei, Development of carbon conductive additives for advanced lithium ion batteries, J. Power Sources. 196 (2011) 3404–3413. https://doi.org/10.1016/j.jpowsour.2010.07.002.

[61] D. McLacklan, M. Blaszkiewics, R. Newnham, Electrical Resistivity of Composites, J. Am. Ceram. Soc. 73 (1990) 2187–2203.

[62] H. Kondo, H. Sawada, C. Okuda, T. Sasaki, Influence of the Active Material on the Electronic Conductivity of the Positive Electrode in Lithium-Ion Batteries, J. Electrochem. Soc. 166 (2019) A1285–A1290.

[63] Y. Liu, X. He, D. Hanlon, A. Harvey, U. Khan, Y. Li, J. Coleman, Electrical, Mechanical, and Capacity Percolation Leads to High-Performance MoS2/Nanotube Composite Lithium Ion Battery Electrodes, ACS Nano. 10 (2016) 5980–5990.

[64] X. Sun, J. Li, C. Shi, Z. Wang, E. Liu, C. He, X. Du, N. Zhao, Enhanced electrochemical performance of LiFePO4 cathode with in-situ chemical vapor deposition synthesized carbon nanotubes as conductor, J. Power Sources. 220 (2012) 264–268. https://doi.org/10.1016/j.jpowsour.2012.07.082.

[65] Y. Shi, L. Wen, S. Pei, M. Wu, F. Li, Choice for graphene as conductive additive for cathode of lithium-ion batteries, J. Energy Chem. 30 (2019) 19–26. https://doi.org/10.1016/j.jechem.2018.03.009.

[66] G. Kucinskis, G. Bajars, J. Kleperis, Graphene in lithium ion battery cathode materials: A review, J. Power Sources. 240 (2013) 66–79. https://doi.org/10.1016/j.jpowsour.2013.03.160.

[67] Z. Liu, L. Lin, H. Ren, X. Sun, Chapter 2 - CVD Synthesis of Graphene, in: G. Zhang (Ed.), Therm. Transp. Carbon-Based Nanomater., Elsevier, 2017: pp. 19–56. https://doi.org/10.1016/B978-0-32-346240-2.00002-9.

[68] S. Pei, H.-M. Cheng, The reduction of graphene oxide, Carbon. 50 (2012) 3210–3228. https://doi.org/10.1016/j.carbon.2011.11.010.

[69] A.T. Dideikin, A.Y. Vul, Graphene Oxide and Derivatives: The Place in Graphene Family | Physics, Front. Phys. 6 (2019). https://doi.org/10.3389/fphy.2018.00149.

[70] E. Aliyev, V. Filiz, M.M. Khan, Y.J. Lee, C. Abetz, V. Abetz, Structural Characterization of Graphene Oxide: Surface Functional Groups and Fractionated Oxidative Debris, Nanomaterials. 9 (2019). https://doi.org/doi.org/10.3390/nano9081180.

[71] A. Ganguly, S. Sharma, P. Papakonstantinou, J. Hamilton, Probing the Thermal Deoxygenation of Graphene Oxide Using High-Resolution In Situ X-ray-Based Spectroscopies, J. Phys. Chem. C. 115 (2011) 17009–17019.

[72] I. Jung, D. Field, N.J. Clark, Y. Zhu, D. Yang, R.D. Piner, S. Stankovich, D.A. Dikin, H. Geisler, Carl.A.Jr. Ventrice, R.S. Ruoff, Reduction Kinetics of Graphene Oxide Determined by Electrical Transport Measurements and Temperature Programmed Desorption, J. Phys. Chem. C. 113 (2009) 18480–18486.

[73] D. Liu, L.-C. Chen, T. Fan, E.-Y. Tsou, C. Tiu, An Effective Mixing for Lithium Ion Battery Slurries, Adv. Chem. Eng. Sci. 4 (2014) 515–528. https://doi.org/10.4236/aces.2014.44053.

[74] A. Ponrouch, M.R. Palacín, On the impact of the slurry mixing procedure in the electrochemical performance of composite electrodes for Li-ion batteries: A case study for mesocarbon microbeads (MCMB) graphite and Co3O4, J. Power Sources. 196 (2011) 9682–9688. https://doi.org/10.1016/j.jpowsour.2011.07.045.

[75] X. Zhang, Y. Zhu, A.M. Bruck, L.M. Housel, L. Wang, C.D. Quilty, K.J. Takeuchi, E.S. Takeuchi, A.C. Marschilok, G. Yu, Understanding aggregation hindered Li-ion transport in transition metal oxide at mesoscale, Energy Storage Mater. 19 (2019) 439–445. https://doi.org/10.1016/j.ensm.2019.03.017.

[76] G. Zhang, C.E. Shaffer, C.-Y. Wang, C.D. Rahn, Effects of Non-Uniform Current Distribution on Energy Density of Li-Ion Cells, J. Electrochem. Soc. 160 (2013) A2299–A2305. https://doi.org/10.1149/2.061311jes.

[77] D.C. Bock, C.J. Pelliccione, W. Zhang, J. Timoshenko, K.W. Knehr, A.C. West, F. Wang, Y. Li, A.I. Frenkel, E.S. Takeuchi, K.J. Takeuchi, A.C. Marschilok, Size dependent behavior of Fe3O4 crystals during electrochemical (de)lithiation: an in situ X-ray diffraction, ex situ X-ray absorption spectroscopy, transmission electron microscopy and theoretical investigation, Phys. Chem. Chem. Phys. 19 (2017) 20867–20880. https://doi.org/10.1039/C7CP03312E.

[78] B. Tran, I.O. Oladeji, Z. Wang, J. Calderon, G. Chai, D. Atherton, L. Zhai, Adhesive PEG-based binder for aqueous fabrication of thick Li4Ti5O12 electrode, Electrochimica Acta. 88 (2013) 536–542. https://doi.org/10.1016/j.electacta.2012.10.139.

[79] D. Bresser, D. Buchholz, A. Moretti, A. Varzi, S. Passerini, Alternative binders for sustainable electrochemical energy storage – the transition to aqueous electrode processing and bio-derived polymers, Energy Environ. Sci. 11 (2018) 3096–3127. https://doi.org/10.1039/C8EE00640G.

[80] B. Ludwig, Z. Zheng, W. Shou, Y. Wang, H. Pan, Solvent-Free Manufacturing of Electrodes for Lithium-ion Batteries, Sci. Rep. 6 (2016) 23150. https://doi.org/10.1038/srep23150.

[81] L. Besra, M. Liu, A review on fundamentals and applications of electrophoretic deposition (EPD), Prog. Mater. Sci. 52 (2007) 1–61. https://doi.org/10.1016/j.pmatsci.2006.07.001.

[82] H. Ohshima, Encyclopedia of Biocolloid and Biointerface, Wiley, 2016. https://doi.org/10.1002/9781119075691.

[83] P. Sarkar, P.S. Nicholson, Electrophoretic Deposition (EPD): Mechanisms, Kinetics, and Application to Ceramics, J. Am. Ceram. Soc. 79 (1996) 1987–2002. https://doi.org/10.1111/j.1151-2916.1996.tb08929.x.

[84] K.S. Birdi, Handbook of Surface and Colloid Chemistry, 2nd ed., CRC Press, 2015. https://doi.org/10.1201/b18633.

[85] T. Cosgrove, Colloid Science: Principles, Methods and Applications, 2nd ed., John Wiley & Sons, Incorporated, Hoboken, UNITED KINGDOM, 2010.

[86] C.J. van Oss, Interfacial Forces in Aqueous Media, 2nd ed., CRC Press, 2006. https://doi.org/10.1201/9781420015768.

[87] I. Aznam, J.C.W. Mah, A. Muchtar, M.R. Somalu, M.J. Ghazali, A review of key parameters for effective electrophoretic deposition in the fabrication of solid oxide fuel cells, J. Zhejiang Univ.-Sci. A. 19 (2018) 811–823. https://doi.org/10.1631/jzus.A1700604.

[88] P. Amrollahi, J.S. Krasinski, R. Vaidyanathan, L. Tayebi, D. Vashaee, Electrophoretic Deposition (EPD): Fundamentals and Applications from Nano- to Microscale Structures, in: M. Aliofkhazraei, A.S.H. Makhlouf (Eds.), Handb. Nanoelectrochemistry Electrochem. Synth. Methods Prop. Charact. Tech., Springer International Publishing, Cham, 2016: pp. 561–591. https://doi.org/10.1007/978-3-319-15266-0_7.

[89] S. Dor, S. Rühle, A. Ofir, M. Adler, L. Grinis, A. Zaban, The influence of suspension composition and deposition mode on the electrophoretic deposition of TiO2 nanoparticle agglomerates, Colloids Surf. Physicochem. Eng. Asp. 342 (2009) 70–75. https://doi.org/10.1016/j.colsurfa.2009.04.009.

[90] O.O. Van der Biest, L.J. Vandeperre, Electrophoretic deposition of materials, Annu. Rev. Mater. Sci. 29 (1999) 327–352. https://doi.org/10.1146/annurev.matsci.29.1.327.

[91] O. van der Biest, S. Put, G. Anné, J. Vleugels, Electrophoretic deposition for coatings and free standing objects, J. Mater. Sci. 39 (2004) 779–785. https://doi.org/10.1023/B:JMSC.0000012905.62256.39.

[92] B. Ferrari, R. Moreno, EPD kinetics: A review, J. Eur. Ceram. Soc. 30 (2010) 1069–1078. https://doi.org/10.1016/j.jeurceramsoc.2009.08.022.

[93] R. Moreno, B. Ferrari, Nanoparticles Dispersion and the Effect of Related Parameters in the EPD Kinetics, in: J.H. Dickerson, A.R. Boccaccini (Eds.), Electrophor. Depos. Nanomater., Springer New York, New York, NY, 2012: pp. 73–128. https://doi.org/10.1007/978-1-4419-9730-2_2.

[94] L. Ye, K. Wen, Z. Zhang, F. Yang, Y. Liang, W. Lv, Y. Lin, J. Gu, J.H. Dickerson, W. He, Highly Efficient Materials Assembly Via Electrophoretic Deposition for Electrochemical Energy Conversion and Storage Devices, Adv. Energy Mater. 6 (2016). https://doi.org/10.1002/aenm.201502018.

[95] X. Michaud, K. Shi, I. Zhitomirsky, Electrophoretic deposition of LiFePO4 for Li-ion batteries, Mater. Lett. 241 (2019) 10–13. https://doi.org/10.1016/j.matlet.2019.01.032.

[96] K. Moyer, R. Carter, T. Hanken, A. Douglas, L. Oakes, C.L. Pint, Electrophoretic deposition of LiFePO4 onto 3-D current collectors for high areal loading battery cathodes, Mater. Sci. Eng. B. 241 (2019) 42–47. https://doi.org/10.1016/j.mseb.2019.02.003.

[97] Y. Tang, H. Zhang, J. Li, G. Hou, H. Cao, L. Wu, G. Zheng, Q. Wu, Three-dimensional ordered macroporous Cu/Fe3O4 composite as binder-free anode for lithium-ion batteries, J. Alloys Compd. 719 (2017) 203–209. https://doi.org/10.1016/j.jallcom.2017.05.172.

[98] W. Yuan, Z. Qiu, Y. Chen, B. Zhao, M. Liu, Y. Tang, A binder-free composite anode composed of CuO nanosheets and multi-wall carbon nanotubes for high-performance lithium-ion batteries, Electrochimica Acta. 267 (2018) 150–160. https://doi.org/10.1016/j.electacta.2018.02.081.

[99] N.P. Benehkohal, M.J. Sussman, H. Chiu, M. Uceda, R. Gauvin, G.P. Demopoulos, Enabling Green Fabrication of Li-Ion Battery Electrodes by Electrophoretic Deposition: Growth of Thick Binder-Free Mesoporous TiO2-Carbon Anode Films, J. Electrochem. Soc. 162 (2015) D3013–D3018. https://doi.org/10.1149/2.0111511jes.

[100] S. Azuma, H. Yamada, G. Kawamura, H. Muto, T. Mizushima, A. Matsuda, Development of multilayer coating system based on electrophoretic deposition process, J. Ceram. Soc. Jpn. 125 (2017) 317–321. https://doi.org/10.2109/jcersj2.16278.

[101] C.C. Lalau, C.T.J. Low, Electrophoretic Deposition for Lithium-Ion Battery Electrode Manufacture, Batter. Supercaps. 2 (2019) 551–559. https://doi.org/10.1002/batt.201900017.

[102] G. Jha, T. Tran, S. Qiao, J. M. Ziegler, A. F Ogata, S. Dai, M. Xu, M. Le, G. Thesma Chandran, X. Pan, R. Penner, Electrophoretic Deposition of Mesoporous Niobium(V)Oxide Nanoscopic Films, Chem. Mater. 30 (2018). https://doi.org/10.1021/acs.chemmater.8b03254.

[103] N.A. Kyeremateng, T.M. Dinh, D. Pech, Electrophoretic deposition of Li4Ti5O12 nanoparticles with a novel additive for Li-ion microbatteries, RSC Adv. 5 (2015) 61502–61507. https://doi.org/10.1039/C5RA11039D.

[104] K. Kaprans, J. Mateuss, A. Dorondo, G. Bajars, G. Kucinskis, P. Lesnicenoks, J. Kleperis, Electrophoretically deposited α-Fe2O3 and TiO2 composite anchored on rGO with excellent cycle performance as anode for lithium ion batteries, Solid State Ion. 319 (2018) 1–6. https://doi.org/10.1016/j.ssi.2018.01.042.

[105] M.K. Keshmarzi, A.A. Daryakenari, H. Omidvar, M. Javanbakht, Z. Ahmadi, J.-J. Delaunay, R. Badrnezhad, Pulsed electrophoretic deposition of nanographitic flake-nanostructured Co3O4 layers for efficient lithium-ion-battery anode, J. Alloys Compd. 805 (2019) 924–933. https://doi.org/10.1016/j.jallcom.2019.07.078.

[106] C.J. Hung, P. Lin, T.Y. Tseng, Electrophoretic fabrication and pseudocapacitive properties of graphene/manganese oxide/carbon nanotube nanocomposites, J. Power Sources. 243 (2013) 594–602. https://doi.org/10.1016/j.jpowsour.2013.06.055.

[107] M. Diba, D.W.H. Fam, A.R. Boccaccini, M.S.P. Shaffer, Electrophoretic deposition of graphene-related materials: A review of the fundamentals, Prog. Mater. Sci. 82 (2016) 83–117. https://doi.org/10.1016/j.pmatsci.2016.03.002.

[108] Y. Huang, H. Liu, Y.-C. Lu, Y. Hou, Q. Li, Electrophoretic lithium iron phosphate/reduced graphene oxide composite for lithium ion battery cathode application, J. Power Sources. 284 (2015) 236–244. https://doi.org/10.1016/j.jpowsour.2015.03.037.

[109] X. Xia, J. Tu, Y. Mai, R. Chen, X. Wang, C. Gu, X. Zhao, Graphene Sheet/Porous NiO Hybrid Film for Supercapacitor Applications, Chem. – Eur. J. 17 (2011) 10898–10905. https://doi.org/10.1002/chem.201100727.

[110] X. Zhang, Y. Lai, M. Ge, Y. Zheng, K.-Q. Zhang, Z. Lin, Fibrous and flexible supercapacitors comprising hierarchical nanostructures with carbon spheres and graphene oxide nanosheets, J. Mater. Chem. A. 3 (2015) 12761–12768. https://doi.org/10.1039/C5TA03252K.

[111] S.-H. Lee, S.-D. Seo, K.-S. Park, H.-W. Shim, D.-W. Kim, Synthesis of graphene nanosheets by the electrolytic exfoliation of graphite and their direct assembly for lithium ion battery anodes, Mater. Chem. Phys. 135 (2012) 309–316. https://doi.org/10.1016/j.matchemphys.2012.04.043.

[112] S.-D. Seo, I.-S. Hwang, S.-H. Lee, H.-W. Shim, D.-W. Kim, 1D/2D carbon nanotube/graphene nanosheet composite anodes fabricated using electrophoretic assembly, Ceram. Int. 38 (2012) 3017–3021. https://doi.org/10.1016/j.ceramint.2011.11.083.

3 Nano-lithium titanate/carbon composite electrodes

As mentioned in section 2.2 the current PVDF-based electrode fabrication technique has two key problems: 1) the use of the toxic NMP solvent and 2) its unsuitability when nanoparticles are involved. One of the principal objectives of this research is to design an EPD-enabled system that allows for fabrication of homogeneous multi-component coatings. This intimate component self-assembly and deposition will minimize the coating internal polarization and improve electrode kinetics and performance.

Thus, in this first study, an EPD-based fabrication system was investigated to build a LIB anode composite made of carbon-coated LTO nanoparticles, carbon black, and styrene butadiene rubber (SBR) as binder and compare its electrochemical performance to conventionally built-electrodes. To this end 1) suspension and EPD parameter optimization was performed to determine optimal EPD conditions, 2) electrochemical characterization was carried out on the EPD electrodes and compared to conventionally prepared electrodes (EIS, cycling, and rate cycling), and 3) characterization of the coating was performed to explain the performance difference (XRD, Raman, TGA, XPS, TEM, and cross-sectional SEM and EDS).

These findings are published in: **Marianna Uceda**, Jigang Zhou, Jian Wang, Reynald Gauvin, Karim Zaghib, and George P. Demopoulos (2019). **Highly conductive NMP-free carbon-coated nano-lithium titanate/carbon composite electrodes via SBR-assisted electrophoretic deposition**. *Electrochimica Acta* 299 (2019) 107-115.

3.1 Abstract

Li-ion storage electrodes are manufactured through the conventional cast process involving the use of a toxic solvent (n-methyl-2- pyrrolidone, NMP) and the binder polyvinylidene fluoride (PVDF). This process can be problematic for nanosized materials as they form viscous suspensions that prevent the formation of uniformly dense coatings. Additionally, the NMP solvent is very hazardous. Herein lies the viability of using electrophoretic deposition (EPD) as an alternative manufacturing process that would both eliminate the need for a toxic solvent and improve electrode properties is presented. In particular, it is shown that styrene- butadiene rubber (SBR) enables the assembly of carbon-coated LTO and carbon nanoparticles into bridged hetero-aggregates that render themselves to fast growth of adherent highly performing LIB electrodes. The electrodes are built by suspending C-coated LTO, carbon, and SBR at 80/10/10 wt.% ratio in a medium consisting of 90/10 vol.% acetonitrile and water, performing 3-5 stages of 15-second constant current deposition cycles followed by pressing at 4MPa and drying in a vacuum oven. Raman spectroscopy, thermogravimetric analysis (TGA), and energy-dispersive X-ray spectroscopy (EDS) with SEM were performed to examine carbon/LTO composite film homogeneity and compared to conventional PVDF-based electrodes. More importantly, photoemission electron microscopy (PEEM) and X-ray absorption near edge structure (XANES) were used to probe the presence/distribution of the SBR binder in the coating. The EPD-based electrode exhibits superior rate capability when compared to the PVDF-based electrodes. The conductivity, as shown by EIS, of the pressed EPD electrodes was 15 times higher than that of the pressed PVDF electrodes demonstrating the superiority of EPD in fabricating highly conductive electrodes for high-power LIB application.

3.2 Introduction

Electrochemical energy-storage devices such as lithium-ion batteries (LIB) play a critical role in the integration of renewables into the grid, electrical load balancing, and electric transportation [2]. LIBs in particular using nanosized lithium titanate spinel ($Li_4Ti_5O_{12}$, LTO) as the anode material have been identified as one of the safest and longer lifecycle electrochemical energy storage devices for power applications [3]. The outstanding performance of LTO is the result of its ideal intercalation crystallographic characteristics. During electrochemical Li intercalation/deintercalation, there is a negligible (0.2%) volume change from the pristine

$Li_4Ti_5O_{12}$ (8.3595Å) to the lithiated $Li_7Ti_5O_{12}$ (8.3538Å) form[4],[5]. This "zero strain" feature directly contributes to their excellent cycle life[6,7]. During lithiation (intercalation), the external Li ions and the original Li ions occupying tetrahedral sites jump into the neighboring octahedral vacancies in the spinel $Li_4Ti_5O_{12}$ to rock-salt $Li_7Ti_5O_{12}$, hence a specific capacity of 175 mAh/g. The coexistence of spinel and rock-salt structure also fixes the redox potential at 1.55 V vs. Li^+/Li, which is a voltage plateau over a wide stoichiometric range of $Li_{4+x}Ti_5O_{12}$, $0.1<x<2.9$ [4,8,9]. Thus, electrolyte reduction on the electrode surface that usually occurs at 0.5 V vs. Li^+/Li to form the solid-electrolyte interphase (SEI) layer is minimized. This guarantees the outstanding safety of LTO.

For nanosized LTO, its electrochemical performance, including rate capability and capacity fade [10,11] is determined by the electrolyte/LTO interface where the charge-transfer reaction and excess Li storage occur [12]. As a result, surface modification of LTO, such as carbon coating, is an effective strategy when designing the high-performance nano-LTO electrodes [13,14]. One difficulty encountered in nano-LTO electrode fabrication is their low tap density which imposes rheological restrictions on the suspension conditioning of conventional colloidal cast processes. The suspension consisting of nanosized active materials, conductive additives, with polyvinyldene fluoride (PVDF) binder and n-methyl-2-pyrrolidone (NMP) usually exhibits higher viscosity when compared to methods using microsized electrode materials (prepared at similar solid loading). This high viscosity makes it difficult to prepare electrodes that consistently contain the same film density and thickness. In this respect, electrophoretic deposition (EPD) is a possible effective fabrication alternative. EPD involves electrical field-driven colloidal particle migration and deposition onto a conductive substrate like aluminum metal. The process offers unique versatility and control of the deposit microstructure via proper regulation of suspension and electrodeposition parameters such as applied electrical field, current density and deposition time or frequency[15]. As a result, EPD has been explored as a technique to prepare nanostructured coatings for medical applications [16], exposure protection [17], dye-sensitized solar cells [18–20], solid oxide fuel cells, energy storage devices [15]. Examples of fabrication of electrodes for electrochemical energy storage devices include materials such as nickel oxides [21], titania composites [15,22], tin oxide [23], lithium iron phosphate composites [24],[25], and graphite [26].

The present study uses carbon-coated, nanosized lithium titanate to study the effectiveness of using EPD to fabricate thick highly-conductive LTO electrodes with superior rate capability when compared to the conventionally manufactured electrodes. Kyeremateng et al. [1] fabricated 3.3 μm thick LTO electrodes for microbatteries via EPD using a 95/5 vol% ethanol/water medium, $\mathrm{MgCl_2}$ as the charging agent, and a pulsed potential. The $\mathrm{Mg^{2+}}$ cations induced by cathodic hydrolysis, as demonstrated by Benehkohal et al. in the case of $\mathrm{Zn^{2+}}$ [27] , co-deposited as $\mathrm{Mg(OH)_2}$ the latter acting as a binding agent improving the conductivity of the LTO (which is a very poor electronic conductor). The film, however, became irregular and not uniform with progressive growth limiting its thickness to only 6.5 μm.

In this work a new EPD process is developed capable of producing strongly adherent thick ($20\mu m$) and highly conductive LTO-Carbon (Acetylene Black) composite electrodes featuring C-coated LTO nanoparticles. This is achieved by using styrene butadiene rubber (SBR), an aqueous based binder that is already commonly used in the battery fabrication industry [28]. SBR serves as stabilizing additive for the nano-C-coated LTO/Acetylene Black suspension as well as binder for the electrode assembly.

The challenge with the LTO/carbon combination is that the two materials are dissimilar (LTO is polar and carbon is not), this makes it difficult to find a common solvent to formulate a stable suspension. Through a judicious selection process, we found that an acetonitrile medium containing 10% water can fulfil this requirement. In comparison to water, with a relative permittivity and dipole moment of 80.1 and 1.86 D respectively, acetonitrile is less polar having relative permittivity of ~36 and a dipole moment of 3.92 D. This mixed solvent with the added benefit of SBR enabled the novel EPD system to be designed achieving fast deposition kinetics of much thicker than ever before LIB electrodes.

After EPD, the deposits were characterized to determine the composition. SEM EDS images were used to determine the distribution between carbon black and LTO. Distinguishing carbon sources between carbon and SBR was challenging as they decompose at similar temperatures (ruling out thermogravimetric analysis). Photoemission electron microscopy (PEEM) was then used to probe the electrodes revealing that SBR and carbon are uniformly interconnected to C-coated LTO nanoparticles (a property also observed in SEM analysis). Finally, EPD- and PVDF-based electrodes were assembled into cells and electrochemically evaluated to demonstrate the superiority of EPD in fabricating highly conductive electrodes for LIB application.

3.3 Experimental Procedure

3.3.1 Materials

Commercial $Li_4Ti_5O_{12}$ spinel (LTO) (Aldrich, CAS No. 12031-95-7) with a typical nanoparticle size of 50 nm and a surface area of 11 m^2/g (determined through BET, Micromeritics TriStar 3000) was used as the active material, the conductive material was Acetylene black (Alfa Aesar, CAS No. 1333-86-4) with an average particle size of 60 nm and area of $75m^2/g$. For carbon coating, lactose (Sigma, CAS. 63-42-3) was used. The main EPD solvent was ACS certified Acetonitrile (Fischer, CAS No. 75-05-8). The binder used was modified styrene butadiene rubber copolymer (SBR) (SSBR100, Targray 15 wt.% polymer and 0.3 wt.% surfactant). The conventional (tape-cast) electrodes used polyvinyldene fluoride (PVDF) (Solvay, Solef 6020) and 2-n-methyl-pyrrolidone (NMP) (Sigma).

3.3.2 Carbon Coating on LTO

22.4 g/L of lactose was mixed with DI water for 30 min. 10 mL of the lactose solution was then mixed with 2g of LTO at a ratio of 0.112 g lactose/g LTO in a graphite crucible. The slurry was dried in an oven and transferred to an MTI mini tube furnace (model OTF-1200X) and heated to $700℃$ for ~400 min to allow for lactose decomposition and carbonization of LTO. The carbon coating was confirmed through Raman Spectroscopy using a Bruker SENTERRA confocal Raman microscope.

3.3.3 Electrode Preparation

The electrodes were prepared via EPD process and the conventional PVDF-based tape casting process for comparison. The EPD suspension was prepared by mixing 3 g/L of carbon-coated LTO, carbon (Acetylene Black, AB), and SBR at 80/10/10 wt.% respectively within a medium consisting of acetonitrile and water at 90/10 vol.% respectively. The suspension was sonicated for 15 minutes to break down aggregates. The suspension zeta potential was analyzed using a Malvern Zetasizer Nano ZS. Different ratios of acetonitrile and water were tested and the ratio selected had the best stability. Two aluminum electrodes are then submerged into the suspension. The cathode is a thick aluminum electrode and anode is thin 15 μm aluminum foil (kept rigid using glass) placed 8mm apart. The electrodes are connected to a Keithley 2600 SourceMeter used to apply a constant current. EPD was performed at $3.5 - 4\, mA/cm^2$ for 3-5 stages each at 15 seconds. Ambient temperature drying between each stage for 5 minutes was allowed. Deposition was anodic on a deposition area of $5.3\, cm^2$. The electrodes were then punched out of the foil in preparation for cell assembly.

The conventional electrodes (hereafter referred to as the "PVDF electrodes") were fabricated by mixing the carbon-coated LTO, carbon (AB), and PVDF binder at 80/10/10 wt.% in NMP solvent to fabricate a paste with a solid concentration of 200 g/L. It was then tape cast by doctor blading onto aluminum foil and dried for 6h in an oven at 80℃, transferred to a vacuum oven and dried at $100℃$ for 24h. This was done to ensure the removal of NMP from the coating. Just as with EPD, the electrodes were punched out of the Al foil. Both EPD and tape-cast PVDF electrodes had an average mass density of $6.4 \pm 0.6\, mg/cm^2$. Tape-cast prepared electrodes will be referred to as "PVDF electrodes".

Both EPD and PVDF electrodes were then pressed at 4MPa and placed into the vacuum oven and dried at $100℃$ for 24h. They were then transferred to a glovebox for battery assembly. Both coin cells and Swagelok-type cells were assembled with lithium metal as the anode and $200\, \mu L\ 1M\ LiPF_6$ in EC:DMC:DEC at 2:2:1 by weight as the electrolyte.

3.3.4 Electrode Characterization and Performance

The thickness of the EPD electrode deposits was measured through a Dektak 3ST profilometer. Both EPD and PVDF electrodes were imaged (BSE and EDS) using a Hitachi SU8230 SEM. Thermogravimetric Analysis (TGA) was performed using a TGA/DSC 2 (Mettler Toledo). 3-5 mg of the sample was weighed on a platinum pan and heated to 800℃ at a ramping rate of $10℃/min$ under continuous air-flow (60mL/min) to eliminate the carbon. To characterize post-EPD samples, the powder was scraped off the substrate.

The LTO electrodes were chemically imaged by photoemission electron microscopy (PEEM) at the Spectromicroscopy (SM) Beamline of the Canadian Light Source (CLS). Internal X-ray near edge spectroscopy (XANES) reference spectra at oxygen K-edge and Ti L-edge are used to generate the corresponding chemical mappings. The incident X-ray beam is 16 degrees with the sample surface. PEEM image secondary electron emission from the sample following X-ray photon absorption process. The narrow escape depth (~10nm) of the secondary electron determines PEEM as a surface sensitive technique.

Electrochemical Impedance Spectroscopy (EIS) measurements were taken using a BioLogic VSP Potentiostat/Galvanostat/EIS system on pristine cells in the frequency range of 1000 kHz to 10 mHz, a sinus amplitude of 10 mV, and a voltage range between 10V and -10V.

Galvanostatic charge/discharge testing was performed on the half-cells between 1 and 2.5V at 1C Rate (where 1C=175 mAh/g) for 150 cycles. Rate cycling was performed by varying the rate between C/5, 1C, 5C, 10C, 20C, and 1C at 5 cycles per rate.

3.4 Results and Discussion

3.4.1 C-coated LTO Nanomaterial

SEM images of the pristine LTO can be found in Figure A-1 in Appendix A. The images show the pristine material is around 40-100nm. Figure 3-1 shows TEM images of the (a) pristine and (b, c) C-coated LTO nanoparticles. As it can be seen the average nanoparticle size in the pristine material is around 50 nm. There is no significant nanoparticle growth or sintering upon C-coating at 700 ºC as also confirmed through BET measurements that found the pristine LTO and C-coated LTO to have equivalent surface areas of 11.8 and 11.4 m^2/g respectively. TGA analysis (see Figure A-3 in Appendix A) determined the carbon coating content to be 1.75 ± 0.25 wt.%. SEM and EDS analysis presented in Figure A-2 in Appendix A indicate that carbon is dispersed throughout the entire particle cluster suggesting uniform nanoparticle coating.

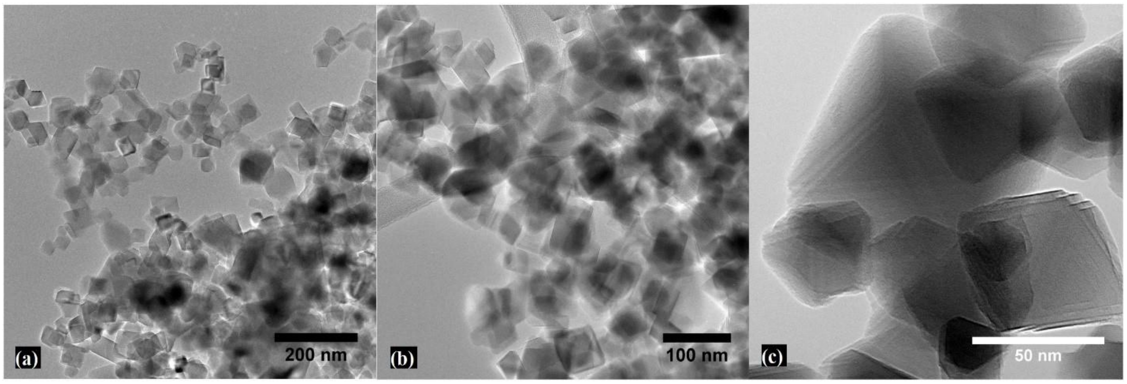

Figure 3-1: TEM images of (a) pristine LTO and (b, c) C-coated LTO nanoparticles.

The C-coated LTO particles were characterized further using Raman spectroscopy. Figure 3-2 shows the Raman spectra for pristine LTO and C-coated LTO (C-LTO) recorded at a laser excitation wavelength of 532 nm. Kellerman et al. [29] report that pristine LTO has three high intensity peaks at 238, 439, and 679 $cm^{-1}$and five low intensity peaks at 276, 349, 514, 620, and

761 cm^{-1}. Table A-1 in Appendix A compares the measured peaks for LTO and C-LTO with literature values. The carbon peaks can be observed in the C-LTO sample at 1334 and 1594 cm^{-1} confirming the presence of carbon on the surface of the powder. These peaks are referred to as the "D" (1340 cm^{-1}) and "G" (1580 cm^{-1}) bands respectively. The D band is attributed to defects (sp^3 bonds) within the graphite and the presence of disordered carbon, pure graphite would not contain a D band [30]. The intensity ratio (I_D/I_G) between these bands gives an indication of how perfect or pure the graphite structure/coating is. The calculated ratio was 0.79 which is indicative of a significant amount of disordered carbon other than graphitic [30–32].

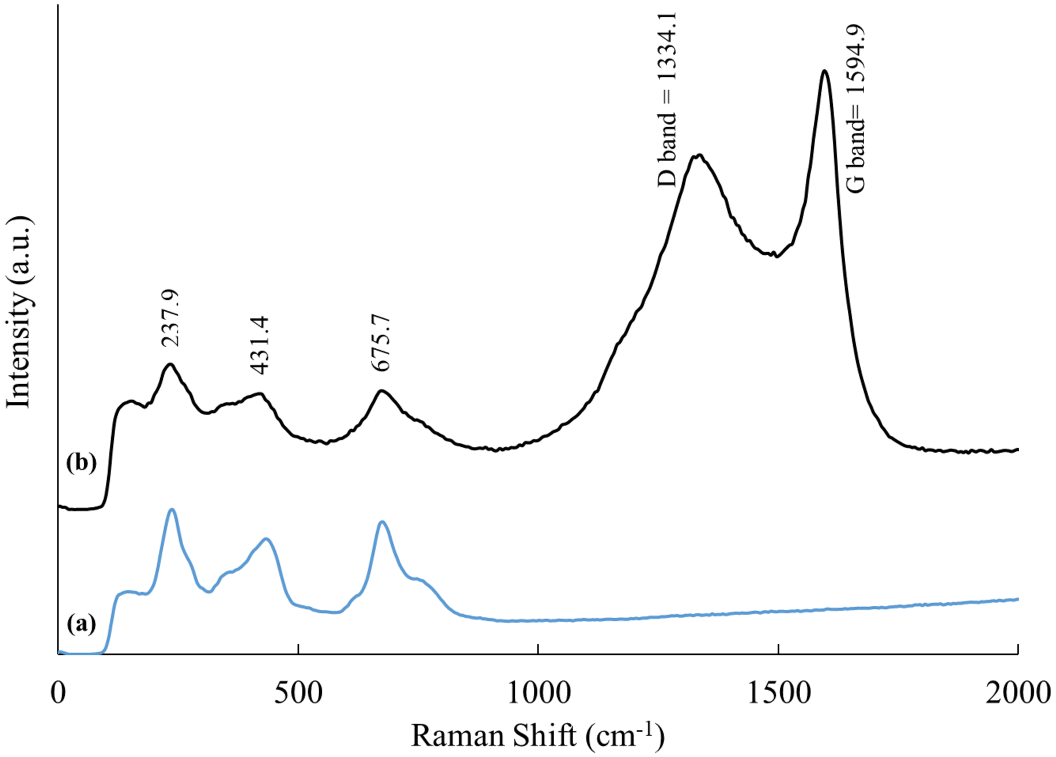

Figure 3-2: Raman spectra of (a) pristine LTO and (b) carbon-coated LTO (C-LTO).

According to Leonidov et al.[33], heating, such as in carbonization, leads to redistribution of the lithium ions from *8a* tetrahedral site to the vacant *16c* octahedral sites. This would lead to changes in the location and intensity of the Raman peaks. Indeed, a shift in the middle high intensity peak (431 to 419 cm^{-1}) coupled with a decrease in intensity was observed. This peak corresponds to vibrations in the Li-O bonds. To exclude the possibility this alteration in the position of the 431 cm^{-1} peak was due to the carbon deposit, pure lactose was carbonized, and the residue was also tested using Raman. Only two peaks were observed at 1340 and 1593 nm, hence the 431 cm^{-1} peak alteration can be attributed to Li-O bonds.

3.4.2 Deposition Kinetics and Composition

3.4.2.1 Suspension stability

Prior to selecting the mixed acetonitrile/water solvent, a series of different media were tested. Organic solvents were the predominant focus as the required high potential for EPD leads to the electrolysis of aqueous suspension (water decomposition). Among the organic media attempted were ethanol, ethylene glycol, isopropanol, methanol, dimethylformamide, acetylacetone, and toluene. Varying compositions of water (5-25 vol.%) were also added to these media to improve suspension stability. In addition, charging agents such as $MgCl_2$, $AlCl_3$, HCl, and NaOH were tested alongside the surfactant Triton X100. The suspension consisting of 90/10 vol.% acetonitrile/water as solvent plus the hydrophilic styrene-butadiene rubber (SBR) binder was ultimately selected as it was stable and enabled the formation of good composite coatings. Further information on solvent selection (as well as selection of EPD parameters) is given in section A.1 of Appendix A.

Carbon-coated LTO, carbon, and SBR were suspended separately in the acetonitrile/water medium to measure the zeta potential of individual materials. The zeta potential for carbon-coated LTO, carbon, and SBR was -42 mV, -28 mV, -41 mV respectively. When these materials are mixed in the suspension, along with SBR, the zeta potential becomes -41 mV. This negative zeta potential led to anodic deposition. Note that no charging agents were used. Charging of the particles is attributed to surface dissociation of water and release of hydroxyl ions. This was evidenced by a pH increase from ~7.4 to ~9.0 upon addition of the LTO and carbon black into the 90/10 vol.% acetonitrile/water solvent system. The suspension was very stable and lasted ~48 hours before any noticeable sedimentation started occurring. Further information is given in section A.1 of Appendix A.

Via Dynamic Light Scattering the suspended nanoparticles (C-coated LTO and Carbon) were found to form hetero-aggregates of $251.3 \pm 0.5\%$ nm size. Considering that the TEM analysis showed individual primary LTO and Carbon (Acetylene Black) nanoparticles to be between 50-70nm in the dry powder and the suspension contained a small fraction of water, we propose the hydrophilic SBR polymer to have played a key role in forming these hetero-aggregates. As graphically illustrated in Figure A-4 of Appendix A, we propose SBR to serve as a bridge to aggregate the otherwise negatively charged nanoparticles. This enabled the homogeneous – at nanoparticle scale – intimate assembly and co-deposition of active and conductive components which will become clear by the film characterization analysis.

3.4.2.2 Effect of current density

The effect of current density on deposit growth was studied and plotted on Figure 3-3. As can be seen, a current density of 3.8 mA/cm^2 produces a deposit around ~18μm thick with a mass density of ~5.5 mg/cm^2 (a yield of 15 wt.% of the total suspended solids) after 6 stages of 15-sec deposition. Increasing the current density by 50% produces a deposit of ~35μm thick with similar deposit mass density. As both electrodes were the same area, this would indicate the increase in thickness was not a result of more material being deposited. The accumulation rate of the particles on the electrode surface will affect the deposition packing, a larger current density would lead to a faster accumulation rate and result in a more loosely packed deposit that is thicker, i.e. more voluminous [34]. These results show that EPD can be appropriately regulated to change the packing density, thickness, and porosity of the electrode as per intended use in supercapacitor or battery applications.

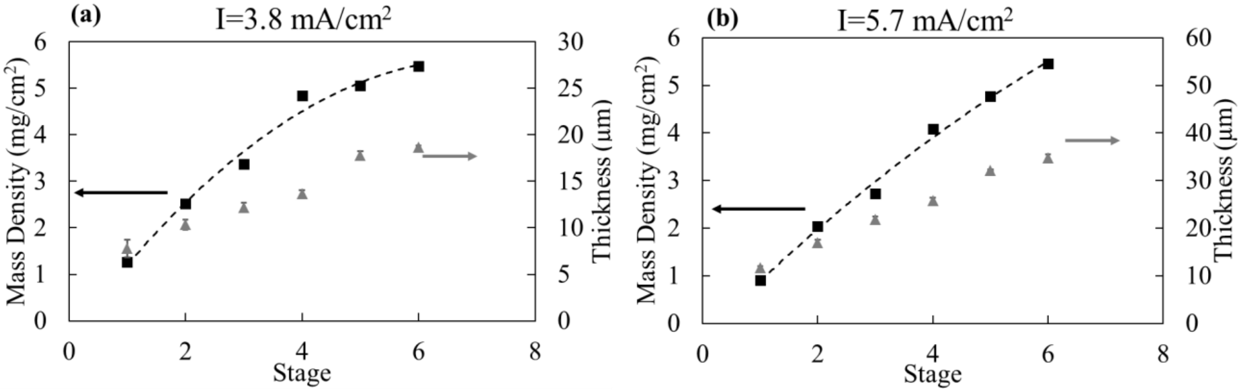

Figure 3-3: Deposit growth over stage/time for (a) low and (b) high current densities.

Figure 3-3 also shows the largest current density exhibits a linear increase in mass yield when compared to the lower current density which plateaus after 4 stages. EPD growth is pseudo-linear and at short deposition times a linear growth can be observed. The widely-accepted Sarkar and Nicholson deposit growth model [34,35] under constant current condition is shown in Eq. 3-1.

$$w(t) = w_o(1 - e^{-\kappa t}) \qquad \text{Eq. 3-1}$$

Where $w(t)$ is the total mass deposited at time t, w_o is the initial mass in suspension, and κ is the rate constant. The rate constant can be related to particle velocity through equation Eq. 3-2.

$$v = \frac{\kappa V}{Sf} \qquad \text{Eq. 3-2}$$

Where v is the particle velocity ($\mu m/s$), V is suspension volume (m^3), S is deposition area (m^2), and f is the efficiency factor. In an ideal system, $f = 1$, if all particles that accumulate at the electrode surface form part of the deposit; for a stable system with a high zeta potential it is expected that the efficiency factor is close to 1 [35].

By plotting $\ln\left(\frac{w_o}{w_o - w}\right)$ vs. time, where $w_o = 180mg$ (the initial mass of the powders in suspension), the rate constant can be calculated. For the high current density experiment, this was determined to be $\kappa = 1.63 \times 10^{-3}\ s^{-1}$. Using Eq. 3-2 the particle velocity for the high current density was calculated at $297\ \mu m/s$. Similarly, the low current density experiment yielded a rate constant $\kappa = 1.67 \times 10^{-3} s^{-1}$ and a velocity of $281\ \mu m/s$. This indicates that increasing the current density leads to faster kinetics and the formation of relatively loosely packed coatings. However, this shows that increasing the current density could potentially yield a heavier deposit as growth remains linear for the higher current density.

3.4.2.3 Deposit composition

TGA was performed (results are given in Figure A-3 of the Appendix A) to measure the carbon content of the carbon-coated LTO and EPD electrodes. Electrodes were prepared using a suspension consisting of 93/3/4 and 80/10/10 wt.% C-LTO/C/SBR respectively. This was to test the effect of increasing LTO while decreasing the SBR and carbon which would mean less binding material. The results show the carbon coating decomposes between 300-520℃. The SBR slurry received from Targray has two decomposition temperatures at 340 and 400℃. And finally, the carbon black decomposes after ~ 550℃. For the coatings, loss of mass prior to this temperature is attributed to decomposition of SBR, the carbon-coating, and the evaporation of moisture and volatile organic components. The total weight lost for the 80/10/10 and 93/3/4 electrodes was 14.5 and 9.7 wt.% respectively. The weight lost after 550℃ for the 80/10/10 and 93/3/4 electrodes was 12.2 and 5.4 wt.%, this could potentially be a close estimation of what the carbon black composition is in the electrode, however since the decomposition temperatures of the carbon-coating and the carbon black are so close this isn't certain. Additionally, the mass lost prior to $550°\mathrm{C}$ differs largely between the electrodes. This could be due to a larger amount of moisture or uneven carbon-coating of the particles. In this case TGA is unable to specify the exact composition of the electrodes.

It is important to note the apparent disparity between suspension and deposition composition. Suspensions consisting of 80 and 93 wt.% LTO produced deposits with ~86 and ~92 wt.% LTO (using the mass retained after $550°\mathrm{C}$ and accounting for the moisture – see TGA results). The LTO has a higher zeta potential implying the electrophoretic mobility, and therefore deposition rate, is the highest. This could partly explain the difference between suspension and deposition composition. However, as the suspension content of LTO is increased this does not lead to an equivalent increase in deposit LTO as seen from the suspension containing 93 wt.% LTO which yielded 92 wt.% LTO in the deposit. Additionally, the particle velocities for the 93/3/4 electrode (fabricated using a low current density of 3.8 mA/cm^2) was calculated to be $278\ \mu m/s$. When compared to the 80/10/10 electrode with a velocity of 281 $\mu m/s$, this means that adding more carbon (with the lower zeta potential) does not lead to a dramatic reduction in electrophoretic mobility as theorized. This implies there are other factors at work that dictate deposit composition such as the aforementioned formation of hetero-aggregates between particles in suspension.

Figure 3-4 Figure 3-5 show cross-sectional SEM images along EDS maps for the PVDF and EPD electrodes (prepared from 80/10/10 wt.% C-LTO/C/SBR at 3.8 mA/cm^2) respectively. The images showed that the EPD thickness was around 20 μm after 4 stages of EPD and pressing at 4 MPa. The thickness of the PVDF electrodes was $\sim 18 \mu m$ after pressing at the same loading. Both electrodes had a film density of $6.4 mg/cm^2$. The initial thickness is determined by the height of the doctor blade used and the viscosity of the slurry. As this parameter is constant, the EPD electrode thickness was maintained as closely as possible for comparison purposes. The PVDF BSE image in Figure 3-4 (a) shows a section within the layer composed of mainly LTO. This is further supported by the EDS imaging which shows these sections are composed of low carbon and high oxygen and titanium. This suggests an uneven distribution of carbon and LTO nanoparticles throughout the layer. Ideally, carbon (AB and C-coating) distribution should be a uniform monolayer around each active particle to improve lithium insertion and de-insertion kinetics [36]. For both BSE images, a dark layer between the deposit and the substrate can be seen caused by the deposit separating during handling. This layer is thinner in the EPD electrode which indicates it has improved adhesion to the substrate. As both electrodes used the same substrate (aluminum foil), it is safe to assume the improved adhesion is the result of EPD coating.

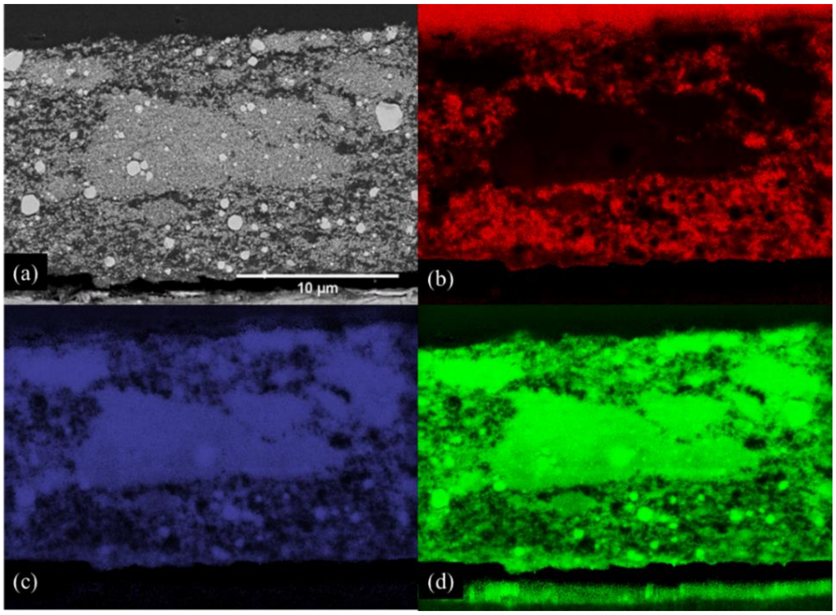

Figure 3-4: (a) BSE SEM cross-sectional image of PVDF electrode and corresponding EDS maps of (b) C, (c) Ti, and (d) O.

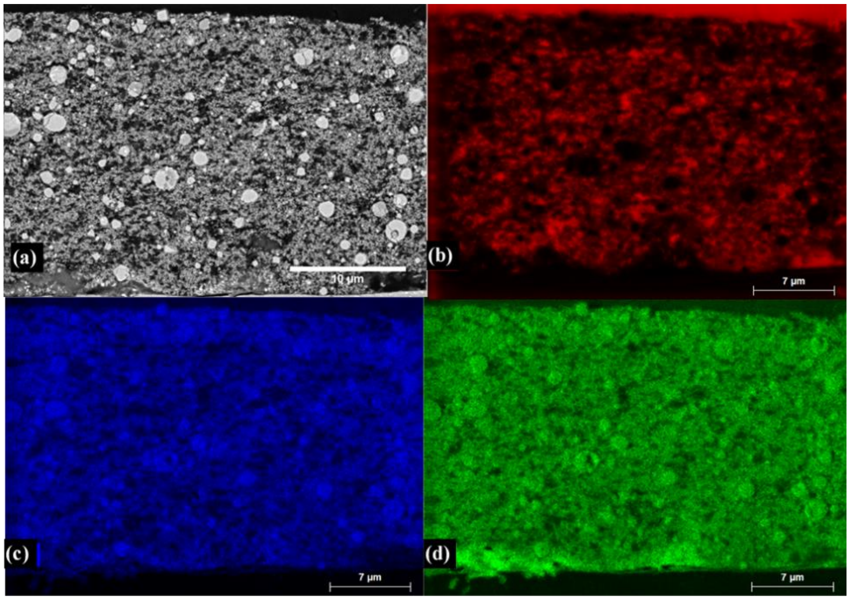

Figure 3-5: (a) BSE SEM cross-sectional image of EPD electrode and corresponding EDS maps of C (b), Ti (c), and O (d).

3.4.2.4 *PEEM analysis of electrode film*

Synchrotron-based photoemission electron microscopy (PEEM) combined with X-ray absorption near edge structure (XANES) technique was employed to probe in more detail the element-specific component distribution on the prepared EPD electrodes. Notably, it was performed to distinguish between SBR and the other components to determine homogeneity.

Figure 3-6 shows the PEEM images and XANES spectra at Ti L-edge (a-c) and O K-edge (d-f) respectively. The XANES spectra in green and red color corresponds to the green and red areas in the PEEM images. As identified from the XANES, the green area corresponds to areas of high concentration of Ti or O (i.e. LTO) relative to the red area.

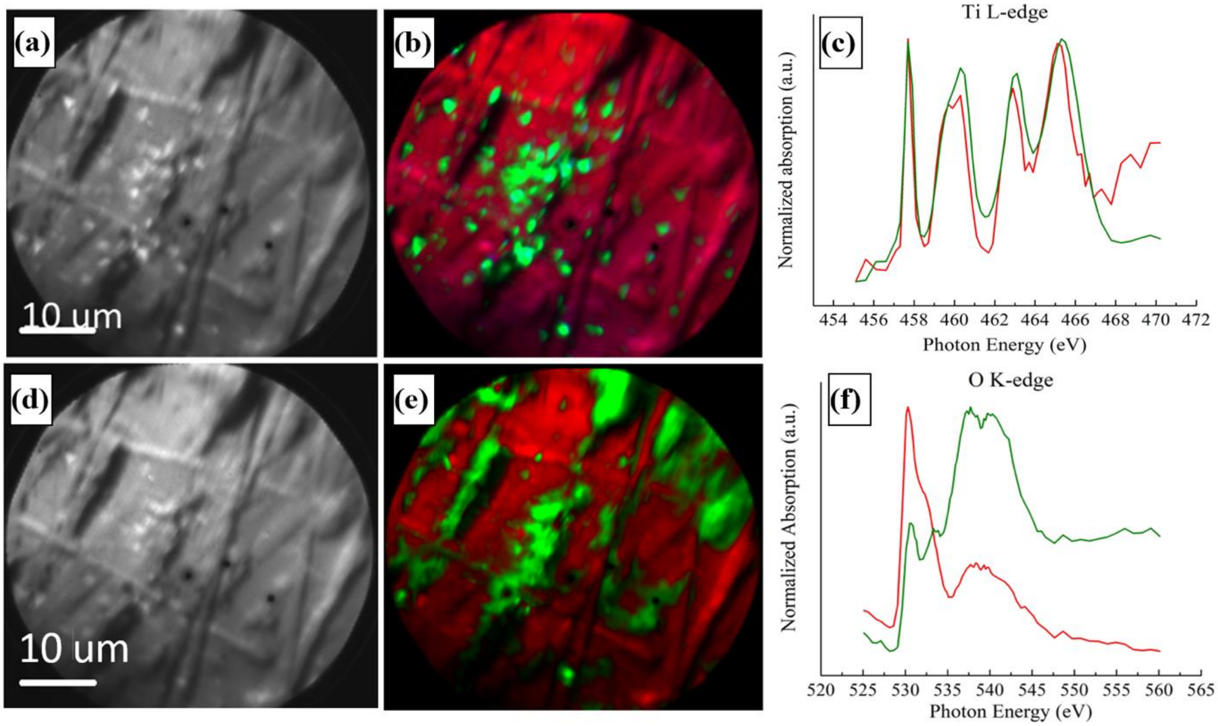

Figure 3-6: PEEM for EPD electrodes of (a-b) Ti L-edge and (d-e) O K-edge and corresponding XANES image for (c) Ti L-edge and (f) O K-edge.

Comparing the PEEM images for Ti L-edge and O K-edge (Figure 3-6 (b) and (e) respectively) shows the high concentration (green) areas of oxygen does not overlap with the high concentration areas found in the titanium map. Additionally, the XANES spectrum for oxygen in Figure 3-6 (f) is not characteristic to LTO (as seen from literature [10]). This indicates the presence of another oxygen-containing species on top of the LTO.

The other two possible sources are the carbon black and the SBR binder. The carbon black can be ruled out due to the EDS images in Figure 3-5 which show areas that have a high carbon black content (this is more obvious in the PVDF electrode image, Figure 3-4) are low in oxygen. In the meantime, analysis of a pure SBR sample (see O K-edge PEEM mapping and XANES in Figure A-5 in Appendix A) was shown to indeed contain oxygen. This O K-edge spectrum for the pure SBR also has similar characteristic peak positions at close energies to the green line in Figure 3-6 (f) indicating the alteration to this green line is due to the presence of the SBR.

The presence of oxygen in SBR is counterintuitive as this polymer is a long chain hydrocarbon molecule with styrene groups that does not typically contain oxygen functional groups. Presumably, the source of oxygen could stem from the proprietary modification or surfactants that Targray adds to make the polymer hydrophilic. Further work is needed to identify the reason oxygen is present within SBR in this case.

This indicates that the SBR is the second oxygen source seen in the O K-edge image. Coupled with the EDS data, this is strong evidence that the components (SBR, C-LTO, and carbon black) are homogeneously intermixed.

3.4.3 Electrochemical Energy Storage Performance

Figure 3-7 shows the electrochemical impedance (EIS) data. The circuit used to model the system is shown in Figure A-7 of Appendix A. This circuit is similar to published models [37,38] but without the SEI circuit as these were pristine cells. In this model, R_1 represents the electrolyte resistance which can be found from the high frequency area where the semi-circle initially intersects the x-axis. The diameter of the semi-circle – see Figure 3-7 – represents the charge transfer resistance (R_2 of the circuit model in Figure A-7 in Appendix A), with Q_2 as the related capacitance, that is indicative of the electronic conductivity/resistance experienced within the coating.

A comparison between the R_2 resistance experienced by the tape-cast PVDF electrode and the two types of EPD-built electrodes (at 80% and 93% LTO) shows the significant improvement in conductivity when the LTO/C electrodes are fabricated using SBR-assisted EPD. A comparison between PVDF- and EPD-electrodes shows the resistance decreasing more than one order of magnitude, namely from ~880Ω to ∼57Ω. Because the SEI contribution on LTO electrodes is negligible under the test condition employed (LTO lithiation occurs outside the electrochemical stability window of electrolyte decomposition which minimizes SEI formation), the improvement can be attributed to the declining ohmic resistance and charge-transfer polarization as the result of good interparticle (C-LTO/C) connectivity. This is further corroborated by comparing EIS results between pressed and non-pressed PVDF- and EPD-based electrodes (Figure A-6 in Appendix A). The graph shows a large reduction in resistance after pressing for both types of electrodes.

A second EPD-based electrode (labeled EPD93) was also fabricated which consisted of 93/3/4 wt% LTO/C/SBR. The EIS results show that decreasing the carbon black and SBR in the EPD electrodes increases the resistance from ~57Ω to ~250Ω. During testing, the EPD93 electrodes were observed not to be robust enough apparently due to lower SBR binder content. Meanwhile, a PVDF electrode with similar composition could not be tested as it was too delicate with its coating easily falling apart.

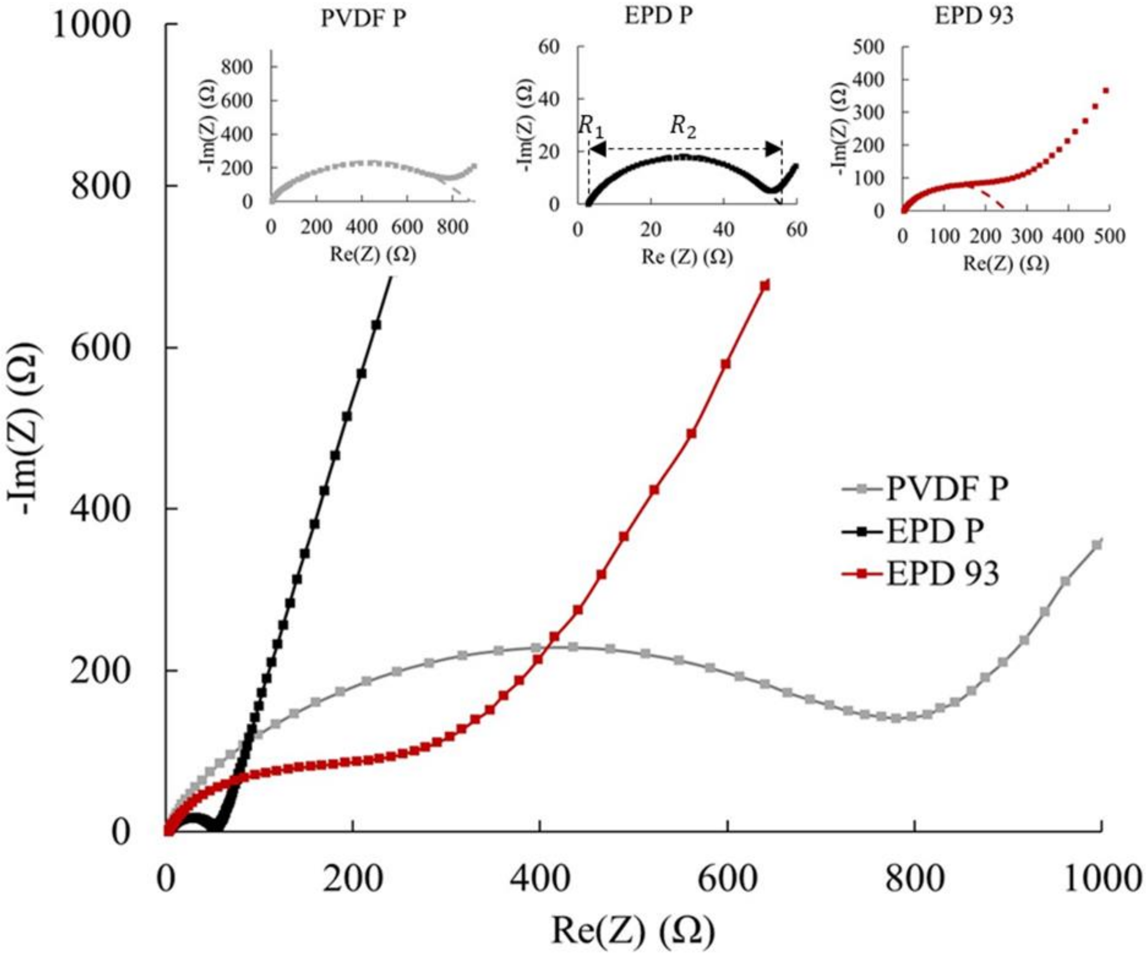

Figure 3-7: EIS Analysis for pressed PVDF and EPD electrodes. The semicircles models are shown inset.

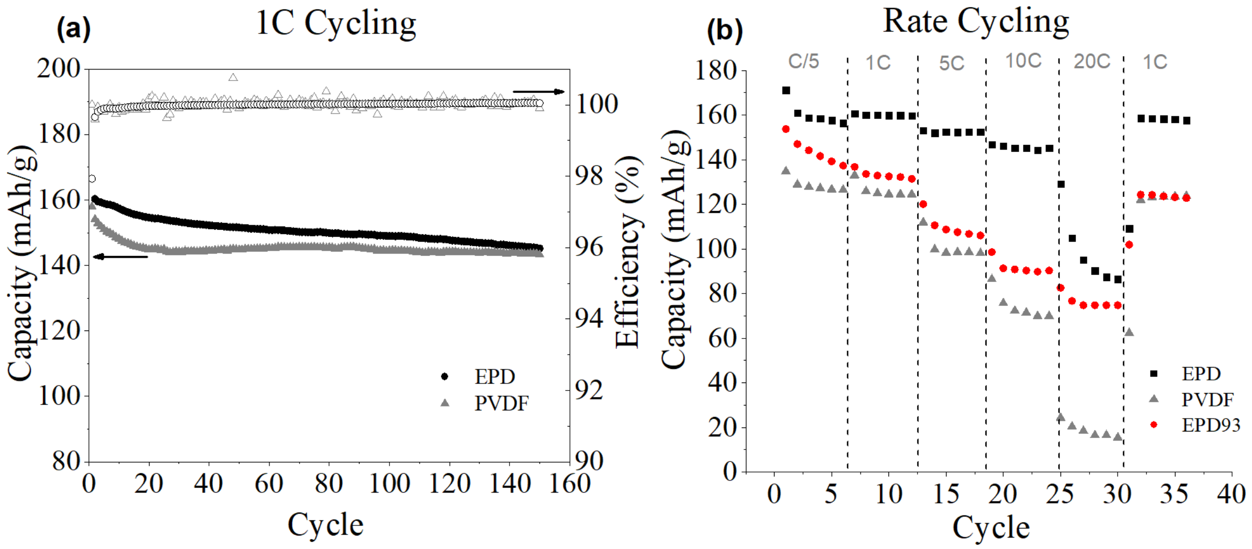

Figure 3-8: (a) Cycling at 1C and (b) Cycling at varying rates of the EPD- and PVDF- based C-LTO/C composite electrodes.

Both EPD and PVDF electrodes (with 80/10/10 nominal composition) were cycled at 1C for 150 cycles to determine and compare their performance. The discharge capacity and Coulombic efficiency as function of number of cycles is shown to be at par after 150 cycles in Figure 3-8 (a). The rate performance was also tested by increasing the C-Rate every 5 cycles starting at C/5 until 20C. From these results, it is clear the EPD-built electrode performs better than the PVDF electrode. During 1C cycling the initial capacity is 160 mAh/g which is close to the LTO theoretical capacity of 175 mAh/g. After 150 cycles the capacity drop is <10%. In comparison, the PVDF batteries had an initial capacity of 154 mAh/g with a similar capacity drop after 150 cycles. The lower resistance shown in the EIS results and the improved particle connectivity shown through the SEM/EDS images explain the difference in initial capacities between EPD and PVDF electrodes. Lower internal resistance attained as result of an improved percolation network will result in improved Li-ion and electron transport which increases loading capability and benefits fast charging/discharging. This effect is magnified during high rate cycling when fast ion movement is key. The high-rate cycling results show the electrode fabricated via EPD outperforms the PVDF-based electrodes. During rate cycling, the EPD93 capacity measured was not as high as the EPD electrode but the performance is on par with the PVDF (80/10/10) electrode that contains more conductive material (10% vs. 3%). The improved performance of the EPD electrodes reflects the inherent powerful assembling property of EPD [15] enhanced in this system with the bridging/binding action of SBR as demonstrating by the hetero-aggregate formation in Figure A-4 in Appendix A) and the SEM/EDS and PEEM/XANES film results (Figure 3-5Figure 3-6).

3.5 Conclusion

This study examined the viability of fabricating thick LTO-Carbon nanocomposite electrodes using EPD. The conventional fabrication technique experiences problems with the viscous slurry which leads to the formation of uneven coatings. This problem is visually shown in the EDS images of the PVDF electrode cross-section when compared to the EPD electrode. The PVDF electrodes showed large agglomerations of LTO which contrasted to the homogeneous dispersion between LTO and carbon observed for the EPD electrodes. The binder used in EPD, SBR, was difficult to observe in EDS as it could not be distinguished from the carbon. Additionally, using TGA only indicated the coatings were composed of ~12 wt.% carbon (for a suspension consisting of 80/10/10 wt.% C-LTO/C/SBR) but not whether this carbon stemmed from carbon black or SBR. With the goal of identifying SBR dispersion in the coating PEEM-XANES was performed where the modified SBR could be distinguished from the carbon through oxygen K-edge signals. The image showed an even distribution between SBR, carbon, and LTO where the binding action of SBR bridges the carbon and LTO nanoparticles. Thus, it was theorized that the C-LTO, carbon, and SBR form bridged hetero-aggregates in suspension which can deposit uniformly. This excellent homogeneity led to the EPD electrodes having a conductivity 15x higher than the tape-cast electrodes as shown through EIS measurements. This allowed for an improved battery performance when cycling between C/5 and 20C. Thus, the fabrication of highly homogeneous and conductive LTO-carbon nanocomposites is feasible using EPD without the PVDF binder and the toxic NMP suspension.

3.6 Acknowledgements

This work is supported by a NSERC/Hydro-Quebec CRD grant. MU and GPD acknowledge additional support by the McGill Engineering Doctoral Award (MEDA) and McGill Sustainability Systems Initiative (MSSI) programs. The authors thank and acknowledge Nicholas Brodusch for SEM and EDS images, Frédéric Voisard for TEM images, Dr. Nathalie Tufenkji for use of the Malvern Zetasizer Nano ZS, Ranjan Roy for use of the Dektak 3ST, and Dr. Marta Cerruti for use of the Bruker SENTERRA confocal Raman microscope.

3.7 References

[1] N.A. Kyeremateng, T.M. Dinh, D. Pech, Electrophoretic deposition of Li4Ti5O12 nanoparticles with a novel additive for Li-ion microbatteries, RSC Adv. 5 (2015) 61502–61507. doi:10.1039/C5RA11039D.

[2] D. Larcher, J.-M. Tarascon, Towards greener and more sustainable batteries for electrical energy storage, Nat. Chem. 7 (2015) 19–29. doi:10.1038/nchem.2085.

[3] B. Zhao, R. Ran, M. Liu, Z. Shao, A comprehensive review of Li4Ti5O12-based electrodes for lithium-ion batteries: The latest advancements and future perspectives, Mater. Sci. Eng. R Rep. 98 (2015) 1–71. doi:10.1016/j.mser.2015.10.001.

[4] S. Scharner, W. Weppner, P. Schmid-Beurmann, Evidence of Two-Phase Formation upon Lithium Insertion into the Li1.33Ti1.67 O 4 Spinel, J. Electrochem. Soc. 146 (1999) 857–861. doi:10.1149/1.1391692.

[5] A. Deschanvres, B. Raveau, Z. Sekkal, Mise en evidence et etude cristallographique d'une nouvelle solution solide de type spinelle Li1+xTi2−xO4 0 ⩽ x ⩽ 0, 333, Mater. Res. Bull. 6 (1971) 699–704. doi:10.1016/0025-5408(71)90103-6.

[6] M. Wagemaker, F.M. Mulder, A. Van der Ven, The Role of Surface and Interface Energy on Phase Stability of Nanosized Insertion Compounds, Adv. Mater. 21 (2009) 2703–2709. doi:10.1002/adma.200803038.

[7] K. Zaghib, M. Dontigny, A. Guerfi, J. Trottier, J. Hamel-Paquet, V. Gariepy, K. Galoutov, P. Hovington, A. Mauger, H. Groult, C.M. Julien, An improved high-power battery with increased thermal operating range: C–LiFePO4//C–Li4Ti5O12, J. Power Sources. 216 (2012) 192–200. doi:10.1016/j.jpowsour.2012.05.025.

[8] D.W. Murphy, R.J. Cava, S.M. Zahurak, A. Santoro, Ternary LixTiO2 phases from insertion reactions, Solid State Ion. 9 (1983) 413–417. doi:10.1016/0167-2738(83)90268-0.

[9] K.M. Colbow, J.R. Dahn, R.R. Haering, Structure and electrochemistry of the spinel oxides LiTi2O4 and Li43Ti53O4, J. Power Sources. 26 (1989) 397–402. doi:10.1016/0378-7753(89)80152-1.

[10] H.-C. Chiu, X. Lu, J. Zhou, L. Gu, J. Reid, R. Gauvin, K. Zaghib, G.P. Demopoulos, Capacity Fade Mechanism of Li4Ti5O12 Nanosheet Anode, Adv. Energy Mater. 7 (2017) n/a-n/a. doi:10.1002/aenm.201601825.

[11] H.-C. Chiu, X. Lu, J. Zhou, L. Gu, J. Reid, R. Gauvin, K. Zaghib, G.P. Demopoulos, Annealing-regulated elimination of residual strain-induced structural relaxation for stable high-power Li4Ti5O12 nanosheet anodes, Nano Energy. 32 (2017) 533–541. doi:10.1016/j.nanoen.2016.12.063.

[12] X. Lu, L. Gu, Y.-S. Hu, H.-C. Chiu, H. Li, G.P. Demopoulos, L. Chen, New Insight into the Atomic-Scale Bulk and Surface Structure Evolution of Li4Ti5O12 Anode, J. Am. Chem. Soc. 137 (2015) 1581–1586. doi:10.1021/ja5115562.

[13] S.-J. Ciou, K.-Z. Fung, K.-W. Chiang, The mathematical expression for kinetics of electrophoretic deposition and the effects of applied voltage, J. Power Sources. 172 (2007) 358–362. doi:10.1016/j.jpowsour.2007.07.046.

[14] K. Zaghib, A. Mauger, H. Groult, J.B. Goodenough, C.M. Julien, Advanced Electrodes for High Power Li-ion Batteries, Mater. Basel Switz. 6 (2013) 1028–1049. doi:10.3390/ma6031028.

[15] L. Ye, K. Wen, Z. Zhang, F. Yang, Y. Liang, W. Lv, Y. Lin, J. Gu, J.H. Dickerson, W. He, Highly Efficient Materials Assembly Via Electrophoretic Deposition for Electrochemical Energy Conversion and Storage Devices, Adv. Energy Mater. 6 (2016) n/a-n/a. doi:10.1002/aenm.201502018.

[16] R. Drevet, N. Ben Jaber, J. Fauré, A. Tara, A. Ben Cheikh Larbi, H. Benhayoune, Electrophoretic deposition (EPD) of nano-hydroxyapatite coatings with improved mechanical properties on prosthetic Ti6Al4V substrates, Surf. Coat. Technol. 301 (2016) 94–99. doi:10.1016/j.surfcoat.2015.12.058.

[17] X.-M. Zhong, I. Wyman, H. Yang, J.-B. Wang, X. Wu, Preparation of robust anti-smudge coatings via electrophoretic deposition, Chem. Eng. J. 302 (2016) 744–751. doi:10.1016/j.cej.2016.05.112.

[18] R.K. Chava, S. Raj, Y.-T. Yu, Synthesis and electrophoretic deposition of hollow-TiO2 nanoparticles for dye sensitized solar cell applications, J. Alloys Compd. 672 (2016) 212–222. doi:10.1016/j.jallcom.2016.02.164.

[19] Z. Li, Y. Zhou, Y. Yang, H. Dai, Electrophoretic deposition of graphene-TiO2 hierarchical spheres onto Ti thread for flexible fiber-shaped dye-sensitized solar cells, Mater. Des. 105 (2016) 352–358. doi:10.1016/j.matdes.2016.05.060.

[20] N. Parsi Benehkohal, G.P. Demopoulos, Electrophoretically self-assembled mixed metal oxide-TiO2 nano-composite film structures for photoelectrochemical energy conversion: Probing of charge recombination and electron transport resistances, J. Power Sources. 240 (2013) 667–675. doi:10.1016/j.jpowsour.2013.04.065.

[21] Z. Gonzalez, B. Ferrari, A.J. Sanchez-Herencia, A. Caballero, J. Morales, Use of Polyelectrolytes for the Fabrication of Porous NiO Films by Electrophoretic Deposition for Supercapacitor Electrodes, Electrochimica Acta. 211 (2016) 110–118. doi:10.1016/j.electacta.2016.06.014.

[22] N.P. Benehkohal, M.J. Sussman, H. Chiu, M. Uceda, R. Gauvin, G.P. Demopoulos, Enabling Green Fabrication of Li-Ion Battery Electrodes by Electrophoretic Deposition: Growth of Thick Binder-Free Mesoporous TiO2-Carbon Anode Films, J. Electrochem. Soc. 162 (2015) D3013–D3018. doi:10.1149/2.0111511jes.

[23] K. Ui, S. Kawamura, N. Kumagai, Fabrication of binder-free SnO2 nanoparticle electrode for lithium secondary batteries by electrophoretic deposition method, Electrochimica Acta. 76 (2012) 383–388. doi:10.1016/j.electacta.2012.05.048.

[24] H. Mazor, D. Golodnitsky, L. Burstein, A. Gladkich, E. Peled, Electrophoretic deposition of lithium iron phosphate cathode for thin-film 3D-microbatteries, J. Power Sources. 198 (2012) 264–272. doi:10.1016/j.jpowsour.2011.09.108.

[25] Y. Huang, H. Liu, Y.-C. Lu, Y. Hou, Q. Li, Electrophoretic lithium iron phosphate/reduced graphene oxide composite for lithium ion battery cathode application, J. Power Sources. 284 (2015) 236–244. doi:10.1016/j.jpowsour.2015.03.037.

[26] Y. Lu, D. Zhang, L. Wang, M. Xu, J. Song, J.B. Goodenough, Electrochemical Behavior of a Graphite Electrode Prepared by Anodic Electrophoretic Deposition, J. Electrochem. Soc. 159 (2012) A321–A324. doi:10.1149/2.078203jes.

[27] N. Parsi Benehkohal, M.A. Gomez, R. Gauvin, G.P. Demopoulos, Enabling aqueous electrophoretic growth of adherent nanotitania mesoporous films via intrafilm cathodic deposition of hydrous zinc oxide, Electrochimica Acta. 87 (2013) 169–179. doi:10.1016/j.electacta.2012.10.005.

[28] M. Yoshio, R.J. Brodd, A. Kozawa, Lithium ion Battery Science and Technologies, Springer, New York, NY, 2009.

[29] D.G. Kellerman, V.S. Gorshkov, E.V. Shalaeva, B.A. Tsaryev, E.G. Vovkotrub, Structure peculiarities of carbon-coated lithium titanate: Raman spectroscopy and electron microscopic study, Solid State Sci. 14 (2012) 72–79. doi:10.1016/j.solidstatesciences.2011.10.018.

[30] J. Schwan, S. Ulrich, V. Batori, H. Ehrhardt, S.R.P. Silva, Raman spectroscopy on amorphous carbon films, J. Appl. Phys. 80 (1996) 440–447. doi:10.1063/1.362745.

[31] T. Yuan, X. Yu, R. Cai, Y. Zhou, Z. Shao, Synthesis of pristine and carbon-coated Li4Ti5O12 and their low-temperature electrochemical performance, J. Power Sources. 195 (2010) 4997–5004. doi:10.1016/j.jpowsour.2010.02.020.

[32] J.B. Kim, D.J. Kim, K.Y. Chung, D. Byun, B.W. Cho, Research on carbon-coated Li 4 Ti 5 O 12 material for lithium ion batteries, Phys. Scr. 2010 (2010) 014026. doi:10.1088/0031-8949/2010/T139/014026.

[33] I.A. Leonidov, O.N. Leonidova, L.A. Perelyaeva, R.F. Samigullina, S.A. Kovyazina, M.V. Patrakeev, Structure, ionic conduction, and phase transformations in lithium titanate Li4Ti5O12, Phys. Solid State. 45 (n.d.) 2183–2188. doi:10.1134/1.1626760.

[34] L. Besra, M. Liu, A review on fundamentals and applications of electrophoretic deposition (EPD), Prog. Mater. Sci. 52 (2007) 1–61. doi:10.1016/j.pmatsci.2006.07.001.

[35] P. Sarkar, P.S. Nicholson, Electrophoretic Deposition (EPD): Mechanisms, Kinetics, and Application to Ceramics, J. Am. Ceram. Soc. 79 (1996) 1987–2002. doi:10.1111/j.1151-2916.1996.tb08929.x.

[36] R. Dominko, M. Gaberšček, J. Drofenik, M. Bele, J. Jamnik, Influence of carbon black distribution on performance of oxide cathodes for Li ion batteries, Electrochimica Acta. 48 (2003) 3709–3716. doi:10.1016/S0013-4686(03)00522-X.

[37] M. Krajewski, B. Hamankiewicz, M. Michalska, M. Andrzejczuk, L. Lipinska, A. Czerwinski, Electrochemical properties of lithium–titanium oxide, modified with Ag–Cu particles, as a negative electrode for lithium-ion batteries, RSC Adv. 7 (2017) 52151–52164. doi:10.1039/C7RA10608D.

[38] T. Hang, D. Mukoyama, H. Nara, N. Takami, T. Momma, T. Osaka, Electrochemical impedance spectroscopy analysis for lithium-ion battery using Li4Ti5O12 anode, J. Power Sources. 222 (2013) 442–447. doi:10.1016/j.jpowsour.2012.09.010.

4 $Li_4Ti_5O_{12}$/reduced graphene oxide nanolayered composites

In the first part (Chapter 3) the internal resistance of a nano-LTO/C composite anode was minimized by designing an efficient EPD system with a water-soluble binder. The goal of this second investigation was also to design an EPD system for electrode fabrication however this tackled the second objective of this thesis: the use of graphene as a conductive replacement to carbon black which will also enable the fabrication of a binderless electrode. The use of the more conductive graphene can further enhance the coating conductivity (as mentioned in section 2.1.7), however its 2D nature presents dispersion issues in both tape-casting and EPD. Thus, the challenge was to engineer an EPD system that would allow for the fabrication of a binderless LTO and graphene composite coatings. This was achieved with the use of graphene oxide and LTO precursor nanosheets that were converted to a binderless uniform composition electrode upon reductive annealing.

To design and characterize the EPD fabrication system: 1) EPD parameters were optimized based on coating quality, 2) electrochemical characterization was carried out to compare EPD and PVDF electrodes (CV, EIS, and cycling), and 3) characterization of the coatings (XRD, TGA, XPS, and cross-sectional SEM and EDS) were used to explain the performance difference. Focus is placed on effect of percolation network on material utilization.

These findings have been submitted for publication in *Energy Storage* Materials (currently under review). **Marianna Uceda**, Hsien-Chieh Chiu, Reynald Gauvin, Karim Zaghib, and George P. Demopoulos (2019). **Electrophoretically co-deposited $Li_4Ti_5O_{12}$/reduced graphene oxide nanolayered composites for high-performance battery application**.

4.1 Abstract

Achieving aggregation-free nanocomposites is a challenge for the conventional casting process in Li-ion battery electrode fabrication, which leads to inhomogeneous dispersion of active and conductive components – a property which further accelerates, or triggers, battery degradation. This becomes even more challenging when using 2D nanomaterials. In this paper, electrophoretic deposition (EPD) is used to fabricate nanolayered composite anodes composed of spinel lithium titanate (LTO) and reduced graphene oxide (rGO). First, the electrode material precursors, 2D-lithium titanate hydrate (LTH) and graphene oxide nanosheets, are formulated into a stable colloidal suspension and electrophoretically co-deposited (EPD) onto copper substrate. Subsequently, the binder-free deposits are annealed at 600 ºC in a 5% hydrogen environment for 6 hours to induce *in-situ* topotactic transformation of the precursors into LTO/rGO nanolayered composites. Comparing to their PVDF-built electrodes, the EPD nanolayered composites exhibit robust electrochemical performance in terms of power capability, cyclability and impedance control. This performance enhancement is due to a well-established graphene oxide-based percolation network for both electronic and ionic conduction engineered with the help of EPD. Therefore, the local deep discharge to lower state-of-charges is avoided, hence avoiding the serious capacity fade from which nano-LTO suffers. Through this research, EPD casting technology presents itself as superior mesoscale construction strategy for nanostructured LIB electrodes.

4.2 Introduction

Minimization of the internal resistance of Li-ion batteries (LIBs) and its control has long been one of the serious limitations for today’s battery technology. This is especially true in electromobility where the fast charge of LIBs requires their internal resistance to be as low as possible to reduce heat dissipation; the cyclability is also determined by limiting the increase of this internal resistance [1]. The key factor to fabricate LIBs with low internal resistance lies in achieving good homogeneity among the binder, conductive fillers, and active materials and establishing an effective percolation network for electron and ion conductive pathways [2–4]. In other words, there is a critical need for the development of aggregation-free microstructure in electrode deposits to enable construction of high-performance batteries.

Two-dimensional (2D) nanomaterials, such as reduced graphene oxides (rGO) or its hybrid nanolayered composites, provide the answer to this challenge in impedance reduction. First, 2D nanostructures offer short Li-ion diffusion lengths and open channels that benefit charge transport, hence their great potential in high-power application. Second, the electrical properties of reduced graphene oxide can be controlled by manipulating both *sp2* and *sp3* carbon hybridization [5–8]. Finally, the excellent mechanical properties make rGO an indispensable component to design a strain-durable electrode microstructure.

However, the conventional casting process for lithium ion electrodes fails in this essential task of enabling an aggregation-free microstructure when nanomaterials, such as nanolayered composites, are used as raw materials. In the conventional fabrication process, the active and conductive materials are mixed alongside with Polyvinylidene Fluoride (PVDF) binder in N-Methyl-2-Pyrrolidone (NMP) as the solvent. This makes a dense slurry which can then be doctor bladed onto the current collector. However, the high surface area of nanomaterials leads to high viscosity and severe aggregation of the slurry used, which is aggravated further when using rGO due to the strong interactions among them [5]. This imposes rheological problems during the casting process which often result in difficulty fabricating electrodes that consistently have the same film density, homogeneous mesoscale composition, and thickness.

Electrophoretic Deposition (EPD), thanks to its directed assembling power [9], is a highly promising alternative colloidal technique that can potentially overcome these issues. The technique involves applying an electric field to a suspension to induce the migration and deposition of particles onto a conductive substrate. The nature of deposits (i.e. composition, thickness, and density) can be controlled through variation of process parameters (i.e. suspension concentration/composition, voltage/current magnitude, and deposition time) [9,10]. Depending on the suspension, the process can be made to be environmentally friendly which is an advantage over the conventional process which uses the highly toxic NMP solvent [11].

Herein, a nanolayered mesoscale electrode is fabricated by a systematic process involving EPD. The end result is a nanolayered composite comprised of reduced graphene oxide and nanosheet crystals of spinel lithium titanate ($Li_4Ti_5O_{12}$, LTO). LTO has been proven as an excellent anode material in Li-ion battery application because of its zero-strain property [12] and outstanding safety performance [13], despite its low electronic conductivity (~$10^{-13} S/cm$). Unlike other commonly used strategies, such as carbon coating [14–17] or doping [18], this study addresses the issue of conductivity enhancement by directly embedding LTO nanosheets into the electronic percolation framework of rGO. The fabrication of LTO/rGO nanolayered composite begins with EPD of their

2D nanosheet precursors of lithium titanate hydrate ($(Li_{2-x}H_x)Ti_2O_5 \cdot yH_2O$, LTH) [19] and graphene oxide onto Cu foils. The coatings are then annealed at high temperature under hydrogen to induce topotactic transformation of LTH→ LTO [20] and GO → rGO. Electrodes made using the conventional casting method (PVDF-based) are also fabricated as benchmark for comparison.

4.3 Experimental Procedure

4.3.1 LTH Synthesis

The 2D lithium titanate hydrate ($(Li_{2-x}H_x)Ti_2O_5 \cdot yH_2O$, LTH) was synthesized using the method developed in our group [19–22]. Essentially, this is a two-step process that involves 1) cold neutralization and 2) isothermal aging as explained below.

4.3.1.1 Cold Neutralization

In stage 1, a solution consisting of 720 mL of 1.33M lithium hydroxide (98% $LiOH \cdot 4H_2O$, Sigma) was prepared in a closed reaction vessel with baffles, stirrer, and a thermometer. The reactor was placed in an ice bath to control temperature and the stirrer was set at 1000 RPM. A second solution consisting of 80 mL of 2M titanium tetrachloride (99% $TiCl_4$, Sigma CAS No. 7550-45-0) was prepared. The 2M $TiCl_4$ was added dropwise to the $LiOH$ solution and the temperature was maintained at $5℃ \pm 2$ to prevent premature nucleation of titania. Once the $TiCl_4$ was completely added the solution was stirred for 2hrs. This produced a titania precipitate that was recovered and rinsed with DI water.

4.3.1.2 Isothermal Aging

The precipitate was then mixed with 0.25M LiOH to adjust the Li/Ti ratio to 1.3 (pH=10.5). This solution was reintroduced into the reactor and the reactor was placed in an oil bath at 85℃ for 24 hours under 1000 RPM. The LTH crystals were then recovered, washed, and stored as a slurry.

4.3.2 Electrode Preparation: EPD and PVDF

4.3.2.1 EPD electrodes

The electrodes were prepared through a 3-stage method that consisted of 1) co-deposition of precursors, 2) pressing and “re-lithiation”, and 3) controlled annealing in a hydrogen gas environment. A process schematic can be seen in Figure B-4 of Appendix B.

1) EPD Co-deposition: The suspension was prepared by mixing 0.66g of LTH slurry (21% solid loading) and 0.011g of GO powder (Abalonyx) in 60 mL of pure ethanol (Les Alcools de Commerce, CAS No. 323236) for a loading of 2.5 g/L. This amounted to a suspension consisting of ~93/7 wt.% LTH/GO respectively. The suspension was sonicated for 40 minutes and allowed to stand for 1 min prior to EPD to ensure settlement of the larger particles.

The substrate used was copper foil (99.99% Cu, $25\ \mu m$ thick, MTI Corporation) placed on glass to make it rigid. The counter was aluminum. Both electrodes were 8mm apart and connected to a Keithley 2600 Sourcemeter. Once both electrodes were immersed in the suspension a voltage of 35 V was applied for twenty 15-second stages. Drying for 5 mins was allowed between each stage. The short deposition time was selected to 1) avoid the deposit from falling off and 2) to minimize cracking due to evaporation of solvent. The submerged electrode area was 10-13 cm^2. The deposit was air dried for 24 hours and weighed, the deposited mass density was $1.67\ mg/cm^2 \pm 12\%$ with thickness in the range of 15-20 µm.

2) Pressing and "re-lithiation": The prepared electrodes were then submerged in an aqueous 0.3M LiOH for 10s and allowed to dry overnight (in ambient atmosphere) to ensure solvent and water removal. The electrodes were pressed at 2MPa to increase interparticle contact.

3) Controlled annealing: The dried electrodes were then placed in a graphite crucible and transferred into a CVD mini tube furnace (MTI OTF-1200X) under 5% hydrogen environment. The temperature was raised to $600\ ℃$ for 6 hours using a ramping temperature of $5\ ℃/min$. This resulted in the conversion of lithium titanate hydrate to lithium titanate spinel ($(Li_{2-x}H_x)Ti_2O_5 \cdot yH_2O \rightarrow Li_4Ti_5O_{12}$) and graphene oxide to reduced graphene oxide ($GO \rightarrow rGO$).

4.3.2.2 PVDF electrodes

Electrodes using the conventional method were prepared (hereafter referred to as "PVDF electrodes") for comparison purposes. The LTH slurry was first dried and placed into a graphite crucible, along with GO in a separate crucible, and heated to $600\ ℃$ for 6 hours using a ramping temperature of $5\ ℃/min$. LTO, rGO, and PVDF powders were manually mixed together at a ratio of 84/6/10 wt% (maintaining the LTO/rGO ratio of 93/7 wt% found in the EPD electrodes through TGA). PVDF electrode mass density was $2.2\ mg/cm^2$ with the thickness larger than 50 µm. The same process was repeated to fabricate PVDF electrodes with carbon black.

Both EPD and PVDF electrodes were then pressed at 2MPa and placed into a vacuum oven and dried at $100℃$ for 24h after being cut into 10-mm disks. Battery assembly was conducted in an argon-filled glove box (M. Braun Co., [O_2] < 0.5 ppm, [H_2O] < 0.5 ppm), with a 25 μm polypropylene (PP)/polyethylene (PE) separator (PP/PE/PP, Celgard 2325). Swagelok-type cells were assembled with lithium metal as the anode and $200\ \mu L\ \ 1M\ LiPF_6$ in EC:DMC:DEC at 2:2:1 by weight as the electrolyte.

4.3.3 Material/Electrode Characterization

The GO, synthesized LTH, and LTO powders after annealing were characterized by Transmission Electron Microscopy (TEM) using a FEI Titan Krios 300 kV Cryo-STEM to determine the nature of the GO powder and LTH/LTO particle size.

The LTH, EPD deposits and annealed deposits were characterized through X-Ray Diffraction (XRD) patterns using a Bruker D8 Discovery X-Ray Diffractometer (VANTEC Detector Cu-Source). Since the coating was relatively thin in terms of XRD depth of penetration, the grazing angle technique was used to analyze the EPD deposits. The chemical information of GO is determined through X-ray Photoelectron Spectroscopy (XPS) and Raman spectroscopy. These characterizations were conducted using the Thermo Scientific K-Alpha XPS instrument and Bruker SENTERRA confocal Raman microscope with 532-nm laser, respectively.

For the post-mortem analysis of the cycled electrodes – the electrodes were first cleaned and dried inside the glovebox, then allowed to dry in a vacuum oven overnight prior to XPS analysis. A survey of the post-mortem cells revealed the surface had fluoride remnants from the electrolyte thus argon etching was done until a Ti 2p signal was clear.

To determine GO and rGO content, Thermogravimetric Analysis (TGA) was performed on the LTH powders and EPD-fabricated coatings using a TGA/DSC 2 (Mettler Toledo). For both powders and coating, 3-5 mg of the sample was weighed on a platinum pan and heated to 1000℃ at a ramping rate of $10℃/min$ under continuous air-flow (60mL/min). To measure post-EPD samples, the powder was scraped off the substrate.

Raman Microscopy was performed using a Bruker SENTERRA confocal Raman microscope with 532 nm wavelength.

Cross-sectional images of the electrodes were taken using Hitachi cold field-emission (SU8000 and SU8230) scanning electron microscopes. The samples are placed between two aluminum plates and mounted using Technovic 5000 conductive resin and polished using 600, 800, 1200 grit sand paper and then fine polished with diamond and silica suspension down to 50 nm. The plates served to: 1) minimize resin infiltration (observed in earlier attempts) which caused the coating to fall apart and 2) to improve conductivity and minimize charging during imaging (as they provided a conduit for the electrons from the top of the sample to the base on which it was placed). Scanning electron microscopy was performed to capture backscattered electron (BSE) images of the cross-sectional microstructure. Electron dispersive spectroscopy (EDS) mapping was performed to capture elemental dispersion of oxygen, carbon, titanium, copper, and fluoride.

4.3.4 Electrochemical Characterization

Electrochemical Impedance Spectroscopy (EIS) measurements were taken using a BioLogic VSP Potentiostat/Galvanostat/EIS system on pristine cells in the frequency range of 1 MHz to 0.02 Hz, a sinus amplitude of 100 mV, and a voltage range between 10V and -10V. Cyclic Voltammetry was scanned from 1 to 2.5V vs. Li^+/Li at varying sweep rates (0.083, 0.208, 0.416, and 0.833 mV/s).

Galvanostatic experiments were performed using a standard battery cycler (BST8 WA, MTI Corp) at 1C, where 1C = 175 mAh/g. The same equipment was used to perform rate cycling at 5C, 10C, 15C, 20C, 30C, 40C, and 50C.

4.4 Results and Discussion

4.4.1 Performing EPD

TEM images of the precursors LTH and GO can be seen in the inset in Figure 4-1 (a). The TEM results indicate LTH consists of 2D nanosheets ranging between 15-170 nm long and around 10 nm thin. This semi crystalline nature of LTH allows for the differentiation of LTH from GO in the coating cross-sectional image. XRD analysis of the synthesized LTH, shown in Figure 4-1 (c) shows this material synthesized at 80℃ [19] to have relatively low crystallinity.

TEM imaging for GO reveals a sheet-like morphology with corrugations (that appear as wrinkles) on the surface. GO is highly electron transparent in TEM images due to its low atomic number. Selected area electron diffraction (SAED) for multiple spots on the graphene sheets revealed both few-layer and multi-stacked graphene (the former is shown in Figure 4-1)– the TEM and SAED included inset in Figure 4-1 (a) has individual spots with a hexagonal symmetry which is characteristic of crystalline few-layer graphene [23]. It is important to note that the concentration of graphene in the suspension is quite low (~0.18 mg/mL) and it is sonicated for 40 min to ensure dispersion. This sonication also has the added benefit of exfoliating the GO sheets (that agglomerate while the GO is dry) which allows for the suspension to contain the few-layer GO observed through TEM. Raman Spectroscopy was performed on the pristine GO (Figure B-1 of Appendix B). The observed peaks are the D and G bands at 1350 and 1590 cm^{-1} respectively. The G band represents in-plane $sp2$ carbon vibrations and the D band, often referred to as the defect band, is the out-of-plane $sp3$ vibrations (i.e. the defects arising from the presence of the functional groups). The de-convoluted 2D, D+G, and 2D' modes are also given in Figure B-1 (d) of Appendix B.

Various media were tested and ultimately the selected suspension was pure ethanol with 2.5 g/L solids of LTH and GO (93/7 wt% respectively). Further information regarding solvent selection is given in section B.2 of Appendix B. The LTH/GO ethanol suspension had a negative zeta potential of -24mV (zeta potential distribution for the LTH/GO mixture can be seen in Figure B-2 (d) in Appendix B) which led to anodic deposition. Individually suspending LTH or GO in ethanol led to zeta potential values of -22 mV and -18 mV respectively. The suspension was found to be stable with negligible sedimentation occurring within the first 12 hours.

To induce deposition, the EPD parameters selected must allow for 1) particle electrophoresis and 2) interparticle interactions during deposition. However, during EPD, degradation of the Cu foil was visually observed through the formation of a green tinge meaning that the Cu was being oxidized (Section B.2 of Appendix B). In an attempt to minimize Cu contamination, EPD was carried out at 35V. This meant that the deposition rate was slow and required twenty 15-second stages to deposit a coating with a mass density of $1.67\,mg/cm^2 \pm 12\%$. Further information regarding parameter selection is discussed in section B.2 of Appendix B.

XRD spectra for the EPD coating and the pristine LTH material are shown in Figure 4-1 (c). The matching patterns indicate the LTH is not affected by applying 35V.

4.4.2 Material characterization of EPD LTO/rGO nanolayered composites

After pressing and relithiation (discussed in section B.3 of Appendix B), the EPD coatings are treated under high temperature annealing for 6 hours in a 5% hydrogen environment. A step-by-step flowchart can be seen in Figure B-4 of Appendix B. Figure 4-1 (a) and (b) show a high magnification cross-sectional SEM image of the pristine and annealed coating respectively with the TEM images of the LTH, GO, and LTO shown in inset. The formation of spinel LTO after annealing was confirmed through XRD in Figure 4-1 (c). A comparison between pristine and annealed materials show the LTO crystals have maintained their 2D nanosheet shape albeit having shorter length of about 40 nm due to the topotactic transformation. For the PVDF electrodes, the LTH and GO were annealed separately prior to coating. The XRD spectrum for this electrode is also provided to show both coatings have similar LTO crystallinity.

Figure 4-1 (d) shows a comparison between the Ti 2p spectra of the pristine and annealed coating. The Ti 2p 1/2 and 3/2 peak positions for the pristine coating, indicate the presence of Ti^{4+} for both LTH and LTO (pristine and annealed respectively), i.e. the reductive annealing step did not reduce $Ti^{4+}\ to\ Ti^{3+}$. There exists a peak shift from about 458 of LTH to 459.3 eV of LTO, which is due to a difference in the coordination environment of Ti atoms in LTH and LTO.

A comparison between the pristine and annealed GO (labeled as Pure GO and rGO respectively) Raman spectra is shown in Figure B-1 of appendix B (c) shows the characteristic D and G peaks for both pristine and annealed GO. A red shift (shift of ~13 cm^{-1} to lower Raman shift seen in rGO) of the D band is observed that occurs due to increase in tensile strain caused by the annealing stage. The calculated D/G ratios are 0.93 and 0.57 for the pristine and annealed GO respectively. This shows disruption of the *sp2* bonds due to the removal of functional groups. This was confirmed through XPS analysis of the C 1s spectra shown in Figure B-5 of Appendix B. The spectra were de-convoluted to show the individual peaks belonging to the C-C plane of graphene and the out of plane functional groups (i.e. hydroxyl, carbonyl, and carboxyl groups). Table B-2 of Appendix B shows the functional groups with their corresponding binding energies and area ratios relative to the C-C peak. The area ratio between C-C and the sum of the functional groups is 1:1.34 and 1:0.49 for the pristine and annealed EPD coating respectively. The XPS C 1s spectra for rGO annealed separately is shown in Figure B-5 (d) of Appendix B with a corresponding ratio of 1:0.42 meaning a negligible difference between the rGO in the EPD and PVDF electrodes (despite one being annealed as part of a coating and the other separately). The ratio change indicates the reductive annealing step effectively removes most functional groups. Furthermore, a peak at ~290 eV appears in the annealed material. Prior to annealing the final peak was at ~288 eV which is attributed to carboxyl [24]. However, this final peak is drastically shifted towards a more electronegative binding energy; thus, it cannot be attributed to carboxyl functional group. It is assumed to be the shake-up satellite peak for HOMO-LUMO transition of carbon $\pi \rightarrow \pi^{*}$ [25]. This occurs when an outgoing core electron, removed through photoionization, excites a valence electron resulting in the core electron being reduced. This produces a satellite at a higher binding energy. The removal of functional groups and appearance of the HOMO-LUMO transition peak indicate the coating has become more conductive with respect to the non-annealed coating.

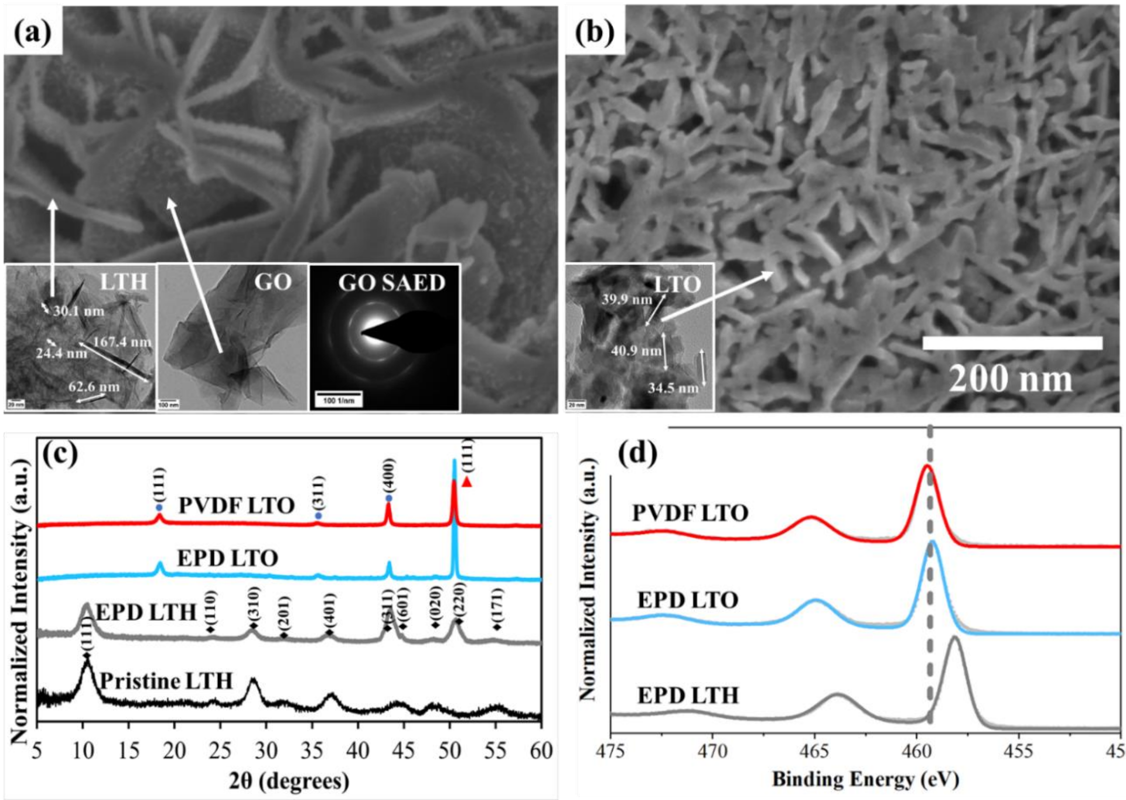

Figure 4-1: (a) Cross-sectional SEM image of non-annealed EPD coating consisting of LTH and GO (TEM shown in inset respectively with the corresponding GO SAED). (b) Cross-sectional SEM image of annealed EPD coating consisting of LTO and rGO (LTO TEM shown in inset). (c) Grazing angle XRD patterns for (from top to bottom) PVDF coating (“PVDF LTO”), annealed EPD coating (“EPD LTO”), non-annealed EPD coating (“EPD LTH”), and pristine LTH powder (the peaks are labeled according to ●LTO, ♦LTH, and ▲Cu). (d) XPS Ti 2p spectra for (top to bottom) PVDF coating, annealed EPD coating, and non-annealed EPD coating. (Note: Both SEM cross-sectional images are at the same magnification).

TGA was performed on pure LTH and on pure GO, respectively, (Figure B-6 of Appendix B) with the corresponding decomposition temperatures (determined through DTG analysis) tabulated in Table B-3 of Appendix B. These results show that LTH is composed of ~5 wt.% moisture (removed < 180℃) and ~9 wt.% crystallized water (weight loss between 180 and 400℃) which is in agreement with the work of Chiu et al. [20]. For GO, the removal of oxygen-containing functional groups occurs between $150 - 250\ ℃$ and the graphene *sp2* structure decomposes after $500\ ℃$ ($450 - 600\ ℃$ according to literature) [26]. Removal of the crystalline water in LTH crystals occurs at a lower temperature than 600 ℃ (in air), however this temperature is required to achieve good crystallinity of LTO for optimum electrochemical performance [21]. The TGA curves for the pristine and annealed coatings show that the pristine coating is composed of ~25% volatile material which is a combination of the water in LTH and the GO. After annealing an initial loss of mass is observed at $\sim 140℃$, since the water was removed from the LTH during the annealing process this is attributed to the loss of moisture and remaining functional groups. The remaining mass loss is due to pyrolysis of the graphene network. On average the annealed coating was composed of 8.5 ± 1.3 wt.% rGO.

4.4.3 Electrode Film Homogeneity and Microstructure Engineering via EPD

Figure 4-2 (a) shows the SEM-BSE image for the PVDF-based fabricated electrode. The EDS images for C Kα and Ti Kα show LTO aggregates that are identified as sections with high titanium and low carbon signals. Such phase separation at macroscopic scale implies the electronic and ionic conduction pathways are established independently at this scale. The PVDF binder is a fluoropolymer, thus a fluoride map was also acquired (Figure B-7 of Appendix B). From the F Kα signal the distribution of PVDF binder throughout the coating shows the GO and PVDF coating mix relatively evenly, however, similarly to the GO, the PVDF is not present within the LTO aggregates.

Figure 4-2 (b) shows the SEM-BSE image for the EPD electrode. The EDS maps for titanium and carbon reveal a homogeneous distribution of the LTO and rGO within the deposit. Unlike the electrode produced via the conventional method, the EPD-based coating exhibits better homogeneity of each raw material. Thus, the EPD process exhibits the strength of fabricating the aggregation-free electrode via controlling the deposit rate and time. The suspension has high concentration and deposition time is short meaning the particles at the electrode surface are not depleted. When depletion occurs, the rate of particle deposition becomes dependent on individual particle mobility which leads to uneven deposition between components [10].

This outstanding homogeneity endowed by the EPD process also unlocks the binding function of rGO. The homogeneously distributed rGO sheets can hold – or envelop due to their sheet-like wrapping nature – the LTO particles together preventing the coating from falling apart and providing binder-like capabilities [27]. Thus, the uniform composition is the result of EPD's self-assembling power at the nanoscale [9]. As shown in the cross-sectional images, the EPD process changes the interface between active LTO and conductive material from point contact (as observed in the conventionally prepared electrode) to area contact. This is schematically represented in Figure 4-2 (c, d) with the LTO that is active (i.e. in contact) highlighted in blue (the characteristic color of lithiated LTO). Hence, it fully utilizes the LTO active material – a concept which is further examined during electrochemical testing (section 4.4.4).

During imaging of the EPD electrode only, bright spots were observed throughout the coating. These were identified as Cu through EDS mapping of Cu Lα (given in Figure 4-3). The XPS Cu 2p spectrum has the 2p 3/2 and 2p 1/2 peaks at 933 and 952 eV which is characteristic of Cu metal and/or Cu^{+}. The shoulders observed at 934 and 954 eV belong to 2p 3/2 and 2p 1/2 for Cu^{2+}. This means that during EPD, the Cu is oxidized and redeposited to form part of the coating (further discussed in section B.2 of Appendix B). Thus, Cu may be present in metallic and/or oxide (such as CuO or Cu_2O) form after annealing. This copper contamination is not electrochemically active in the potential window used to cycle LTO [28].

Nonetheless, the EPD deposit was less adherent onto the Cu substrate than the corresponding PVDF electrode. This implies that further optimization on the surface chemistry of rGO and Cu is required to enhance physical bonding at the deposit/Cu interface.

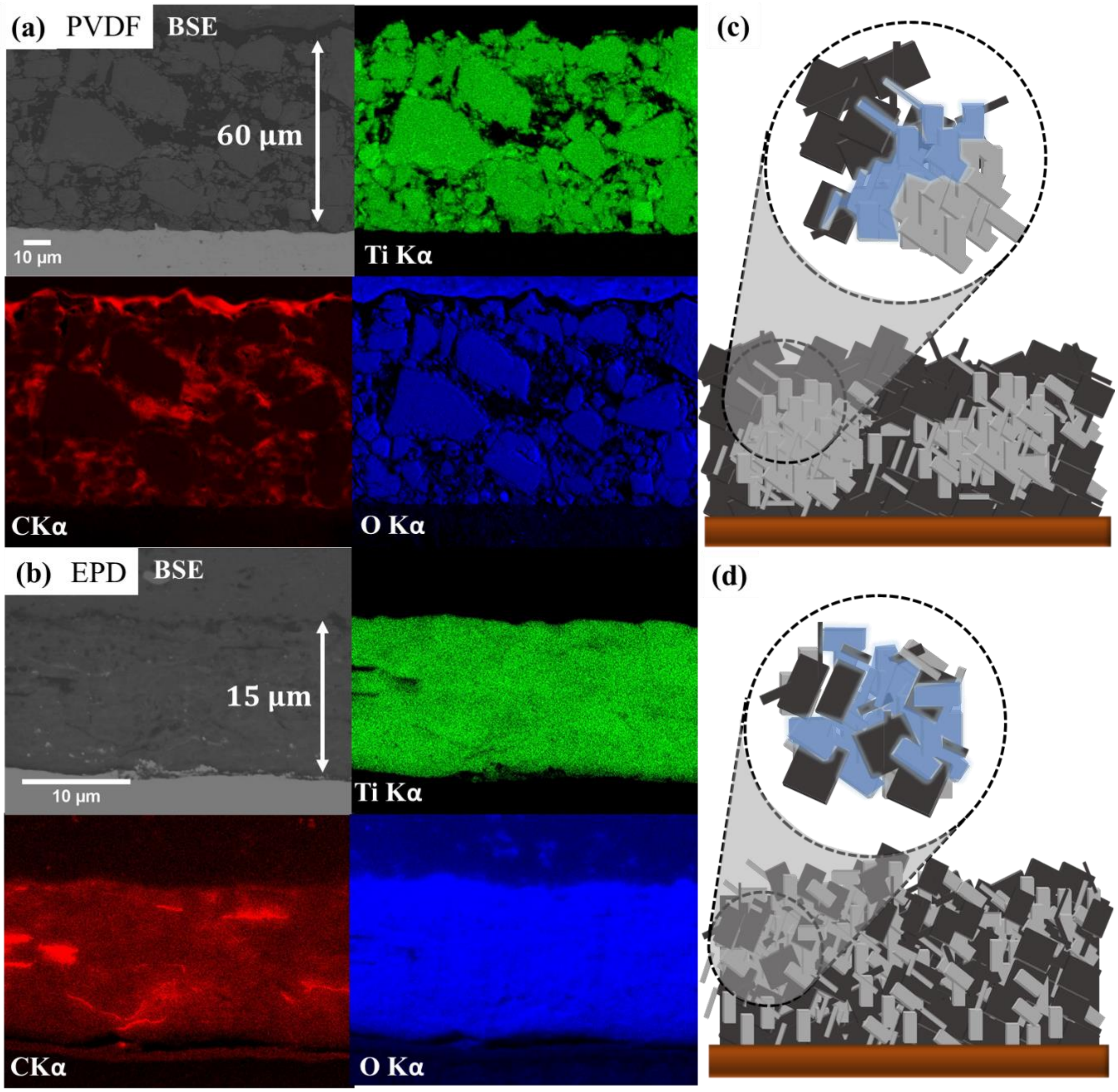

Figure 4-2: Cross-sectional BSE and EDS mapping of Ti Kα, C Kα, and O Kα for (a) PVDF and (b) EPD coatings showing LTO and rGO distribution. Note that the scale of these two samples is different. Coating schematic for (c) PVDF and (d) EPD electrodes illustrating the contact areas (lithiated LTO shown in blue) between rGO and LTO.

4.4.4 Microstructure-Electrochemistry Relationship

Electrochemical Impedance Spectroscopy (EIS) was conducted to elucidate the impact of microstructure variation on the electrochemical performance by comparing 1) using EPD vs. the conventional PVDF casting method and 2) using rGO vs. carbon black. Please note that in order to make a fair comparison between the EPD and PVDF/rGO electrodes, the collected impedance data were normalized against the deposit thickness and geometric area 0.785 cm^2 (Figure 4-3). The preliminary EIS data before normalization is also given in Figure B-8 of Appendix B where PVDF/rGO electrode exhibits a larger impedance.

The equivalent circuit model, given in Figure 4-3 (d), can be divided into four sections [29,30]: 1) R_{ohm} represents the impedance contribution from both electrolyte (ionic) and the ohmic resistance of deposit (electronic), 2) R_{SEI} is the SEI surrounding the lithium ion host material, 3) R_{CT} is the charge transfer resistance within the LTO, and 4) is the low frequency response which is controlled by the Warburg element, W_1, describing the Li-ion diffusion in LTO. The final element Q_3 is to consider the raising of the typical "diffusion tail" due the limited diffusion length of Li ions in LTO. The system was found to behave as an imperfect capacitor thus the constant phase elements Q_{1-3} are used. The deviation from ideality is dictated by the calculated α value – for an ideal capacitor $\alpha = 1$ and for a pure resistor $\alpha = 0$. This deviation from pure capacitor is due to surface inhomogeneity and the porous structure. By fitting the data to this model, we can determine the appropriate resistance and pseudocapacitance (i.e., take into account the α of Q_1 and Q_2 and obtain the pseudocapacitance C_1 and C_2) as listed in Table B-4 of Appendix B.

A comparison between normalized R_{Ohm} values show the EPD electrode possesses larger ohmic resistance. This is the consequence of the relatively imperfect adherence of EPD deposit onto the Cu substrate (Figure 4-2). The R_{SEI} of both pristine EPD and PVDF electrodes is negligible, because of no considerable SEI growth in them before electrochemical Li-ion intercalation. But there exists significant difference in the second semicircle of charge-transfer process between pristine EPD and PVDF electrodes. More specifically, the charge-transfer resistance values (R_{CT}) of both electrodes are similar with only ~7% difference. It is worth mentioning that the density of the deposit of EPD-rGO (1.67 g/cm^3) is lower than that of PVDF/rGO electrodes (2.2 g/cm^3), additionally there exists minor contamination of copper oxides within the EPD deposit. As mentioned before, Cu deposits are found within the annealed EPD coating, from the XPS results CuO and Cu_2O are likely present. Both materials are capable of aiding electronic conductivity but will impede the Li-ion intercalation in the voltage window from 2.5 to 1 V vs. Li+/Li [28]. As a result, the formation of copper oxides may have slightly obstructed the charge-transfer process on the surface of LTO nanosheets, but the influence is still in the acceptable range.

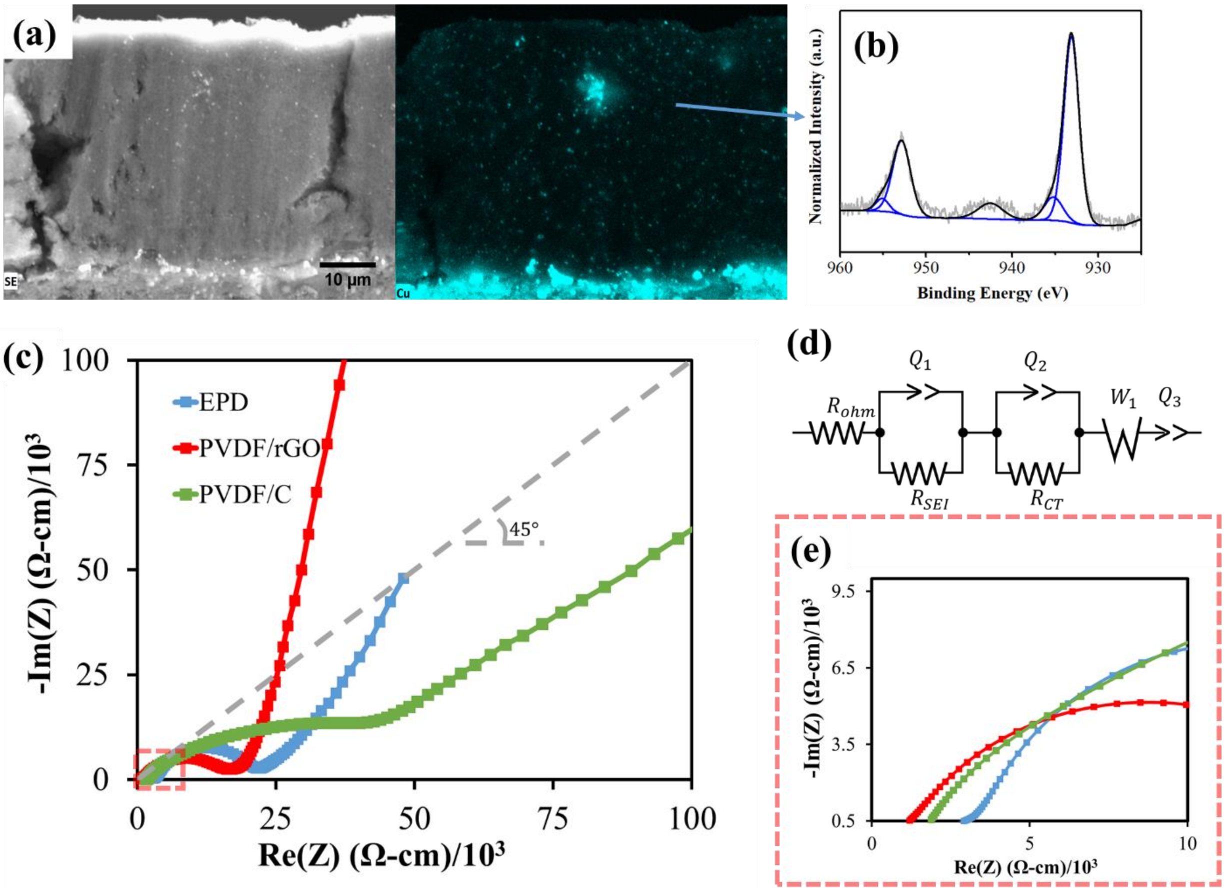

Figure 4-3: (a) Cross-sectional SEM BSE image and corresponding Cu Lα EDS mapping of the annealed EPD electrode, and (b) Cu 2p XPS spectra of the annealed EPD electrode. (c) EIS measurements for the EPD, PVDF/rGO, and PVDF/C electrodes normalized for electrode thickness and geometric area, (d) equivalent circuit used to fit the EIS model, and (e) close-up of high frequency zone – R_{Ohm}.

To compare the effect of using rGO vs. carbon black, a PVDF electrode was fabricated using carbon as the conductive material. The EIS results show that using carbon vs. rGO significantly increases the charge transfer resistance by ~170% compared to the PVDF/rGO electrodes (and ~150% compared to the EPD electrodes).

Interestingly, the height of second semicircle for the EPD electrode is larger than the PVDF electrode. This difference is enhanced after cycling (Figure 4-4 (b)) which means the electrochemical active surface area in the EPD electrode is much higher than the one in the PVDF/rGO electrode. In other words, the EPD process not only establishes a well-constructed electronic percolation network through rGO, but also maintains good ionic percolation of Li ions.

This can be attributed to the superior assembly capability and microstructural engineering, of EPD [9] leading to a homogeneously ordered structure.

At low frequencies, the contribution of Li-ion diffusion in LTO leads to the tail as the summation of W_1 and Q_3 elements. Warburg impedance exhibits a typical straight line with 45-degree slope characteristic of diffusion. The transition to a more vertical line is due to the limited diffusion length in the nanolayered composite. This resistance is experienced by all three types of electrodes. A comparison between the PVDF/rGO and EPD electrodes shows the former has a lower Warburg impedance than the EPD (2.03×10^4 vs 4.47×10^4 $\Omega\mathrm{cm}s^{-0.5}$ respectively) which is in accordance with the larger Li-ion diffusivity calculated for the PVDF/rGO electrodes. In overall, using just 7% rGO can significantly increase the conductivity of electrode deposit even without good homogeneity at nanoscale. This result also indicates the possibility of further reducing the content of rGO as 7% seems to have reached the saturation region, hence the little difference between EPD and PVDF electrodes.

4.4.5 Post-mortem analysis of cycled electrodes

The electrode kinetics were studied by Cyclic Voltammetry using scan rates in the range of 0.083 to 0.833 mV/s on the two-electrode Swagelok cells with Li anode as counter and reference electrodes, whose results are shown in Figure 4-4 (a). The voltammograms give redox peaks at about 1.6 V vs. Li^+/Li as is expected from a reversible spinel-rock salt transformation upon Li-ion intercalation/deintercalation; the peaks correspond to the reduction/oxidation Ti^{4+}/Ti^{3+} couple. Increasing the scan rate also increases the flux of reacting species to the electrode surface hence a larger current response. A comparison between the CV scans of the EPD and PVDF/rGO electrodes shows that the latter has became more polarized with increasing scan rate. This is so because the thickness of PVDF/GO (50 µm) is about 2-3 times larger than that of the EPD electrodes, therefore a higher overall polarization is expected. The same polarization increase is also observed in the PVDF/C electrode (Figure B-10 of Appendix B), as a result of the increased thickness of the PVDF-containing electrodes.

During intercalation, electron transport occurs through the conductive material in the coating and the slowest Li-ion diffusion occurs inside the host material LTO. The latter was calculated to be in the range of 10^{-12} and 10^{-11} cm^2/s for EPD and PVDF electrodes respectively (calculation explained in section B.10 of Appendix B). The values are within the expected $10^{-8} -$

$10^{-13}\ cm^2/s$ range [31]. The $|i_{pc}/i_{pa}|$ ratio is nearly unity (1.06 ± 0.02) for the EPD electrode at all scan rates representing its good reversibility, whereas for the PVDF electrode it changes from 0.62 to 1.23. The irreversible capacity loss of LTO nanosheets is because the surface reconstruction induced by overlithiation of the near-surface region of LTO nanocrystals [22], this is accompanied by peak broadening and the appearance of a shoulder next to the reduction peak. This behaviour is exclusive to the PVDF electrode as it was also found in the PVDF/C electrode (Figure B-10 of Appendix B). As the LTO in both PVDF and EPD coatings is found to have similar crystalline features then this behaviour could be a result of the titanium being present at different oxidation states (Ti^{4+} and Ti^{3+}) as a result of irreversible lithiation. In this case, the presence of lithium within the LTO structure also leads to higher lithium diffusivity of subsequent lithium ions [32,33]. Schmidt et al.[32] determined the increase in diffusivity in the presence of lithium ions within LTO ($Li_{4+x}Ti_5O_{12},$ where $x > 0.1$) is due to repulsive interactions taking place due to the simultaneous occupation of interstitial vacancies. This would explain why lithium diffusivity is faster in the PVDF electrodes vs. the EPD electrodes.

Another interesting feature is that the EPD electrode exhibit well-defined, sharp peaks in the CV results, but PVDF/rGO delivers diffused and broad peak features in Figure 4-4 (a). Such characteristic of CV peak broadness has been observed from the LTO nanosheets annealed at lower temperature, as the consequence of severe surface reconstruction due to overlithiation at the surface [20]. However, in this research, the LTO used in both EPD and PVDF electrodes were annealed at 600°C. Therefore, the diffused peaks in PVDF/rGO is attributed to "forced overlithiation" due to inhomogeneity. As a result, the poor cyclability of PVDF/rGO electrode is predicted.

EIS data was measured after 10 cycles and compared to pristine EIS in Figure 4-4 (b). After 10 cycles, the PVDF/rGO electrode exhibits a significant impedance decrease particularly at the charge-transfer impedance. The CV results alluded to the possibility of irreversible lithiation occurring on the surface of LTO nanosheets. Thus, overlithiated LTO permanently changes from spinel $Li_4Ti_5O_{12}$ to the rock-salt $Li_7Ti_5O_{12}$ – a structure which is more electronically conductive [34] and covers the outmost surface of degraded LTO. Therefore, the decrease of charge-transfer impedance is attributed to the formation of this highly conductive phase forming on the surface. This would mean that, with reference to the EPD electrode, the surface of LTO in PVDF/rGO deposit is irreversibly overlithiated as a result of "deep discharge".

The cycled EIS results for the EPD electrode show a slight increase in the first semicircle due to minor SEI formation on the surface of the nanolayered composite. What is outstanding is the relatively robust charge-transfer impedance – the impedance reduces to about 65% of the original value, meaning the LTO degradation kinetics are much slower in the EPD-built electrode than in the PVDF-cast electrode (which shrinks to 21% of original value).

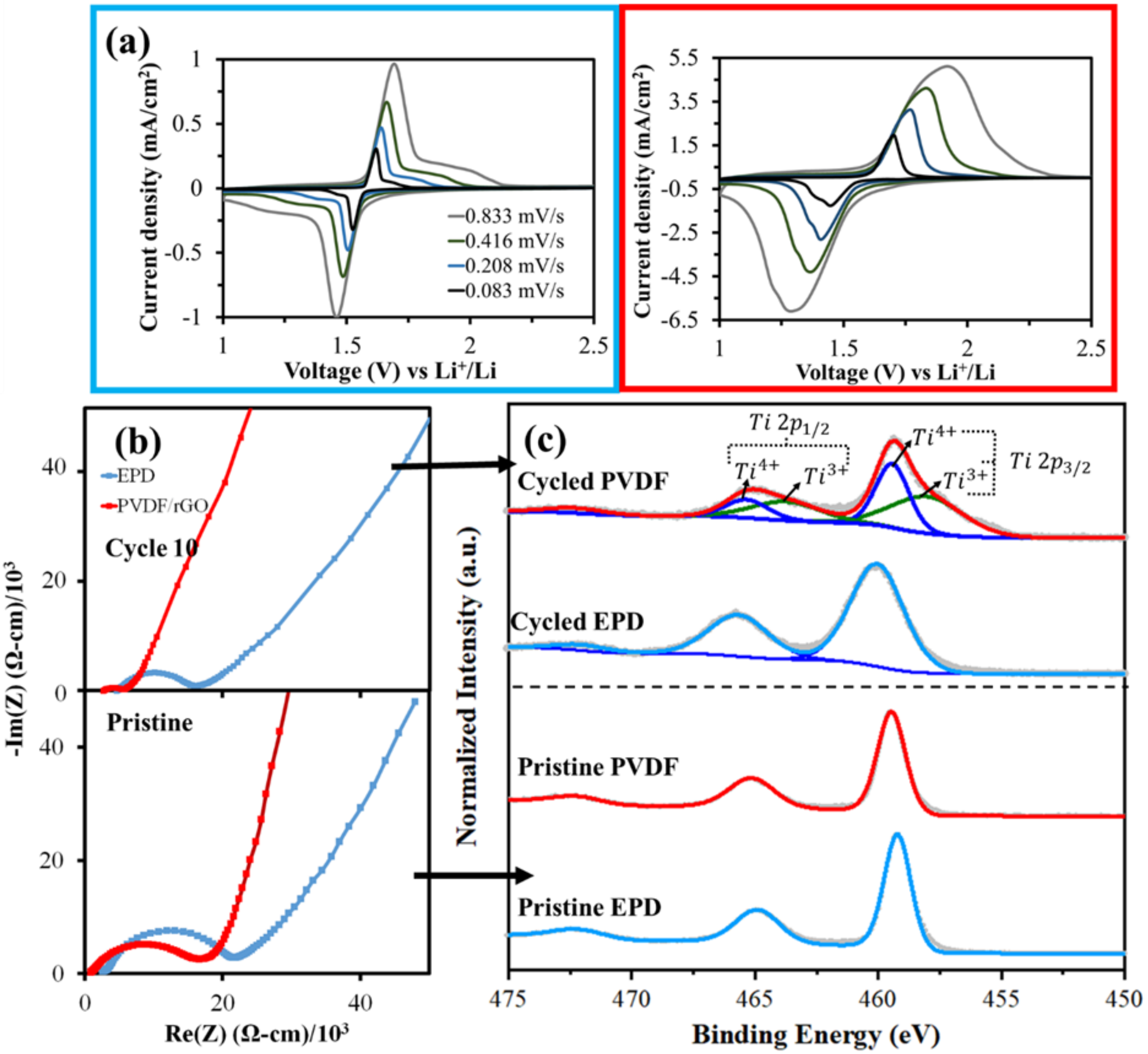

Figure 4-4: (a) CV at varying scan rates for (left to right) EPD and PVDF/rGO electrode. (b) EIS comparison of (top to bottom) cycled and pristine EPD and PVDF/rGO electrodes. (c) Ti 2p XPS spectra for (top to bottom) cycled PVDF/rGO, cycled EPD, pristine PVDF/rGO, and pristine EPD electrodes.

XPS Ti 2p spectra for the post-mortem cells of both EPD and PVDF electrodes are given in Figure 4-4 (c). With reference to the pristine material, both the Ti 2p 3/2 and 1/2 peaks for the cycled electrodes experience a shifting and broadening effect – however the inter-peak distance remains the same at ~5.7 as reported in literature [35,36]. The broad XPS peaks indicate the crystallinity of LTO nanosheets decreases upon Li-ion intercalation/deintercalation cycling. The Ti 2p spectrum for the cycled PVDF electrode experiences the appearance of two clear shoulders to the right of the main 2p 1/2 and 3/2 peaks. Its locations, 458.08 and 463.58 eV for the 3/2 and 1/2 peaks respectively, are characteristic of Ti^{3+} oxidation state. The Ti^{3+} peaks are likely present in the EPD spectra but in small amounts which would make it difficult to de-convolute.

One advantage of using rGO to establish the percolation network is to avoid the local over-utilization of active material which accelerates material degradation. The cross-sectional EDS images (see Figure 4-2), however, hint at the possibility that there would be inaccessible LTO trapped within the large LTO agglomerates. This presents the idea that the conductive phase is forming on the outmost surface of the LTO nanosheet agglomerates that are in contact with the rGO, precluding the "core" LTO trapped within the aggregates. This is schematically shown in Figure 4-2 (c), with the lithiated shell LTO in blue and the untouched core LTO in grey. This would lead to deep discharge of LTO in the PVDF/rGO electrodes.

The cycling performance at 1C for EPD, PVDG/rGO, and PVDF/C electrodes is shown in Figure 4-5 (a). Over the 150 cycles the EPD, PVDF/rGO and PVDF/C electrodes experience a 22%, 27%, and 68% capacity fade respectively. The degradation rate is shown to be on par for both EPD and PVDF/rGO electrodes, however the capacity reached is higher for the EPD electrode. The lower capacity achieved by the PVDF/rGO electrodes, despite having the same LTO/rGO ratio, is indicative of lower material utilization. Reduction of performance due to the formation of large aggregates has already been established [3]. From the voltage profile of each LTO electrode (Figure 4-5 (b)) the capacity loss comes from the tail part that provides the excess capacity over 175 mAh/g. In other words, the degradation occurs on the surface as the result of surface reconstruction due to irreversible overlithiation [22]. Furthermore, the separation gap between charge and discharge voltage profiles is larger for PVDF/rGO than either EPD-built or PVDF/C electrodes for cycle 1. This difference in polarization is also revealed through differential capacity graphs dQ/dV in Figure 4-5 (b), which shows decreasing polarization for the EPD and PVDF/rGO electrodes after 150 cycles (voltage profile and dQ/dV for cycle 10 is provided in Figure B-12 of Appendix B). This decrease in polarization is in accordance with the EIS data. The increase tendency of the conventional PVDF/C electrode has been elucidated in our previous research [20,22] as the result of irreversible excess Li-ion intercalation of LTO nanosheets due to nanostructure-induced relaxation.

Rate cycling between 5C and 50C is also given in Figure 4-5 (c) for the PVDF/rGO and EPD electrodes. The excellent homogeneity and resulting percolation network allow the EPD electrode to maintain the capacity at very high cycling rates. The performance of the EPD electrode at 50C is comparable to that of the PVDF/rGO electrode at only 20C. Furthermore, after 50C the electrodes are cycled again at 5C which demonstrates their ability to recover. This property is maintained by the EPD electrode however the PVDF/rGO electrode drops to 80% of initial 5C capacity after the high rate cycling.

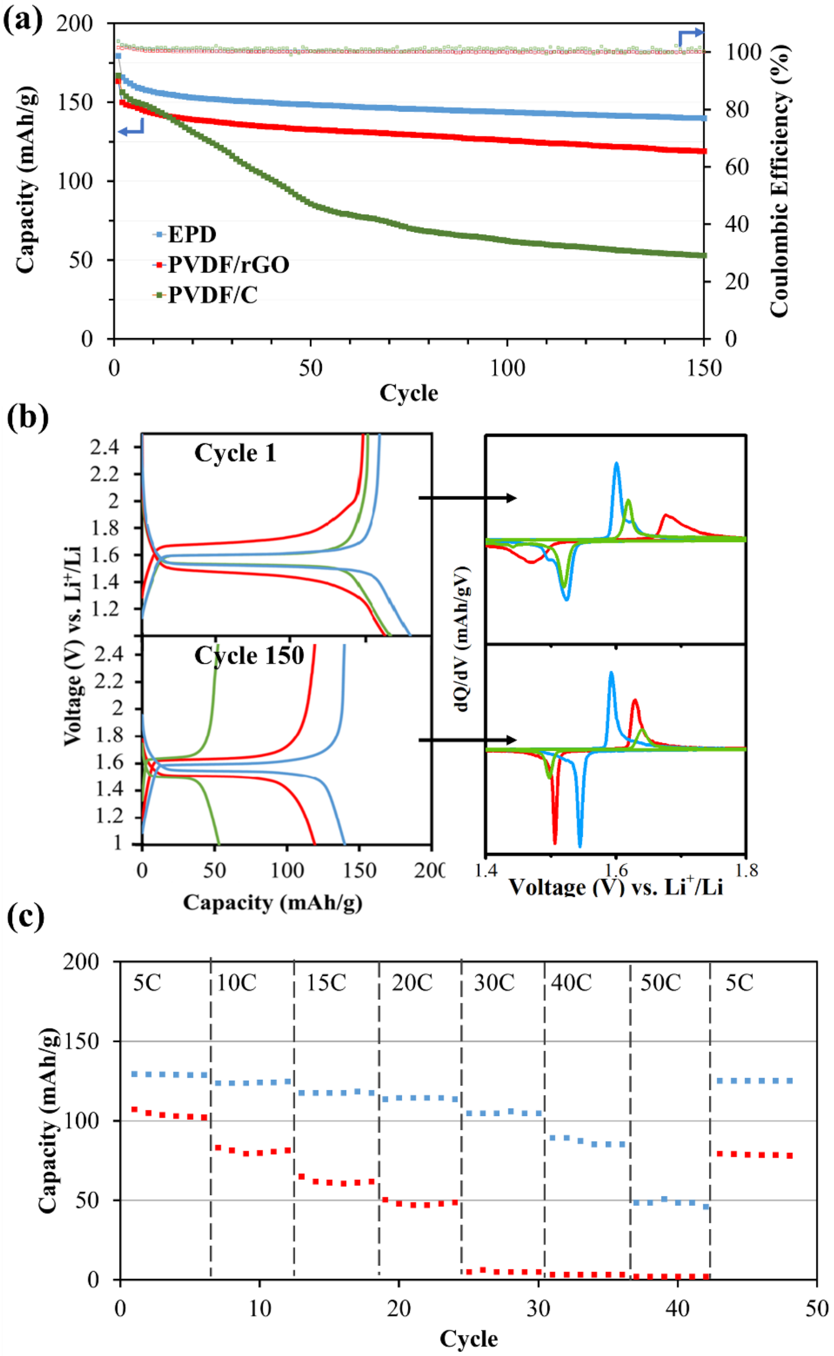

Figure 4-5: (a) 1C cycling over 150 cycles with coulombic efficiency. (b) 1C voltage-capacity curves for PVDF/C, PVDF/rGO, and EPD electrodes at (top to bottom) cycle 1 and cycle 150 with corresponding differential capacity analysis. (c) Rate cycling for EPD and PVDF/rGO electrodes. (Note: In all the diagrams, EPD is shown in blue, PVDF/rGO in red, and PVDF/C in green)[1].

---

[1] Figure 4-5 (b) is changed from the publication to fix the height of the PVDF dQ/dV peaks. The image given here is the correct one.

4.5 Conclusion

Aggregate-free 2D lithium titanate and reduced graphene oxide nanosheet electrodes (LTO/rGO) were fabricated through 1) electrophoretic co-deposition of the LTH and GO precursors, and 2) topotactic transformation in reducing atmosphere into LTO and rGO, respectively. EPD was carried out using Cu substrate at 35 V to minimize copper dissolution and subsequent Cu contamination of the coating. The EPD coating technique led to the establishment of a superior percolation network of both ions and electrons despite minor contamination of copper oxides. GO acts both as self-assembling binder during deposition as well as conductive component after reduction during annealing. In the case of conventional PVDF/rGO electrodes, aggregation leads to inhomogeneous distribution of LTO and poorly constructed electrical percolation network in LTO/rGO composite. This inhomogeneity leads to local overcharge/overdischarge of LTO, which has been proven to accelerate LTO degradation. Both types of electrodes were electrochemically tested through CV, EIS, and battery cycling. Results showed that the PVDF electrodes had a higher conductivity because of the aggregation of rGO that provide a wider current pathway. The deep discharge of some LTO nanosheets further reduce the impedance of the PVDF/rGO electrodes, as the result of irreversibly lithiated LTO. Conversely, the EPD process is very effective at establishing a percolation network that is simultaneously good for both ionic and electronic conduction. Therefore, the EPD/rGO electrode has better overall performance and cyclability. This study has shown that EPD is an excellent alternative fabrication technique for constructing high rate lithium-ion battery electrodes.

4.6 Acknowledgements

This work is supported by a NSERC/Hydro-Quebec CRD grant. We acknowledge additional support by the McGill Engineering Doctoral Award (MEDA) and McGill Sustainability Systems Initiative (MSSI) programs. We thank David Liu at the Facility for Electron Microscopy Research (FEMR) of McGill University for help in microscope operation and data collection. We would also like to thank Stéphanie Bessette for her invaluable assistance with generating the EDS maps and use of the Hitachi SU8230.

4.7 References

[1] X. Li, Q. Wang, Y. Yang, J. Kang, Correlation between capacity loss and measurable parameters of lithium-ion batteries, Int. J. Electr. Power Energy Syst. 110 (2019) 819–826. https://doi.org/10.1016/j.ijepes.2019.03.046.

[2] S. Müller, J. Eller, M. Ebner, C. Burns, J. Dahn, V. Wood, Quantifying Inhomogeneity of Lithium Ion Battery Electrodes and Its Influence on Electrochemical Performance, J. Electrochem. Soc. 165 (2018) A339–A344. https://doi.org/10.1149/2.0311802jes.

[3] X. Zhang, Y. Zhu, A.M. Bruck, L.M. Housel, L. Wang, C.D. Quilty, K.J. Takeuchi, E.S. Takeuchi, A.C. Marschilok, G. Yu, Understanding aggregation hindered Li-ion transport in transition metal oxide at mesoscale, Energy Storage Mater. 19 (2019) 439–445. https://doi.org/10.1016/j.ensm.2019.03.017.

[4] A.J. Marsden, D.G. Papageorgiou, C. Vallés, A. Liscio, V. Palermo, M.A. Bissett, R.J. Young, I.A. Kinloch, Electrical percolation in graphene–polymer composites, 2D Mater. 5 (2018) 032003. https://doi.org/10.1088/2053-1583/aac055.

[5] D. Konios, M.M. Stylianakis, E. Stratakis, E. Kymakis, Dispersion behaviour of graphene oxide and reduced graphene oxide, J. Colloid Interface Sci. 430 (2014) 108–112. https://doi.org/10.1016/j.jcis.2014.05.033.

[6] S. Mitra, S. Banerjee, A. Datta, D. Chakravorty, A brief review on graphene/inorganic nanostructure composites: materials for the future, Indian J. Phys. 90 (2016) 1019–1032. https://doi.org/10.1007/s12648-016-0841-x.

[7] P. Ranjan, S. Agrawal, A. Sinha, T.R. Rao, J. Balakrishnan, A.D. Thakur, A Low-Cost Non-explosive Synthesis of Graphene Oxide for Scalable Applications, Sci. Rep. 8 (2018) 12007. https://doi.org/10.1038/s41598-018-30613-4.

[8] K. Krishnamoorthy, M. Veerapandian, K. Yun, S.-J. Kim, The chemical and structural analysis of graphene oxide with different degrees of oxidation, Carbon. 53 (2013) 38–49. https://doi.org/10.1016/j.carbon.2012.10.013.

[9] L. Ye, K. Wen, Z. Zhang, F. Yang, Y. Liang, W. Lv, Y. Lin, J. Gu, J.H. Dickerson, W. He, Highly Efficient Materials Assembly Via Electrophoretic Deposition for Electrochemical Energy Conversion and Storage Devices, Adv. Energy Mater. 6 (2016). https://doi.org/10.1002/aenm.201502018.

[10] L. Besra, M. Liu, A review on fundamentals and applications of electrophoretic deposition (EPD), Prog. Mater. Sci. 52 (2007) 1–61. https://doi.org/10.1016/j.pmatsci.2006.07.001.

[11] D. Bresser, D. Buchholz, A. Moretti, A. Varzi, S. Passerini, Alternative binders for sustainable electrochemical energy storage – the transition to aqueous electrode processing and bio-derived polymers, Energy Environ. Sci. 11 (2018) 3096–3127. https://doi.org/10.1039/C8EE00640G.

[12] S. Chauque, F.Y. Oliva, A. Visintin, D. Barraco, E.P.M. Leiva, O.R. Cámara, Lithium titanate as anode material for lithium ion batteries: Synthesis, post-treatment and its electrochemical response, J. Electroanal. Chem. 799 (2017) 142–155. https://doi.org/10.1016/j.jelechem.2017.05.052.

[13] C.P. Sandhya, B. John, C. Gouri, Lithium titanate as anode material for lithium-ion cells: a review, Ionics. 20 (2014) 601–620. https://doi.org/10.1007/s11581-014-1113-4.

[14] K. Zaghib, A. Mauger, H. Groult, J.B. Goodenough, C.M. Julien, Advanced Electrodes for High Power Li-ion Batteries, Mater. Basel Switz. 6 (2013) 1028–1049. https://doi.org/10.3390/ma6031028.

[15] K. Zaghib, M. Dontigny, A. Guerfi, J. Trottier, J. Hamel-Paquet, V. Gariepy, K. Galoutov, P. Hovington, A. Mauger, H. Groult, C.M. Julien, An improved high-power battery with increased thermal operating range: C–LiFePO4//C–Li4Ti5O12, J. Power Sources. 216 (2012) 192–200. https://doi.org/10.1016/j.jpowsour.2012.05.025.

[16] G.J. Wang, J. Gao, L.J. Fu, N.H. Zhao, Y.P. Wu, T. Takamura, Preparation and characteristic of carbon-coated Li4Ti5O12 anode material, J. Power Sources. 174 (2007) 1109–1112. https://doi.org/10.1016/j.jpowsour.2007.06.107.

[17] X. Li, J. Xu, P. Huang, W. Yang, Z. Wang, M. Wang, Y. Huang, Y. Zhou, M. Qu, Z. Yu, Y. Lin, In-situ carbon coating to enhance the rate capability of the Li4Ti5O12 anode material and suppress the electrolyte reduction decomposition on the electrode, Electrochimica Acta. 190 (2016) 69–75. https://doi.org/10.1016/j.electacta.2015.12.176.

[18] Z. Ma, G. Shao, G. Wang, J. Du, Y. Zhang, Electrochemical performance of Mo-doped LiFePO<Subscript>4</Subscript>/C composites prepared by two-step solid-state reaction, Ionics. 19 (2013) 437–443. https://doi.org/10.1007/s11581-012-0768-y.

[19] H.-C. Chiu, X. Lu, S. Elouatik, K. Zaghib, G.P. Demopoulos, Formation of Lithium Titanate Hydrate Nanosheets: Insight into a Two-Dimension Growth Mechanism by in Situ Raman, Cryst. Growth Des. 16 (2016) 3898–3904. https://doi.org/10.1021/acs.cgd.6b00470.

[20] H.-C. Chiu, X. Lu, J. Zhou, L. Gu, J. Reid, R. Gauvin, K. Zaghib, G.P. Demopoulos, Annealing-regulated elimination of residual strain-induced structural relaxation for stable high-power Li4Ti5O12 nanosheet anodes, Nano Energy. 32 (2017) 533–541. https://doi.org/10.1016/j.nanoen.2016.12.063.

[21] H. Chiu, N. Brodusch, R. Gauvin, A. Guerfi, K. Zaghib, G.P. Demopoulos, Aqueous Synthesized Nanostructured Li4Ti5O12 for High-Performance Lithium Ion Battery Anodes, J. Electrochem. Soc. 160 (2013) A3041–A3047. https://doi.org/10.1149/2.008305jes.

[22] H.-C. Chiu, X. Lu, J. Zhou, L. Gu, J. Reid, R. Gauvin, K. Zaghib, G.P. Demopoulos, Capacity Fade Mechanism of Li4Ti5O12 Nanosheet Anode, Adv. Energy Mater. 7 (2017) n/a-n/a. https://doi.org/10.1002/aenm.201601825.

[23] N.R. Wilson, P.A. Pandey, R. Beanland, J.P. Rourke, U. Lupo, G. Rowlands, R.A. Römer, On the structure and topography of free-standing chemically modified graphene, New J. Phys. 12 (2010) 125010. https://doi.org/10.1088/1367-2630/12/12/125010.

[24] F.T. Johra, J.-W. Lee, W.-G. Jung, Facile and safe graphene preparation on solution based platform, J. Ind. Eng. Chem. 20 (2014) 2883–2887. https://doi.org/10.1016/j.jiec.2013.11.022.

[25] D.V. Pelegov, A.A. Koshkina, V.I. Pryakhina, V.S. Gorshkov, Efficiency Threshold of Carbon Layer Growth in Li4Ti5O12/C Composites, J. Electrochem. Soc. 166 (2019) A5019–A5024. https://doi.org/10.1149/2.0031903jes.

[26] M. Wojtoniszak, B. Zielińska, R. Kalenczuk, E. Mijowska, Photocatalytic performance of titania nanospheres deposited on graphene in coumarin oxidation reaction, Mater. Sci.-Pol. 30 (2012). https://doi.org/10.2478/s13536-012-0008-1.

[27] D.T.L. Galhena, B.C. Bayer, J.C. Meyer, S. Hofmann, G.A.J. Amaratunga, Reduced Graphene Oxide as a Monolithic Multifunctional Conductive Binder for Activated Carbon Supercapacitors, ACS Omega. 3 (2018) 9246–9255. https://doi.org/10.1021/acsomega.8b01075.

[28] J.C. Park, J. Kim, H. Kwon, H. Song, Gram-Scale Synthesis of Cu2O Nanocubes and Subsequent Oxidation to CuO Hollow Nanostructures for Lithium-Ion Battery Anode Materials, Adv. Mater. 21 (2009) 803–807. https://doi.org/10.1002/adma.200800596.

[29] M. Krajewski, B. Hamankiewicz, M. Michalska, M. Andrzejczuk, L. Lipinska, A. Czerwinski, Electrochemical properties of lithium–titanium oxide, modified with Ag–Cu particles, as a negative electrode for lithium-ion batteries, RSC Adv. 7 (2017) 52151–52164. https://doi.org/10.1039/C7RA10608D.

[30] E. Barsoukov, R. Mcdonald, Impedance Spectroscopy: Theory, Experiment, and Applications, 3rd ed., 2018.

[31] N. Takami, K. Hoshina, H. Inagaki, Lithium Diffusion in Li4/3Ti5/3O4 Particles during Insertion and Extraction, J. Electrochem. Soc. 158 (2011) A725–A730. https://doi.org/10.1149/1.3574037.

[32] W. Schmidt, P. Bottke, M. Sternad, P. Gollob, V. Hennige, M. Wilkening, Small Change—Great Effect: Steep Increase of Li Ion Dynamics in Li4Ti5O12 at the Early Stages of Chemical Li Insertion, Chem. Mater. 27 (2015) 1740–1750. https://doi.org/10.1021/cm504564k.

[33] B. Ziebarth, M. Klinsmann, T. Eckl, C. Elsässer, Lithium diffusion in the spinel phase Li4Ti5O12 and in the rocksalt phase Li7Ti5O12 of lithium titanate from first principles, Phys. Rev. B. 89 (2014) 174301. https://doi.org/10.1103/PhysRevB.89.174301.

[34] M.G. Verde, L. Baggetto, N. Balke, G.M. Veith, J.K. Seo, Z. Wang, Y.S. Meng, Elucidating the Phase Transformation of Li4Ti5O12 Lithiation at the Nanoscale, ACS Nano. 10 (2016) 4312–4321. https://doi.org/10.1021/acsnano.5b07875.

[35] M. Chandra Sekhar, P. Kondaiah, S.V. Jagadeesh Chandra, G. Mohan Rao, S. Uthanna, Effect of substrate bias voltage on the structure, electric and dielectric properties of TiO2 thin films by DC magnetron sputtering, Appl. Surf. Sci. 258 (2011) 1789–1796. https://doi.org/10.1016/j.apsusc.2011.10.047.

[36] S. Nezar, N. Saoula, S. Sali, M. Faiz, M. Mekki, N.A. Laoufi, N. Tabet, Properties of TiO2 thin films deposited by rf reactive magnetron sputtering on biased substrates, Appl. Surf. Sci. 395 (2017) 172–179. https://doi.org/10.1016/j.apsusc.2016.08.125.

5 $TiNb_2O_7$ and Reduced Graphene Oxide Composite Anodes

The previous chapter investigated the electrophoretic co-deposition of rGO and LTO 2D nanomaterials and the fabrication of highly homogeneous anode coatings following reductive annealing with excellent battery performance, particularly at high rates. In this chapter, we substituted titanium niobate (TNO, $TiNb_2O_7$) in lieu of LTO to address LTO's low energy-density issue. TNO has been deemed to be a promising LTO replacement due to sharing the same advantages but delivering higher energy densities (175 mAh/g vs. 387 mAh/g for LTO and TNO respectively, see section 2.1.6). The emphasis was on enhancing the percolation network of the composite anode via optimization of the electrophoretic and annealing steps, thus overcoming the low inherent conductivity of TNO.

The EPD electrodes are assembled using a similar EPD system detailed in Chapter 4 however an increase of GO concentration in suspension was needed to adapt the system to the TNO prepared using solid-state reaction. Like all investigations in this thesis, benchmark PVDF electrodes are made for comparison through electrochemical (CV, galvanostatic charge/discharge, EIS and dQ/dV analysis) and material/coating characterization (XRD, XPS, TGA, Raman, BET, TEM, cross-sectional SEM and EDS imaging/mapping). In this part of the research thesis, the effect of the percolation on the polarization and subsequent capacity fade of the anode is elucidated particularly through EIS and differential capacity analysis.

These findings are to be submitted: **Marianna Uceda**, Hsien-Chieh Chiu, Reynald Gauvin, Karim Zaghib, and George P. Demopoulos. **Percolation Influence on the Fade Mechanism of $TiNb_2O_7$ and Reduced Graphene Oxide Composite Anodes**.

5.1. Abstract

Improving homogeneity in composite electrodes between active and conductive materials has been shown to enhance transport properties and lead to improved electrochemical performance. In this paper, electrophoretic deposition (EPD) is used to fabricate binderless composite titanium niobate ($TiNb_2O_7$, TNO) and reduced graphene oxide (rGO) anodes. This was accomplished through deposition of TNO and the precursor graphene oxide (GO) followed by high-temperature annealing at reductive atmosphere. Using the rGO precursor during EPD takes advantage of the functionalized surface of GO which circumvents the poor dispersibility of graphene and allows for a stable suspension. Cross-sectional SEM-EDS images show that fabrication via EPD enabled excellent homogeneity among every component within the electrodes when compared to the poor dispersion provided by the conventional casting technique. Electrochemical results revealed rGO had the dual role of acting as a 1) flexible binder capable of maintaining the mechanical integrity and 2) pseudocapacitor capable of Li^+ storage. Thus, the robust improved percolation network enabled by the nanoscale assembling power of EPD led to high capacities at 0.5C cycling and slower capacity fade of the TNO/rGO composite anode. In contrast, the conventionally casted electrodes experienced high internal polarization due to rapid degradation of both TNO and rGO materials. Through this study, EPD was shown to be a superior coating technology for fabricating LIB electrodes incorporating rGO as conductive additive and binder.

5.2. Introduction

Titanium niobium oxide (TNO, $TiNb_2O_7$) has emerged as a promising replacement to lithium titanate spinel (LTO, $Li_4Ti_5O_{12}$). LTO is a safe and effective anode material with a long life cycle, "zero-strain" characteristic [1], and high working voltage of 1.55V vs. Li^+/Li which is above the SEI formation voltage [2]. However, LTO is limited by its low electronic conductivity ($10^{-8} - 10^{-13}\ S/cm$ [1]) and low theoretical capacity of $175\ mAh/g$ due to the Ti^{3+}/Ti^{4+} couple. In contrast TNO stands out as a competitor as it has a higher theoretical capacity of $387\ mAh/g$. TNO is a monoclinic layered structure in the *C2/m* space group with lattice constants a = 20.351 Å, b = 3.801 Å, c = 11.882 Å [3,4] in which the Ti^{4+} and Nb^{5+} occupy octahedral sites which share corners and edges. Due to the similar ionic radii between Ti^{4+} and Nb^{5+}, Ti/Nb anti-site disorders are likely [5]. During intercalation lithium can be reversibly inserted into the $(\bar{1}10)$ plane of the TNO primitive cell to occupy interstitial sites [6]. Charge compensation is fulfilled by the Nb^{5+}/Nb^{4+}at around 1.65 V vs. Li/Li^+, Ti^{4+}/Ti^{3+} at 1.9 V, and possible Nb^{4+}/Nb^{3+} at around 1 V vs. Li/Li^+ redox couples which theoretically allow for $5\ Li^+$ storage in the voltage range 0.6-3 V vs. Li^+/Li [4]. Above 1V a $4\ Li^+$ reaction is achievable with Nb^{5+}/Nb^{3+} yielding a 310 mAh/g capacity. TNO has a high working voltage of 1.65 V which also places it outside the SEI formation range. However, it also suffers from the same drawbacks as LTO – low ionic and electronic conductivity. This causes slow solid-state diffusion of Li^+ which results in limited electrochemical performance. Furthermore, it experiences a relatively larger volume change (~7-8 %) compared to LTO (<0.2%) upon Li-ion (de)intercalation [7], which is however less severe than that of graphite upon Li-ion intercalation (~13% [8]). This repeated expansion and contraction leads to cracking and isolation of the active, conductive, and binder material leading to high interfacial impedance. Improving the TNO performance has been done through nanostructuring [9,10] or designing synthesis techniques that fabricate TNO composites with conductive materials such as holey graphene [11] and carbon nanotubes [12]. Although both strategies aim at increasing surface area, the latter methods work more efficiently because of their ability to ensure intimate contact between the TNO and conductive additive. A well established percolation network – meaning no formation of large mesoscale aggregates of the active material – has been identified recently as critical issue in improving battery performance [13].

The two-dimensional planar graphene, or reduced graphene oxide (rGO, so-named due to its synthesis pathway) possesses outstanding flexibility [14], high surface area, and excellent conductivity [15]. Therefore, rGO has been used as a conductive binder [16] that led to improvement (when compared to the conventionally used carbon black) of the electrochemical performance. Nonetheless, conventional tape-casting technique is not effective in preparing homogeneous composite coatings because of the high viscosity and solid loading. Instead, it allows for the formation of large aggregates at macroscopic scale, particularly when nanoparticles (which have a high surface area and tend to form viscous slurries during casting) and 2D materials such as graphene are involved.

To this end, electrophoretic deposition (EPD) is an attractive alternative coating technique. The self-assembly capability inherent to this process [17] is perfectly suited for fabricating composite electrodes using graphene [18,19] and nanosized materials. EPD is an electrocoating technique that involves application of an electric field to force particle migration and deposition onto a conductive substrate such as copper foils. The process is highly versatile and can be tailored, by manipulating the suspension and process parameters (i.e. electric field magnitude and deposition time), based on the material that is to be deposited.

In this paper, TNO/rGO composite coatings are fabricated through electrophoretically depositing TNO and the precursor graphene oxide (GO), followed by reductive annealing at elevated temperature to encourage $GO \rightarrow rGO$ transformation. The mechanism of performance improvement of EPD electrodes is thoroughly elucidated via comparing to conventionally prepared electrodes using the PVDF-NMP binder-solvent system.

5.3. Experimental Procedure

5.3.1. TNO Synthesis

The TNO ($TiNb_2O_7$) was fabricated in-house in a 2-step process that involves 1) mechanical mixing of the two precursors and 2) high temperature sintering.

The precursors used are niobium oxide (Nb_2O_5, Sigma CAS 1313-96-8) and anatase titanium oxide (TiO_2) – the TiO_2 was synthesized in-house using a process reported elsewhere [20]. Stoichiometric amounts of Nb_2O_5 and TiO_2 (accounting for 11 wt.% hydroxyl/crystallized water) are introduced into the ball milling jar (80 mL bowl size) along with 70g of 3mm zirconia beads and ethanol (1 mL per 0.1g of material used) and subjected to high energy ball milling in a Fritsch Planetary Micro Mill (Pulverisette 7). The milling conditions used were 400 rpm for 45 min followed by a 15 min rest cycle – this was repeated for a total of 9 cycles (or 9 hours). The mixture was then recovered and dried overnight. The powder was added subsequently to an alumina crucible and sintered at $1200\ ℃$ for 20 hours (ramping rate = $5\ ℃/min$ followed by the 20 hrs holding time) in air using a Carbolite horizontal tube furnace (Type 3216). The obtained coarse TNO grains is then pulverized via ball-milling at 400 rpm for 45 min followed by a 15 min rest cycle for 5 cycles.

5.3.2. Carbon-coating

Carbon-coating is accomplished using lactose as the carbon precursor followed by high temperature decomposition. The 22.4 g/L of lactose was mixed in DI water. The TNO and lactose solution are then mixed to satisfy the ratio 0.112g lactose/g TNO in an alumina crucible. The slurry is dried at $110\ ℃$ to completely evaporate the water and the crucible is then transferred into an MTI mini tube furnace (model OTF-1200X) and heated in a step-wise manner up to $700℃$ for ~400 min to allow for lactose decomposition under a pure argon environment. The step-wise temperature change can be seen in Figure C-2 of Appendix C.

5.3.3. Reduced Graphene Oxide Synthesis

Graphene oxide (GO, Abalonyx) is placed in an alumina crucible which is transferred into the MTI mini tube furnace (model OTF-1200X). The material is then heated to $600℃$ for 6 hrs (ramping rate = $5\ ℃/min$) of in $3\%\ H_2$ in Ar mixture to ensure transformation of graphene oxide to reduced graphene oxide (hereafter referred to as rGO). This rGO was used in preparing the conventional electrodes.

5.3.4. Electrode Preparation: PVDF and EPD

5.3.4.1 PVDF electrodes

The treated TNO was manually mixed with the conductive rGO (pre-reduced from GO in high temperature reductive environment as described above prior to this step) and polyvinylidene fluoride (PVDF) binder at a wt.% of 80/10/10 or 72/18/10 (to compose the PVDF electrodes with 10% rGO and 18% rGO referred to as “PVDF/10rGO” and “PVDF/18rGO” respectively) in a mortar and pestle. N-Methyl-2-pyrrolidone (NMP) solvent was added to make a paste with a solid density of 250 g/mL and 200 g/mL for the PVDF/10rGO and PVDF/18rGO respectively. The paste was then doctor bladed onto copper foil (99.99% Cu, 25 μm thick, MTI Corporation). The coating is then dried in air overnight, pressed at 2MPa, and further dried at 80℃ in a vacuum overnight to ensure complete removal of the NMP.

5.3.4.2 EPD electrodes

EPD electrodes were fabricated in a pure ethanol suspension with 3 g/L solids composed of ball-milled/carbon-coated TNO and GO at 70/30 wt.% respectively (as the composition had a stabilization effect further discussed in Section C.3 in Appendix C). The suspension was sonicated for 40 mins and allowed to rest for 2 mins. For deposition, 30 V was applied for ten 15s-stages using a Keithley 2600 SourceMeter. The electrodes were then dried overnight, pressed at 1 MPa, and introduced into the MTI mini tube furnace at 600℃ for 6 hr to reduce the GO. These electrodes will be henceforth referred to as "EPD electrodes".

5.3.5. Material Characterization

TNO is identified through X-ray diffraction (XRD) using a Bruker D8 Discovery X-Ray Diffractometer (VANTEC Detector Cu-Source). The carbon-coating is identified through Raman microscopy using Bruker SENTERRA Confocal Raman Microscope with 532-nm laser.

The materials and coatings are characterized via X-ray photoelectron spectroscopy (XPS) using Thermo Scientific K-Alpha X-Ray Photoelectron Spectroscopy and high-resolution spectra at the edges of C 1s, Ti 2p, and Nb 3d.

The TNO is imaged through Transmission Electron Microscopy (TEM) using a FEI Titan Krios 300 kV Cryo-STEM. Scanning Electron Microscope (SEM) images for the powders and coating cross-sections are obtained using a Hitachi Cold Field-Emission (SU8230) Microscope – this is also used to obtain Electron Dispersion Spectroscopy (EDS) maps. In order to image cross-sections, the samples are cut using an Ion-Milling system (IM4000) operated at 4kV for 30 mins and 30 reciprocals/min $\pm$ 30^{o} swing.

Brunnauer-Emmett-Teller (BET) analysis is performed using Micromeritics TriStar Surface area and porosity analyzer on the pristine and ball-milled TNO to determine surface area.

Thermogravimetric analysis (TGA) is performed, using a TGA/DSC 2 (Mettler Toledo), on the TNO material to determine the amount of carbon deposited during carbon-coating and the amount of rGO present in the EPD coating. A small amount (2-6 mg) of the powder is added to a platinum pan and heated to $1000℃$ at a ramping rate of $10℃/min$ under continuous air-flow (60mL/min). EPD coatings are scraped off the substrate for this technique.

5.3.6. Electrochemical Characterization

The EPD and PVDF electrodes are assembled into Swagelok-type half cells with lithium metal as the anode and $200\,\mu L\ 1M\ LiPF_6$ in EC:DMC:DEC at 2:2:1 by weight as the electrolyte. Assembly takes place in a glovebox under a pure argon environment to eliminate oxygen and water content. Pristine EPD and PVDF cells are tested using a BioLogic VSP Potentiostat/galvaonostat/EIS system. Electrochemical Impedance Spectroscopy (EIS) measurements were performed using a frequency range of 1 MHz to 0.01 Hz, a sinus amplitude of 100 mV, and a voltage range between 10V and -10V. Cyclic Voltammetry was performed from 0.6 to 3V at varying sweep rates (0.1 – 10 mV/s). Galvanostatic experiments were performed using a standard battery cycler (BST8 WA, MTI Corp) at 0.5C and a potential range of 0.6 to 3V.

5.4. Results and Discussion

5.4.1. TNO Synthesis and Suspension Characterization

5.4.1.1 C-coated TNO Synthesis

The solid-state synthesis of TNO (flowchart given in Figure C-1 of Appendix C) was an adaptation of the method described by Inada et al [21]. The method involves reaction of two oxides at high temperature. While the used TiO_2 was nanosized at with specific surface area, determined through BET, of ~200 m^2/g the Nb_2O_5 was much coarser ~2 m^2/g hence to promote their reaction the materials were ball milled extensively before thermal treatment at 1200 ^oC. After 20 hrs at 1200 ^oC, XRD analysis (Figure 5-1 a) confirmed the production of $TiNb_2O_7$ as judged from the characteristic XRD pattern (JCPDS: #77-1374). The as-prepared at 1200 ^oC material is referred as the "pristine" TNO. The strong Bragg peaks, particularly at $2\theta = 24^o$ (110), 26^o (003), and 26.4^o $(\bar{6}02)$, correspond to the monoclinic space group *C2/m*. SEM analysis (Figure 5-1 b) revealed the TNO particles to be in the form of large rod-shaped crystals ~0.8 μm in length and ~0.45 μm in width. Apparently, the lengthy reaction at high temperature favored the growth of the crystals.

This large particle size, coupled with this material's poor ionic conductivity [10], would mean large Li^+ diffusion length and therefore slow kinetics [22,23] during charging/discharging. This is manifested through large polarization and low capacities during cycling (discussed in section C.2 of Appendix C). To overcome this limitation, the TNO pristine material was ball-milled prior to carbon-coating. The resulting XRD diffractogram (Figure 5-1 a) showed peak broadening in the ball-milled TNO pattern, as a result of grain size reduction [24]. The grain size was deduced from TEM and SEM images to be in the range of 100-200 nm. High-resolution TEM (Figure 5-1 d) also revealed smaller ~20 nm domains in the ball-milled TNO crystals. Furthermore, BET measurement of the pristine and ball-milled materials indicated an increase in surface area from 0.37 to 25.72 m^2/g respectively upon ball milling.

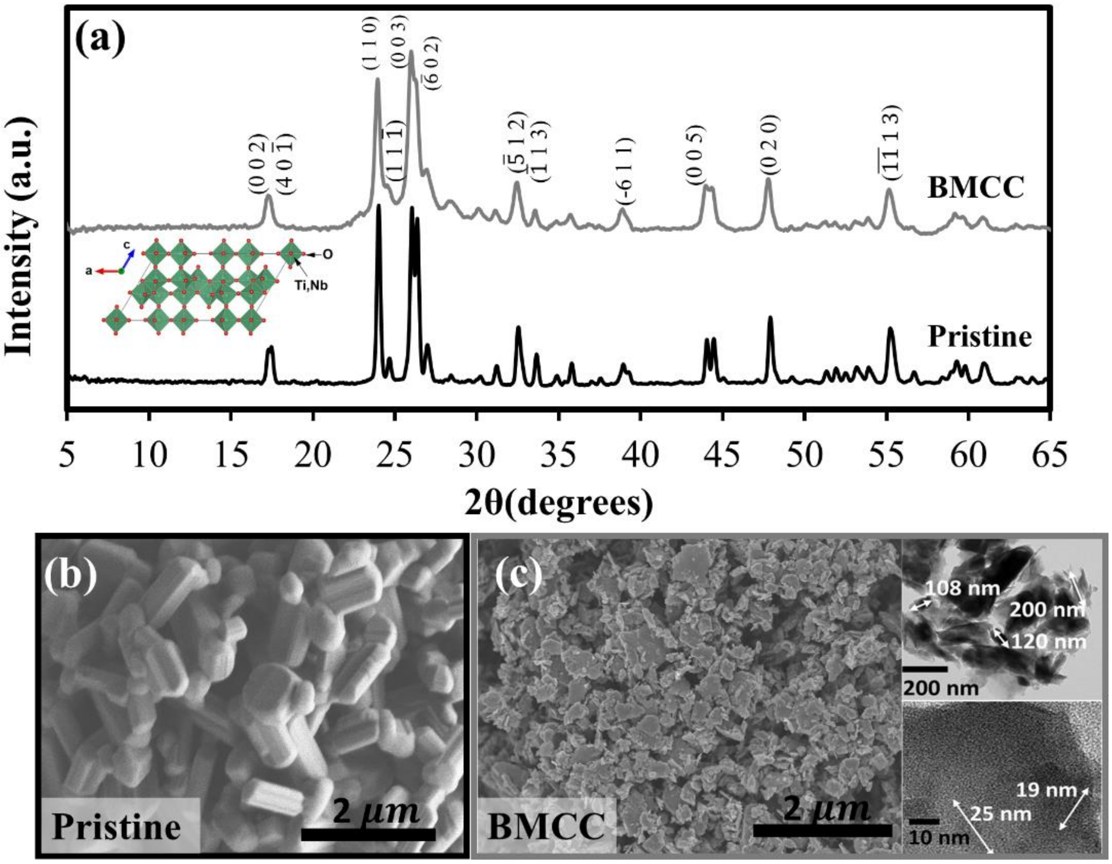

Figure 5-1: (a) XRD pattern (inset is the crystal structure taken from [25]) for pristine and ball-milled/carbon-coated ("BMCC") material. SEM images of (b) pristine and (c) ball-milled/carbon-coated material with corresponding TEM images.

The ball-milled TNO particles were carbon-coated through high-temperature decomposition of a carbon precursor. The carbon-coating present in the material was identified through the Raman "D" and "G" bands at ~1330 and ~1580 cm^{-1} (inset in Figure C-2 of Appendix C) [26]. TGA analysis (shown in Figure C-6 of Appendix C) revealed the carbon-coated ball-milled material contained around 0.6 wt.% moisture and 2% carbon-coating (as identified in section 3.4.1 of Chapter 3 and section A.3 of Appendix A).

5.4.1.2 EPD Suspension

To fabricate the electrophoretically deposited TNO/rGO electrodes, the ball-milled/carbon-coated TNO was suspended alongside the precursor GO in a pure ethanol solvent with 3 g/L solid loadings. The pristine TNO sedimented fast because of its coarse grain size, thus the ball-milled/carbon-coated material was selected (this is further discussed in section C.2 in Appendix C). Milled/carbon-coated TNO and GO had a zeta potential of -28 and -18 mV, respectively. GO suspension in ethanol is stabilized due to van der Waals interactions and H-bonding between the oxygen-containing functional groups on GO and the ethanol molecules [27]. The achieved suspension stability is likely caused by 1) the reduced particle size of TNO, 2) the presence of not fully coordinated positive Nb^{5+} and Ti^{4+} sites on the surface permitting the attachment of ethanol molecules via their OH^- groups, and possibly 3) the surface carbon film which is attracting the nonpolar C_2H_5 group in ethanol. Mixing TNO with GO (70/30 wt.% respectively) caused a subtle reduction in zeta potential, when compared to pure GO and TNO alone, to -15 mV. The consistency of the zeta potential between GO and TNO-GO suspensions means the suspension stability is determined by GO colloidal nanosheets. This means the GO content in suspension, relative to the TNO, can be controlled to influence the dynamics of colloidal sol and deposition kinetics. However, the lower zeta potential for the TNO/GO hetero-aggregates does not lead to fast deposition kinetics but it allows for nanoscale entanglement which ultimately leads to the formation of a homogeneous deposit as characterized later. During EPD a voltage of 30V was applied for ten 15-second stages; this low voltage was selected to minimize the oxidation of the copper foil as it is discussed in section C.3 of Appendix C.

5.4.2. Coating Characterization and EDS Microstructure

5.4.2.1 Surface Characterization

XPS characterization (given in Figure C-7 in Appendix C) of the EPD coating after annealing shows a reduction in the C-O peak in the C 1s spectra indicating loss of functional groups and $GO \rightarrow rGO$ transformation. A broad peak is observed at ~290 eV which is attributed to the HOMO-

LUMO shake-up satellite $\pi - \pi^*$ [28]. This has been previously observed to occur when $GO \rightarrow rGO$ transformation is induced through high temperature annealing (Chapter 4, section 4.4.2) and reflects the enhanced conductivity of the reduced GO.

XPS spectra of Ti 2p and Nb 3d are shown in Figure 5-2 (a) and (b), the results are calibrated with respect to carbon and reveal chemical shifts caused by ball milling, carbon-coating, and annealing. Overall, both spectra exhibit chemical shift towards high energy regardless of the treatment applied. This means that the electronegativity of oxygen in the TMO_6 octahedra (TM = Ti, Nb) increases to attract more electron density, hence the strong binding energy of Nb and Ti and positive chemical shift. For instance, the Nb 3d 5/2 peak shifts by 0.2 eV when ball-milled, 0.28 eV when carbon-coated, 0 eV when electrophoretically deposited, and 0.4 eV when annealed becoming progressively more electronegative. Similarly, annealing at elevated temperature, including carbon coating and GO reduction, results in significant chemical shift also observed in the Ti 2p 3/2 peak shift from 458.88 eV of EPD coating (green) to 459.48 eV after annealing (blue). In other words, TM-O bonds become more ionic after every post-treatment following synthesis and could be the consequence of coulombic interactions causing TM-O bonding property [29] variations.

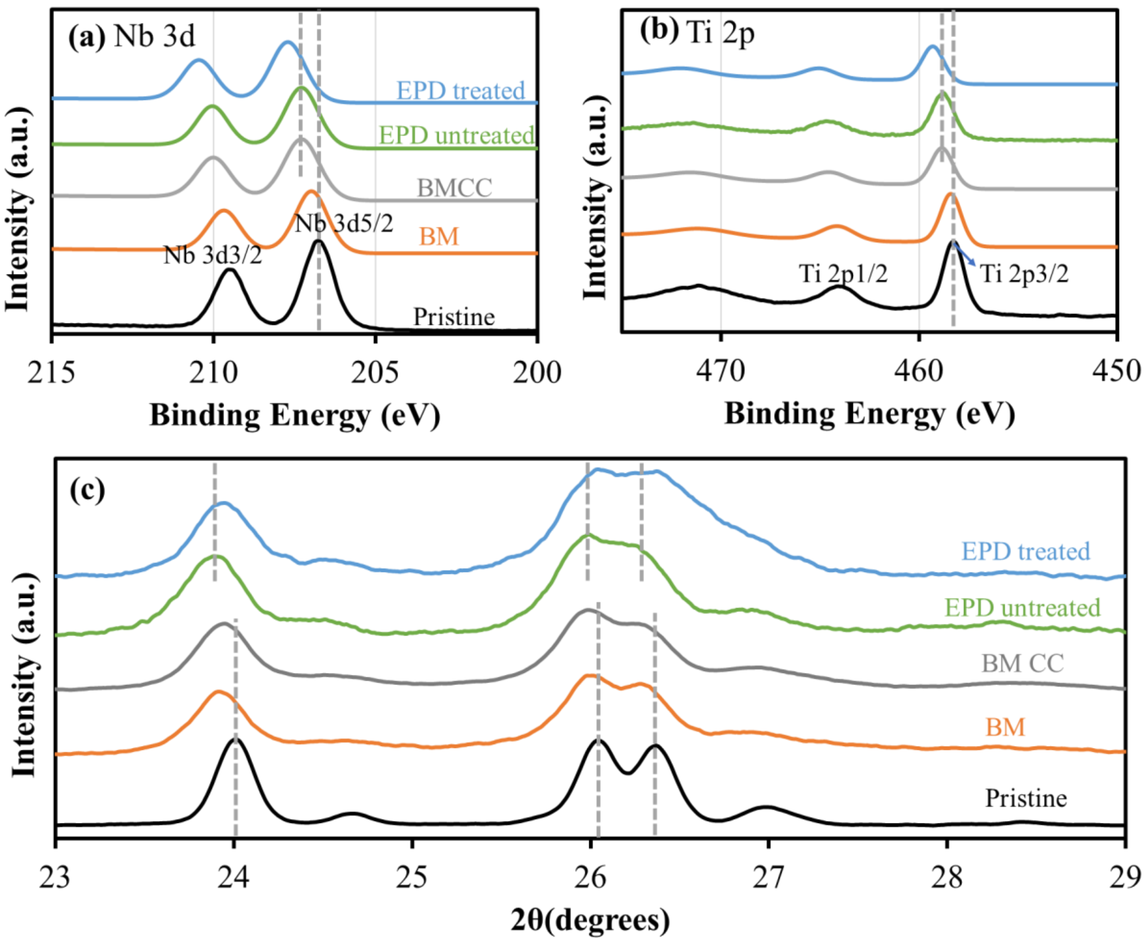

Figure 5-2: XPS spectra for (a) Nb 3d and (b) Ti 2p of the pristine material, ball-milled TNO ("BM") ball-milled/carbon-coated TNO ("BMCC"), the EPD coating, and the annealed EPD coating. (c) Closeup of XRD pattern showing the main peaks at $2\theta = 24°\ (110), 26°\ (003)$, and $26.4°\ (\bar{6}02)$ for pristine, ball-milled, ball-milled/carbon-coated, untreated (non-annealed) EPD coating, and treated (annealed) EPD coating.

5.4.2.2 Crystal Structure

Crystallographic analysis was done using XRD to elucidate the crystal structure variation in the annealed EPD electrode. Figure 5-2 (c) displays the XRD pattern between $2\theta = 23° - 29°$ where clear apparent peak shifts are shown to occur toward a high-angle direction after annealing, particularly the three strongest peaks at 24° (110), 26° (003) and 26.4° ($\bar{6}02$), respectively (the full XRD patterns for the EPD coating before and after annealing are given in Figure C-8 of Appendix C). The extent of these shifts varies, meaning the lattice – which is schematically represented in Figure C-9 in Appendix C – distorted anisotropically. Thus, the (003) peak shift (purple plane) signifies that the interlayer distance between TMO$_6$ octahedra along the a-b plane decreases after annealing. The $(\bar{6}02)$ plane (red plane) belongs to the cross-sectional areas of the 2D structure of the TNO lattice. This peak shift also represents the compression of the TNO lattice along this plane. Typically, in the layered oxides such as perovskite type or the ReO_3-type like TNO, better ion diffusion is obtained via lattice expansion [30]. This means that the Li-ion diffusion in the prepared TNO crystals is expected to be relatively sluggish. Thus, further optimization on the electrode fabrication process is required.

5.4.2.3 Coating Homogeneity

The coating homogeneity between active and conductive components is studied through cross-sectional analysis and EDS mapping of the C Kα, Ti Kα, and Nb Kα (Figure 5-3) of the EPD electrode ("EPD/rGO"), and the PVDF electrodes with 10 and 18 wt.% rGO ("PVDF/10rGO" and "PVDF/18rGO" respectively). The EPD coating thickness was found to be ~5 μm which is dependent on the number of EPD stages applied, which can be potentially increased. The PVDF coating thickness (~$8 - 18\ \mu m$) is dependant on the height of the doctor blade and on the slurry viscosity (which affects the flow and dispersibility).

As can be seen, the EPD process enables intimate contact between TNO and rGO preventing formation of large aggregates due to its inherent self-assembly power [17]. This results in significant improvement to the percolation network when compared to the casted electrodes. TGA analysis of the EPD coating showed the coating is composed of 18% rGO after annealing (considering the carbon-coating) (shown in Figure C-6 of Appendix C). In the casting method, increasing the amount of rGO in the PVDF-based electrodes to 18 wt.% proved to be difficult. Thus, larger rGO content in the slurry led to a significant increase in viscosity, hence requiring 25% excess NMP to improve the slurry consistency during casting. After drying, the PVDF coating with large amounts of rGO had a tendency to flake off – a feature not seen in the PVDF coating with lower rGO content or in the EPD coating. A closeup of the PVDF electrode with 18 wt.% rGO is given in Figure C-10 in Appendix C which shows a fracture occurring within a large TNO aggregate and poor adhesion to the substrate, indicating the amount of PVDF available is not enough (this fluoropolymer is evident through F Kα footprint mapping). Thus, increasing the rGO content led to poor interparticle and substrate adhesion that likely necessitates a corresponding increase in binder fraction. On the other hand, using EPD as a fabricating technique enabled the use of larger amounts of rGO in the coating without the need for a binder. Instead, the rGO has binder capabilities and acts as an anchor between TNO particles preventing them from falling apart [16] – a feature which is aided by the excellent homogeneity afforded through EPD – a very useful attribute in accommodating the volume changes during (de)lithiation of electrode components.

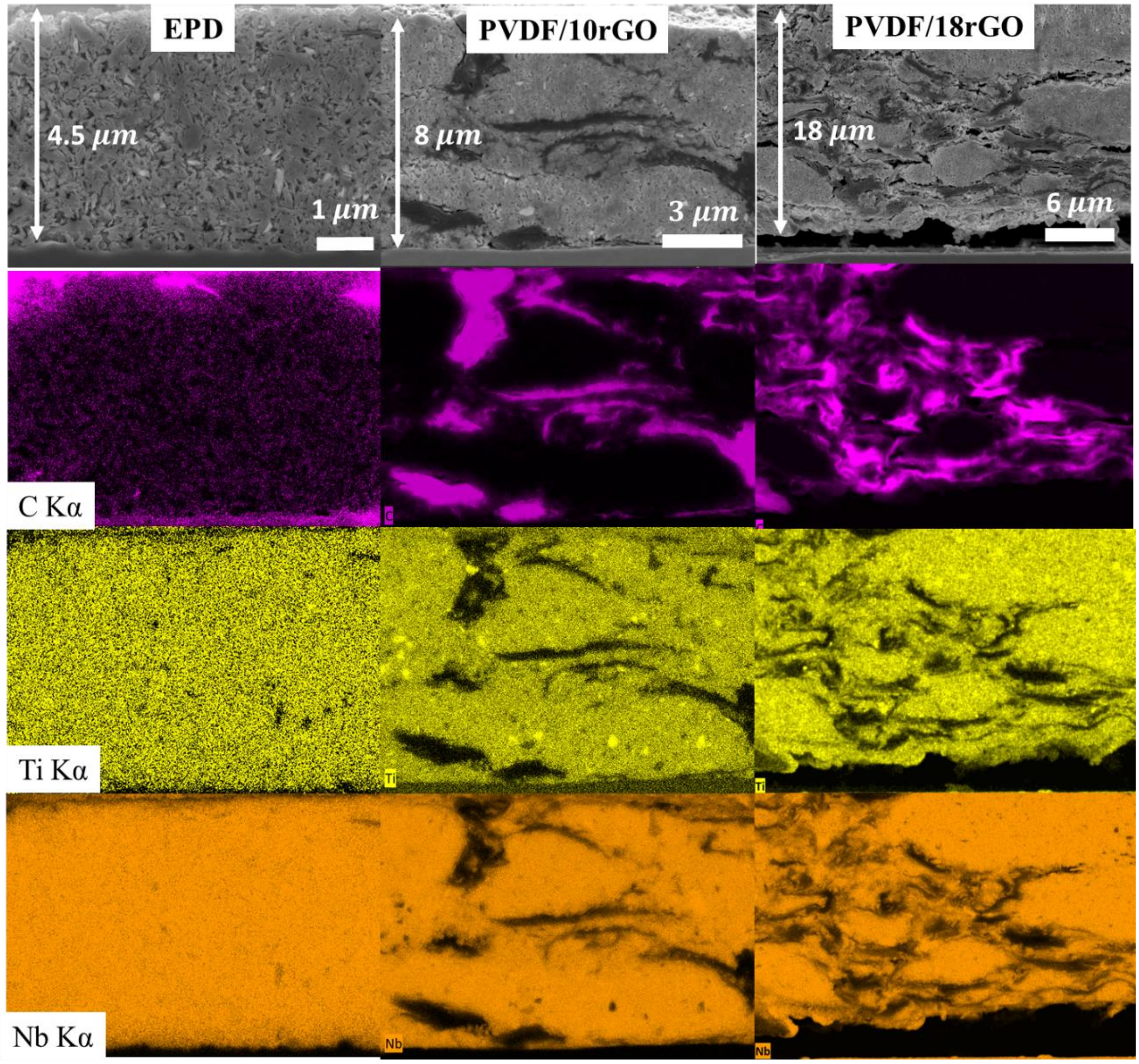

Figure 5-3: cross-sectional SEM images and EDS maps for (left to right) electrodes made with EPD (after annealing), PVDF with 10 wt.% rGO (“PVDF/10rGO”), and PVDF with 18 wt.% rGO (“PVDF/18rGO”) showing SE images and C Kα, Ti Kα, and Nb Kα maps. Please note, the scale varies between the SEM images but remains the same for the corresponding EDS maps.

It is also important to note that the EPD electrode contained Cu-containing deposits due to Cu dissolution and redeposition despite the low voltage used. These are observed in the Cu Lα EDS images and XPS of Cu 2p (Figure C-5 of Appendix C). Through the XPS they are identified as

Cu^{+} and Cu^{2+} (which is mostly reduced during the annealing process). Further information is given in section C.3 of Appendix C.

5.4.3. Electrochemical Performance

5.4.3.1 Li-ion storage

Redox behavior of the PVDF-built (containing 18 and 10 wt.% rGO) and EPD-built electrodes is examined through cyclic voltammograms given in Figure 5-4 (a). For PVDF electrode with 10 wt.% rGO, the obtained voltammograms show the Nb^{5+}/Nb^{4+} redox couple – which corresponds to the dominant peak – appear at 1.69/1.57 V (ox/red). The shoulder observed at 1.53/1.46 V vs. Li/Li^{+} refers also to the redox reaction of Nb^{5+}/Nb^{4+} reflecting the different coordination environment of the Nb atoms (edge- vs. corner-shared octahedral). Meanwhile, the broad peak at 1-1.4 V overlaps with the Nb^{4+}/Nb^{3+} peak expected at ~ 1V, while the shoulder at 1.94/1.84 V belongs to Ti^{4+}/Ti^{3+} couple [4]. The EPD and PVDF electrode with 18 wt.% rGO show the peaks at similar positions at low scan rate (0.1 mV/s) with varying interpeak distances for the main Nb^{5+}/Nb^{4+} redox couple – these being 0.1 V, 0.124 V, and 0.17 V for the EPD, PVDF/10rGO, and PVDF18/rGO electrodes respectively. This interpeak distance was further increased when cyclic voltammetry was subsequently carried out at higher scan rates as a result of increased polarization at high rate. Following the main Nb^{5+}/Nb^{4+} couple, significant polarization is observed at high rates for the PVDF-based electrodes when compared to the EPD electrode. At 2 mV/s the interpeak distances for EPD, PVDF/10rGO, and PVDF/18rGO are 0.51V, 0.92V, and 0.75 V. The lower interpeak distance in EPD electrodes shows that the EPD process is adept at minimizing polarization.

An important observation for both rGO-containing electrodes is the quasi rectangular feature observed at around 0.7V ~1.4V (refer to Figure 5-4 a) which overlaps with the Nb^{4+}/Nb^{3+} couple – a feature not seen for the electrodes using carbon black (also given in Figure 5-4 a). This is understood to be capacitive behaviour. This could be a result of surface storage of Li ions onto rGO sheets which is likely a result of a formation of Li-C compound [31] or due to reaction with the oxygen-containing surface functional groups (i.e. carbonyl and carboxyl) [32,33]. This was confirmed by fabricating an 80/20 wt.% rGO/PVDF electrode, the voltammograms of which (given in Figure C-11 of Appendix C) showed lithium storage on rGO to occur below 1 V although current response is also observed at <1.5 V when higher scan rates are applied. This pseudocapacitive response is further confirmed in the differential capacity analysis (dQ/dV) of the first cycle (refer to Figure 5-4 b) for the rGO-containing electrodes when compared to the one prepared using carbon black. Therefore, the stored charge is the summation from Li^+ intercalation and near surface pseudocapacitance [34,35]. The kinetic parameters, to determine electrode kinetics, can be empirically extracted from CV results based on the following equation [11,34,36]:

$$i = av^b \qquad \text{Eq. 5-1}$$

Where i is the peak current (mA), v is the sweep rate (mV/s), and a/b are constants. The constants can be determined from the slopes and y-intercept of a $\log i$ vs. $\log v$ plot. For b=0.5 the system is said to be diffusion-controlled and indicative of faradaic intercalation process. Conversely, for b=1 the system is said to be dominated by pseudocapacitive behaviour via surface charge transfer. For the EPD, PVDF/10rGO, and PVDF/18rGO the calculated b values at the cathodic peaks are 0.74, 0.72, and 0.75 respectively which indicate the system is possibly derived from both lithium ion intercalation and pseudocapacitance. The $\log i$ vs. $\log v$ plots of the Nb^{5+}/Nb^{4+} cathodic peaks are given in Figure C-12 from Appendix C.

In addition to rGO contributing to this pseudocapacitive behaviour (discussed earlier) given that the value of b corresponding to the Nb^{5+}/Nb^{4+} couple also indicates pseudocapacitive behaviour from TNO, it is possible to have certain Li-ion charge stored near the surface of the ball-milled TNO particles. It is conceivable a thin near surface disordered (or amorphous) zone has formed as it has been observed in other high-energy milling studies [37] that accommodates storage via a faradaic type pseudocapacitance [35,38], although this layer is difficult to observe and distinguish from the carbon-coating. The pseudocapacitive contribution can be calculated by plotting $i/v^{0.5}$ vs. $v^{0.5}$ [11,34,36] as explained in section C.8 of Appendix C, however the relationship loses linearity depending on the state-of-charge of the material (Figure C-13 in Appendix C). Although this makes it difficult to accurately determine the exact pseudocapacitive contribution to the current response over the charge/discharge potential range, a qualitative description can be made that the capacitive storage of BM-TNO/rGO composite electrode becomes more important in the low-voltage range of ~1.5 – 0.6 V vs. Li/Li$^+$.

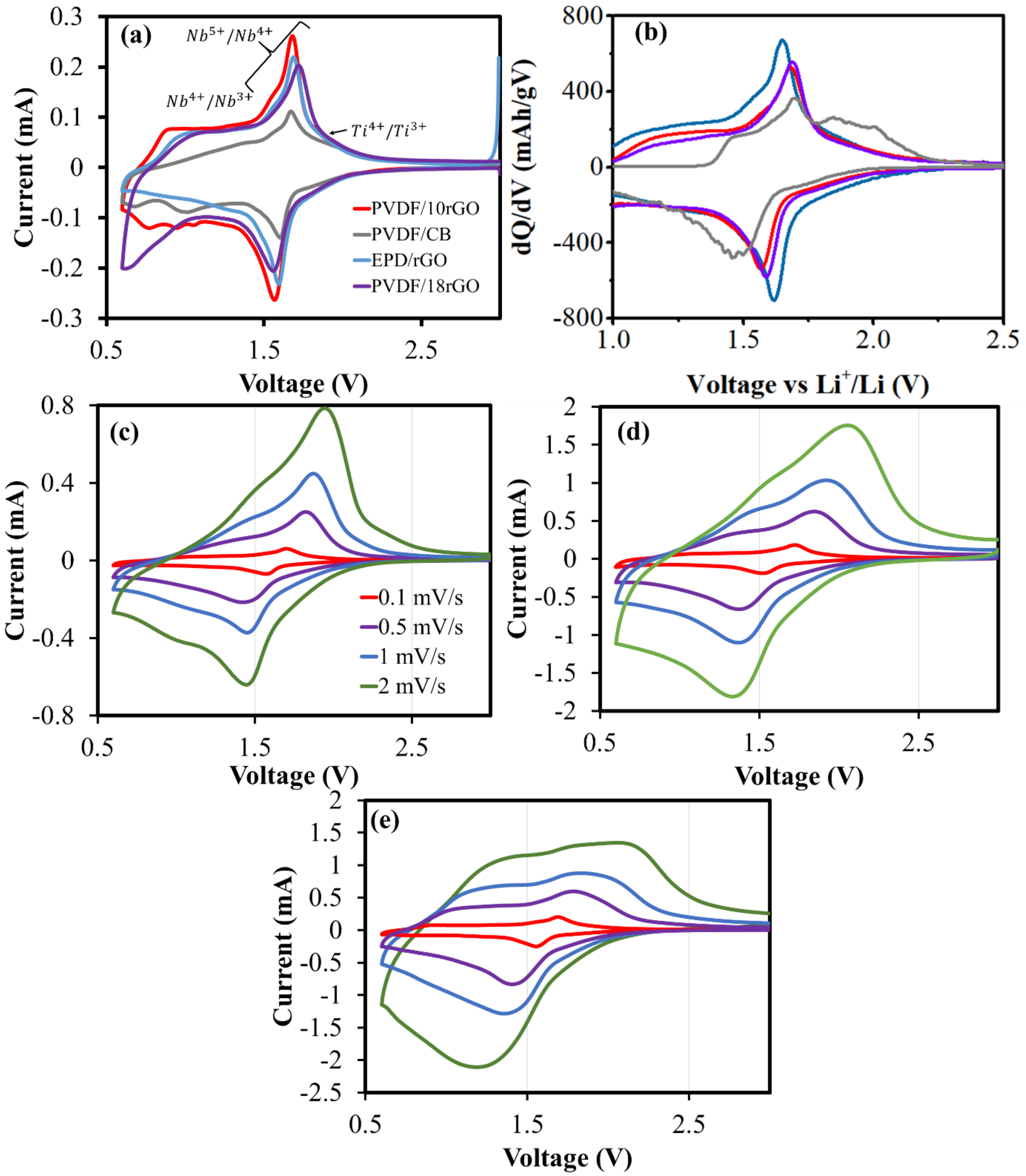

Figure 5-4: (a) CV for 0.1 mV/s showing PVDF electrodes carbon black (“PVDF/CB”), with 10% rGO (“PVDF/10rGO”), 18 wt.% rGO (“PVDF/18rGO”), and EPD electrode with 18 wt.% rGO (“EPD/rGO”). (b) Corresponding dQ/dV for first cycle at 0.5C of the aforementioned electrodes. CV at sweep rates from 0.1-2 mV/s for (c) EPD/rGO (18 wt.% rGO), (d) PVDF/18rGO, and (e) PVDF/10rGO electrodes. Note, all are ball-milled and carbon-coated.

5.4.3.2 Analysis of Cycling Behaviour

Cycling performance at 0.5C is given in Figure 5-5 (a). In general, the electrodes containing rGO all exhibit dramatic increase in capacity when compared the carbon black, which is given in Figure C-3 of Appendix C. It worth remarking that EPD electrodes show highest capacity enhancement among all rGO electrodes. The increase in capacity due to rGO, when compared to conventional carbon black, comes at least in part (other than better electrode conductivity) from its pseudocapacitive storage of Li^+ ions. The rapid initial performance decline (within the first 5 cycles) is attributed to TNO material structural damage (introduction of disorder in addition to size reduction) due to ball-milling. This is revealed by the broadening of the XRD peaks following ball milling (refer to Figure 5-3 c). Post-ball milling annealing only partially restored the crystallinity of TNO, thus it is plausible the observed capacity fade to relate to the induced disorder in the ball-milled electrode that needs to be further investigated. Nevertheless, the use of rGO in lieu of carbon black lowered the drop from 28% to 19%, and further down to 13% when EPD was used attributed to the superior electrode microstructure imparted by EPD as demonstrated earlier.

Voltage profiles with corresponding differential capacity analysis (dQ/dV) are provided in Figure 5-5 (b) and (c) for the EPD and PVDF electrodes at cycles 1, 20, 50, and 150. The differential capacity analysis can provide better information on electrochemical storage behavior, polarization, and capacity fading during cycling. The strongest peak observed belongs to the main Nb^{5+}/Nb^{4+} couple – commonly observed in TNO electrodes [39]. At cycle 1, the dQ/dV analysis reveals anodic/cathodic peaks at 1.65/1.62V; after 150 cycles the peaks are at 1.66/1.61V showing a subtle change in interpeak distance of $\Delta E = 30$ mV and 50 mV for cycles 1 and 150 respectively. Likewise, for the PVDF electrode with 10 wt.% rGO there are peaks at 1.68/1.57V ($\Delta E = 110\,mV$) and 1.71/1.56V ($\Delta E = 150\,mV$) for cycles 1 and 150, respectively. For the PVDF electrode containing 18 wt.% rGO the peaks are at 1.69/1.58 V ($\Delta E = 110\,mV$) and 1.79/1.48V ($\Delta E = 310\,mV$). These interpeak distances are tabulated in Table 5-1. The changing interpeak distance shows significant difference in polarizations between PVDF and EPD coatings. Thus EPD-built electrodes show the smallest polarization after 150 cycles that is 3-6x smaller than that of the PVDF-built electrodes, an observation that is in agreement with the CV data presented earlier. Furthermore, this voltage gap between charge/discharge suggests better electrode kinetics (less polarization) for the TNO material in the EPD electrode in relation to the PVDF electrode.

Table 5-1: Charge/Discharge gap determined from dQ/dV interpeak distances.

	ΔE (mV)	
	Cycle 1	**Cycle 150**
EPD	30	50
PVDF/10rGO	110	150
PVDF/18rGO	110	310

In differential capacity curves, the area under the peaks corresponds to the charge contributed by particular processes [40]. Proportional peak intensity reduction between both peaks is characteristic of loss of active material from irreversible structural changes or phase transformation – this is the dominant mechanism for capacity fade of EPD electrodes. Moreover, different capacity fade mechanisms of degradation of TNO and rGO can be distinguished from the differential capacity curves. In the dQ/dV plot corresponding to the EPD electrode, Figure 5-5 (b), the peak at ~1.65 V of Nb^{5+}/Nb^{4+}redox couple gradually fades, which contrasts to the relatively robust shoulder ranging from 1V to ~1.5V vs. Li^+/Li associated with rGO. Such discrepancy implies that the TNO degrades more quickly than rGO upon cycling in EPD electrode. However, when using the conventional PVDF casting process, both Li-ion intercalation of the accessible TNO and pseudocapacitive storage of rGO deteriorate rapidly upon cycling. Additionally, more rGO leads to faster capacity fade. It is worth mentioning that the TNO peak degradation in PVDF/10rGO electrode is faster than the rGO shoulder, indicating the different kinetics in material deterioration. Based on the microstructural characterization in Figure 5-3, gradual loss of the active materials (both TNO and rGO) can be directly attributed to the high interfacial impedance caused by poor contact. This is critical as the electrode's ability to maintain intimate contact among materials highly depends on initial homogeneity and distribution of constitutive components. For instance, the highly inhomogeneous PVDF/18rGO electrode shows drastic increase in polarization after 150 cycles, as the consequence of losing physical contact among materials.

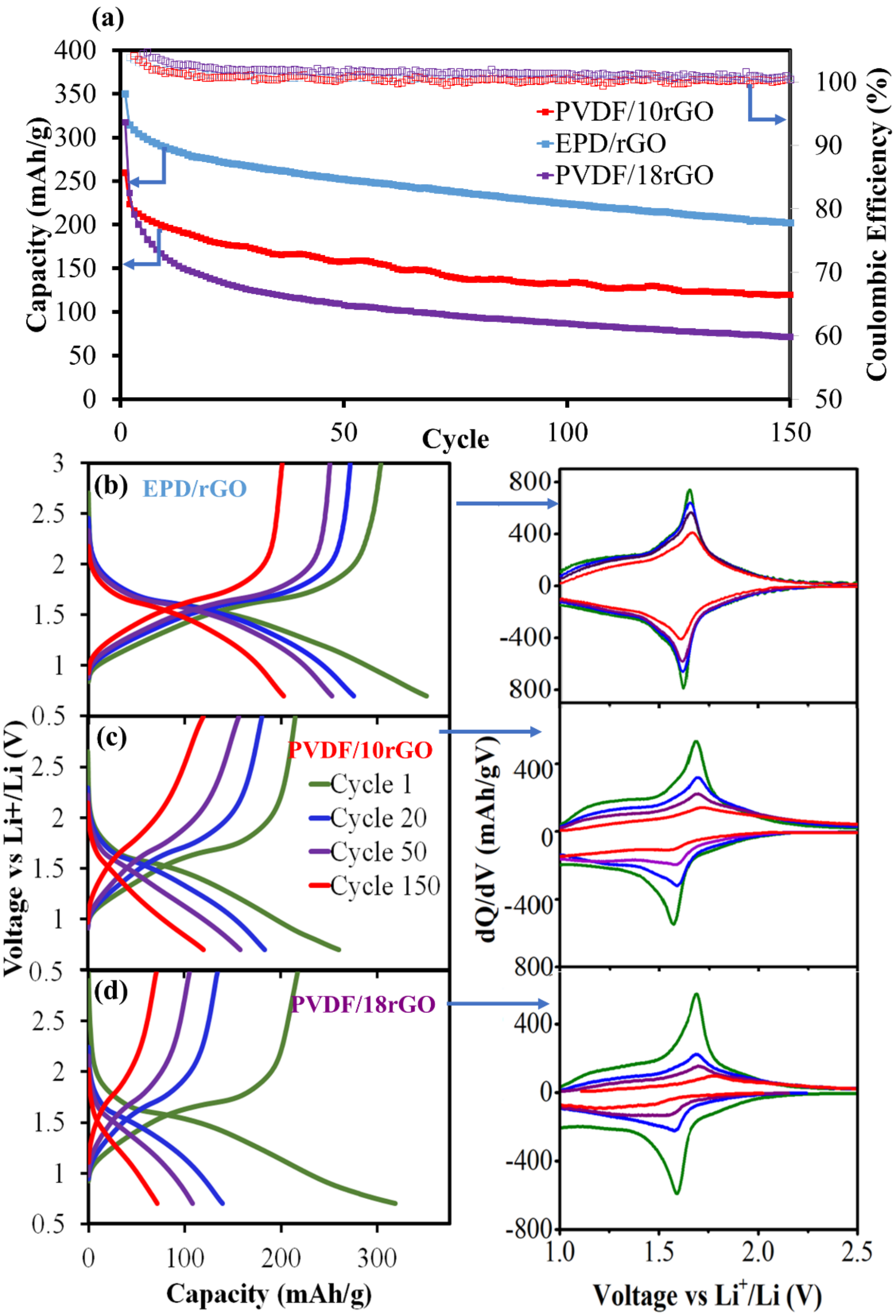

Figure 5-5: (a) 0.5C cycling capacity and coulombic efficiency for EPD/rGO and PVDF/rGO electrodes. Charge/Discharge curves for cycles 1, 20, 50, 150 with corresponding dQ/dV plots for (b), (c) PVDF/rGO electrodes and (d) EPD/rGO electrode.

5.4.3.3 EIS Analysis

Further electrochemical analysis was done by using EIS Nyquist plots for pristine and cycled electrodes, which are given in Figure 5-6. Note that the EIS plots are normalized with respect to the electrode thickness and area (0.785 cm^2). Two equivalent circuit models are used depending on the casting technique applied. For EPD electrode, a simple Randle circuit was used to represent the TNO-rGO nanocomposite structure, which consists of the charge-transfer resistance of the homogeneous TNO/rGO coatings ($R_{TNO/rGO}$), the capacitance between the electrolyte and the particles ($C_{TNO/rGO}$), and the Warburg element (W) due to Li-ion diffusion. Conversely, the non-homogeneous nature of the PVDF electrode system we found to be best described by two circuits in parallel – a TNO intercalation storage circuit (battery) and an additional rGO supercapacitor. Thus, the total impedance (Z) is the sum of impedance from the TNO battery (Z_{TNO}) and the rGO supercapacitor (Z_{rGO}):

$$Z = \frac{1}{\frac{1}{Z_{TNO}} + \frac{1}{Z_{rGO}}} \quad \text{Eq. 5-2}$$

Likewise, the supercapacitor circuit elements are resistance due to the rGO (R_{rGO}) and corresponding capacitance (C_{rGO}).

Among the three electrodes, the EPD electrode has the highest initial impedance. Highly conductive graphene channels enable PVDF electrodes to have lower apparent impedance. After cycling, the increase in impedance of EPD electrode is attributed to the consequence of gradual degradation of the TNO material (also observed in the differential capacity analysis), hence the impedance increases overall. The impedance increase of the EPD electrode due to rGO degradation is assumed to be smaller as the differential capacity analysis showed a slower loss of rGO material with respect to the TNO. Among the PVDF electrodes, the PVDF/18rGO has a higher initial impedance despite the high rGO content – this is attributed to the poor interparticle contact and poor adhesion with the Cu foil due to insufficient PVDF binder used as previously discussed. The EIS plots after cycling show the impedance, in contrast to the EPD electrodes, decreases in the PVDF electrodes. As observed in the dQ/dV of the latter, there is rapid loss of the TNO material. Thus, we believe that the capacity loss in PVDF electrodes is likely due to losing physical contact instead of just TNO degradation. In the meantime, the abnormal reduction in apparent impedance can be explained by the TNO material disordering causing a large increase in impedance in the TNO itself (i.e. $Z_{TNO} \to \infty; \frac{1}{Z_{TNO}} \to 0$) which means the total impedance response is solely due to the supercapacitor device (i.e. the more conductive rGO) that intrinsically exhibits lower impedance than the TNO microbatteries.

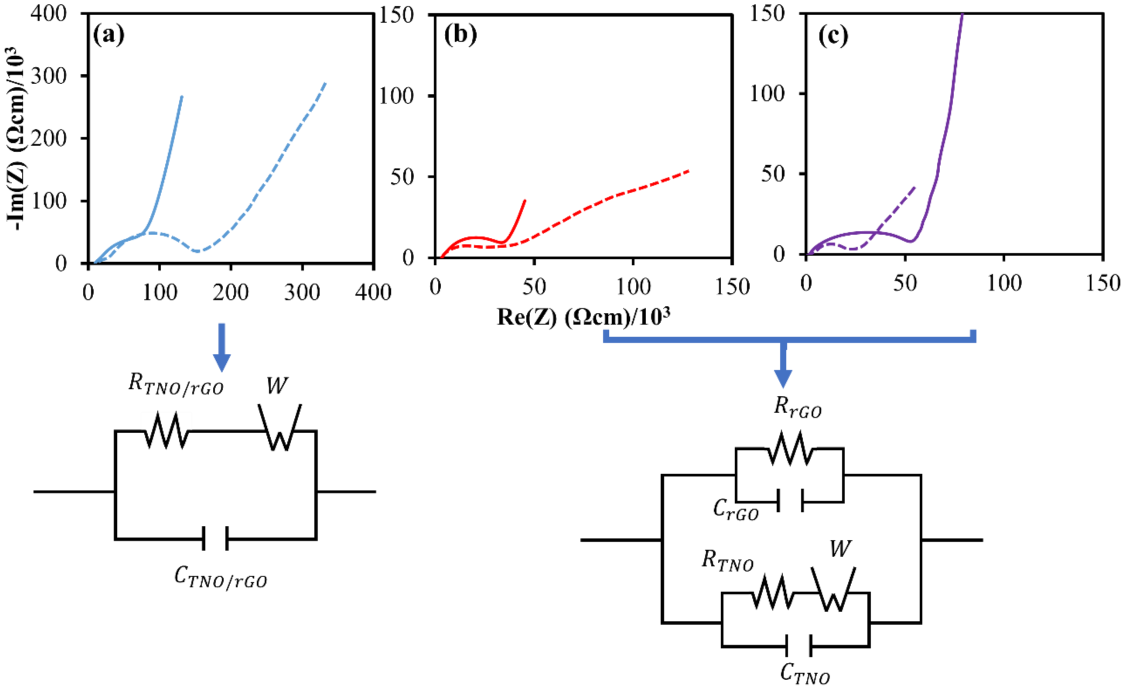

Figure 5-6: EIS for pristine (solid line) and cycled (dotted line) electrodes built with (a) EPD, (b) PVDF/10rGO, and (c) PVDF/18rGO and corresponding equivalent circuits. Please note this EIS model disregards the solid/solution interphase resistance and possible formation of SEI. Additionally, the plots are normalized by dividing by their respective thickness and multiplying by the electrode geometric area 0.785 cm^2.

5.5. Conclusion

This study demonstrates the power of electrophoretic deposition in building TNO/rGO composite electrodes with nanoscale homogeneous microstructure outperforming electrodes built with the same components using the PVDF casting process. The EPD system used involved the co-deposition of ball-milled and carbon-coated TNO sub-micron size particles with graphene oxide followed by a high temperature reducing stage that led to the formation of reduced graphene oxide. EPD enabled the intimate mixture between TNO and rGO components which allowed rGO to act simultaneously as an efficient flexible binder capable of anchoring TNO particles as well as conductive component. The EPD-built TNO/rGO electrode appears to maintain good mechanical integrity without requiring the use of an electrochemically inactive binder –a very useful property for a material that experiences ~8% volume change during lithiation. Moreover, the rGO was found to contribute to extra capacity via pseudocapacitive storage of Li ions. The superior percolation network established through the nanoscale assembling power of EPD led to lower polarization enabling higher capacity level vis-a-vis conventionally built PVDF-based TNO/rGO electrodes. Similarly, the capacity fade was lower with the EPD electrodes but still significant. This is attributed to the introduction of disordering into TNO as result of high-energy ball milling and high temperature annealing needed to induce $GO \rightarrow rGO$ meaning that further optimization of the system can be brought via employment of TNO nanocrystals synthesized via solution synthesis routes. The heterogenous nature of both types of PVDF electrodes led to the formation of TNO microbatteries in parallel with a rGO micro-supercapacitors. Cycling led to the rapid increase in impedance of the TNO microbatteries and hence losing accessible active materials for Li-ion storage. As a result, even though the performance fades severely in the PVDF electrodes, their impedance decreased as the rGO contributions from micro-supercapacitors become dominant. This result enriches the knowledge on diagnosing batteries and sheds light on tailoring the nanostructure to establish a robust percolation network.

5.6. Acknowledgements

This work is supported by a NSERC/Hydro-Quebec CRD grant, additional support is provided by the McGill Engineering Doctoral Award (MEDA) and McGill Sustainability Systems Initiative (MSSI) programs. The authors thank Stéphanie Bessette for SEM and EDS images, David Liu for TEM images, and Dr. Marta Cerruti for use of the Bruker SENTERRA confocal Raman microscope.

5.7. References

[1] B. Zhao, R. Ran, M. Liu, Z. Shao, A comprehensive review of Li4Ti5O12-based electrodes for lithium-ion batteries: The latest advancements and future perspectives, Mater. Sci. Eng. R Rep. 98 (2015) 1–71. https://doi.org/10.1016/j.mser.2015.10.001.

[2] S. Chauque, F.Y. Oliva, A. Visintin, D. Barraco, E.P.M. Leiva, O.R. Cámara, Lithium titanate as anode material for lithium ion batteries: Synthesis, post-treatment and its electrochemical

response, J. Electroanal. Chem. 799 (2017) 142–155. https://doi.org/10.1016/j.jelechem.2017.05.052.

[3] J.-T. Han, Y.-H. Huang, J.B. Goodenough, New Anode Framework for Rechargeable Lithium Batteries, Chem. Mater. 23 (2011) 2027–2029. https://doi.org/dx.doi.org/10.1021/cm200441h.

[4] S. Lou, Y. Ma, X. Cheng, J. Gao, Y. Gao, P. Zuo, C. Du, G. Yin, Facile synthesis of nanostructured TiNb2O7 anode materials with superior performance for high-rate lithium ion batteries, Chem. Commun. 51 (2015) 17293–17296. https://doi.org/10.1039/C5CC07052J.

[5] K. Tang, X. Mu, P.A. van Aken, Y. Yu, J. Maier, "Nano-Pearl-String" TiNb2O7 as Anodes for Rechargeable Lithium Batteries, Adv. Energy Mater. 3 (2013) 49–53. https://doi.org/10.1002/aenm.201200396.

[6] X. Lu, Z. Jian, Z. Fang, L. Gu, Y.-S. Hu, W. Chen, Z. Wang, L. Chen, Atomic-scale investigation on lithium storage mechanism in TiNb 2 O 7 , Energy Environ. Sci. 4 (2011) 2638–2644. https://doi.org/10.1039/C0EE00808G.

[7] B. Guo, X. Yu, X.-G. Sun, M. Chi, Z.-A. Qiao, J. Liu, Y.-S. Hu, X.-Q. Yang, J. B. Goodenough, S. Dai, A long-life lithium-ion battery with a highly porous TiNb 2 O 7 anode for large-scale electrical energy storage, Energy Environ. Sci. 7 (2014) 2220–2226. https://doi.org/10.1039/C4EE00508B.

[8] S. Schweidler, L. de Biasi, A. Schiele, P. Hartmann, T. Brezesinski, J. Janek, Volume Changes of Graphite Anodes Revisited: A Combined Operando X-ray Diffraction and In Situ Pressure Analysis Study, J. Phys. Chem. C. 122 (2018) 8829–8835. https://doi.org/10.1021/acs.jpcc.8b01873.

[9] L. Buannic, J.-F. Colin, M. Chapuis, M. Chakir, S. Patoux, Electrochemical performances and gassing behavior of high surface area titanium niobium oxides, J. Mater. Chem. A. 4 (2016) 11531–11541. https://doi.org/10.1039/C6TA03813A.

[10] K. Ise, S. Morimoto, Y. Harada, N. Takami, Large lithium storage in highly crystalline TiNb2O7 nanoparticles synthesized by a hydrothermal method as anodes for lithium-ion batteries, Solid State Ion. 320 (2018) 7–15. https://doi.org/10.1016/j.ssi.2018.02.027.

[11] S. Li, J. Chen, X. Gong, J. Wang, P.S. Lee, Holey graphene-wrapped porous TiNb 24 O 62 microparticles as high-performance intercalation pseudocapacitive anode materials for

lithium-ion capacitors, NPG Asia Mater. 10 (2018) 406–416. https://doi.org/10.1038/s41427-018-0042-5.

[12] M. Liu, H. Dong, S. Zhang, X. Chen, Y. Sun, S. Gao, J. Xu, X. Wu, A. Yuan, W. Lu, Three-Dimensional Porous TiNb2O7/CNT-KB Composite Microspheres as Lithium-Ion Battery Anode Material, ChemElectroChem. 6 (2019) 3959–3965. https://doi.org/10.1002/celc.201901024.

[13] X. Zhang, Y. Zhu, A.M. Bruck, L.M. Housel, L. Wang, C.D. Quilty, K.J. Takeuchi, E.S. Takeuchi, A.C. Marschilok, G. Yu, Understanding aggregation hindered Li-ion transport in transition metal oxide at mesoscale, Energy Storage Mater. 19 (2019) 439–445. https://doi.org/10.1016/j.ensm.2019.03.017.

[14] K. Chen, Q. Wang, Z. Niu, J. Chen, Graphene-based materials for flexible energy storage devices, J. Energy Chem. 27 (2018) 12–24. https://doi.org/10.1016/j.jechem.2017.08.015.

[15] Y. Shi, L. Wen, S. Pei, M. Wu, F. Li, Choice for graphene as conductive additive for cathode of lithium-ion batteries, J. Energy Chem. 30 (2019) 19–26. https://doi.org/10.1016/j.jechem.2018.03.009.

[16] D.T.L. Galhena, B.C. Bayer, J.C. Meyer, S. Hofmann, G.A.J. Amaratunga, Reduced Graphene Oxide as a Monolithic Multifunctional Conductive Binder for Activated Carbon Supercapacitors, ACS Omega. 3 (2018) 9246–9255. https://doi.org/10.1021/acsomega.8b01075.

[17] L. Ye, K. Wen, Z. Zhang, F. Yang, Y. Liang, W. Lv, Y. Lin, J. Gu, J.H. Dickerson, W. He, Highly Efficient Materials Assembly Via Electrophoretic Deposition for Electrochemical Energy Conversion and Storage Devices, Adv. Energy Mater. 6 (2016). https://doi.org/10.1002/aenm.201502018.

[18] Y. Ma, J. Han, M. Wang, X. Chen, S. Jia, Electrophoretic deposition of graphene-based materials: A review of materials and their applications, J. Materiomics. 4 (2018) 108–120. https://doi.org/10.1016/j.jmat.2018.02.004.

[19] M. Diba, D.W.H. Fam, A.R. Boccaccini, M.S.P. Shaffer, Electrophoretic deposition of graphene-related materials: A review of the fundamentals, Prog. Mater. Sci. 82 (2016) 83–117. https://doi.org/10.1016/j.pmatsci.2016.03.002.

[20] A. Yasin, F. Guo, G.P. Demopoulos, Continuous-reactor, pH-controlled synthesis of multifunctional mesoporous nanocrystalline anatase aggregates, Chem. Eng. J. 287 (2016) 398–409. https://doi.org/10.1016/j.cej.2015.11.045.

[21] R. Inada, R. Kumasaka, S. Inabe, T. Tojo, Y. Sakurai, Li+ Insertion/Extraction Properties for TiNb2O7 Single Particle Characterized by a Particle-Current Collector Integrated Microelectrode, J. Electrochem. Soc. 166 (2019) A5157–A5162. https://doi.org/10.1149/2.0241903jes.

[22] Y. Wang, H. Li, P. He, E. Hosono, H. Zhou, Nano active materials for lithium-ion batteries, Nanoscale. 2 (2010) 1294–1305. https://doi.org/10.1039/C0NR00068J.

[23] A.G. Kashkooli, G. Lui, S. Farhad, D.U. Lee, K. Feng, A. Yu, Z. Chen, Nano-particle size effect on the performance of Li4Ti5O12 spinel, Electrochimica Acta. 196 (2016) 33–40. https://doi.org/10.1016/j.electacta.2016.02.153.

[24] B.B. He, Miscellaneous Applications, in: Two-Dimens. X-Ray Diffr., 2nd ed., John Wiley & Sons, Ltd, 2018: pp. 395–432. https://doi.org/10.1002/9781119356080.ch12.

[25] R. Inada, T. Mori, R. Kumasaka, R. Ito, T. Tojo, Y. Sakurai, Characterization of vacuum-annealed TiNb2O7 as high potential anode material for lithium-ion battery, Int. J. Appl. Ceram. Technol. 16 (2019) 264–272. https://doi.org/10.1111/ijac.13058.

[26] L. Bokobza, J.-L. Bruneel, M. Couzi, Raman Spectra of Carbon-Based Materials (from Graphite to Carbon Black) and of Some Silicone Composites, C. 1 (2015) 77–94. https://doi.org/10.3390/c1010077.

[27] V.V. Neklyudov, N.R. Khafizov, I.A. Sedov, A.M. Dimiev, New insights into the solubility of graphene oxide in water and alcohols, Phys. Chem. Chem. Phys. 19 (2017) 17000–17008. https://doi.org/10.1039/C7CP02303K.

[28] D.V. Pelegov, A.A. Koshkina, V.I. Pryakhina, V.S. Gorshkov, Efficiency Threshold of Carbon Layer Growth in Li4Ti5O12/C Composites, J. Electrochem. Soc. 166 (2019) A5019–A5024. https://doi.org/10.1149/2.0031903jes.

[29] P. Van der Heide, 5. Spectral Interpretation, in: X-Ray Photoelectron Spectrosc. Introd. Princ. Pract., 2011: pp. 101–140.

[30] H. Yamada, M. Hibino, T. Kudo, Lithium insertion to ReO3-type metastable phase in the Nb2O5–WO3 system, Solid State Ion. 140 (2001) 249–255. https://doi.org/10.1016/S0167-2738(01)00822-0.

[31] X. Cai, L. Lai, Z. Shen, J. Lin, Graphene and graphene-based composites as Li-ion battery electrode materials and their application in full cells, J. Mater. Chem. A. 5 (2017) 15423–15446. https://doi.org/10.1039/C7TA04354F.

[32] Z. Xie, Z. Yu, W. Fan, G. Peng, M. Qu, Effects of functional groups of graphene oxide on the electrochemical performance of lithium-ion batteries, RSC Adv. 5 (2015) 90041–90048. https://doi.org/10.1039/C5RA17854A.

[33] L. Ma, S.-S. Lyu, Y. Dai, X.-Y. Pei, D.-C. Mo, Y.-X. Fu, Lithium storage properties of NiO/reduced graphene oxide composites derived from different oxidation degrees of graphite oxide, J. Alloys Compd. 810 (2019) 151954. https://doi.org/10.1016/j.jallcom.2019.151954.

[34] J. Wang, J. Polleux, J. Lim, B. Dunn, Pseudocapacitive Contributions to Electrochemical Energy Storage in TiO2 (Anatase) Nanoparticles, J. Phys. Chem. C. 111 (2007) 14925–14931. https://doi.org/10.1021/jp074464w.

[35] M.J. Sussman, A. Yasin, G.P. Demopoulos, On the complex interplay of crystallinity and surface area effects on Li-ion intercalation and pseudocapacitive storage properties of nanocrystalline anatase, J. Power Sources. 272 (2014) 58–67. https://doi.org/10.1016/j.jpowsour.2014.08.050.

[36] S. Lou, X. Cheng, Y. Zhao, A. Lushington, J. Gao, Q. Li, P. Zuo, B. Wang, Y. Gao, Y. Ma, C. Du, G. Yin, X. Sun, Superior performance of ordered macroporous TiNb2O7 anodes for lithium ion batteries: Understanding from the structural and pseudocapacitive insights on achieving high rate capability, Nano Energy. 34 (2017) 15–25. https://doi.org/10.1016/j.nanoen.2017.01.058.

[37] V. Šepelák, S. Bégin-Colin, G.L. Caër, Transformations in oxides induced by high-energy ball-milling, Dalton Trans. 41 (2012) 11927–11948. https://doi.org/10.1039/C2DT30349C.

[38] Y. Jiang, C. Hall, N. Song, D. Lau, P.A. Burr, R. Patterson, D.-W. Wang, Z. Ouyang, A. Lennon, Evidence for Fast Lithium-Ion Diffusion and Charge-Transfer Reactions in Amorphous TiOx Nanotubes: Insights for High-Rate Electrochemical Energy Storage, ACS Appl. Mater. Interfaces. 10 (2018) 42513–42523. https://doi.org/10.1021/acsami.8b16994.

[39] C. Jo, Y. Kim, J. Hwang, J. Shim, J. Chun, J. Lee, Block Copolymer Directed Ordered Mesostructured TiNb2O7 Multimetallic Oxide Constructed of Nanocrystals as High Power Li-Ion Battery Anodes, Chem. Mater. 26 (2014) 3508–3514. https://doi.org/10.1021/cm501011d.

[40] E. Talaie, P. Bonnick, X. Sun, Q. Pang, X. Liang, L. Nazar, Methods and Protocols for Electrochemical Energy Storage Materials Research, Chem. Mater. (2017) 90–105. https://doi.org/10.1021/acs.chemmater.6b02726.

6 Synopsis

In this final chapter the *Global Conclusions* of this work with reference to the thesis objectives detailed in Chapter 1 are outlined. This is followed by the *Claims to Originality* that stemmed from this work. Finally, suggestions for *Future Work* are given.

6.1 Global Conclusions

With respect to the objectives stated in Chapter 1: through this work, engineered systems using the coating technique electrophoretic deposition (EPD) were successfully developed to fabricate composite electrodes for Li-ion battery (LIB) application. Three electrode composites were studied, namely lithium titanate ($Li_4Ti_5O_{12}$, LTO)/carbon black, LTO/rGO, and titanium niobite ($TiNb_2O_7$, TNO)/rGO as LIB anodes. The corresponding effect of using EPD on the homogeneity of these composites was investigated followed by the effect of a robust percolation network on the internal polarization, cycling performance, and – particularly in the last two chapters – capacity fade.

First, we demonstrated EPD fabrication of commercially sourced nano-LTO, carbon black, and SBR binder as LIB anode through design of an EPD system that proved superior in terms of performance and sustainability potential to the conventional PVDF/NMP coating method. Enhanced colloid stability was achieved via employment of a mixed 90/10 vol.% acetonitrile/water solvent with optimum dielectric constant and the use of water-soluble styrene- butadiene rubber (SBR) as binder. It is proposed that the bridging action of SBR favours the formation of C-coated LTO/carbon nanoparticle hetero-aggregates that enable fast growth of adherent electrodes on metal substrate. Improved homogeneity came hand-in-hand with better battery performance, particularly at high rates. A study on deposition rates also showed the thickness and coating density could be controlled based on deposition time and electric field magnitude. This deposition system enabled relatively thick (in comparison to previous EPD studies) $+20\mu m$ coatings. Thus, this study demonstrated the viability of electrophoretically coating thick composite coatings for LIB applications.

The second study focused on achieving aggregation-free LTO nanocomposite electrode fabrication via binderless EPD using reduced graphene that acts both as binder and as superior conductive component vs. carbon black. An important element of this study is that not only the conductive material (reduced GO) but also the active material (LTO) are in the form of 2D nanosheets that inherently impose greater challenges in obtaining homogeneous deposits. As graphene is difficult to suspend, the precursor graphene oxide is suspended along the LTO precursor lithium titanate hydrate (LTH, $(Li_{2-x}H_x)Ti_2O_5 \cdot yH_2O$) and co-deposited together. The resulting coating is then annealed in the presence of hydrogen at high temperature to induce topotactic 2D-LTH and GO transformation to 2D-LTO and rGO respectively. This resulted in nanolayered homogeneous LTO and rGO nanocomposite electrode structure with superior percolation network. The EPD process led to higher active material utilization when compared to the PVDF-casted electrode which contained large mesoscale aggregates resulting in inaccessible LTO (at the core of the aggregates) and overdischarged LTO (on the surface of the aggregates). Overall the newly EPD-assembled nanocomposite anodes via EIS and dQ/dV analysis determined to have reduced polarization, improved the cell discharge performance, and reduced rate of material degradation when compared to conventional built electrodes.

The final part of this work seeks to expand the benefits of EPD-based building a robust graphene percolation network in a LIB electrode structure by focusing on a higher capacity (double of that of LTO) anode material, TNO. Once more binderless electrode fabrication is accomplished through co-deposition of ball-milled TNO particles and graphene oxide (GO) followed by high-temperature annealing at reductive atmosphere. TNO experiences volume changes during (de)lithiation which result in cracking and isolation of the active material (i.e. the breakdown of the conductive network). The resulting homogeneous distribution enabled through EPD allowed for reduced GO (rGO) to act as both conductive and binding agent. Furthermore, the pseudocapacitive capabilities of rGO led to better lithium storage. This translated into higher capacities achieved and lower rate of material degradation observed through dQ/dV. This was a result of the nanoscale assembling power of EPD combined with the binding capabilities of the rGO that led to a robust percolation network.

Overall, through these integrated electrode construction and electrochemical performance analysis studies, EPD is shown to be a superior coating technology with great application potential in manufacturing advanced LIB electrodes.

6.2 Claims to Originality

- Developed a novel EPD system enabling highly homogeneous deposition of nano LTO, carbon black, and styrene butadiene rubber (SBR). Furthermore, the deposits were +20 μm which is higher than previously accomplished for electrophoretically deposited LTO [1,2]. This also provided an opportunity to explore the homogeneity of SBR through PEEM-XANES which differentiated SBR from the other carbon sources (carbon black) which allowed us to propose SBR as a bridge that forms hetero-aggregates in suspension enabling intimate assembly during deposition.
- Designed an EPD fabrication system allowing the production of robust, nanolayered, and binderless 2D LTO/rGO anodes through the co-deposition of lithium titanate hydrate and graphene oxide nanosheets followed by relithiation and topotactic transformation during reductive annealing. This was the first time lithium titanate hydrate was assembled electrophoretically as a film and converted in situ to LTO while preserving its 2D nanosheet morphology. Through detailed structural and electrochemical characterization, the EPD-built electrodes were shown to have a percolation network that is simultaneously good for both ionic and electronic conduction that contrasts with the PVDF-built electrodes suffering from localized poor material utilization and overdischarge spots.
- Extended the benefits of electrophoretically assembling TNO and reduced graphene oxide electrodes. This was the first time TNO was deposited electrophoretically. Through this work the effect of percolation network, enabled through EPD, on controlling the fade mechanism of the TNO/rGO composite electrode was analyzed for the first time.

6.3 Future Work

From Chapter 4, the conductive network constructed via EPD was found to mitigate the overdischarge of LTO. A similar effect on the TNO composites will be explored through scanning transmission X-ray microscopy (STXM) available at Canadian Light Source (CLS). This would allow the mapping of the particles to visualize the state of charge (of TNO and graphene) based on valence differences. Comparing pristine and cycled electrodes would support whether TNO or graphene contributes more to capacity fade.

During the work outlined in Chapters 4 and 5, Cu deposits were found within the coating when anodic deposition happened. No direct indication of performance loss or contribution could be attributed to their presence meaning they became part of the inactive material present in the deposit. This needlessly increases the volume/mass which lowers the energy density calculated. Further research on encouraging cathodic deposition (as opposed to anodic deposition in this work) to prevent Cu formation in deposits on LTH/GO and TNO/GO should be pursued. These results also highlighted the need to improve the coating adhesion onto the substrate. This could be accomplished through surface modification of the substrate or addition of a binder. In Chapter 3, SBR binder was used, however this material is nonconductive and electrochemically inactive. Thus, conductive binders such as sodium poly(9,9-bis(3-propanoate)fluorine) (PF-COONa) [3], and polyvinyl pyrrolidone/polyaniline (PVP/PANI) [4], poly(3,4-ethylenedioxythiophene) (PEDOT) [5] have been suggested as anodic binders in LIBs thereby combining the function of conductive and binder material. During EPD, the conductive binder in the deposit would also minimize the voltage drop in suspension and encourage the formation of thicker deposits.

The efficient self-assembly capabilities of EPD can be utilized to fabricating electrodes for solid-state batteries consisting of active material, conductive material, and ionic conductor (such as $Li_7La_3Zr_2O_{12}$). This combination has been determined to increase ionic transportation within the electrode [6,7] provided there is sufficient contact area between active and conductive components. EPD could potentially be a low-cost alternative to establishing a homogeneous mixture which can be followed by pressing stages to improve interparticle contact.

6.4 References

[1] N.A. Kyeremateng, T.M. Dinh, D. Pech, Electrophoretic deposition of Li4Ti5O12 nanoparticles with a novel additive for Li-ion microbatteries, RSC Adv. 5 (2015) 61502–61507. https://doi.org/10.1039/C5RA11039D.

[2] C.C. Lalau, C.T.J. Low, Electrophoretic Deposition for Lithium-Ion Battery Electrode Manufacture, Batter. Supercaps. 2 (2019) 551–559. https://doi.org/10.1002/batt.201900017.

[3] Y. Zhao, L. Yang, D. Liu, J. Hu, L. Han, Z. Wang, F. Pan, A Conductive Binder for High-Performance Sn Electrodes in Lithium-Ion Batteries, ACS Appl. Mater. Interfaces. 10 (2018) 1672–1677. https://doi.org/10.1021/acsami.7b13692.

[4] M. Zheng, C. Wang, Y. Xu, K. Li, D. Liu, A water-soluble binary conductive binder for Si anode lithium ion battery, Electrochim. Acta. 305 (2019) 555–562. https://doi.org/10.1016/j.electacta.2019.02.080.

[5] S.-J. Park, H. Zhao, G. Ai, C. Wang, X. Song, N. Yuca, V.S. Battaglia, W. Yang, G. Liu, Side-Chain Conducting and Phase-Separated Polymeric Binders for High-Performance Silicon Anodes in Lithium-Ion Batteries, J. Am. Chem. Soc. 137 (2015) 2565–2571. https://doi.org/10.1021/ja511181p.

[6] H. Shen, E. Yi, M. Amores, L. Cheng, N. Tamura, D.Y. Parkinson, G. Chen, K. Chen, M. Doeff, Oriented porous LLZO 3D structures obtained by freeze casting for battery applications, J. Mater. Chem. A. 7 (2019) 20861–20870. https://doi.org/10.1039/C9TA06520B.

[7] C. Park, S. Lee, K. Kim, M. Kim, S. Choi, D. Shin, Electrochemical Properties of Composite Cathode Using Bimodal Sized Electrolyte for All-Solid-State Batteries, J. Electrochem. Soc. 166 (2019) A5318–A5322. https://doi.org/10.1149/2.0481903jes.

7 Appendix

A. **Supporting information[1]** for Chapter 3: Highly conductive NMP-free carbon-coated nano-lithium titanate/carbon composite electrodes via SBR-assisted electrophoretic deposition

This supporting information section contains more information regarding the selection process for EPD suspension and parameters, EDS and SEM characterization of the C-LTO, TGA curves to determine the carbon content in C-LTO and EPD coatings, Raman characterization information for the pristine and C-LTO, a possible schematic for the fabricated aggregates, PEEM O K-edge image and XANES spectra for the pure SBR binder, and EIS measurements comparing the effect on pressing on the electrodes.

---

[1] Supporting Information associated with paper published in *Electrochimica Acta* 299 (2019) 107-115.

A.1 Suspension Selection and EPD Parameters

The suspension selection was done through trial and error. The tested media were pure ethanol, ethylene glycol, isopropanol, methanol, dimethylformamide, acetylacetone, and toluene. The organic media that were miscible with water were tested at varying water content between 5, 10, 15, 20, and 25 vol%. This was performed in 15 mL centrifuge tubes with 3g/L solid content. The suspensions were sonicated for 15 mins and allowed to sit for 1 hour.

If significant sedimentation occurred, then charging agents would be added. The charging agents tested were $MgCl_2$, $AlCl_3$, HCl, NaOH, acetic acid, ethylene glycol, and Triton X100. Again, the suspensions were sonicated for 15 mins and allowed to sit for 1 hour. Ball milling the solids to have smaller particles to suspend was also attempted however this only increased aggregation.

Of the organic solvents ethanol, isopropanol, acetylacetone, and acetone formed stable suspensions with carbon but LTO quickly sedimented – the most relatively stable combination was 50% acetylacetone/acetone. Ethylene glycol, dimethylformamide, and toluene did not suspend carbon or LTO. Of the aforementioned charging agents acetic acid (1 mL in 60 mL suspension) was the only one to lower the LTO rate of sedimentation in the 50% acetylacetone/acetone suspension but no deposition was seen when 10-60V were applied. A suspension composed of ethanol and charging agents $MgCl_2$, $AlCl_3$ and HCl also showed stability for both LTO and carbon but deposition rate was slow.

Water with triton X100 was stable as the water was polar enough to suspend the LTO and Triton stabilized the carbon. However, during EPD bubbles formed when the voltage applied was higher than 5V which prevented the formation of a coating. A lower voltage did not form a coating.

The next solvent to form a stable suspension for both LTO and carbon was acetonitrile. Though sedimentation of the LTO was observed (a white deposit at the bottom while the carbon seemingly remained in suspension) after 4 hours. Applying a voltage of 80V for 30s allowed for a thin coating to form with a current of 0.8 mA. Adding 10% water increased the current to 12.5 mA (same electrode area) and improved the appearance of the first layer. Adding more water increased the current however bubbles were visually observed after 25 vol%. The suspension consisting of 90/10 vol.% acetonitrile/water was selected as it was stable and formed an even, and seemingly thick, coating once the EPD parameters were optimized. The efficiency of acetonitrile stemmed from the fact that it has a dielectric constant of 36.64 at 25ºC. This is lower than water's (78.54) but higher

[1] Supporting Information associated with paper published in *Electrochimica Acta* 299 (2019) 107-115.

than that of regular organic solvents (24.6 and 18.3 for ethanol and isopropanol respectively). This medium-polarity solvent system allowed for the suspension of both polar LTO and non-polar carbon.

The 90/10 vol% acetonitrile/water medium had a natural pH of around 7.4. The pH of individual cLTO, carbon black (CB), and SBR in the pristine medium was measured to be 9, 8, and 8.7 respectively. When cLTO and carbon black were both added to the medium the pH was 9 and it stayed the same when SBR was added to this mix. This showed the cLTO has the biggest impact on suspension pH. Addition of SBR did show to enhance suspension stability as the dispersion was visually observed to improve and onset of sedimentation to be delayed. It is important to note that co-deposition of cLTO and CB occurs on the positive electrode (and zeta potential was measured to be negative). It is proposed the water is dissociating at the LTO surface which leads to the pH increase. This would then mean hydroxyl ions are responsible for the surface charge.

Finally, to improve the stability of the suspension and promote coating interparticle adhesion (and ultimately the film thickness) styrene-butadiene rubber (SBR) was added. SBR was selected as it is a tested anode binder in water-based pastes[1], hence been compatible with the water-containing acetonitrile solvent as opposed the non-aqueous PVDF binder.

During EPD as the coating thickness increased the current dropped. Thus, a constant-current experiment was attempted. It was determined that by maintaining a current density ~ 3.5 mA/cm^2 a uniform coating could be made. To control coating growth and crack formation the stages were limited to 15 seconds followed by 5 mins of air drying. The final number of stages was selected based on the desired thickness.

---

[1] Supporting Information associated with paper published in *Electrochimica Acta* 299 (2019) 107-115.

A.2 Powder Characterization: SEM and EDS

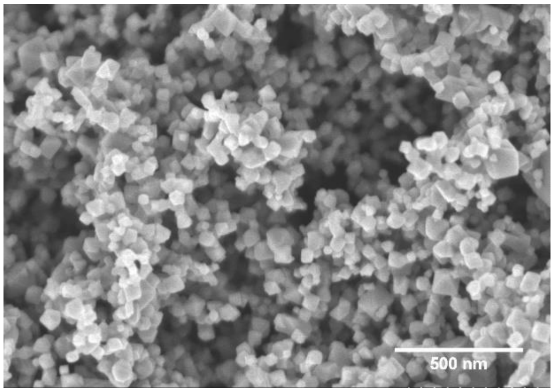

Figure A-1: SEM 2.0kV, 2.6mm, x60k of pristine LTO.

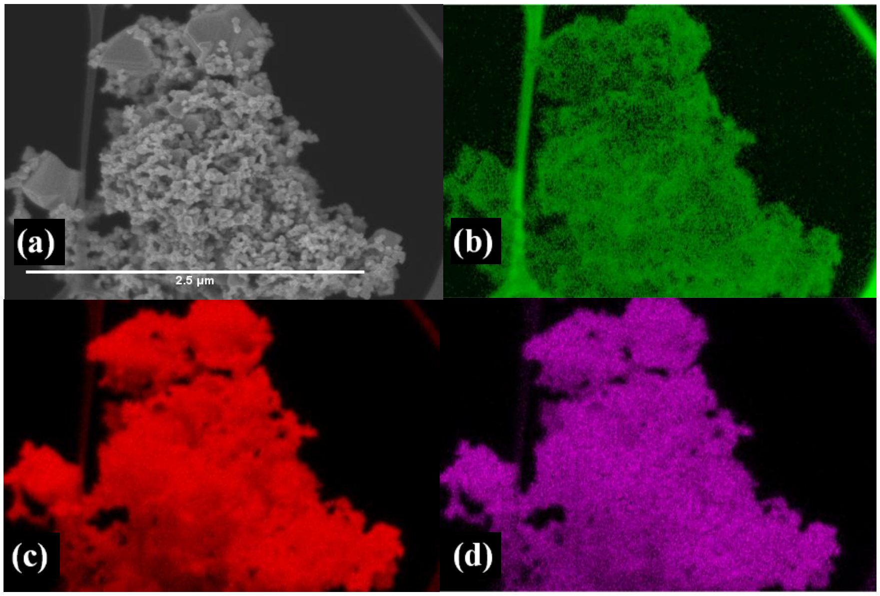

Figure A-2: SEM image of carbon-coated LTO (C-LTO) powder with corresponding EDS maps of (b) C, (c) O, and (d) Ti.

[1] Supporting Information associated with paper published in *Electrochimica Acta* 299 (2019) 107-115.

A.3 TGA Curves

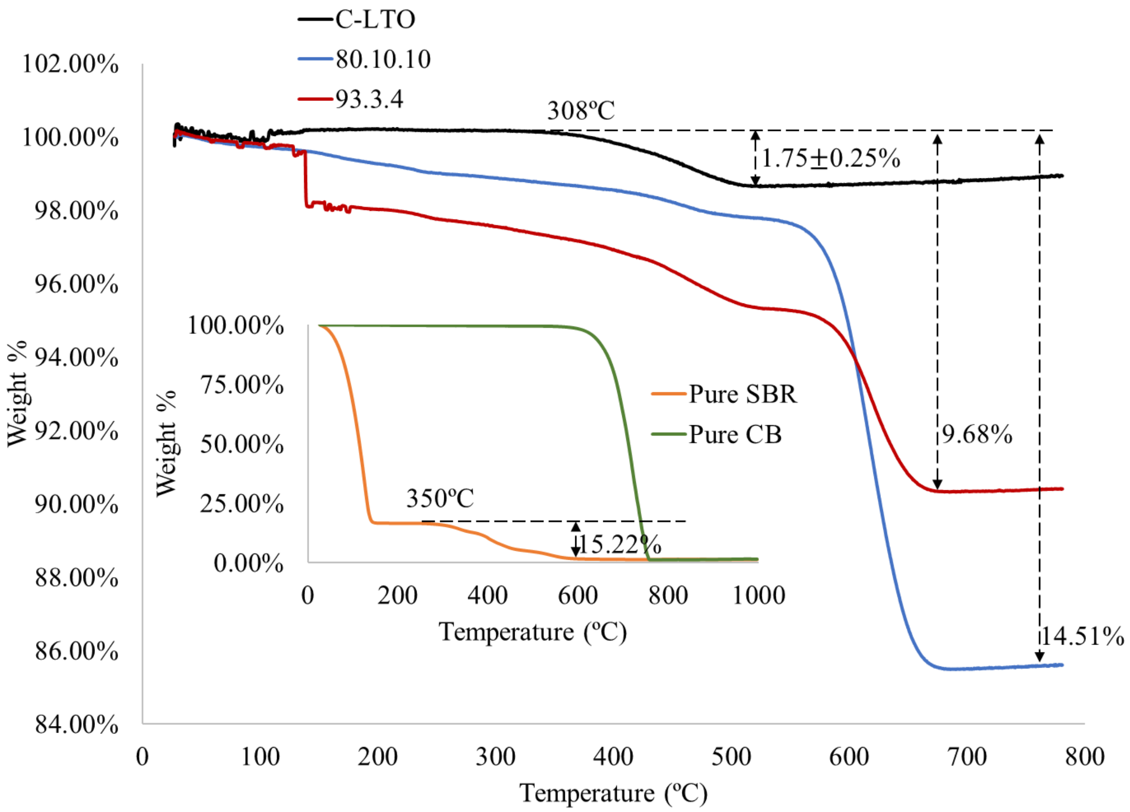

Figure A-3: TGA curves for pristine carbon-coated LTO (C-LTO) and electrodes composed of 93/3/4 and 80/10/10 C-LTO/C/SBR respectively. (Inset) TGA for Pure SBR.

Figure A-3 shows TGA analysis of the carbon-coated LTO powder, and two electrodes fabricated using EPD suspensions with varying compositions. The coatings were made and then the powders were removed from the substrate for TGA analysis.

The black line representing C-LTO powder shows the carbon-coating decomposes between $300 - 520℃$ and accounts for 1.75 ± 0.25 wt%. Inset of Figure A-3 shows the TGA for pure SBR and pure carbon black. For the SBR the initial loss <200℃ is attributed to the water. At 340℃ the polymer begins to decompose and, as mentioned in the SDS of the product, the slurry prepared by Targray is composed of ~15 wt% solids. The carbon black begins decomposing after 550℃.

The blue line belongs to electrode deposit made from a suspension consisting of 80/10/10 wt.% C-LTO/C/SBR showing the total carbon content in the deposit to be 14.51 wt%. Likewise, the red line is from a deposit made from a suspension consisting of 93/3/4 wt% C-LTO/C/SBR

---

[1] Supporting Information associated with paper published in *Electrochimica Acta* 299 (2019) 107-115.

respectively. The carbon content in this case is 9.68 wt% This carbon content represents carbon from the carbon coating, SBR, and from the added carbon black.

A.4 Raman Characterization

Table A-1: Raman Peaks of pristine LTO, and carbon-coated LTO (C-LTO) compared to literature values (taken from [2]).

	Raman shift position (cm^{-1})		
Peak	Literature	LTO	c-LTO
LTO high intensity	238	237	237
	439	431	425
	679	675	675
LTO low intensity	276	275	275
	349	356	356
	514	N/A	N/A
	620	621	621
	761	759	759
Carbon peaks	1340	N/A	1334
	1580	N/A	1594

The first column in Table A-1 shows literature values of high and low intensity Raman peaks for LTO as well as characteristic peaks for carbon. The second and third columns show the experimental peaks found for pristine LTO and carbon-coated LTO. The peak positions found in this work are observed to be close to the reported literature values. To determine the nature of the carbon deposited during the carbon coating step the integrated area under the D and G peaks is first determined by peak-fitting. The larger intensity observed in the D peak ($I_D/I_G = 195.3/69.6 = 2.81$) is indicative of the presence of significant fraction of disordered carbon layer.

[1] Supporting Information associated with paper published in *Electrochimica Acta* 299 (2019) 107-115.

Table A-2: Raman D and G carbon peaks of carbon-coated LTO (C-LTO).

Peaks	Literature	This work	Intensity[1]	Integrated Area	FWHM
D	1340	1334.14	0.62	195.3	295.9
G	1580	1600.41	0.73	69.6	89.8

[1] normalized and baseline corrected

A.5 Hetero-aggregate schematic

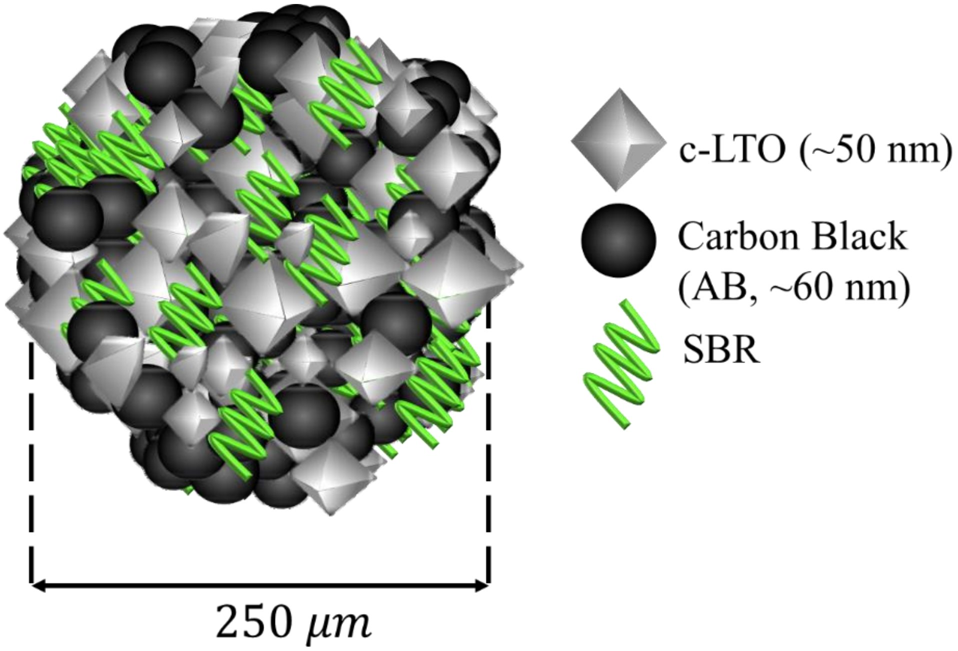

Figure A-4: C-coated LTO and Carbon (Acetylene Black) nanoparticles are assembled into hetero-aggregates via the bridging action of SBR polymers.

[1] Supporting Information associated with paper published in *Electrochimica Acta* 299 (2019) 107-115.

A.6 PEEM O K-edge

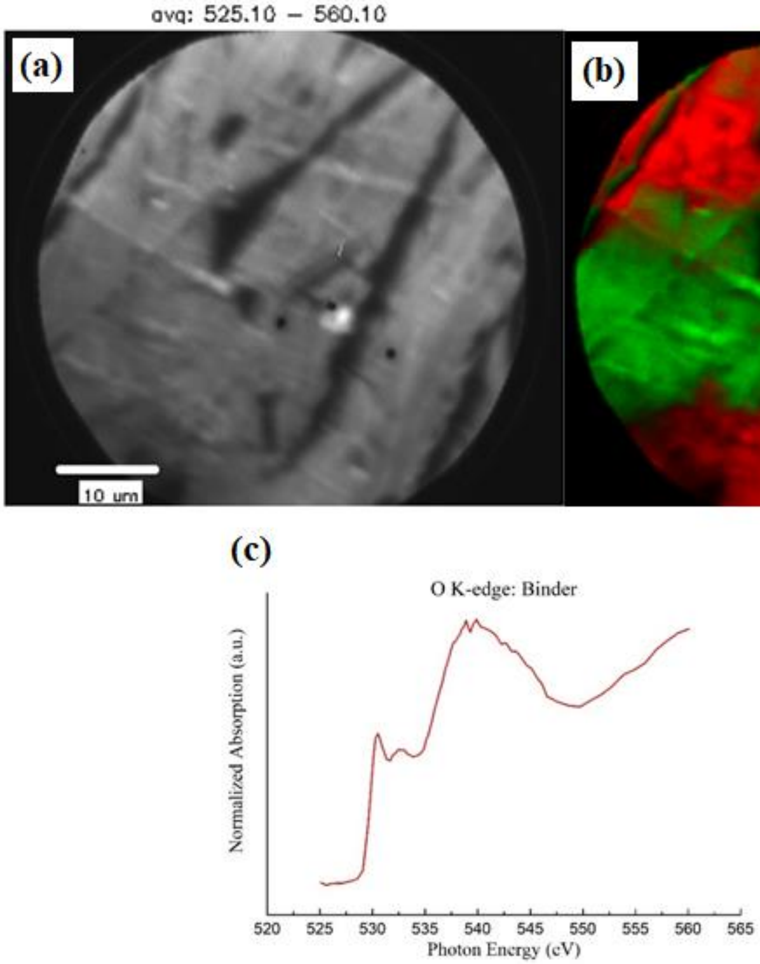

Figure A-5: (a, b) PEEM O-K edge of coating of pure SBR and (c) XANES of pure SBR.

[1] Supporting Information associated with paper published in *Electrochimica Acta* 299 (2019) 107-115.

A.7 Electrochemical Impedance Spectroscopy

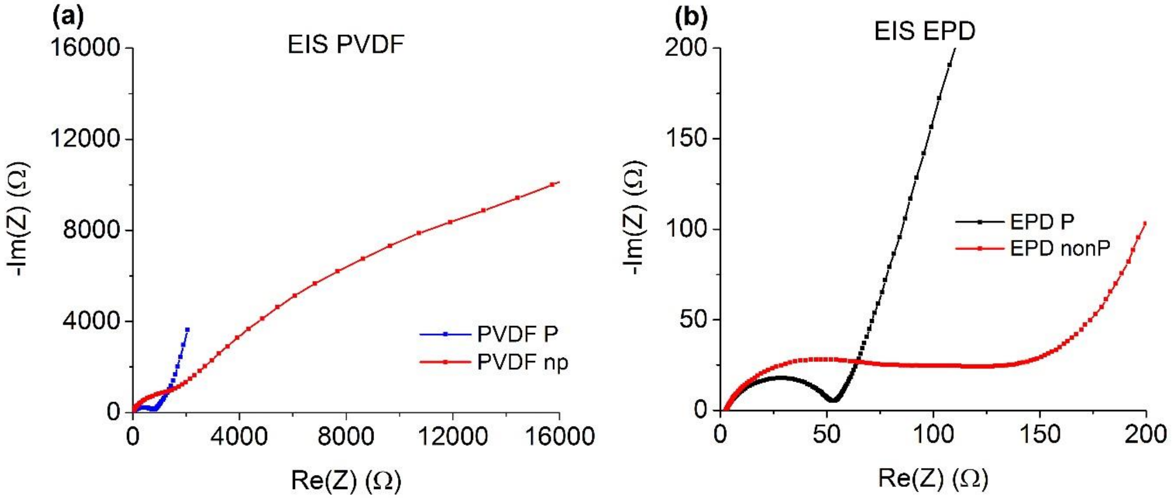

Figure A-6: EIS comparison between pressed ("P") and non-pressed ("nonP") electrodes made with (a)PVDF and (b) SBR-EPD.

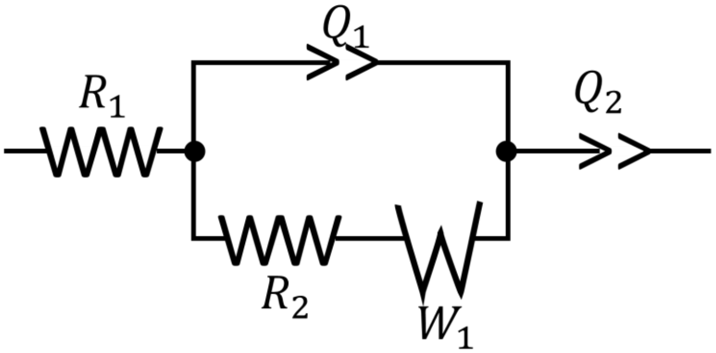

Figure A-7: EIS circuit model. In this model R_1 is the resistance experienced due to the electrolyte and the current collector and R_2 is the charge transfer resistance within the deposited layer. The variables Q_1 and Q_2 are constant phase elements and the W_1 is the Warburg element.

---

[1] Supporting Information associated with paper published in *Electrochimica Acta* 299 (2019) 107-115.

A.8 References

[1] M. Yoshio, R.J. Brodd, A. Kozawa, Lithium ion Battery Science and Technologies, Springer, New York, NY, 2009.

[2] D.G. Kellerman, V.S. Gorshkov, E.V. Shalaeva, B.A. Tsaryev, E.G. Vovkotrub, Structure peculiarities of carbon-coated lithium titanate: Raman spectroscopy and electron microscopic study, Solid State Sci. 14 (2012) 72–79. doi:10.1016/j.solidstatesciences.2011.10.018.

[3] M. Krajewski, B. Hamankiewicz, M. Michalska, M. Andrzejczuk, L. Lipinska, A. Czerwinski, Electrochemical properties of lithium–titanium oxide, modified with Ag–Cu particles, as a negative electrode for lithium-ion batteries, RSC Adv. 7 (2017) 52151–52164. doi:10.1039/C7RA10608D.

[1] Supporting Information associated with paper published in *Electrochimica Acta* 299 (2019) 107-115.

B. **Supporting Information**[2] for Chapter 4: Electrophoretically co-deposited $Li_4Ti_5O_{12}$/reducedgraphene oxide nanolayered composites for high-performance battery application

The following document contains further characterization of the precursor GO through TEM and SAED. Detailed information on solvent and EPD parameter selection is given to show why the ultimate suspension and deposition parameters were selected. The relithiation process that is necessary after EPD is provided in detail as well as a fabrication schematic elucidating said EPD process. Characterization of $GO \rightarrow rGO$ transformation is shown through XPS C1s spectra; TGA analysis of all precursor material, pristine EPD, and annealed EPD coating is shown to determine the final composition of the EPD electrode. Cross-sectional EDS maps of the PVDF electrode are provided including Ti kα, C kα, and F kα – the latter to show fluoride dispersion. EIS data for the pristine electrodes – pre-normalization – and EIS data for cycle 10 including the PVDF/C electrode is given. Further cyclic voltammograms for the PVDF/C electrode, as well as the calculation on how to determine lithium diffusivity from CVs, is shown.

[2] Supporting Information associated with the manuscript submitted to *Energy Storage Materials*.

B.1 GO TEM and Raman

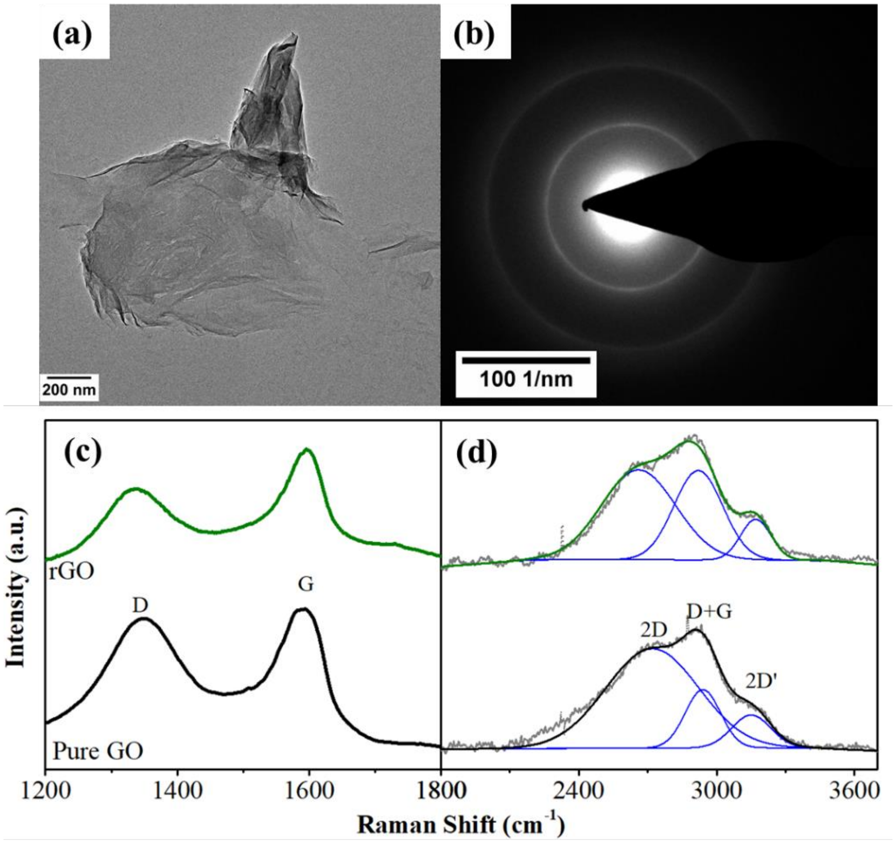

Figure B-1: (a) TEM for Pristine GO powder and (b) accompanying SAED pattern showing a multi-stacked structure. Raman Spectroscopy of Pure GO and rGO (after annealing) showing (c) D and G peaks and (d) the 2D, D+G, and 2D’ peaks.

B.2 EPD Solvent and Parameter Selection

EPD suspension is selected based on solid stability. To this end, a variety of media was tested including isopropanol, acetonitrile, dimethyl formamide (DMF), water, and ethanol. The organic solvents were also tested alongside 5-10 vol% water and with charging agents such as $MgCl_2$, polyacrylic acid (PAA), acetic acid, and dilute NaOH. Ultimately, a simple ethanol suspension proved to be the most effective for both LTH and GO. Among these precursors, LTH proved the most difficult to stabilize – it would quickly sediment despite ball milling. In these tests the synthesized LTH was initially dried (after synthesis) prior to suspension testing. However due to the long shape of the nano-platelets it led to agglomeration after drying which made the particles difficult to resuspend. Thus, after the final washing/centrifugation the samples were kept as dense

[2] Supporting Information associated with the manuscript submitted to *Energy Storage Materials.*

slurries and refrigerated, and the same media mentioned before were tested again. Of these the most stable suspensions proved to be pure organic DMF and ethanol. DMF was particularly interesting as the coatings fabricated were uniform and appeared thick. The problem arose during the drying stage, allowing the coating to air-dry would cause severe cracking as shown Figure B-2 (a). Controlled drying was attempted by placing the coating in an enclosed glass box with high DMF partial pressure. The coating did begin drying and the cracking was minimized but it was still too severe. This suspension has potential if the drying can be controlled.

Ethanol proved the simplest and most effective system. However, it required a 40-minute sonication stage to fully suspend the materials. Additionally, deposition, while uniform, is slow due to low charge. The tested parameters for ethanol/water suspension with 2.5 g/L LTH/GO at 93/7 wt% are shown in Table B-1. Water was added to improve the deposition rate, but this led to destabilization of the suspension.

The pure ethanol system proved to be optimal as a suspension. The effect of EPD voltage on the deposition using this ethanol suspension was studied by depositing LTH on copper at 35, 50, 70, and 100V. There is a clear change in color where the LTH goes from white to having a green tinge (Figure B-3 (b), 50V). XPS was used to determine if there was an effect on the LTH or copper substrate. The Cu substrate has a thin native protective oxide that is <10nm thick that sits on top of the Cu metal, XPS spectra for both Cu oxide and metal are given in Figure B-3 (a). Figure B-3 (c) has the Ti 2p spectra for the deposited coating using 35V and 100V. The characteristic $Ti2p_{1/2}$, $Ti2p_{3/2}$, and satellite peaks for Ti^{4+} are present at the expected binding energies meaning LTH was not affected by the EPD voltage. However, a comparison of the corresponding Cu 2p spectra, shows the formation of new peaks. This Cu 2p signal is coming from within the coating as the penetration range of XPS is <10nm. At 35V the Cu 2p peaks present at 932 and 952 eV are characteristic of Cu and Cu^{+}. The shoulders at 934 and 955 are characteristic of the presence of Cu^{2+} indicating copper oxidation. However, at 100V the Cu^{2+} peaks are comparatively larger which means the increasing voltage will increase the amount of copper oxidized that redeposits. Thus, a voltage of 35V was selected. Deposition time was kept to short 15-second stages as 60-second stages (5 layers) caused uneven deposits to form as seen in Figure B-2 (b). Figure B-2 (c) shows the progression of the coating over 20 stages using 15 second deposition time and 35V.

[2] Supporting Information associated with the manuscript submitted to *Energy Storage Materials*.

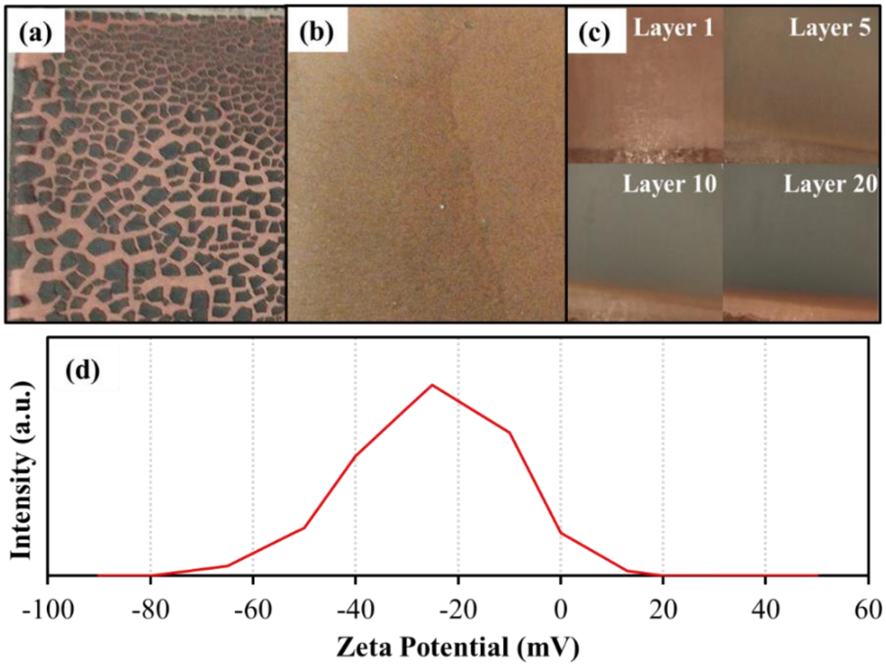

Figure B-2: Coatings made of (a) DMF/15s/5stages/35V after drying, (b) ethanol/60s/5stages/35V, and (c) ethanol/15s/20stages/35V. (d) Zeta potential distribution of LTH/GO suspension in ethanol.

Table B-1: EPD Parameter selection and water content for ethanol suspension. Solids were 2.5 g/L LTH/GO 93/7 wt% respectively

% Water	Applied Voltage (V)	Current Density (mA/cm^2)
0	80	1.99
0	100	2.75
10	100	8.91
20	100	16.61

---

[2] Supporting Information associated with the manuscript submitted to *Energy Storage Materials*.

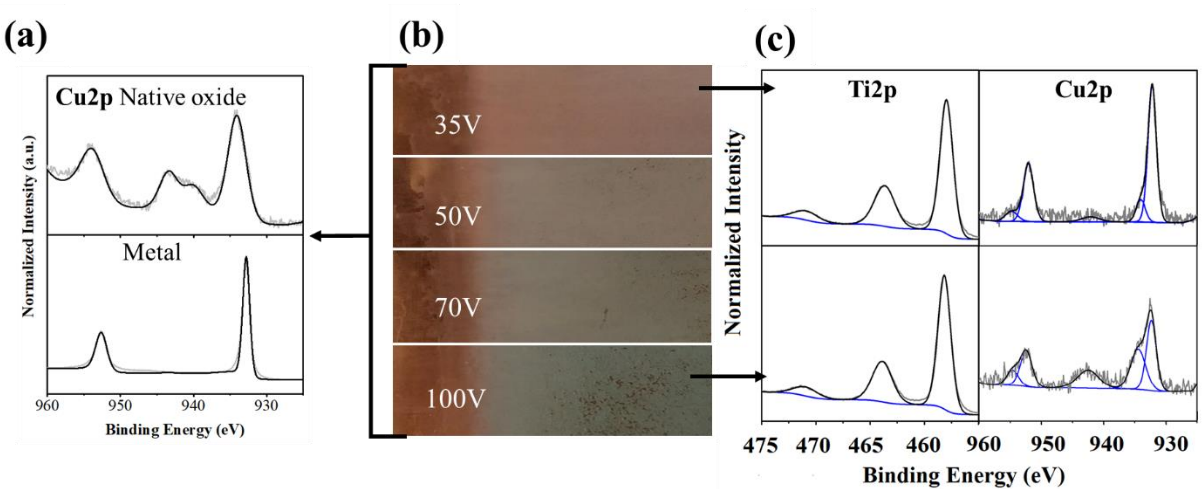

Figure B-3: (a) Cu 2p XPS spectra of the Cu substrate, (top) native oxide and (bottom) the Cu metal underneath. (b)EPD coatings made from ethanol at 35, 50, 70, and 100V and (c) Ti 2p and Cu 2p spectra for (top) 35V and (bottom) 100V.

B.3 EPD-Induced Delithiation

The EPD coatings are first pressed at 2MPa followed by a 6-hour annealing stage at 600 ℃ under a 5% H_2/Ar atmosphere. This led to the transformation of LTH to LTO, however, this transformation was initially incomplete. Instead of $Li_4Ti_5O_{12}$, anatase and rutile titania were detected after annealing. As this problem was exclusive to the EPD fabricated electrodes, it was hypothesized to happen due to loss of lithium in the suspension. This proved true as the issue was fixed by submerging the electrodes in a 0.3M $LiOH$ bath. A series of concentrations between 0.2-2M were attempted where a low concentration led to the formation of lithium-poor Li_2TiO_3 and a concentration beyond 0.3M was unnecessary. Thus, it became important to press the electrode after LiOH submersion and prior to annealing. The porous structure maximized the percolation of the aqueous LiOH solution throughout the coating.

[2] Supporting Information associated with the manuscript submitted to *Energy Storage Materials.*

B.4 Fabrication Schematic

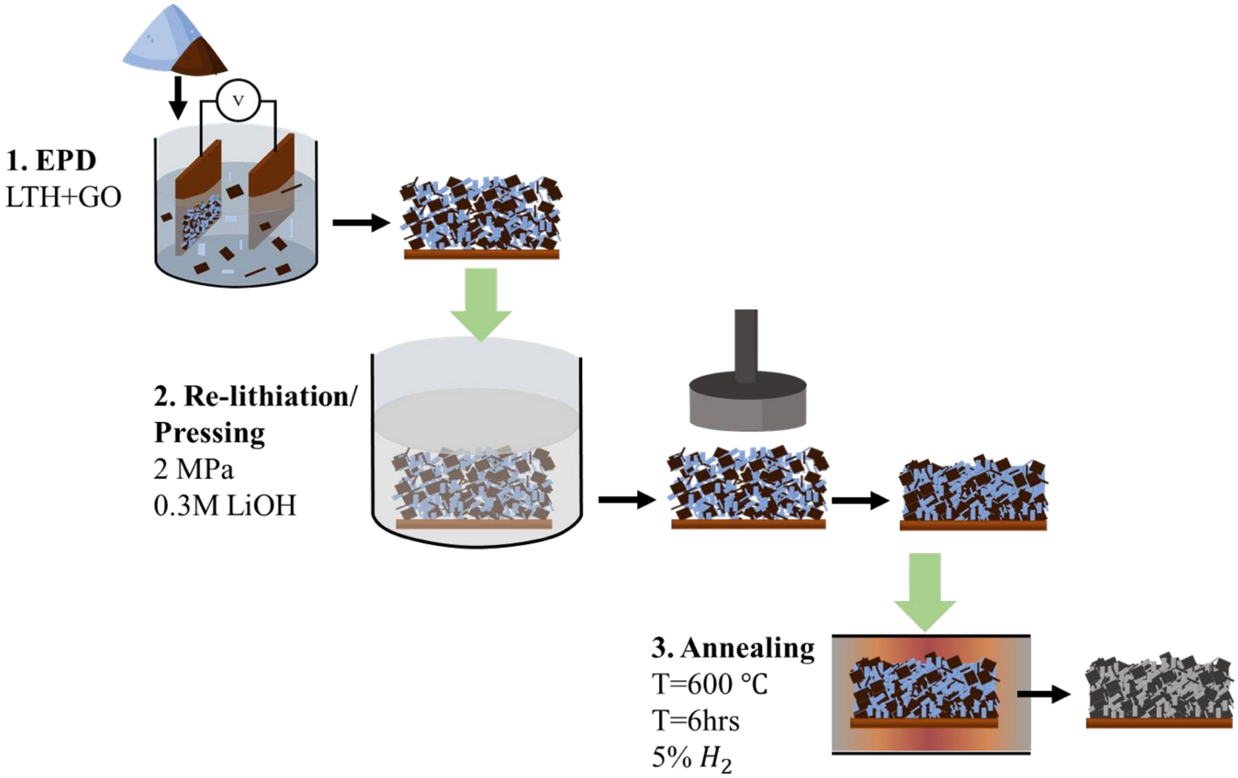

Figure B-4: EPD fabrication flowchart showing 1. EPD of precursors, 2. Re-lithiation and pressing of the coating, and 3. Annealing to induce precursor transformation to LTO and rGO.

---

[2] Supporting Information associated with the manuscript submitted to *Energy Storage Materials*.

B.5 $GO \rightarrow rGO$ transformation XPS

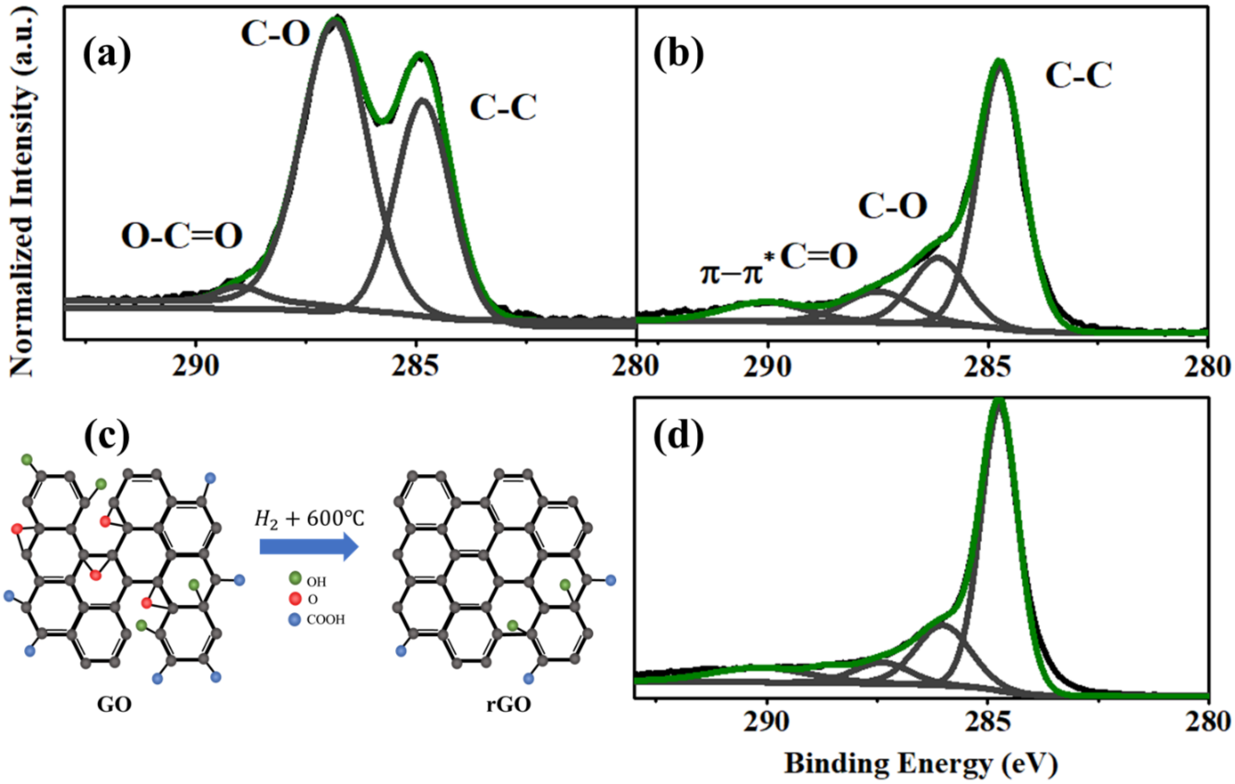

Figure B-5: XPS C1s spectra for (a) non-annealed and (b) annealed EPD coating. (c) A schematic of the functional groups on the GO and rGO. (d) XPS C1s spectra for pristine rGO powder.

Table B-2: XPS C1s de-convoluted peaks and corresponding binding energy (BE) and area intensity normalized relative to the C-C peak.

	Pristine EPD Coating		**Annealed EPD Coating**		**Pristine rGO powder**	
Group	BE (eV)	Area (a.u.)	BE (eV)	Area (a.u.)	BE (eV)	Area (a.u.)
C-C	284.84	1	284.78	1	284.78	1
C-O	286.73	1.17	286.18	0.33	286.18	0.29
C=O	N/A	N/A	287.54	0.16	287.42	0.11
O-C=O	288.38	0.17	N/A	N/A	N/A	N/A
$\boldsymbol{\pi - \pi^*}$	N/A	N/A	289.98	0.19	290.05	0.13

[2] Supporting Information associated with the manuscript submitted to *Energy Storage Materials*.

B.6 Thermogravimetric Analysis

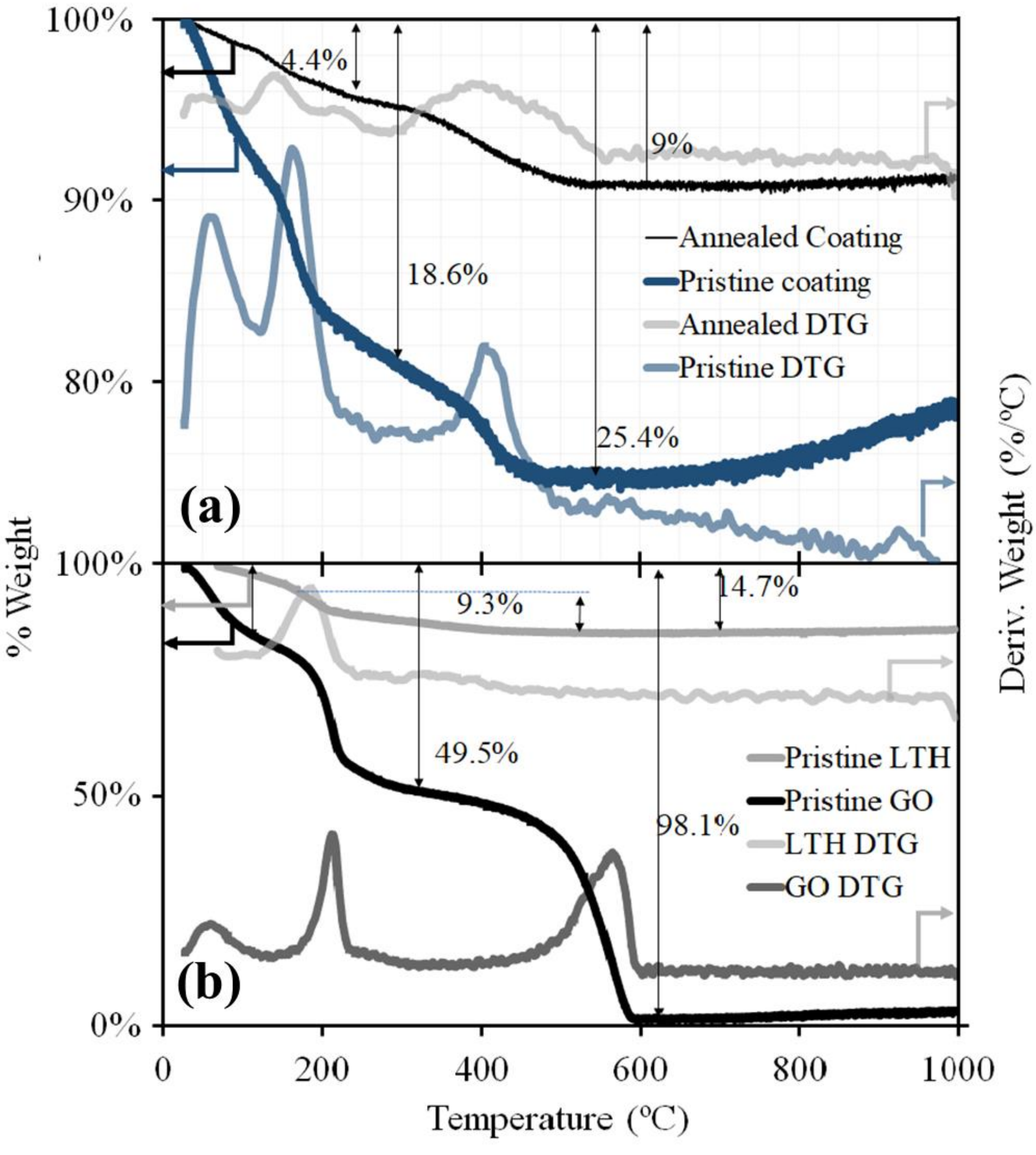

Figure B-6: TGA results and corresponding DTG for (a) for the pristine and annealed EPD coating and (b) pristine LTH slurry and GO powder.

---

[2] Supporting Information associated with the manuscript submitted to *Energy Storage Materials*.

Table B-3: Decomposition temperatures and cumulative mass loss for pristine LTH/GO and pristine and annealed coating determined through the derivative thermogravimetric curves (DTG).

Material	**Decomposition Temperature** (℃)	**~Cumulative mass loss (%)**
Pristine LTH	187	5.4
	370	14.7
Pristine GO	59	16.5
	212	49.5
	564	98.1
Pristine Coating	160	18.6
	411	25.4
Annealed Coating	140	4.4
	430	9.1

B.7 Cross-sectional EDS for PVDF electrode

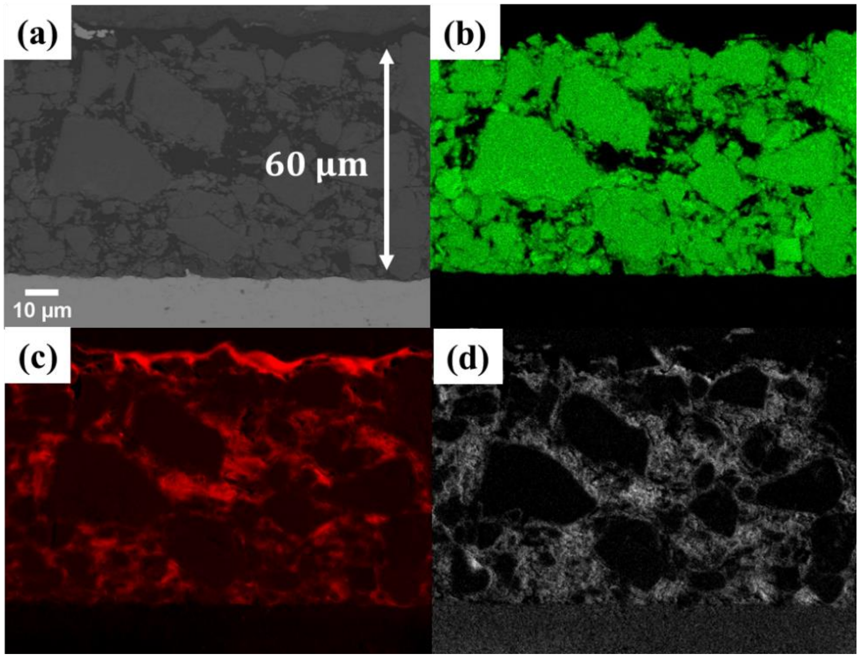

Figure B-7: Cross-sectional EDS map of PVDF electrode, (a) BSE image, (b) Ti Kα, (c) C Kα, and (d) F Kα.

---

[2]Supporting Information associated with the manuscript submitted to *Energy Storage Materials.*

B.8 EIS Measurements and Modeling

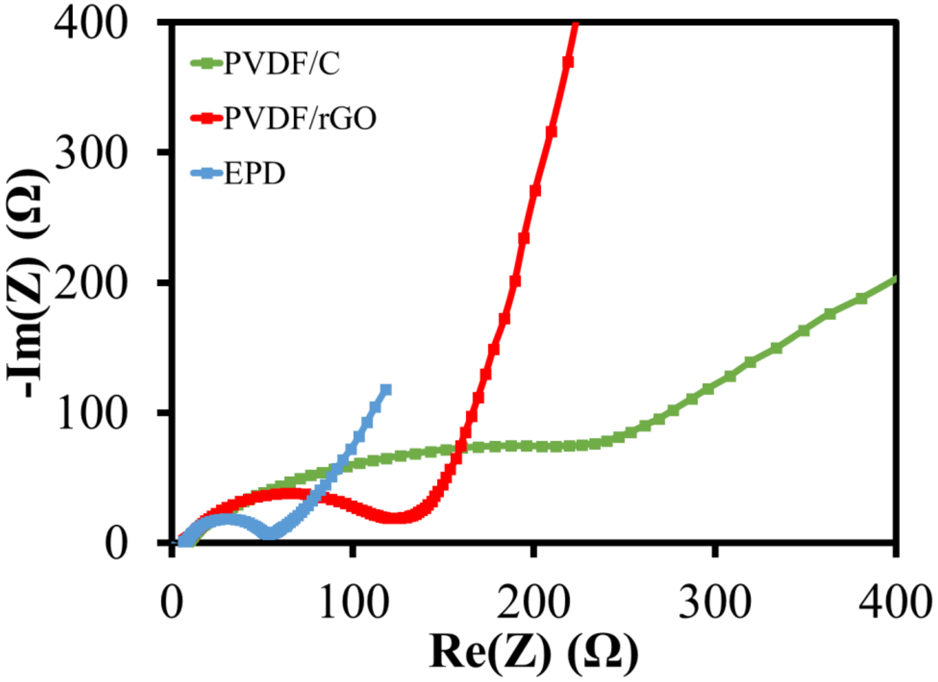

Figure B-8: Preliminary EIS data – Pristine.

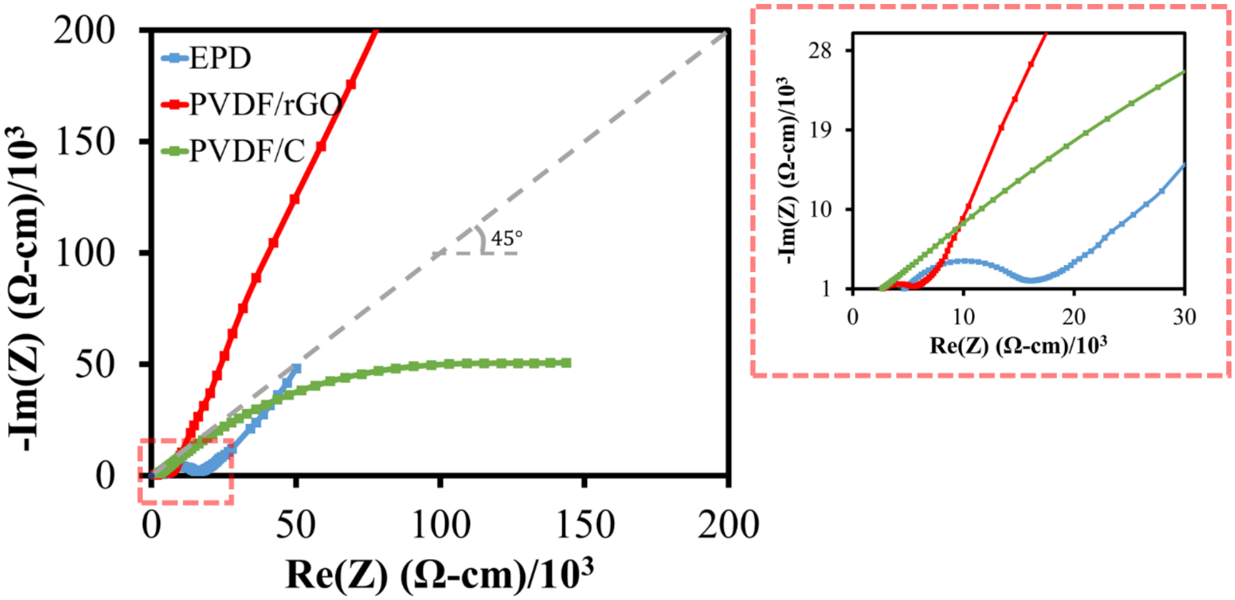

Figure B-9: EIS data taken after 10 cycles with closeup of the high frequency range.

---

[2] Supporting Information associated with the manuscript submitted to *Energy Storage Materials*.

Table B-4: Pristine and Cycled EIS calculated resistance (divided by 10^3 as per the EIS graphs) and pseudocapacitance values. All values are normalized with respect to the coating thickness and geometric area (divided by thickness and multiplied by area – 0.785cm^2). The model used is given in Figure 4-3.

	Pristine			**Cycle 10**		
	EPD	**PVDF/rGO**	**PVDF/C**	**EPD**	**PVDF/rGO**	**PVDF/C**
$\boldsymbol{R_{ohm}}$ (Ω-cm)$/\mathbf{10^3}$	2.84	0.68	0.91	1.62	0.81	1.10
$\boldsymbol{R_{SEI}}$ (Ω-cm)$/\mathbf{10^3}$	0.28	0.14	0.18	2.84	1.08	0.18
$\boldsymbol{R_{CT}}$ (Ω-cm)$/\mathbf{10^3}$	17.46	16.24	43.81	11.37	3.38	182.56
$\boldsymbol{C_1}$ (F)	2.30E-07	2.50E-13	2.36E-07	2.29E-09	1.50E-07	2.36E-07
$\boldsymbol{C_2}$ (F)	1.23E-06	9.00E-07	1.50E-07	8.76E-06	3.98E-06	3.89E-07
$\boldsymbol{Q_3}$ (F·s$^{(a-1)}$)	6.80E-03	1.00E-03	1.00E+00	3.65E+00	5.41E-01	1.83E+02
$\boldsymbol{a_3}$	1	0.95	1	1	0.88	1
$\boldsymbol{W_1}$ (Ωs$^{-0.5}$cm)	4.47E+04	2.03E+04	4.56E+05	6.09E+04	1.08E+04	4.56E+05

B.9 Cyclic Voltammetry

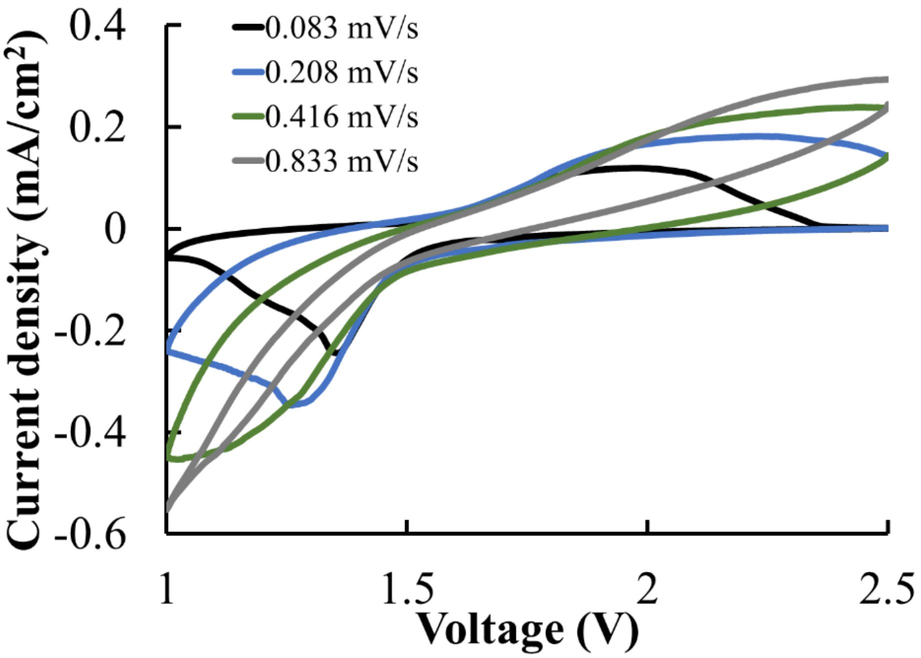

Figure B-10: Cyclic voltammetry at varying scan rates for the PVDF/C electrode.

[2] Supporting Information associated with the manuscript submitted to *Energy Storage Materials.*

B.10 Lithium Diffusivity Calculation

Diffusion of lithium ions and electrons through the host matrix can be determined by the Randles-Sevcik equation shown in Eq. B-1 [1].

$$I_p = 0.4463AC\sqrt{\frac{n^3F^3D_o}{RT}v} \qquad \text{Eq. B-1}$$

Where I_p is the peak current (A), A is the geometric surface area (cm^2), C is the concentration of Li^+ ions in LTO crystal (mol/cm^3, found using the molar volume of LTO – 45.73 cm^3/mol), [1] n is the number of electrons exchanged, F is Faraday's constant (96485 C/mol), R is the gas constant (8.314 $J/mol \bullet K$), T is the temperature (K), v is the scan rate (V/s) and D_o is the diffusion coefficient (cm^2/s).

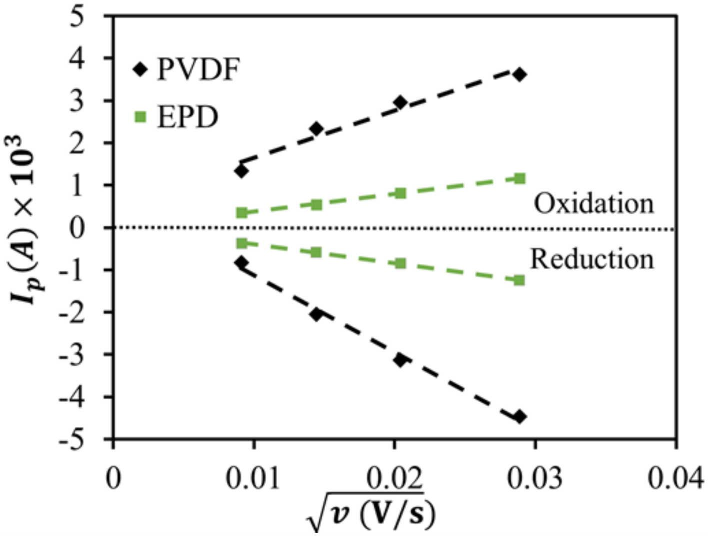

Figure B-11: I_p vs $v^{1/2}$ relationship from CV curves.

Table B-5: Li^+ diffusion coefficient values calculated from CV.

	D (cm^2/s)	
	EPD	**PVDF/GO**
Oxidation	2.99E-12	2.18E-11
Reduction	3.47E-12	5.76E-11

---

[2] Supporting Information associated with the manuscript submitted to *Energy Storage Materials.*

B.11 Battery Cycling

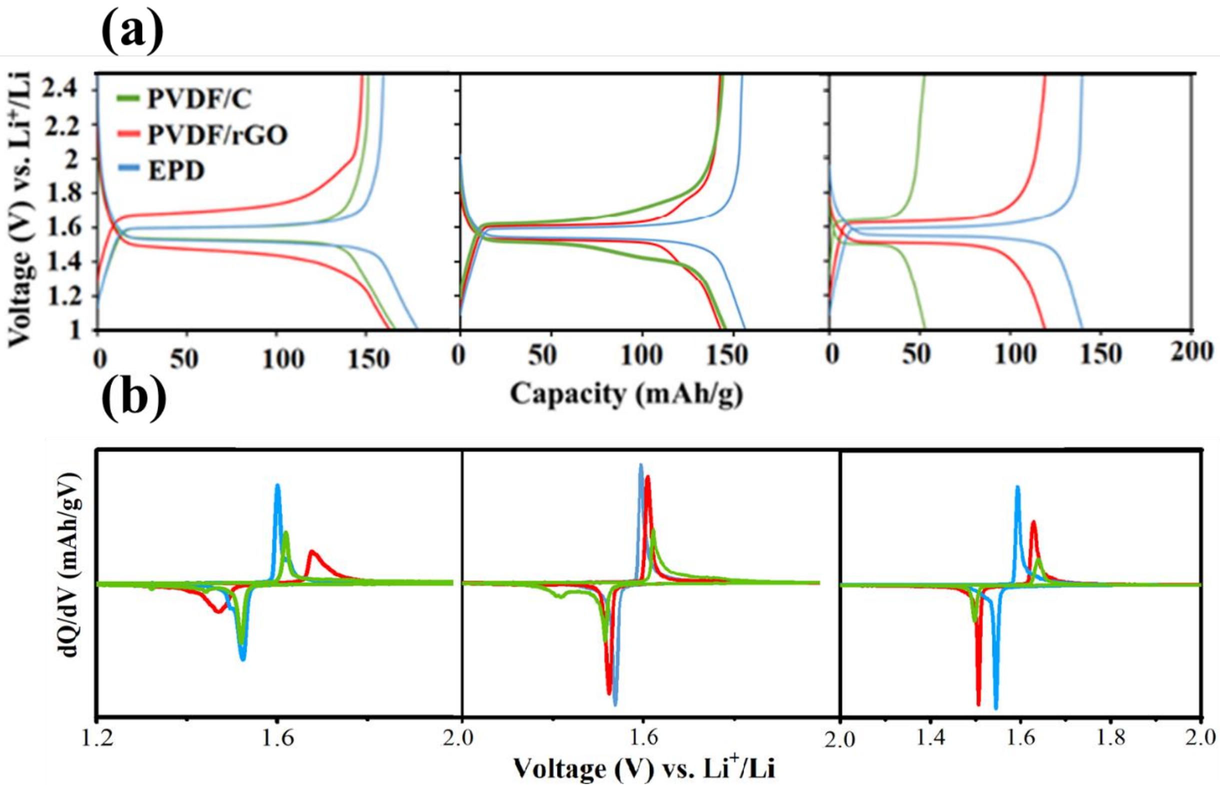

Figure B-12: (a) Discharge/Charge curves and (b) corresponding differential capacity analysis dQ/dV for EPD, PVDF/rGO, and PVDF/C electrodes at (left to right) cycle 1, cycle 10, and cycle 150[3].

B.12 References

[1] M. Krajewski, B. Hamankiewicz, M. Michalska, M. Andrzejczuk, L. Lipinska, A. Czerwinski, Electrochemical properties of lithium–titanium oxide, modified with Ag–Cu particles, as a negative electrode for lithium-ion batteries, RSC Adv. 7 (2017) 52151–52164. doi:10.1039/C7RA10608D.

---

[3] Figure B-12 is modified from the published SI version to correct the dQ/dV calculations. This is the correct version.

[2] Supporting Information associated with the manuscript submitted to *Energy Storage Materials*.

C. **Supporting Information**[4] for Chapter 5: Percolation Influence on Fade Mechanism of $TiNbO_7$ and reduced graphene oxide composite anodes

The present document contains information regarding the solid-state synthesis of TNO, its ball-milling, carbon coating, characterization and electrochemistry.

A graph showing the temperature changes during carbon-coating of TNO is given including Raman characterization of the D and G bands showing the presence of carbon. The effect of ball-milling on TNO electrochemical performance (cycling and cyclic voltammetry) is shown to explain the need for particle size reduction. EPD suspension and parameter selection is elucidated to explain the necessity of high amounts of GO in the suspension and the reason for voltage selection. After annealing of the EPD coatings, thermogravimetric analysis is used to quantitatively determine the amount of rGO in the coating. Additionally, XPS of C 1s spectra is used to show the $GO \rightarrow rGO$ transformation during the annealing step. XRD patterns of the EPD coating before and after annealing are included, along with a schematic of the TNO lattice showing the planes of the main peaks observed in the XRD pattern. EDS F kα mapping of the PVDF electrode cross-section is given to show the cracking observed for the 18 wt.% rGO PVDF electrode and the dispersion of the fluoropolymer binder. The final section includes cyclic voltammograms of an electrode composed of 80/20 wt.% rGO/PVDF at varying scan rates to show the current response of pure rGO. Additionally, the voltammograms of the EPD and PVDF electrodes (10 and 18 wt.% rGO) at varying scan rates is also included along with the analysis used to study pseudocapacitive contributions from rGO, these include 1) plots of the log of peak cathodic current vs. log of scan rate and 2) plots of $i(V)/v^{0.5}$ vs $v^{0.5}$.

---

[4] Supporting Information associated with the manuscript for Chapter 5 (to be submitted).

C.1 TNO Synthesis and Carbon-Coating

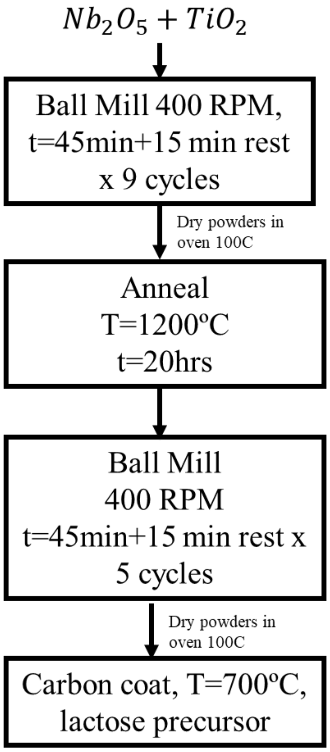

Figure C-1: Solid-state synthesis flowchart for ball-milled and carbon-coated TNO.

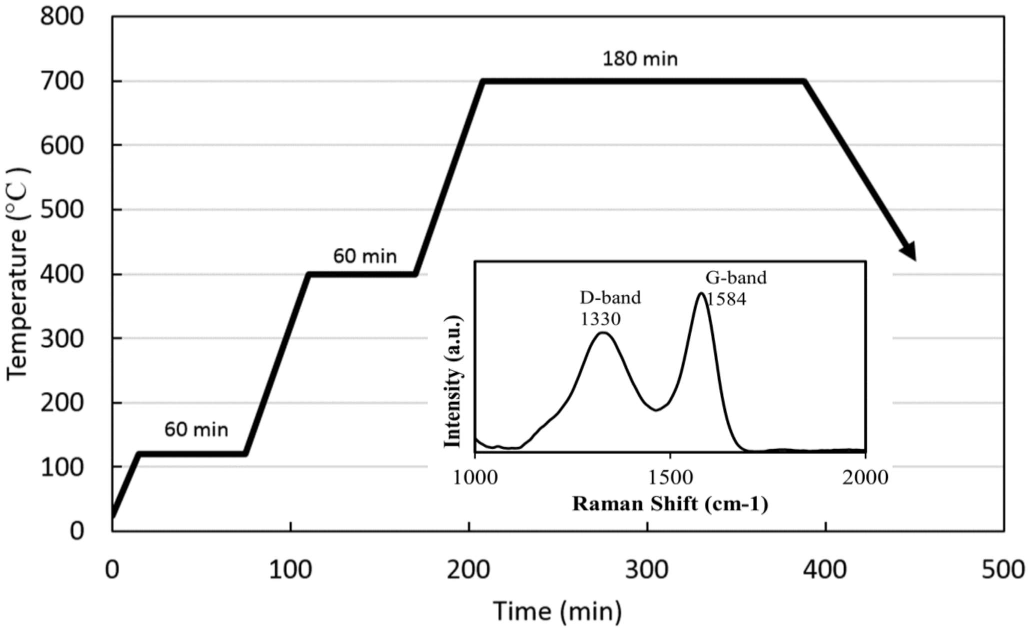

Figure C-2: carbon-coating temperature profile and resulting carbon-coating identified through Raman by the “D” and “G” peaks shown in inset.

[4] Supporting Information associated with the manuscript for Chapter 5 (to be submitted).

C.2 Ball-milling effect on electrochemical performance

The initial high capacity followed by a rapid drop is characteristic of the ball-milled material as the pristine material shown in Figure C-3 does not exhibit the same behavior. This initially high capacity is attributed to the small particle size minimizing the lithium diffusion length. However, the rapid and irreversible capacity has been associated to structural disordering induced by ball-milling [2]. While the degradation/disordering is not desirable, the ball-milling and size reduction of these particles is necessary. Cyclic voltammetry for the pristine TNO (with carbon black) shown in Figure C-3 shows broad peaks and severe polarization – as a result of the large particle size and Li^{+} diffusion lengths [3]. When compared to the pristine material, ball-milling had positive effect on the initial performance. As seen in in Figure C-3, the resulting voltammogram for the carbon-coated ball-milled material with carbon black shows the Nb^{5+}/Nb^{4+} redox couple dominant peaks at 1.62/1.67 V vs. Li^{+}/Li, shoulders at 1.57/1.47 V, which arise from the different positions of Nb atoms (of edge- or corner-shared octahedra). The broad peaks at 1.79/1.93 V and 1.4/1 V correspond to Ti^{4+}/Ti^{3+} and Nb^{4+}/Nb^{3+} redox couples respectively [4]. However, prolonged cycling showed rapid deterioration within the first 10 cycles.

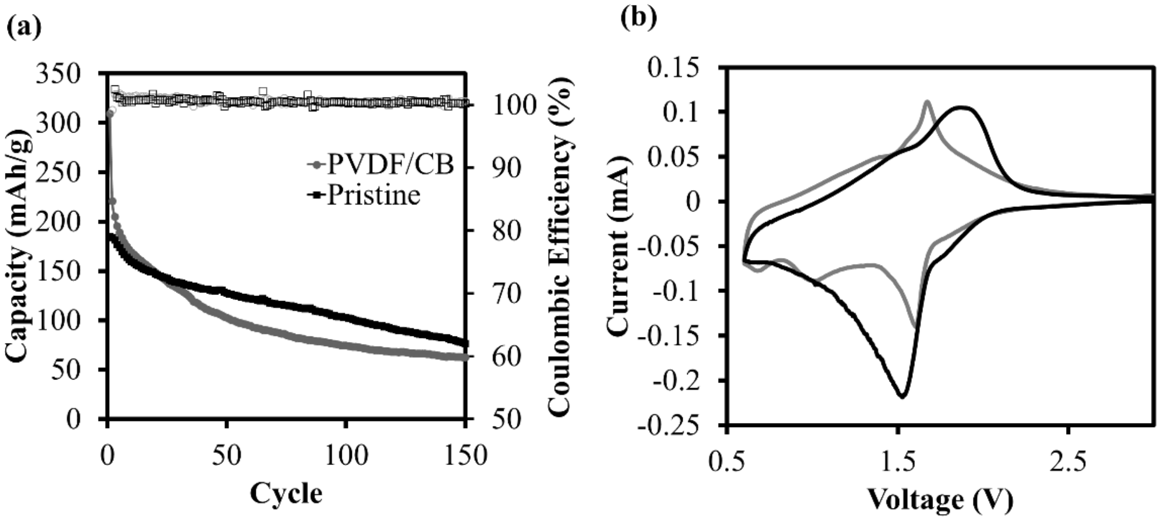

Figure C-3: (a) 0.5C cycling and (b) 0.1 mV/s CV from 0.5 to 3 V vs. Li^{+}/Li of the PVDF coatings using pristine material and milled material mixed with carbon black (“PVDF/CB”).

---

[4] Supporting Information associated with the manuscript for Chapter 5 (to be submitted).

C.3 EPD Suspension and Parameter Selection

The ethanol suspension has been previously tested in an EPD system to deposit LTO composite coatings with GO (see Chapter 4). In this paper ethanol was found to be a suitable medium for TNO. As mentioned in section 5.4.1.2 of Chapter 5, pure GO and TNO in suspension yield a zeta potential of -28 mV and -18 mV respectively. Mixing 90/10 wt.% TNO/GO gave a zeta potential of -29 mV, however increasing the GO content to 30% lowered the zeta potential to -15 mV. The low GO suspension yielded a poor deposit due to a low current response when 30V was applied for ten 15s stages (see Figure C-4), however increasing the amount of GO led to a drastic increase in current response and visible improvement of deposit quality using the same conditions. The poor deposit quality of the low GO suspensions is attributed to the higher colloid stability which makes it difficult to overcome the interparticle distance (needed for deposition to occur) without increasing the voltage. However, at lower zeta potentials this barrier is lower.

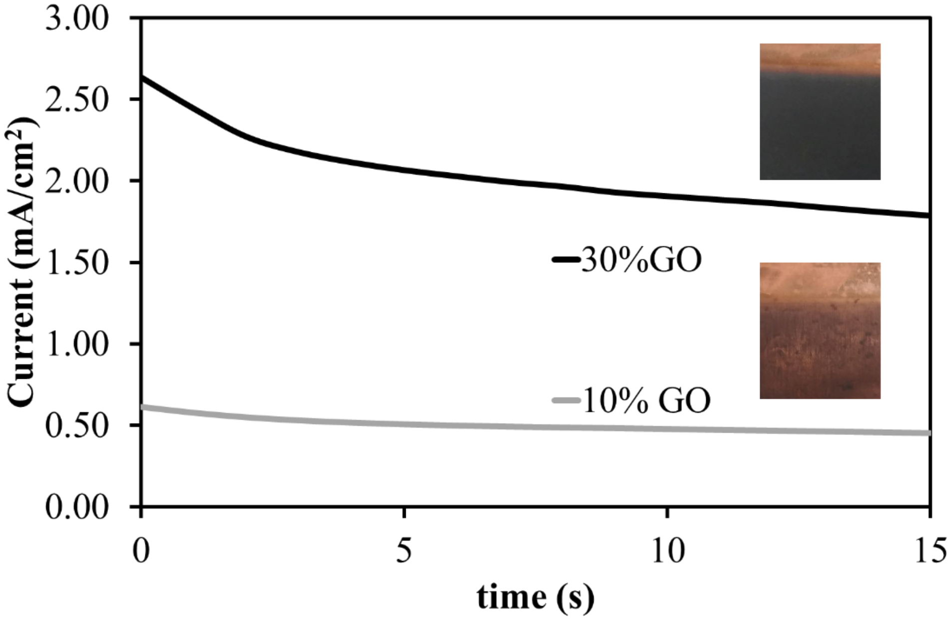

Figure C-4: Current response for varying suspension compositions of GO with achieved coating after ten 15-second deposition stages.

The voltage was maintained at 30V in an attempt to mitigate the oxidation, and subsequent redeposition, of copper (copper foil oxidation was also observed in section 4.4.4 of Chapter 4 and section B.2 of Appendix B). However, some faint copper deposits are still observed through cross-sectional EDS and XPS of the untreated and annealed EPD coating (Figure C-5). The XPS of Cu

---

[4] Supporting Information associated with the manuscript for Chapter 5 (to be submitted).

2p shows peaks belonging to Cu/Cu^{+} at 932 and 952 eV (for 2p 3/2 and 1/2 respectively) and Cu^{2+} peaks at 934 and 954 eV (for 2p 3/2 and 1/2 respectively). They are present before and after annealing although the annealing stage removes some of the Cu^{2+}, as the result of reduction under H_2 atmosphere. Thus, the 30V is maintained, however applying a low voltage will lead to low deposition kinetics – this is countered by the increase of the charged GO sheets.

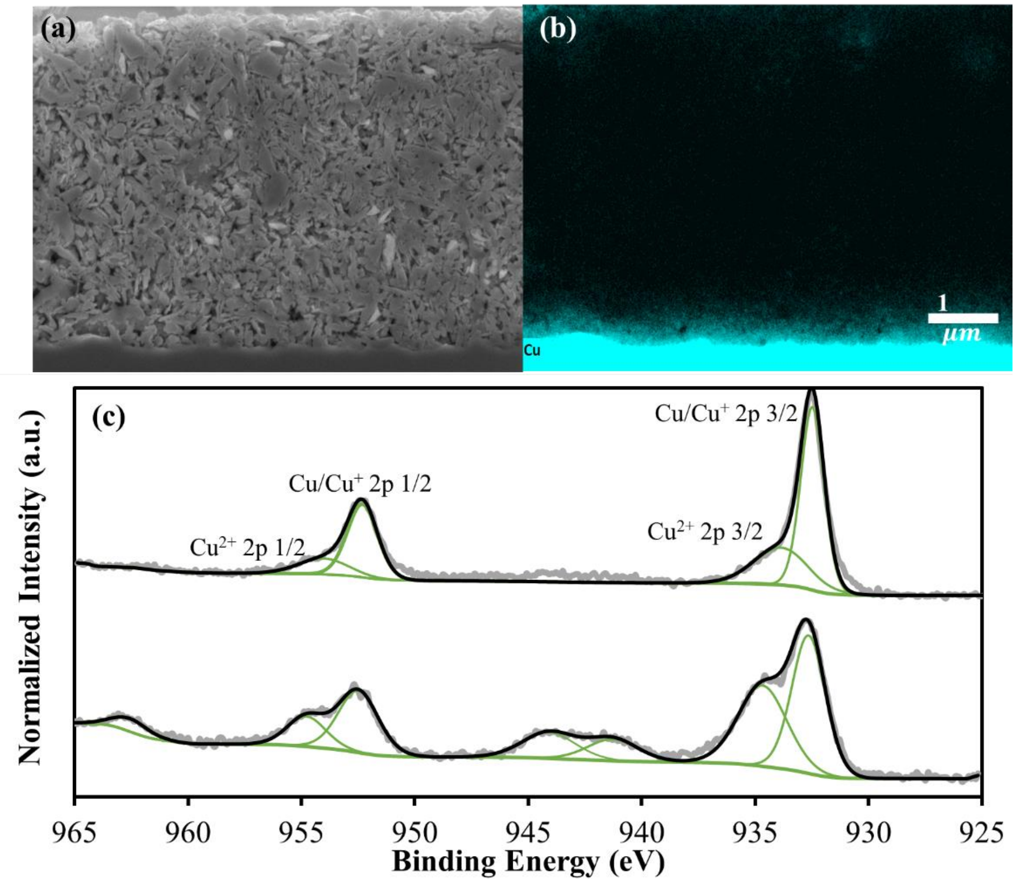

Figure C-5: EPD annealed coating cross-sectional (a) SE image, (b) EDS of Cu Lα, and (c) XPS of Cu 2p for (bottom) non-annealed and (top) annealed EPD coating.

[4] Supporting Information associated with the manuscript for Chapter 5 (to be submitted).

C.4 TGA of EPD Annealed Coating

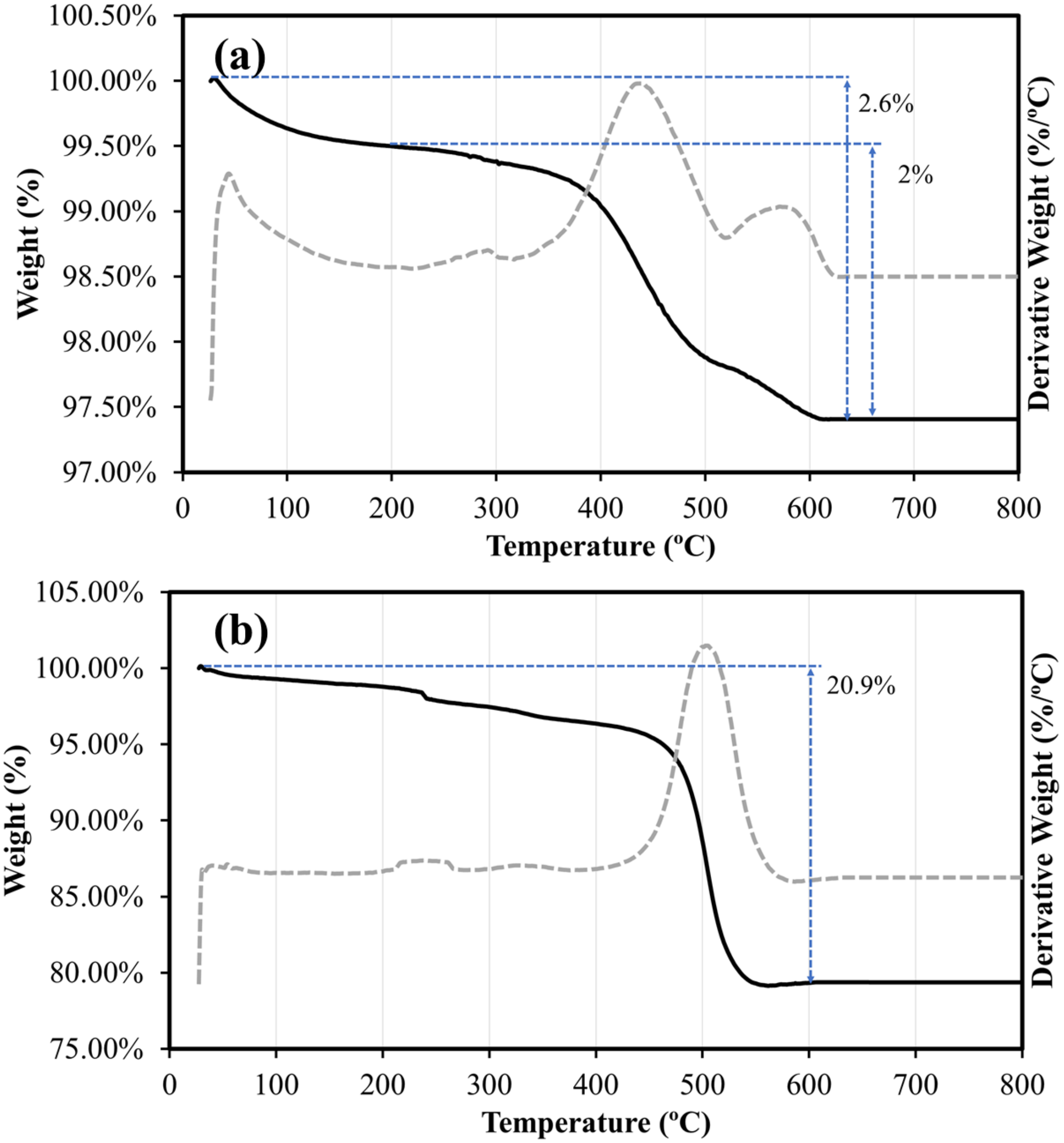

Figure C-6: TGA of (a) ball-milled carbon-coated TNO and (b) annealed EPD coating

[4] Supporting Information associated with the manuscript for Chapter 5 (to be submitted).

C.5 XPS of C 1s

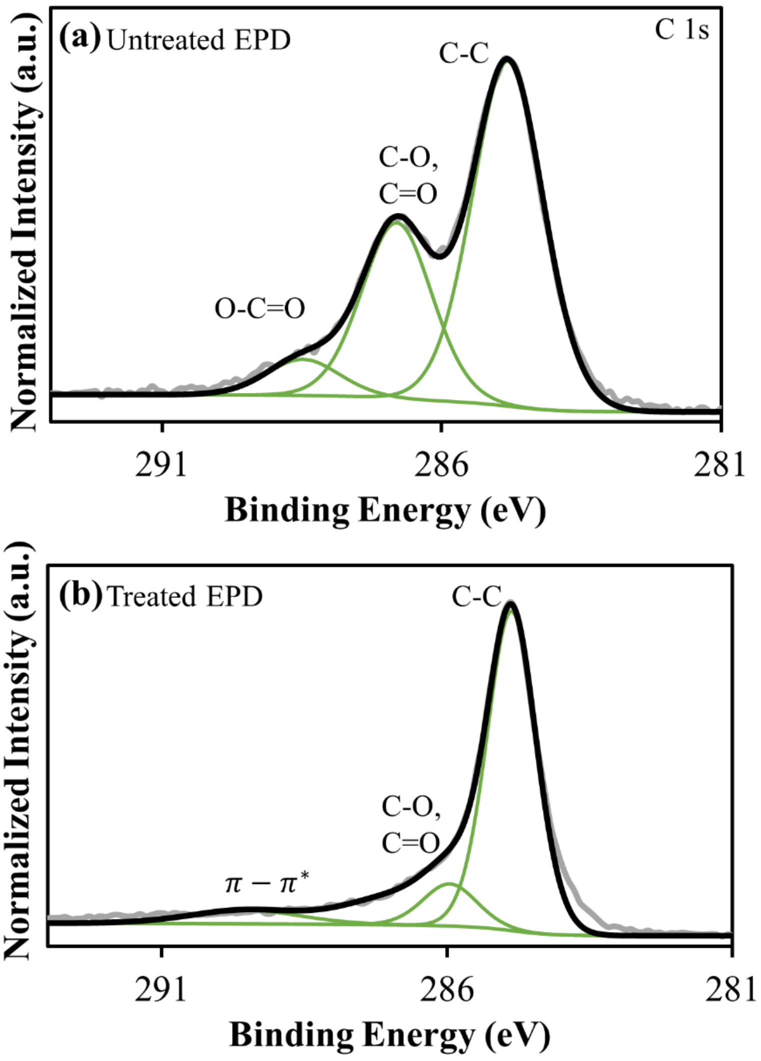

Figure C-7: C 1s spectra for (a) untreated (as is deposit formed through EPD) and (b) treated (i.e. annealed at high temperature) EPD coating

---

[4] Supporting Information associated with the manuscript for Chapter 5 (to be submitted).

C.6 TNO Structure Schematic and XRD

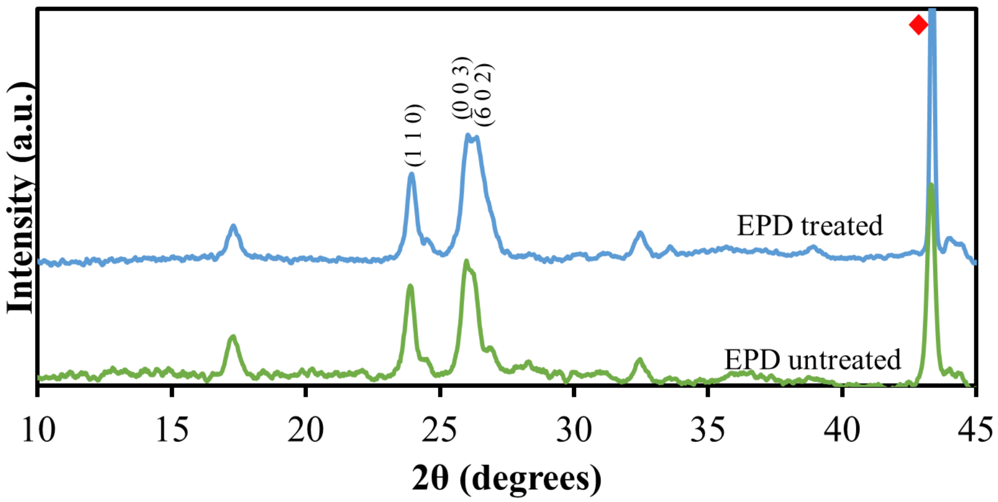

Figure C-8: XRD pattern for the EPD coating before and after annealing with ♦ denoting the position of the Cu substrate.

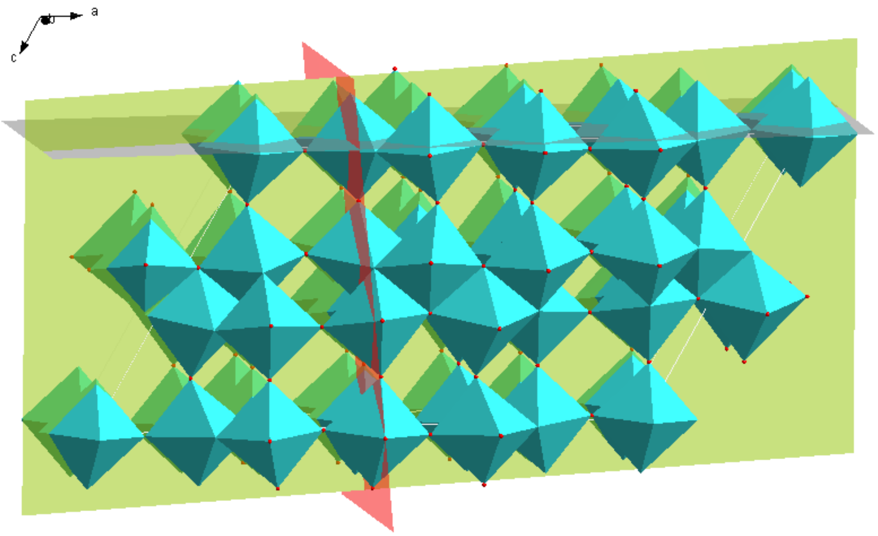

Figure C-9: TNO structure where the inserted lattice planes are: green (110), purple (003) and red $(\bar{6}02)$. The cyan-colored octahedra consist of the transition metals Ti and Nb at the center with the red spheres representing oxygen atoms.

[4] Supporting Information associated with the manuscript for Chapter 5 (to be submitted).

C.7 PVDF Fluoride Maps

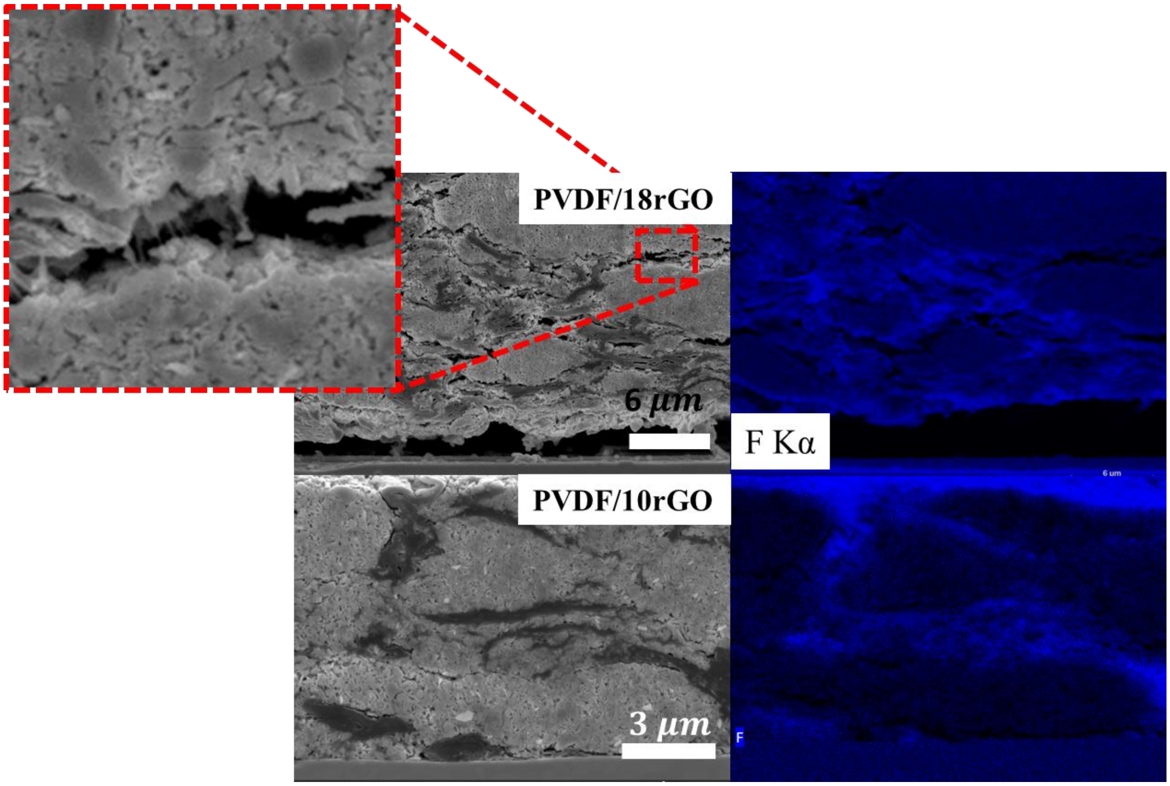

Figure C-10: cross-sectional SEM images of the PVDF/18rGO and PVDF/10rGO with corresponding F Kα showing PVDF binder dispersion.

C.8 Cyclic Voltammetry and Pseudocapacitance

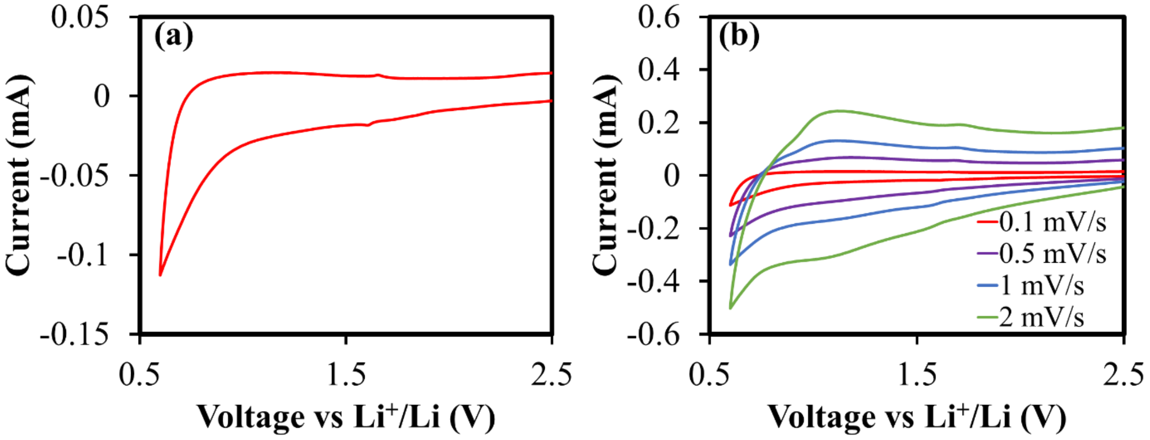

Figure C-11: Cyclic voltammetry for rGO/PVDF 80/20 wt.% electrode at (a) 0.1 mV/s and (b) at varying scan rates 0.1-2 mV/s.

---

[4] Supporting Information associated with the manuscript for Chapter 5 (to be submitted).

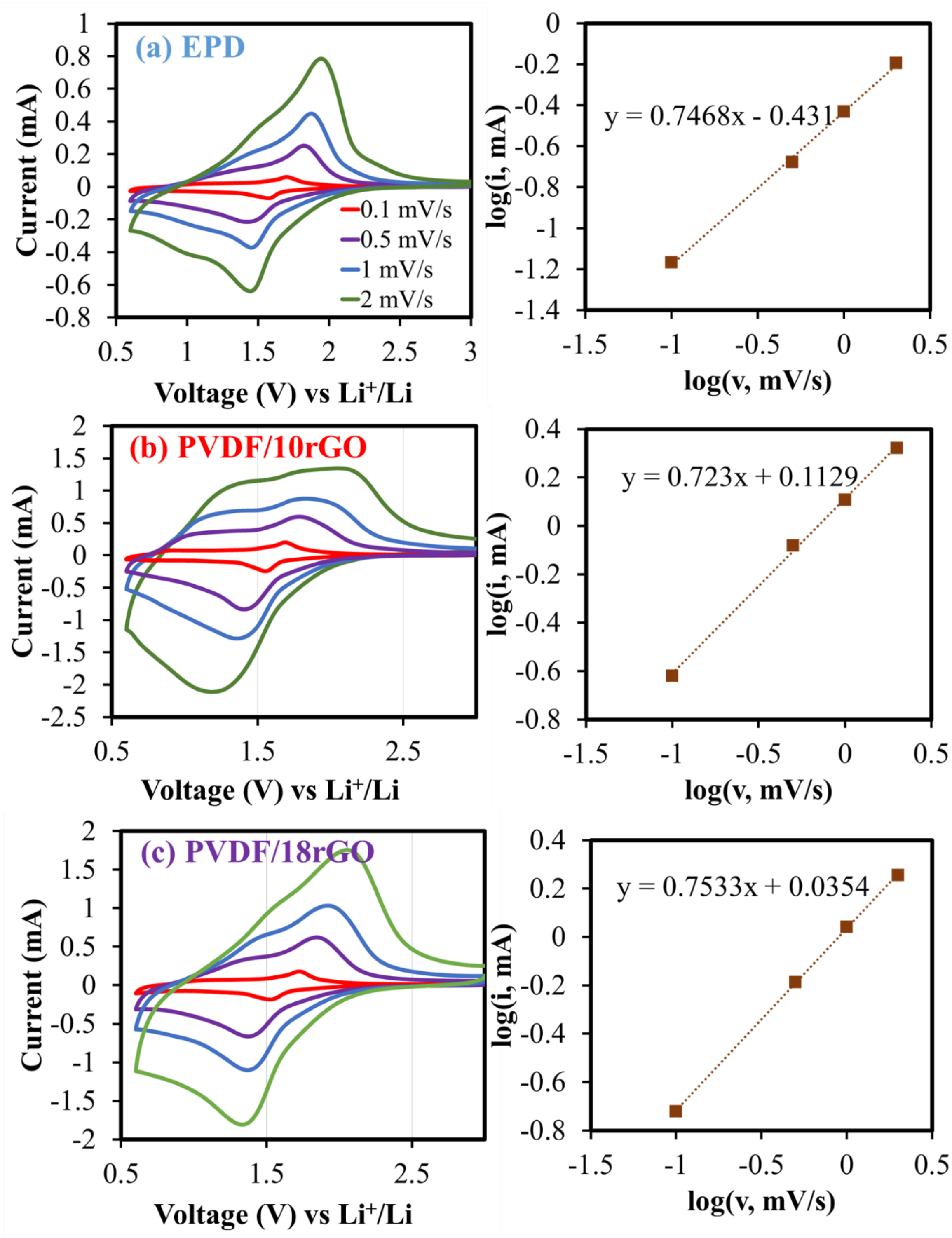

Figure C-12: Cyclic voltammetry at increasing scan rate for (a) EPD/rGO, (b) PVDF/10rGO, and (c) PVDF/18rGO electrodes along with the plotted log of peak cathodic Nb^{5+}/Nb^{4+} current vs. log of sweep rate.

[4] Supporting Information associated with the manuscript for Chapter 5 (to be submitted).

The pseudocapacitive contribution to the current response $i(V)$ can be calculated using the following equation [5–7]:

$$i(V) = k_1 v^{0.5} + k_2 v$$

Where $k_1 v^{0.5}$ and $k_2 v$ are the current contributions stemming from surface capacitive effects and diffusion-controlled intercalation respectively. The constants k_1 and k_2 can be determined at fixed potential (V) values by varying the scan rates (v). A plot of $i(V)/v^{0.5}$ vs. $v^{0.5}$ will yield k_1 and k_2 from the y-intercepts and slopes respectively. This calculation was performed on the EPD, PVDF/10rGO, and PVDF/18rGO and showed that the relationship was not linear across this voltage range. This indicates the pseudocapacitive contribution differs depending on the state-of-charge. Thus, the exact quantitative contribution from pseudocapacitance is difficult to calculate. An example of this is shown in Figure C-13.

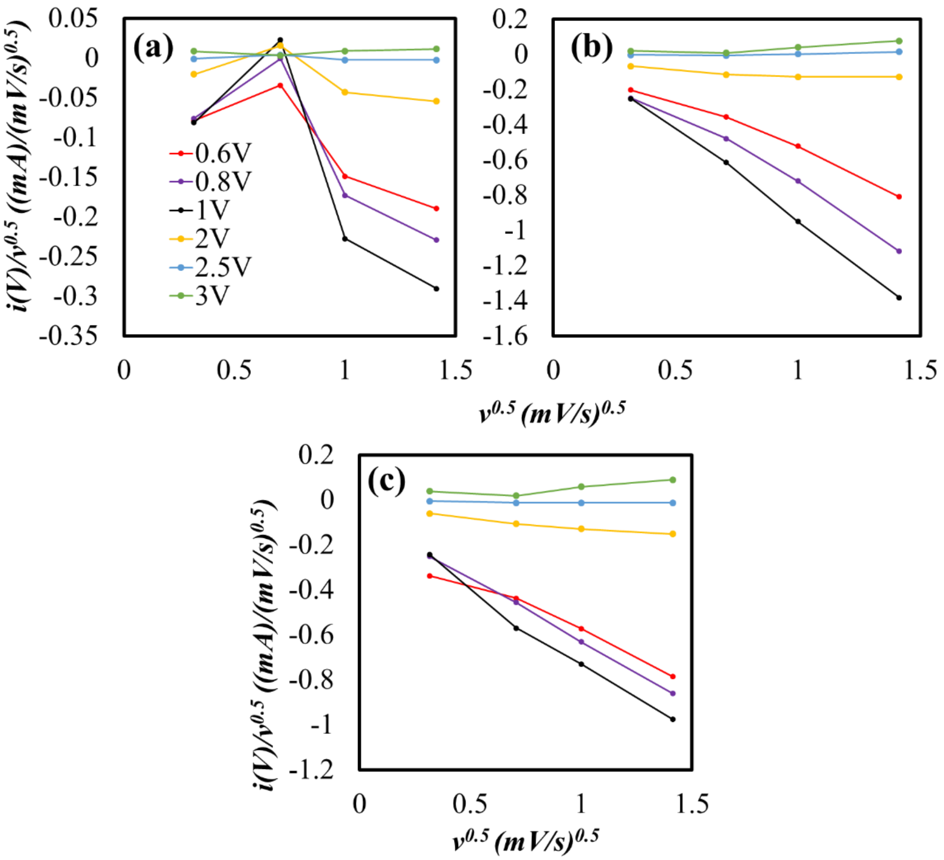

Figure C-13: correlation between $i(V)/v^{0.5}$ vs. $v^{0.5}$ for the cathodic sweep of the (a) EPD, (b) PVDF/10rGO, and (c) PVDF/18rGO electrode from 0.6V-3V at sweep rates of 0.1, 0.5, 1, and 2 mV/s showing loss of linearity at varying voltages.

---

[4] Supporting Information associated with the manuscript for Chapter 5 (to be submitted).

C.9 References

[1] S. Schweidler, L. de Biasi, A. Schiele, P. Hartmann, T. Brezesinski, J. Janek, Volume Changes of Graphite Anodes Revisited: A Combined Operando X-ray Diffraction and In Situ Pressure Analysis Study, J. Phys. Chem. C. 122 (2018) 8829–8835. doi:10.1021/acs.jpcc.8b01873.

[2] T. Pan, J. Alvarado, J. Zhu, Y. Yue, H.L. Xin, D. Nordlund, F. Lin, M.M. Doeff, Structural Degradation of Layered Cathode Materials in Lithium-Ion Batteries Induced by Ball Milling, J. Electrochem. Soc. 166 (2019) A1964–A1971. doi:10.1149/2.0091910jes.

[3] Y. Wang, H. Li, P. He, E. Hosono, H. Zhou, Nano active materials for lithium-ion batteries, Nanoscale. 2 (2010) 1294–1305. doi:10.1039/C0NR00068J.

[4] S. Lou, Y. Ma, X. Cheng, J. Gao, Y. Gao, P. Zuo, C. Du, G. Yin, Facile synthesis of nanostructured TiNb2O7 anode materials with superior performance for high-rate lithium ion batteries, Chem. Commun. 51 (2015) 17293–17296. doi:10.1039/C5CC07052J.

[5] S. Li, J. Chen, X. Gong, J. Wang, P.S. Lee, Holey graphene-wrapped porous TiNb 24 O 62 microparticles as high-performance intercalation pseudocapacitive anode materials for lithium-ion capacitors, NPG Asia Mater. 10 (2018) 406–416. doi:10.1038/s41427-018-0042-5.

[6] J. Wang, J. Polleux, J. Lim, B. Dunn, Pseudocapacitive Contributions to Electrochemical Energy Storage in TiO2 (Anatase) Nanoparticles, J. Phys. Chem. C. 111 (2007) 14925–14931. doi:10.1021/jp074464w.

[7] S. Lou, X. Cheng, Y. Zhao, A. Lushington, J. Gao, Q. Li, P. Zuo, B. Wang, Y. Gao, Y. Ma, C. Du, G. Yin, X. Sun, Superior performance of ordered macroporous TiNb2O7 anodes for lithium ion batteries: Understanding from the structural and pseudocapacitive insights on achieving high rate capability, Nano Energy. 34 (2017) 15–25. doi:10.1016/j.nanoen.2017.01.058.

---

[4] Supporting Information associated with the manuscript for Chapter 5 (to be submitted).